

Galvanic Localized Corrosion of Mild Steel under Iron Sulfide Corrosion Product Layers

A dissertation presented to  
the faculty of  
the Russ College of Engineering and Technology of Ohio University

In partial fulfillment  
of the requirements for the degree  
Doctor of Philosophy

Saba Navabzadeh Esmaeely

May 2018

© 2018 Saba Navabzadeh Esmaeely. All Rights Reserved.

This dissertation titled  
Galvanic Localized Corrosion of Mild Steel under Iron Sulfide Corrosion Product Layers

by

SABA NAVABZADEH ESMAEELY

has been approved for  
the Department of Chemical and Biomolecular Engineering  
and the Russ College of Engineering and Technology by

Srdjan Nestic

Russ Professor of Chemical and Biomolecular Engineering

Dennis Irwin

Dean, Russ College of Engineering and Technology

## ABSTRACT

NAVABZADEH ESMAEELY, SABA, Ph.D., May 2018, Chemical Engineering

Galvanic Localized Corrosion of Mild Steel under Iron Sulfide Corrosion Product Layers

Director of Dissertation: Srdjan Nestic

Iron sulfide corrosion product layers commonly form on mild steel surfaces corroding in aqueous H<sub>2</sub>S environments. These layers present a barrier which may retard the corrosion rate. However, their semiconductive nature leads to an acceleration of corrosion *via* galvanic coupling, by increasing the cathodic surface area. The electrocatalytic properties of different iron sulfides, which are important in this process, were heretofore unknown. The research herein reports cathodic reaction rates on the surfaces of geological specimens of both pyrite and pyrrhotite along with mild steel in HCl, CO<sub>2</sub> and H<sub>2</sub>S aqueous solutions at different pH values. The results show that in solutions where H<sup>+</sup> reduction dominates pyrite has similar electroactivity to X65 steel, while pyrrhotite exhibits approximately one order of magnitude smaller current densities. An extra wave observed in the cathodic sweeps on pyrrhotite was due to conversion of pyrrhotite to troilite. In aqueous CO<sub>2</sub> solutions similar results were obtained, while in H<sub>2</sub>S aqueous environments both pyrite and pyrrhotite showed similar electroactivity that was slightly less than that of X65 steel.

Zero resistance ammeter (ZRA) measurements were utilized in order to measure the galvanic current between an X65 mild steel surface and a pyrite or pyrrhotite surface; cathode to anode surface area ratios of *circa* 20 and 7 were employed in separate sets of experiments. The results were compared with the proposed model which takes into account

the reduction rates, changes in surface characteristics of the iron sulfides and their surface area.

Due to the electrical conductivity and the observed galvanic current between pyrrhotite and a mild steel, it was hypothesized that its presence in the corrosion product layer on a steel surface could lead to localized corrosion. Mild steel specimens (API 5L X65) were pretreated to form a pyrrhotite layer on the surface by high temperature sulfidation in oil. The pretreated specimens were then exposed to a range of aqueous CO<sub>2</sub> and H<sub>2</sub>S corrosion environments at 30 and 60°C. X-ray diffraction data showed that the pyrrhotite layer changed during these exposures; in an aqueous CO<sub>2</sub> solution it underwent dissolution, in a mixed CO<sub>2</sub>/H<sub>2</sub>S solution it partially transformed to troilite with some mackinawite formation. Initiation of localized corrosion was observed in both cases. It was concluded that this was due to a galvanic coupling between the pyrrhotite layer and the steel surface. The intensity of the observed localized corrosion varied with solution conductivity (NaCl concentration), a more conductive solution resulted in higher localized corrosion rates consistent with the galvanic nature of the attack.

One of the aims of the present research project was to establish physicochemical scenarios where localized corrosion should be expected in H<sub>2</sub>S containing environments. It is hypothesized that any disruption leading to a discontinuity of a corrosion product layer results in initiation of localized corrosion, where a galvanic coupling between the underlying steel and the conductive iron sulfide layer would lead to propagation of localized corrosion *via* a galvanic effect at an enhanced rate. This hypothesis was investigated based on five case studies from the research conducted by J. Ning, S.

Navabzadeh Esmaeely, W. Zhang, and S. Gao. In all cases, localized corrosion was observed confirming the proposed mechanism (case 1: a partially dissolved pyrrhotite layer; case 2: a disrupted pyrrhotite layer due to pyrite formation; case 3: a disrupted pyrrhotite layer due to interference by sand; case 4: a disrupted mackinawite layer due to pyrite interference; case 5: a poorly formed mackinawite layer).

## DEDICATION

*To*

*My parents, Parivash Jahanshahi and Heshmat Navabzadeh Esmaeely*

*For their immense unconditional love and support*

*And my niece Darya and my nephew Nikan who have changed my world for the better*

## ACKNOWLEDGMENTS

I would like to thank all and everyone who contributed in some way to my work reflected in this dissertation. First and foremost, I would like to express my sincere appreciation to my advisor Professor Srdjan Nestic, who has supported me during my Ph.D. journey at Ohio University. His commitment to education and his immense respect for the science has been a great inspiration. I dearly cherish our debates with Dr. Nestic which occasionally turned into heated intellectual discussions. What has always inspired me is that even in the midst of disagreement, Dr. Nestic heard my arguments and graciously counter argued never ceasing to challenge me further. He also gave me intellectual freedom in my work and supported my attendance at conferences and events that contributed to my professional growth.

I would also like to express my appreciation to my committee members, Dr. Marc Singer, Dr. Monica Burdick, Dr. Howard Dewald, Dr. David Young, and Dr. Dina Lopez for their interest in my work and willingness to be on my committee.

Additionally, I express my gratefulness to Dr. David Young for his unconditional support over these years. His friendship has changed both my professional and personal life for the better. I also thank my project leader Dr. Bruce Brown whose keen insights and suggestions greatly contributed to the quality of my work.

My accomplishments would not be possible without the help and support of fellow lab mates and collaborators at the Institute for Corrosion and Multiphase Technology (ICMT). I was fortunate to work with our administrative coordinator Ms. Becky Gill, technicians Mr. Alexis Barxias, Mr. Phillip Bullington and the lab engineer Mr. Cody

Shafer. Additionally, I would like to thank the students and staff at ICMT for making me feel supported and providing much needed assistance with H<sub>2</sub>S experiments. The H<sub>2</sub>S research team members generously offered their time and were my safety buddies during the difficult experiments, which are a great part of my work. I have been fortunate to work in a friendly and cooperative atmosphere.

I would like to acknowledge Russ College of Engineering faculty. My graduate experience benefitted greatly from the courses I took, the opportunities I had as a teaching assistant as well as a participant of high-quality seminars.

Finally, I would like to acknowledge friends and family who supported me during my time here, without their emotional support this journey would not be as joyful as it was.

## TABLE OF CONTENTS

	Page
Abstract.....	3
Dedication.....	6
Acknowledgments.....	7
List of Tables.....	11
List of Figures.....	12
Nomenclature.....	17
Chapter 1: Introduction.....	19
Chapter 2: Background.....	22
Chapter 3: Research Objectives.....	29
Chapter 4: Uniform Corrosion of Mild Steel in Aqueous H <sub>2</sub> S Environments.....	31
Experimental Method and Set-up.....	36
Modeling.....	40
Cathodic Reactions.....	40
H <sup>+</sup> Reduction.....	40
H <sub>2</sub> S Direct Reduction.....	43
H <sub>2</sub> O Reduction.....	44
Anodic Dissolution of Iron.....	45
Calculation Procedure.....	46
Results and Discussion.....	47
Summary.....	56
Chapter 5: Localized Corrosion of Mild Steel in H <sub>2</sub> S Containing Environments.....	58
Rate of Reduction Reactions on Iron Sulfides in Aqueous Acidic Solutions.....	58
Experimental Method and Set-up.....	59
Results and Discussion.....	63
Strong Acid Aqueous Solutions.....	63
Aqueous CO <sub>2</sub> Solution.....	71
Aqueous H <sub>2</sub> S Solution.....	74
Summary.....	77
Galvanic Current between X65-Pyrite and X65-Pyrrhotite.....	78
Experimental Method and Set-Up.....	80
Results and Discussion.....	83
Modeling.....	97
H <sup>+</sup> Reduction.....	99
Pyrrhotite Reduction to Troilite.....	101
Summary.....	114
Partially Dissolved Pyrrhotite Layer.....	115
Experimental Method.....	116
Experimental Setup (Electrochemical Measurements).....	116
Specimen Pretreatment (Pyrrhotite Layer Generation).....	117
Pyrrhotite Layer Surface Analysis.....	119

Results and Discussion .....	119
Pretreated Specimens .....	119
Corrosion of Steel with a Preformed Pyrrhotite Layer Exposed to an Aqueous CO <sub>2</sub> Solution .....	121
Corrosion of Steel with a Preformed Pyrrhotite Layer Exposed to Aqueous H <sub>2</sub> S Solution.....	129
Corrosion of Steel with a Preformed Pyrrhotite Layer Exposed to a Mixed CO <sub>2</sub> /H <sub>2</sub> S Solutions.....	135
Summary .....	140
Localized Corrosion under Pyrrhotite Containing Deposit Layers .....	141
Experimental Method and Setup .....	144
Results and Discussion .....	146
Summary .....	152
Role of Poorly Formed Mackinawite Layer on Mild Steel Corrosion .....	152
Experimental Method and Setup .....	153
Results .....	155
Discussion .....	167
Summary .....	170
Chapter 6: Overall Summary and Conclusions.....	171
Case 1 - A Partially Dissolved Pyrrhotite Layer .....	171
Case 2 –A Disrupted Pyrrhotite Layer due to Pyrite Formation .....	173
Case 3 – A Disrupted Pyrrhotite Layer due to Interference by Sand .....	175
Case 4 – A Disrupted Mackinawite Layer due to Pyrite Interference.....	176
Case 5 - A Poorly Formed Mackinawite Layer.....	177
Chapter 7: Future Work .....	180
References.....	181
Appendix A: Publications.....	193
Appendix B: Safety.....	195

## LIST OF TABLES

	Page
Table 1: Chemical reactions and associated equilibrium expressions in H <sub>2</sub> S environments .....	22
Table 2: Electrochemical reactions in H <sub>2</sub> S environments.....	23
Table 3: Iron sulfide polymorphs.....	24
Table 4: Iron sulfide properties.....	27
Table 5: Summary of results .....	35
Table 6: Experimental matrix .....	40
Table 7: Calculation of the H <sup>+</sup> reduction current density .....	42
Table 8: Calculation of H <sub>2</sub> S reduction current density .....	44
Table 9: Calculation of H <sub>2</sub> O reduction current density .....	45
Table 10: Calculation of current density for iron dissolution.....	46
Table 11: Experimental matrix .....	62
Table 12: Experimental matrix .....	83
Table 13: Calculation of the H <sup>+</sup> reduction current density on pyrite and pyrrhotite .....	100
Table 14: Calculation of pyrrhotite reduction current density.....	102
Table 15: Pyrite and pyrrhotite surface area .....	113
Table 16: Galvanic current densities vs. uncoupled X65 current densities .....	114
Table 17: Experimental matrix .....	119
Table 18: Experimental matrix .....	145
Table 19: Experimental matrix - glass cell .....	155
Table 20: API 5L X65 elemental analysis (wt%).....	155

## LIST OF FIGURES

	Page
Figure 1: Iron sulfide characteristics: (a) conductivity map [81]–[83]; (b) OCP in a deoxygenated solution at pH 4.0 ( $\pm 0.1$ ) [87]–[89].	27
Figure 2: Parity plot of the predicted data using a mechanistic sour corrosion model when there is no iron sulfide layer vs. experimental data at higher pH <sub>2</sub> S. [54], [58], [91], [92]	36
Figure 3: Experimental setup with 1. N <sub>2</sub> gas cylinder 2. H <sub>2</sub> S gas cylinder 3. rotameter 4. hot plate 5. temperature probe 6. gas inlet 7. Luggin capillary 8. pH-electrode 9. reference electrode 10. condenser 11. rotating cylinder shaft 12. working electrode 13. platinum counter electrode 14. stir bar (1/2" inch length) 15. sodium hydroxide solution 16. carbon scrubber 17. gas outlet	39
Figure 4: Potentiodynamic sweeps on mild steel in N <sub>2</sub> purged solutions, 1 wt. % NaCl, 30°C, and 1000 rpm RCE, scan rate 5 mV/S, (a) pH 2.0 (2 repeats); (b) pH 3.0 (6 repeats).	49
Figure 5: Potentiodynamic sweeps on mild steel in H <sub>2</sub> S saturated solution with 0.096 MPa H <sub>2</sub> S (960,000 ppm) in the gas phase, 3 wt. % NaCl, 30°C, and 1000 rpm RCE, scan rate 5 mV/s, (a) pH 3.0 (5 repeats); (b) pH 4.0 (4 repeats); (c) pH 5.0 (6 repeats).	52
Figure 6: Potentiodynamic sweeps on mild steel in H <sub>2</sub> S saturated solution with 0.096 MPa H <sub>2</sub> S (960,000 ppm) in the gas phase, pH 4.0, 3 wt. % NaCl, 30°C, and 100 rpm RCE, scan rate 5 mV/s, 2 repeats.	53
Figure 7: Potentiodynamic sweeps on carbon steel in H <sub>2</sub> S saturated solution with 0.053 MPa H <sub>2</sub> S (530,000 ppm) in the gas phase, pH 4.0, 3 wt. % NaCl, 80°C, and 1000 rpm RCE, scan rate 5 mV/S, 2 repeats.	54
Figure 8: LPR uniform corrosion rate of X65 in a bulk solution (a) 0.096 MPa H <sub>2</sub> S (960,000 ppm), 30°C, 1000 rpm, (b) 0.96 bar H <sub>2</sub> S, 30°C, pH 4.0, (C) 0.096 and 0.053 MPa H <sub>2</sub> S, pH 4.0, 3 wt% NaCl, B= 23 mV/decade less than 2 hours exposure.	55
Figure 9: Parity plot of the predicted uniform corrosion rate using a mechanistic sour corrosion model [20] for short term exposure of mild steel to H <sub>2</sub> S environments at different conditions in the absence of an iron sulfide layer on the surface vs. measured LPR corrosion rate.	56
Figure 10: XRD data (a) geological pyrite (b) geological pyrrhotite (c) synthesized troilite.	63
Figure 11: Potentiodynamic sweeps on X65 mild steel, pyrite, and pyrrhotite in N <sub>2</sub> purged solutions, 1 wt% NaCl, 30°C, and 1000 rpm RDE, scan rate 1 mVs <sup>-1</sup> , (a) pH 2.0, (b) pH 3.0, (c) pH 4.0 (d) pH 5.0.	69
Figure 12: Potentiodynamic sweeps on pyrrhotite in N <sub>2</sub> purged solutions, 1 wt% NaCl, 30°C, scan rate 1 mVs <sup>-1</sup> , 1000 rpm at different pH.	70
Figure 13: Potentiodynamic sweeps on pyrrhotite in N <sub>2</sub> purged solutions, 1 wt% NaCl, 30°C, scan rate 1 mVs <sup>-1</sup> , pH 3.0, at different rotational velocity.	70
Figure 14: Potentiodynamic sweeps on pyrrhotite and troilite in N <sub>2</sub> purged solutions, 1 wt% NaCl, 30°C, scan rate 1 mVs <sup>-1</sup> , different pH at 1000 rpm.	71

Figure 15: Potentiodynamic sweeps on X65 mild steel, pyrite and pyrrhotite in CO <sub>2</sub> purged solutions, 1 wt. % NaCl, 30°C, 1000 rpm, scan rate 1 mVs <sup>-1</sup> , (a) pH 2.0, (b) pH 3.0, (c) pH 4.0, (d) pH 5.0. ....	74
Figure 16: Potentiodynamic sweeps on X65 mild steel, pyrite, and pyrrhotite in aqueous solutions with 0.01 MPa H <sub>2</sub> S, 1 wt. % NaCl, 30°C, 1000 rpm, scan rate 1 mVs <sup>-1</sup> , (a) pH 2.0, (b) pH 3.0, (c) pH 4.0, (d) pH 5.0. ....	77
Figure 17: Galvanic current measurement specimens of mild steel X65 (CS) with (a) pyrite or (b) pyrrhotite geological materials. ....	83
Figure 18: X65 galvanic current density with respect to anodic surface area coupled with pyrite or pyrrhotite, in aqueous (a) strong acid purged with N <sub>2</sub> , (b) CO <sub>2</sub> sparged with 0.96 bar CO <sub>2</sub> , and (c) H <sub>2</sub> S sparged with 0.1 bar H <sub>2</sub> S, pH 4.0, at 30°C, 1wt% NaCl, 400 rpm 0.5" stir bar, cathode to anode surface area ratio was approximately 20 for each case. ....	86
Figure 19: Galvanic corrosion rate and uniform corrosion rate of X65 exposed to different aqueous solutions at pH 4.0, 30°C, 1wt% NaCl, 400 rpm 0.5" stir bar, cathode to anode surface area ratio approximately 20, 20 hours of exposure. ....	87
Figure 20: Galvanic current for pyrite or, pyrrhotite and X65 at their mixed potential in aqueous strong acid sparged with N <sub>2</sub> , at (a) pH 3.0, (b) pH 4.0, (c) pH 5.0, 30°C, 1wt% NaCl, and 300 rpm 0.5" stir bar. ....	90
Figure 21: Potentiostatic current on uncoupled pyrite, pyrrhotite and X65 at the stable mixed potential of coupled pyrite-X65 and pyrrhotite-X65 in N <sub>2</sub> purged solution at (a) pH 3.0, (b) pH 4.0, (c) pH 5.0, 30°C, 1wt% NaCl, and 300 rpm 0.5" stir bar. ....	92
Figure 22: Initial and final potentiostatic current on uncoupled pyrite and pyrrhotite at the stable mixed potential of coupled pyrite-X65 and pyrrhotite-X65 in N <sub>2</sub> sparged solution at (a) pH 3.0 (b) pH 4.0, (c) pH 5.0, 30°C, 1wt% NaCl, 300 rpm 0.5" stir bar. ....	96
Figure 23: Galvanic corrosion rate and uniform corrosion rate of X65 exposed to N <sub>2</sub> sparged aqueous solutions at pH 3.0, pH 4.0, and pH 5.0, at 30°C, 1wt% NaCl, 300 rpm 0.5" stir bar, cathode to anode surface area ratio approximately 7, 20 hours of exposure. ....	97
Figure 24: pH dependence of current density for pyrite electrode at -0.6V and -0.7 V (vs. saturated Ag/AgCl), at 1000 rpm, 30°C and 1 wt% NaCl. ....	98
Figure 25: pH dependence of current density for pyrrhotite electrode at -0.25V, -0.3 V, -0.75 V, and -0.8 V (vs. saturated Ag/AgCl), at 1000 rpm, 30°C and 1 wt% NaCl. ....	99
Figure 26: Potentiodynamic sweeps on pyrite in deoxygenated solutions, 1 wt% NaCl, 30°C, and 1000 rpm RDE, scan rate 1 mVs <sup>-1</sup> , at different pH values. ....	103
Figure 27: Potentiodynamic sweeps on pyrrhotite in deoxygenated solutions, 1 wt% NaCl, 30°C, and 1000 rpm RDE, scan rate 1 mVs <sup>-1</sup> , at different pH values. ....	103
Figure 28: Cathodic potentiodynamic sweeps prior and after potentiostatic experiments (a) pyrrhotite and troilite (b) measured and modeled pyrrhotite. ....	106
Figure 29: Cathodic potentiodynamic sweeps prior and after potentiostatic experiments on pyrite. ....	108
Figure 30: Modeled galvanic currents with a 7 times higher cathodic surface area in deoxygenated solutions, 1 wt% NaCl, 10 rpm RDE, (a) X65-pyrite at pH 3.0 (b) X65-pyrrhotite at pH 3.0, (c) X65-pyrite at pH 4.0, (d) X65-pyrrhotite at pH 4.0, (e) X65-pyrite at pH 5.0, (f) X65-pyrrhotite at pH 5.0. ....	111

Figure 31: Measured galvanic corrosion versus calculated galvanic corrosion in deoxygenated solution, 1 wt% NaCl, 30°C, (a) pH 3.0, (b) pH 4.0, (c) pH 5.0. ....	112
Figure 32: SEM images of representative pretreated steel specimen: (a) Top surface; (b) Cross-section.....	120
Figure 33: XRD pattern of the pretreated X65 specimens. (P: pyrrhotite, T: troilite)....	121
Figure 34: Corrosion rate and OCP of X65 specimen with pyrrhotite type layer vs. time of a sparged solution with 0.097 MPa CO <sub>2</sub> at 30°C and pH 4.0. ....	122
Figure 35: SEM image of pretreated specimens after exposure to an aqueous solution sparged with 0.097 MPa CO <sub>2</sub> at 30°C and pH 4.0 (a) 1 wt% NaCl, (b) no NaCl.....	123
Figure 36: Cross-section image of pretreated specimens after exposure to an aqueous solution sparged with 0.097 MPa CO <sub>2</sub> at 30°C and pH 4.0 (a) 1 wt% NaCl, (b) no NaCl. ....	124
Figure 37: XRD of the pretreated specimen after exposure to an aqueous solution sparged with 0.097 MPa CO <sub>2</sub> at 30°C and pH 4.0. (P: pyrrhotite, T: troilite) .....	125
Figure 38: SEM image of pretreated specimens after exposure to an aqueous solution sparged with 0.097 MPa CO <sub>2</sub> at 30°C and pH 4.0 without corrosion product layer (a) 1 wt.% NaCl, (b) no NaCl.....	127
Figure 39: Profilometry image of pretreated specimens after exposure to an aqueous solution sparged with 0.097 MPa CO <sub>2</sub> at 30°C and pH 4.0 without layer (a) 1 wt% NaCl, (b) no NaCl. ....	128
Figure 40: Pit penetration rate of the specimens in an aqueous solution sparged with 0.97 bar CO <sub>2</sub> at 30°C and pH 4.0. ....	128
Figure 41: (a) Corrosion rate of pretreated specimen (b) the OCP vs. time in an aqueous solution sparged with 0.01 MPa H <sub>2</sub> S in N <sub>2</sub> , 1 wt% NaCl. ....	130
Figure 42: SEM image of pretreated specimens after exposure to an aqueous solution sparged with 0.01 MPa H <sub>2</sub> S, 1 wt% NaCl at (a) 60°C and pH 6.2 (b) 30°C and pH 4.1. ....	131
Figure 43: Cross-section image of pretreated specimens after exposure to an aqueous solution sparged with 0.01 MPa H <sub>2</sub> S, 1 wt% NaCl at (a) 60°C and pH 6.2 (b) 30°C and pH 4.1.....	132
Figure 44: XRD of the pretreated specimens after exposure to an aqueous solution sparged with with 0.01 MPa H <sub>2</sub> S at 60°C and pH 6.2, 30°C and pH 4.0, 1 wt% NaCl. (P: pyrrhotite, T: troilite, M: mackinawite).....	133
Figure 45: SEM image of the pretreated specimens after exposure to an aqueous solution sparged with 0.01 MPa H <sub>2</sub> S, 1 wt% NaCl at (a) 60°C and pH 6.2, (b) 30°C and pH 4.0, after removal of the corrosion product layer.....	134
Figure 46: Profilometry image of the pretreated specimen after exposure to an aqueous solution sparged with 0.01 MPa H <sub>2</sub> S, 1 wt% NaCl at 30°C and pH 4.0 without layer... ..	135
Figure 47: (a) Corrosion rate (b) OCP of pretreated specimen vs. time sparged with 0.01 MPa H <sub>2</sub> S with and without 0.07 MPa CO <sub>2</sub> , at pH 6.1 and 60°C, 1 wt% NaCl.....	136
Figure 48: SEM image of pretreated specimens after exposure to an aqueous solution sparged with 0.01 MPa H <sub>2</sub> S, 1 wt% NaCl at 60°C and pH 6.2 (a) no CO <sub>2</sub> , (b) 0.07 MPa CO <sub>2</sub> .....	137

Figure 49: Cross section image of pretreated specimens after exposure to an aqueous solution sparged with 0.01 MPa H <sub>2</sub> S, 1 wt% NaCl at 60°C and pH 6.2 (a) no CO <sub>2</sub> , (b) 0.07 MPa CO <sub>2</sub> .	138
Figure 50: XRD of the pretreated specimens after exposure to an aqueous solution sparged with 0.01 MPa H <sub>2</sub> S at 60°C and pH 6.2 with and without 0.07 MPa CO <sub>2</sub> , 1 wt% NaCl. (P: pyrrhotite, T: troilite, M: mackinawite)	139
Figure 51: SEM image of the pretreated specimens after exposure to an aqueous solution sparged with 0.01 MPa H <sub>2</sub> S, 1 wt% NaCl at 60°C and pH 6.2, (a) without CO <sub>2</sub> , and (b) 0.07 MPa CO <sub>2</sub> , after removal of the corrosion product layer.	140
Figure 52: Profilometry image of pretreated specimen after exposure to an aqueous solution sparged with 0.01 MPa H <sub>2</sub> S, 0.07 MPa CO <sub>2</sub> , 1 wt% NaCl at 60°C and pH 6.2 without layer.	140
Figure 53: Under deposit specimen holder with and without the deposit layer.	146
Figure 54: X65 under deposit corrosion in sparged with 0.96 bar CO <sub>2</sub> , at pH 4.0, 30°C, 1wt% NaCl, and 300 rpm 0.5" stir bar, 2 gr of deposit.	147
Figure 55: SEM top views of specimens under (a) 0.25 gcm <sup>-2</sup> sand (b) 0.25 gcm <sup>-2</sup> pyrrhotite (c) 0.125 gcm <sup>-2</sup> pyrrhotite + 0.125 gcm <sup>-2</sup> pyrite, and (d) 0.125 gcm <sup>-2</sup> pyrrhotite + 0.125 gcm <sup>-2</sup> sand deposit exposed to aqueous CO <sub>2</sub> solution at pH 4.0, 30°C, 1wt% NaCl, 300 rpm 0.5" stir bar, 2 grams of deposit.	148
Figure 56: Pitting penetration of X65 under deposit exposed to aqueous CO <sub>2</sub> solution, at pH 4.0, 30°C, 1wt% NaCl, 400 rpm 0.5" stir bar, 0.25 gcm <sup>-2</sup> of deposit.	150
Figure 57: Profilometry image of the specimen under (a) pyrrhotite (b) pyrrhotite and pyrite (c) pyrrhotite and sand deposit, exposed to aqueous CO <sub>2</sub> solution at pH 4.0, 30°C, 300 rpm 0.5" stir bar, 1 wt% NaCl after the corrosion product was removed.	150
Figure 58: Comparison of general and localized corrosion rates of X65 under different size pyrrhotite particle deposits exposed to aqueous CO <sub>2</sub> solution, at pH 4.0, 30°C, 1 wt% NaCl, 400 rpm 0.5" stir bar, 2 grams of deposit.	151
Figure 59: (a) OCP (b) LPR Corrosion rate from X65 specimen in a 1 wt% NaCl, CO <sub>2</sub> saturated solution at 30°C, pH5 at 0.1 MPa total pressure, with and without H <sub>2</sub> S.	157
Figure 60: (a) pH variation (b) iron carbonate saturation degree (c) mackinawite saturation degree of the bulk solution during the experiments; 1 wt% NaCl CO <sub>2</sub> saturated solution at 30°C with at 0.1 MPa total pressure, with and without H <sub>2</sub> S.	160
Figure 61: SEM image of recovered X65 specimens after 6 days of exposure to an aqueous solution sparged with (a) no H <sub>2</sub> S, (b) 40 ppm H <sub>2</sub> S, (c) 90 ppm H <sub>2</sub> S in CO <sub>2</sub> at 30°C and pH 5.0, 1 wt% NaCl, 6 days exposure.	161
Figure 62: XRD of the recovered X65 after 6 days exposure to a saturated CO <sub>2</sub> solution at 30°C and pH 5.0 (a) no H <sub>2</sub> S, (b) 40 ppm H <sub>2</sub> S, (c) 90 ppm H <sub>2</sub> S, 1 wt% NaCl.	162
Figure 63: Cross section image of X65 specimen after 6 days of exposure to an aqueous CO <sub>2</sub> solution at 30°C and pH 5.0 (a) no H <sub>2</sub> S, (b) 40 ppm H <sub>2</sub> S, (c) 90 ppm H <sub>2</sub> S H <sub>2</sub> S, 1 wt% NaCl.	163
Figure 64: SEM image of X65 specimen after exposure to a saturated CO <sub>2</sub> solution at 30°C and pH 5.0 without corrosion product layer (a) no H <sub>2</sub> S, (b) 40 ppm H <sub>2</sub> S, (c) 90 ppm H <sub>2</sub> S, 1 wt% NaCl, 6 days exposure.	165

Figure 65: Profilometry image of recovered X65 specimens after 6 days of exposure to an aqueous CO <sub>2</sub> solution at 30°C and pH 5.0 without corrosion product layer (a) no H <sub>2</sub> S (b), 40 ppm H <sub>2</sub> S, (c) 90 ppm H <sub>2</sub> S, 1 wt% NaCl. ....	166
Figure 66: Weight loss corrosion rate and pitting penetration rate of X65 specimen in aqueous CO <sub>2</sub> solution with and without H <sub>2</sub> S at 30°C and pH 5.0, 1 wt% NaCl.....	167
Figure 67: H <sub>2</sub> S detection sensor layout in the H <sub>2</sub> S laboratory.....	196

## NOMENCLATURE

$\alpha_c$	Transfer coefficient of electrochemical reaction, -
$b$	Tafel slope, V
$c_i$	Concentration of species i in the bulk, mol.m <sup>-3</sup>
$c_{i,ref}$	Concentration of species i in the bulk at reference
$D_i$	Diffusion coefficient of species i, m <sup>2</sup> .s <sup>-1</sup>
$D_{i,ref}$	Reference diffusion coefficient of species i at reference
$d_{RCE}$	RCE diameter, m
$\rho$	Iron density, kg.m <sup>-3</sup>
$\Delta H$	Enthalpy of activation, j.mol <sup>-1</sup>
$E_{corr}$	Electrode corrosion potential, V
$E_{rev(H^+)}$	Reversible potential, V
$F$	Faraday's constant, C.mol <sup>-1</sup>
$I$	Ionic strength
$i_c$	Current density, A.m <sup>-2</sup>
$i_\alpha$	Charge transfer current density, A.m <sup>-2</sup>
$i_{d(j)}$	Mass transfer limiting current density for reaction j , A.m <sup>-2</sup>
$i_{o(j)}$	Exchange current density for reaction j, A.m <sup>-2</sup>
$i_{oref(j)}$	Exchange current density of reaction j at reference
$k_m$	Mass transfer coefficient, m.s <sup>-1</sup>
$k_{sol}$	Henry's constant, mol.bar <sup>-1</sup>
$K_{H_2S}$	H <sub>2</sub> S first dissociation constant
$K_{sp}$	$K_{sp}$ stands for the solubility limit
$K_1$	H <sub>2</sub> S first dissociation constant (molL <sup>-1</sup> )
$M_{fe}$	Iron molar mass, kg. kmol <sup>-1</sup>
$\mu$	Water viscosity, kg.m <sup>-1</sup> .s <sup>-1</sup>
$\mu_{ref}$	Water viscosity at reference conditions , kg.m <sup>-1</sup> .s <sup>-1</sup>
$\nu$	kinematic viscosity(m <sup>2</sup> s <sup>-1</sup> )

$P_{H_2S}$	H <sub>2</sub> S partial pressure, bar
$P_{H_2}$	H <sub>2</sub> partial pressure, bar
$R$	Universal gas constant, J.mol <sup>-1</sup> .K <sup>-1</sup>
$Re$	Reynolds number, -
$Sc$	Schmidt number, -
$Sh$	Sherwood number, -
$T_c$	Temperature, °C
$T_{ref}$	Reference temperature, K
$T_K$	Temperature, K
$\omega$	Rotational velocity (rad s <sup>-1</sup> )
$n$	The number moles of electrons transferred in the half
$\theta_{HS^-}$	Surface coverage

## CHAPTER 1: INTRODUCTION

New production of oil and gas is often from sour geologic hydrocarbon reservoirs. Sour is a common term for reservoirs that contain hydrogen sulfide ( $\text{H}_2\text{S}$ ), and in its absence the term sweet is frequently used.  $\text{H}_2\text{S}$  naturally forms by the decay of organic matter or by sulfate reduction, thermochemically or microbially, thus it is expected to be present in a geologic reservoir at different concentrations in combination with hydrocarbons and carbon dioxide ( $\text{CO}_2$ ). Due to hazards and technical difficulties associated with  $\text{H}_2\text{S}$  handling, reservoirs with high concentrations of  $\text{H}_2\text{S}$  would often not be exploited. However, their exploitation is required and possible as sweet reservoirs become depleted and new technologies emerge. The increasing demand for energy has led to exploration of all possible extraction options, which includes oil and gas production from highly sour wells.

Work related to environments that contain  $\text{H}_2\text{S}$  includes significant challenges in terms of both safety and economy.  $\text{H}_2\text{S}$  is a hazardous gas that presents great danger to human health for chronic exposures at concentrations as low as 10 ppm and, according to safety standards, being exposed to concentrations higher than 700 ppm may lead to immediate death. Hence, work at a location where  $\text{H}_2\text{S}$  is present is to be carried out with extreme caution. Safety issues have made conducting  $\text{H}_2\text{S}$  related experiments in laboratory research a serious challenge, which has resulted in limited availability of experimental data sets. Most of the reported experimental work has been performed at lower concentrations and partial pressures of  $\text{H}_2\text{S}$ . Corrosion research conducted at higher

partial pressures of H<sub>2</sub>S has been very rare and was often proprietary, with minimal data available in the open literature.

The abovementioned challenges have led to the current understanding of H<sub>2</sub>S corrosion being very rudimentary. Mild steel corrosion in aqueous hydrogen sulfide (H<sub>2</sub>S) has been one of the areas of corrosion related research since 20<sup>th</sup> century [1]–[13]. Early controlled H<sub>2</sub>S corrosion studies was initiated by a group of researchs, which Ewing [14] and Sardisco, *et al.*, [15] were among the first scholars focusing on H<sub>2</sub>S. This was later continued by other researchers [13], [16]–[20]. There have been several studies at the Institute for Corrosion and Multiphase Technology (ICMT), Ohio University, over the past decade dealing with H<sub>2</sub>S as a corrosive species. However, most of these studies have been conducted below 0.1 bar H<sub>2</sub>S with some focusing on the uniform corrosion while others looked at localized corrosion mechanisms. Lee [21] proposed a model for CO<sub>2</sub>/H<sub>2</sub>S corrosion with low concentrations of H<sub>2</sub>S up to 100 ppm at atmospheric pressure. He provided conclusive evidence for the immediate formation of a mackinawite corrosion product layer on a mild steel surface exposed to aqueous H<sub>2</sub>S. This explains the low uniform corrosion rate at low concentration of H<sub>2</sub>S. Later, Sun [22] studied the development of iron carbonate and iron sulfide corrosion products on mild steel and reported relatively faster kinetics for iron sulfide formation as compared to iron carbonate. A mass transfer control model, with the iron sulfide layer being dominant, was proposed with the main assumptions being that the reduction/oxidation reactions take place at the same place, suggesting that H<sub>2</sub>S corrosion was not considered an electrochemical process. However, Zheng [23] provided convincing evidence in support of the electrochemical

nature of the reaction involved in the H<sub>2</sub>S corrosion process. He investigated the electrochemical corrosion mechanisms related to H<sub>2</sub>S based on experimental results at different H<sub>2</sub>S partial pressures up to 0.1 bar. Zheng proposed a mechanistic electrochemical model for the uniform corrosion in the H<sub>2</sub>S solutions.

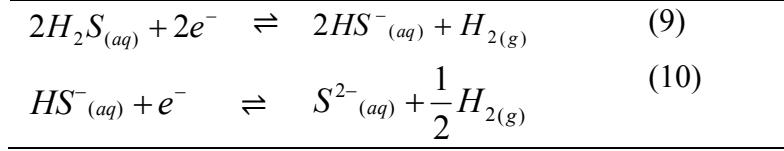
In other environments dealing with H<sub>2</sub>S corrosion, localized corrosion has been often referred to as one of the main causes of failure in the oil and gas industry where H<sub>2</sub>S is present [24]. Brown [25] studied the likelihood of localized corrosion in CO<sub>2</sub>/H<sub>2</sub>S corrosion at total pressures up to 8 bar and H<sub>2</sub>S partial pressures up to 0.1 bar in a large scale multiphase flow loop. He reported that the bulk pH, concentrations of carbonates and sulfides in solution, the ionic strength and temperature are key influential parameters related to localized corrosion. One of the difficulties associated with investigation of H<sub>2</sub>S corrosion is the possibility of formation of different iron sulfides [3], [26]–[31], which could result in different localized corrosion mechanisms. Ning [32] investigated the thermodynamics of different iron sulfides in detail, and suggested that under a corrosion product layer containing pyrite, localized corrosion takes place. However, the exact role of pyrite on localized corrosion was not fully investigated. The current study investigates the role of iron sulfide corrosion product layers in localized H<sub>2</sub>S corrosion of mild steel in aqueous solutions.

## CHAPTER 2: BACKGROUND

Compared to CO<sub>2</sub>, H<sub>2</sub>S brings many new challenges in corrosion studies, and unlike CO<sub>2</sub> corrosion, understanding of H<sub>2</sub>S corrosion is still in its infancy. In addition to the relative complexity of H<sub>2</sub>S environments due to the additional cathodic reaction and the H<sub>2</sub>S impact on the anodic reaction [23], formation of different iron sulfides [33] imposes further complications. As for the anodic reaction Iofa *et al.* [34] reported that aqueous H<sub>2</sub>S has a catalytic effect on the anodic dissolution of the steel upon its adsorption on the surface. Zheng *et al.* [20] elucidated the direct reduction of H<sub>2</sub>S on the steel surface which appeared as the “second wave” on the current density – potential plot with the H<sup>+</sup> reduction being the “first wave”. This will be discussed in more details in Chapter 4. The chemical and electrochemical reactions in the H<sub>2</sub>S environments are listed in Table 1 and Table 2, respectively.

Table 1: Chemical reactions and associated equilibrium expressions in H<sub>2</sub>S environments

$H_2S_{(g)} \rightleftharpoons H_2S_{(aq)}$	(1)	$[H_2S] = K_{H_2S,Sol} p_{H_2S}$	(2)
$H_2S_{(aq)} \rightleftharpoons HS^-_{(aq)} + H^+_{(aq)}$	(3)	$K_{H_2S} = \frac{[H^+][HS^-]}{[H_2S]}$	(4)
$HS^-_{(aq)} \rightleftharpoons S^{2-}_{(aq)} + H^+_{(aq)}$	(5)	$K_{HS^-} = \frac{[H^+][S^{2-}]}{[HS^-]}$	(6)
$Fe^{2+}_{(aq)} + HS^-_{(aq)} \rightleftharpoons FeS_s + H^+_{(aq)}$	(7)	$K_{pt} = \frac{1}{K_{sp}} = \frac{[H^+]}{[Fe^{2+}][HS^-]}$	(8)

Table 2: Electrochemical reactions in H<sub>2</sub>S environments

As mentioned earlier, iron sulfides can be found in various polymorphous and structurally related forms, the most common being mackinawite (FeS; tetragonal crystal structure), cubic ferrous sulfide (FeS), troilite (FeS; hexagonal structure), pyrrhotite (Fe<sub>1-x</sub>S; hexagonal or monoclinic), smythite (Fe<sub>3+x</sub>S<sub>4</sub>; hexagonal), greigite (Fe<sub>3</sub>S<sub>4</sub>; cubic spinel-type structure), pyrite (FeS<sub>2</sub>; cubic) and marcasite (FeS<sub>2</sub>; orthorhombic) [35]. Table 3 summarizes different iron sulfides with different crystalline structures. One of the difficulties associated with dealing with the iron sulfides is that they contain iron in different oxidation states (Fe<sup>2+</sup> and Fe<sup>3+</sup>), with a broad range of non-stoichiometric compositions and distinct physicochemical as well as electrical properties.

Among the listed iron sulfides, pyrrhotite, a nonstoichiometric compound, forms with different crystal structures [36], [37]; hexagonal pyrrhotite (Fe<sub>10</sub>S<sub>11</sub>) and monoclinic pyrrhotite (Fe<sub>7</sub>S<sub>8</sub>) are the most common pyrrhotites [35]. There are other polymorphs of pyrrhotite, however, there has not been any evidence to support different corrosion behavior as a result of the existence of different polymorphs of pyrrhotite.

Troilite, pyrrhotite and smythite all belong to a polymorphic group of iron sulfides, with troilite being the stoichiometric end-member pyrrhotite. Over time troilite transforms to pyrrhotite, which later transforms to pyrite [38], [39]; note that this transformation is accompanied by changes in electrical characteristics. If the thermodynamics of the system

allows, this sequence of transformations is quite common and relatively fast especially at high temperature and high H<sub>2</sub>S partial pressures.

Moreover, iron sulfides are classified as semiconductors [35] with their electrochemistry being an important area of investigation across different fields and applications including clean energy related research [40]–[44], corrosion of steel in H<sub>2</sub>S containing environments [45]–[50], geochemical studies [50]–[53], etc. These properties will be discussed at length in Chapter 5.

The formation and properties of different iron sulfides is governed by the H<sub>2</sub>S partial pressure, temperature, pH value [6], [14], [54]–[58], presence of CO<sub>2</sub> [45], salt, and available oxidants in the environment. An example where iron sulfide corrosion product layer formation is affected by the presence of dissolved salts such as NaCl is cubic iron sulfide that has not been reported to form in laboratory studies where NaCl was present. Cubic iron sulfide has been mostly reported in top of the line corrosion where the corrosion environment is in condensed water [3], [6], [59], [60].

Table 3: Iron sulfide polymorphs and related phases  
[61], [5], [11], [28], [62], [63]

Polymorph	Formula	Crystal Structure
Mackinawite	FeS	Tetragonal
Cubic FeS	FeS	Cubic
Troilite	FeS	Hexagonal
Pyrrhotite	Fe <sub>1-x</sub> S (x=0-0.17)	Hexagonal, Monoclinic
Smythite	Fe <sub>3+x</sub> S <sub>4</sub>	Hexagonal
Greigite	Fe <sub>3</sub> S <sub>4</sub>	Cubic
Pyrite	FeS <sub>2</sub>	Cubic

Thermodynamically, mackinawite is the least stable phase of iron sulfide with a rapid kinetics of formation. Thus, it often forms shortly upon steel exposure to the H<sub>2</sub>S solution [3], [28], [33], [64] and is expected to transform to more thermodynamically stable iron sulfides over time [4], [18], [65]. On the other hand, pyrite is the most thermodynamically stable iron sulfide with the slowest kinetics of formation [35].

Localized corrosion presents a threat to the integrity of mild steel pipelines and equipment in the oil and gas industry, given that it often proceeds at a much faster rate than uniform corrosion at the same conditions. It frequently results in failure, when the penetration depth exceeds far beyond the built in corrosion allowance, which is based on the predicted uniform corrosion rates. The lack of ability to predict localized corrosion and to detect it by using conventional corrosion monitoring methods [66], [67] makes a difficult situation even worse. Considering the often random spatial distribution of localized attack and the limited number of monitoring probes that can be installed in any given facility, the chances of detecting localized corrosion this way are slim at best. Also, internal line inspection techniques, which could theoretically detect localized attack, are complicated, expensive and therefore are used infrequently. Thus, a better understanding of localized corrosion mechanisms would be essential for the development of predictive models and implementation of corrosion mitigation strategies.

Since the presence of H<sub>2</sub>S in upstream oil and gas pipelines has been associated with an increased risk of localized corrosion [24], a significant research effort has been focused on understanding H<sub>2</sub>S corrosion mechanisms. The investigation on mild steel corrosion in such environments has been mostly concentrated on uniform corrosion [1]–

[15], [68]–[70]. There are few studies available in the literature that have addressed localized corrosion in H<sub>2</sub>S containing environments.

Localized H<sub>2</sub>S corrosion in electrolytes, typically an aqueous NaCl solution, has been attributed to three main reasons: the presence of elemental sulfur [71]–[74] partial formation/failure of the iron sulfide corrosion product layer [75], and formation of multiple iron sulfide polymorphs in a corrosion product layer, leading to non-uniform electrical conductivity [24], [46], [76]. The presence of chloride was also listed as a risk factor for localized corrosion in H<sub>2</sub>S containing environments [77]. One explanation is that chloride impact is via changing the electrolyte conductivity and iron sulfide solubility, which are directly linked to the abovementioned mechanisms [78].

The recently found electrochemical mechanisms involving direct reduction of H<sub>2</sub>S at the metal surface [20], [79], [80] and the role of different iron sulfides [3], [26]–[31] that can form on the metal surface in the corrosion process has made the investigation of localized corrosion in aqueous H<sub>2</sub>S even more challenging. In H<sub>2</sub>S solutions, the corrosion product layer can be composed of various iron sulfides with distinct physicochemical and electrical properties [35], [81]–[85]. The electrical conductivity of various iron sulfides is one of the key parameters. For example, pyrrhotite (Fe<sub>1-x</sub>S), troilite (FeS) and pyrite (FeS<sub>2</sub>) all occur as stable corrosion products and have similar electrical conductivities [81]–[83] (Table 4) while for the more unstable mackinawite (FeS) there are far fewer values reported for its conductivity [86]. Mackinawite has anisotropic electrical properties, being conductive in the direction of oriented layers in its crystal structure and much less conductive in the perpendicular direction [86]. The existence of conductive phases on a

steel surface significantly impacts the electrochemically driven corrosion process [12], [14], [20]. The conductive corrosion product layer may intensify the electrochemical reaction rate through providing a larger cathodic surface area, locally or uniformly across the corroding steel surface. However, this is only possible where the corrosive species reduction rates on these layers are not substantially retarded.

Table 4: Iron sulfide properties

Material	Resistivity [81]–[83]	OCP in a deoxygenated solution at pH 4.0 vs. sat. Ag/AgCl[87]–[89]
Mild steel	$\leq 10^{-8} \Omega\text{m}$	from -0.65 to -0.7 V
Pyrite	$10^{-5} - 10 \Omega\text{m}$	from +0.16 to -0.22 V
Pyrrhotite	$10^{-6} - 0.1 \Omega\text{m}$	from -0.08 to -0.22 V
Troilite	$10^{-6} - 0.1 \Omega\text{m}$	

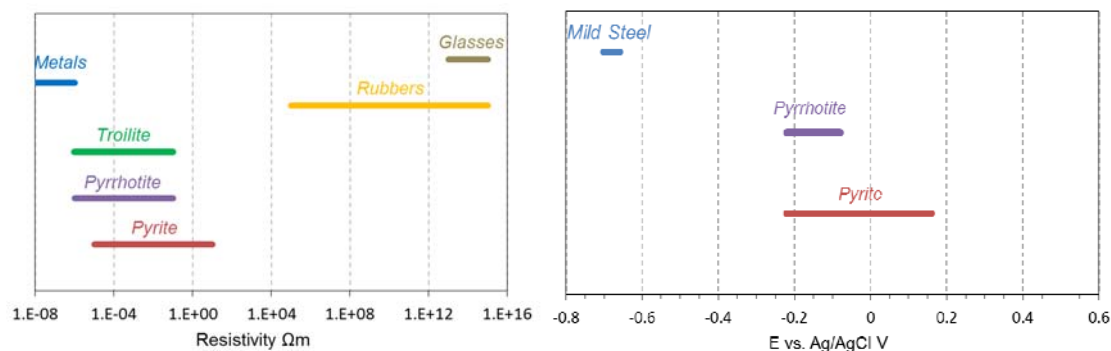


Figure 1: Iron sulfide characteristics: (a) conductivity map [81]–[83]; (b) OCP in a deoxygenated solution at pH 4.0 ( $\pm 0.1$ ) [87]–[89].

The objectives of the current study are listed in the following chapter (Chapter 3). A detailed presentation of uniform corrosion mechanisms of a mild steel exposed to high partial pressure  $\text{H}_2\text{S}$  environment is presented in Chapter 4. Localized corrosion

mechanisms under iron sulfide corrosion product layers are discussed at length in Chapter

5.

### CHAPTER 3: RESEARCH OBJECTIVES

Based on the presented background the following research questions are going to be addressed:

- Does the current understanding of sour corrosion mechanisms of mild steel and the resulting electrochemical model based on experiments conducted at low H<sub>2</sub>S partial pressures carry successfully to higher partial pressure conditions?
- What is the cause of localized corrosion in H<sub>2</sub>S containing environments and what is the effect of iron sulfide corrosion product layers.

In order to answer these questions, the following topics were individually investigated; and the results were used to propose an explanation of localized corrosion of mild steel exposed to H<sub>2</sub>S containing aqueous environments.

- Pyrite and pyrrhotite electroactivity
- Galvanic current between coupled X65-pyrite and X65-pyrrhotite
- Effect of a partially dissolved pyrrhotite layer on corrosion mechanisms
- Role of disrupted pyrrhotite layer due to the interference by pyrite and sand
- Role of poorly formed mackinawite layer on mild steel corrosion

Initially, it was deemed important to investigate pyrite and pyrrhotite electroactivity in different aqueous environments, the result of which is discussed in details in Chapter 5. This was an essential first step required to improve the understanding of underlying mechanisms of galvanically driven localized corrosion of mild steel under such layers.

The second step was to measure the galvanic current between X65 mild steel coupled with pyrite or pyrrhotite, the results of which are reported in Chapter 5.

The kinetics of formation for pyrrhotite is much faster than for pyrite [90], and pyrrhotite is a more common iron sulfide found in the corrosion product layers. Thus, it was of key importance to investigate the role of pyrrhotite on galvanically driven localized corrosion given its electronic conductivity, as described in Chapter 2. Its role was further studied under the interference of other phases, as explained in Chapter 5.

Most of the scenarios described above are associated with aqueous environments containing significant amounts of  $H_2S$ . In the last section (Chapter 5), localized corrosion under a non-uniform mackinawite corrosion product layer was investigated in order to understand the possibility of localized corrosion initiation under aqueous environments with very small (trace) amounts of  $H_2S$ .

## CHAPTER 4: UNIFORM CORROSION OF MILD STEEL IN AQUEOUS H<sub>2</sub>S ENVIRONMENTS<sup>1</sup>

The focus of much of the H<sub>2</sub>S related studies in the past has been on iron sulfide formation and the resulting effect on corrosion [3], [28]–[30]. Among limited available research results the vast majority come from experiments conducted at lower H<sub>2</sub>S partial pressures ( $p_{\text{H}_2\text{S}} < 10^{-2}$  MPa). Over the past few decades, a significant number of new oil and gas fields are sour, ranging from a few ppm up to 15-20 mol% H<sub>2</sub>S (e.g., the Kashagan Field [54]). This indicated a growing need for better understanding of H<sub>2</sub>S corrosion mechanisms and more effective prediction tools, particularly at higher  $p_{\text{H}_2\text{S}}$ .

Uncertainties related to modeling of H<sub>2</sub>S corrosion are particularly pronounced at higher  $p_{\text{H}_2\text{S}}$ . Under those conditions, limited results are available. Therefore, most of the models developed so far are based on lower  $p_{\text{H}_2\text{S}}$ . Despite the progress in understandings of H<sub>2</sub>S corrosion, there is still a lack of systematic studies where the parameter space has been explored in an organized way. Again, the problem is even more distinct at higher  $p_{\text{H}_2\text{S}}$  where the challenges associated with conducting experiments are much bigger. Corrosion data that have been reported under these conditions in the literature are very few, with widely scattered operating conditions.

There has been substantial progress in understanding and modeling of H<sub>2</sub>S-related corrosion since the 1990s. In 2009, Sun, *et al.*, [19] proposed a mechanistic H<sub>2</sub>S model that

---

<sup>1</sup> This chapter has been published as two journal publications: Corrosion J., 72, No.10, p. 1220 (2016) and Corrosion J., 73, No.2, p. 144 (2017), and also was presented at NACE International proceeding # 9098 (2017)

accounted for iron sulfide layer formation. It was assumed that the corrosion rate was always under mass transfer control with the iron sulfide layer being dominant, and it did not take into account the kinetics of electrochemical reactions. While this has been proven to be an overly restrictive assumption, the work conducted by Sun, *et al.*, [19] provided a foundation for further investigation and modeling of H<sub>2</sub>S corrosion mechanisms in a more systematic way.

In 2014 and 2015, Zheng, *et al.*, [20], [79] developed a mechanistic model of pure H<sub>2</sub>S and mixed CO<sub>2</sub>/H<sub>2</sub>S corrosion of mild steel that considered both the electrochemical and mass transfer controlled reactions. This model calculates the corrosion rate in the absence of iron sulfide layers. The authors were able to demonstrate that when mild steel was exposed to aqueous H<sub>2</sub>S, the direct reduction of H<sub>2</sub>S occurs on the steel surface as an additional hydrogen evolution reaction. The model was validated with experimental data from corrosion experiments conducted in an aqueous solution sparged with H<sub>2</sub>S at partial pressures from 10<sup>-7</sup> to 10<sup>-2</sup> MPa [20], [79].

The focus of the work presented below is on the higher pH<sub>2</sub>S and the corrosion mechanisms of mild steel at those conditions. One of the key hypotheses is that the mechanistic model [20], [79] based on low pH<sub>2</sub>S data, will perform at higher pH<sub>2</sub>S. To prove this, one needs reliable experimental data at higher pH<sub>2</sub>S, thus a number of experimental studies were found in the literature. The choice of literature data was made according to the following criteria: the corrosion study had to be comprehensively reported, including a proper description of the experimental set-up, procedures and data analysis. For example studies that failed to describe the water chemistry or some other key

experimental parameters were not considered, even if the corrosion results were reported. Furthermore, only the experimental data that were obtained in short-term exposures, prior to formation of protective iron sulfide corrosion product layers were considered, in order to compare with the model [20], [79].

The results are given in Figure 2(a), which shows parity plots where all of the selected experimental corrosion rate data from the literature at high  $\text{pH}_2\text{S}$  are plotted vs. the predictions made by the model. The solid lines in Figure 2 represent a perfect agreement, while the dashed lines represent a factor of two difference between the measured and predicted values. The different colors of the symbols indicate data from different experimental conditions and/or different studies.

In this comparison, it appears that the model over-predicts the majority of the measured corrosion rates. However, before drawing any conclusions about the performance of the model, it is essential to reconfirm that the experimental data were consistent and suitable for the present exercise. All the outliers, shown on the parity plot in Figure 2(a), were generated in a single experimental study by Omar, *et al.* [54]. The authors presented time series from long-term experiments, hence only the data points reported at time “zero” were used here. After analyzing the data of Omar, *et al.*, [54] it seems likely that an iron sulfide layer had formed on the specimens’ surface prior to their first reported corrosion rate measurement. The challenge the authors faced was in the fast kinetics of iron sulfide formation reactions in high  $\text{H}_2\text{S}$  containing environments [21]. They reported lower corrosion rates for higher  $\text{pH}_2\text{S}$  and  $\text{pCO}_2$  (as listed in Table 5), which can only happen if

protective iron carbonate and/or iron sulfide layers formed. Consequently, these data points were eliminated from the present study.

The reduced number of data points collected at high  $\text{pH}_2\text{S}$  now appears to be within a factor of two of the model predictions, as shown in Figure 2(b). The remaining eight data points came from three different high  $\text{pH}_2\text{S}$  corrosion studies, with widely different conditions and with no additional information on underlying corrosion mechanisms. This illustrates that there is a clear lack of reliable, systematically collected, coherent corrosion data from high  $\text{pH}_2\text{S}$  experiments, based on sound electrochemical measurements. Therefore, the work presented below is meant to fill this gap, and provide a solid base for verification of mechanisms and models for mild steel corrosion in high  $\text{pH}_2\text{S}$  environments.

Table 5: Summary of results

Legend	Test Conditions	Reported CR <sup>2</sup> mmy <sup>-1</sup>	Predicted CR mmy <sup>-1</sup>	Reference
a	3 MPa H <sub>2</sub> S; 1 MPa CO <sub>2</sub> ; pH 3.0; 1, 3 and 5 m/s; 80°C	0.8 to 2	27 to 28	Omar, <i>et al.</i> , [54]
b	1 MPa H <sub>2</sub> S; 0.33 MPa CO <sub>2</sub> ; pH 3.1; 1, 3 and 5 m/s; 80°C	1 to 10	19 to 21	
c	1 MPa H <sub>2</sub> S; 0.33 MPa CO <sub>2</sub> ; pH 3.2; 1, 3 and 5 m/s; 25°C	2 to 3	5 to 6	
d	0.14 MPa H <sub>2</sub> S; 0.06 MPa CO <sub>2</sub> ; pH 4.5; 1 m/s; 60°C	5.5	3.8	Kvarekval, <i>et al.</i> , [58]
e	0.088 MPa H <sub>2</sub> S; pH 4.2; 50°C	3.7	2.4	Abayarathna, <i>et al.</i> , [91]
	0.069 MPa H <sub>2</sub> S; pH 4.2; 70°C	5.1	3.9	
	0.03 MPa H <sub>2</sub> S; pH 4.2; 90°C	6.9	6.3	
	0.044 MPa H <sub>2</sub> S; 0.044 MPa CO <sub>2</sub> ; pH 4.2; 50°C	3.8	2.3	
	0.034 MPa H <sub>2</sub> S; 0.034 MPa CO <sub>2</sub> ; pH 4.2; 70°C	6.4	3.6	
	0.015 MPa H <sub>2</sub> S; 0.015 MPa CO <sub>2</sub> ; pH 4.2; 90°C	6.5	5.8	
f	1.6 MPa H <sub>2</sub> S; 90°C	8	12.8	Liu, <i>et al.</i> , [92]

---

<sup>2</sup> CR is referred to corrosion rate

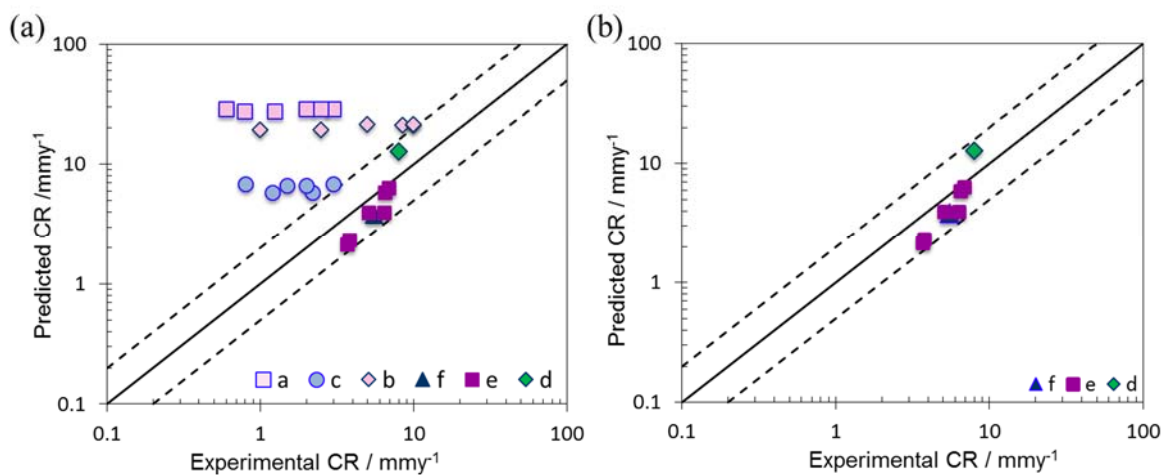


Figure 2: Parity plot of the predicted data using a mechanistic sour corrosion model when there is no iron sulfide layer vs. experimental data at higher  $p\text{H}_2\text{S}$ . [54], [58], [91], [92]

#### Experimental Method and Set-Up

Experiments were conducted in a glass cell (Figure 3), which was filled with 2 L of deionized water (DI) and 60.6 g NaCl to obtain a 3.0 wt% solution. The solution was deoxygenated by purging with  $\text{N}_2$  for at least 3 hours and was then saturated with  $\text{H}_2\text{S}$  by continuously sparging the solution with  $\text{H}_2\text{S}$  gas throughout the remainder of the experiment. The gas outlet was scrubbed using a 5 M solution of sodium hydroxide (NaOH) and a series of dry carbon scrubbers. The solution pH was adjusted to the desired value by addition of a deoxygenated hydrochloric acid (HCl) or a NaOH solution. It was deemed that equilibrium in the solution was reached approximately 1 hour after the introduction of  $\text{H}_2\text{S}$  gas into the glass cell.

A cylindrical mild steel API 5L X65 specimen was sequentially polished with 150, 400, and 600 grit sand paper, rinsed with isopropyl alcohol in an ultrasonic bath, and air dried. It was then mounted onto the rotating cylinder electrode (RCE) rotator and inserted

into the glass cell for electrochemical measurements. The rotator was set to the desired rotational speed and the corrosion measurements were initiated.

Electrochemical measurements were conducted using a Gamry Reference 600<sup>3</sup> potentiostat in a three electrode setup with a mild steel RCE as the working electrode (WE). A platinum mesh plate was used as the counter electrode (CE). An external saturated silver/silver chloride (Ag/AgCl) reference electrode (RE) was connected using a 1 molL<sup>-1</sup> KCl salt bridge *via* a Luggin capillary. Open circuit potential (OCP), measurements were done first to ensure that a reasonably stable state was reached, where the OCP drift was less than 1 mV per min and the magnitude of the OCP fluctuation was less than 1 mV (this occurred typically within the first 5 min). The OCP measurements were immediately followed by electrochemical impedance spectroscopy (EIS), in order to determine the solution resistance (IR drop). Then, the linear polarization resistance (LPR) measurements were conducted in order to estimate the polarization resistance ( $R_p$ ) and the corrosion rate. Finally, potentiodynamic measurements were conducted by first sweeping the potential from the OCP in the negative direction. After the OCP stabilized (usually within 10 min) the positive potential sweep was performed.

During the LPR measurements, the WE was polarized  $\pm 5$  mV from the OCP in order to determine the ( $R_p$ ), using a scan rate of 0.125 mV/s. The measured  $R_p$  was corrected for the solution resistance that was obtained from the high frequency portion of the EIS spectrum (frequency range around 5 kHz). The linear polarization constant,  $B = 23$  mV/decade, was used in the current work based on comparison of LPR

---

<sup>3</sup> Trade name

measurements with weight loss [20]. Potentiodynamic sweeps were conducted at a rate of 5 mV/s. While this is generally considered a very fast sweep rate, where transient effects could interfere, it was an imperative to complete the measurements in the shortest possible time, in order to avoid formation of protective iron sulfide layers. Also, the fast sweep rate minimized the atomic hydrogen diffusion in to the steel, which allowed the surface to recover to the OCP in a shorter period. In order to confirm that the fast sweep rate was acceptable, the potentiodynamic sweeps obtained at a low pH and low temperature (where formation of iron sulfide was slower) were compared by using sweep rates of 1 mV/s and 5 mV/s, with no substantial difference seen. Each potentiodynamic sweep was corrected for the ohmic drop due to solution resistance. The experiments were conducted at three different pH values, two different velocities and temperatures as summarized in Table 6.

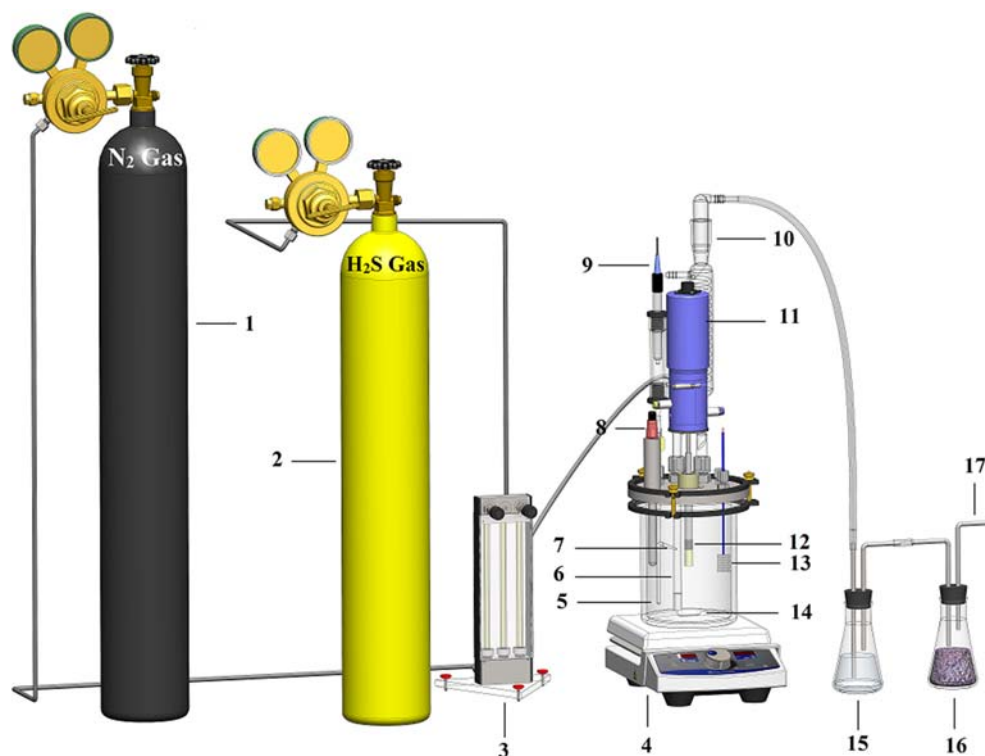


Figure 3: Experimental setup with 1. N<sub>2</sub> gas cylinder 2. H<sub>2</sub>S gas cylinder 3. rotameter 4. hot plate 5. temperature probe 6. gas inlet 7. Luggin capillary 8. pH-electrode 9. reference electrode 10. condenser 11. rotating cylinder shaft 12. working electrode 13. platinum counter electrode 14. stir bar (½" inch length) 15. sodium hydroxide solution 16. carbon scrubber 17. gas outlet<sup>4</sup>

---

<sup>4</sup> Image is courtesy of Cody Shafer

Table 6: Experimental matrix

Parameters	Conditions
Total pressure	0.1 MPa
pH <sub>2</sub> S in the gas phase	0, 0.053 and 0.096 MPa
pH value	2.0, 3.0, 4.0 and 5.0 ( $\pm 0.1$ )
Temperature	30 and 80°C
Test condition	1000, 100 rpm
Test solution	3 wt% NaCl
Material	X65
Methods	LPR, EIS, and Potentiodynamic Sweep

### Modeling

The electrochemical corrosion model used in the current study was previously described in detail by Zheng, *et al.* [23] Based on details presented in that publication and the references within, the model was reconstructed by using MATLAB – a numerical computing environment. In the text presented below, the key elements of the model are given, in order to facilitate the following the arguments and analysis. The model is based on a standard mathematical description of electrochemical, chemical and mass transfer processes, underlying the theory of aqueous H<sub>2</sub>S corrosion of mild steel.

#### *Cathodic Reactions*

In H<sub>2</sub>S containing environments three main cathodic reactions are considered: H<sup>+</sup> reduction, H<sub>2</sub>S reduction and H<sub>2</sub>O reduction.

#### *H<sup>+</sup> Reduction*

The H<sup>+</sup> reduction is the dominant cathodic reaction in acidic solutions:



Due to fast kinetics, it is often limited by  $\text{H}^+$  diffusion to the steel surface. The  $\text{H}^+$  reduction current density  $i_{c(\text{H}^+)}$  is calculated using the equations given in Table 7 below, which considers both charge transfer and mass transfer limiting currents [66]. The charge transfer current density is calculated by the Tafel equation. The mass transfer current density is calculated with the aid of a mass transfer coefficient, utilizing the empirical correlation between the Sherwood number and the Reynolds/Schmidt numbers for the flow geometry of interest (in the present case a RCE).[93]

Table 7: Calculation of the H<sup>+</sup> reduction current density<sup>5</sup>

$$\frac{1}{i_{c(H^+)}} = \frac{1}{i_{\alpha(H^+)}} + \frac{1}{i_{d(H^+)}} \quad (12)$$

$$i_{\alpha(H^+)} = i_{o(H^+)} 10^{(-E_{\text{corr}} - E_{\text{rev}(H^+)})/b_c(H^+)} \quad (13)$$

$$i_{o(H^+)} = i_{o\text{ref}} \left( \frac{c_{(H^+)}}{c_{\text{ref}(H^+)}} \right)^{0.5} e^{\frac{-\Delta H}{R} \left( \frac{1}{T} - \frac{1}{T_{\text{ref}}} \right)} \quad [94](14)$$

$$i_{o\text{ref}} = 0.03 \text{ Am}^{-2} \quad c_{(H^+)\text{ref}} = 1.10^{-4} \text{ molL}^{-1} \quad \Delta H = 30 \text{ kJmol}^{-1}$$

$$E_{\text{rev}(H^+)} = -\frac{2.303 RT}{F} \text{pH} - \frac{2.303 RT}{2F} \log P_{H_2} \quad (15)$$

$$b_c = \frac{2.303 RT}{\alpha_c F} \quad \alpha_c = 0.5 \quad b_c = 0.5 \text{ Vdecade}^{-1} \quad [95](16)$$

$$i_{d(H^+)} = k_{m(H^+)} F c_{(H^+)} \quad (17)$$

$$\text{Sh} = \frac{k_{m(H^+)} d_{\text{RCE}}}{D_{H^+}} = 0.0791 \text{Re}^{0.7} \text{Sc}^{0.356} \quad (18)$$

$$D_{H^+} = D_{\text{ref}H^+} \frac{T_K}{T_{\text{ref}}} \frac{\mu_{\text{ref}}}{\mu} \quad (19)$$

$$\mu = \mu_{\text{ref}} 10^{\frac{1.3272(20-T_C) - 0.001053(20-T_C)^2}{T_C + 105}} \quad (20)$$

<sup>5</sup> The nomenclature is defined in a separate section at the end of the document.

### *H<sub>2</sub>S Direct Reduction*

Aqueous H<sub>2</sub>S is a weak acid, and is the main source of H<sup>+</sup> ions, obtained by partial dissociation (Reaction (3) and Reaction (5)):

However, Zheng, *et al.*, [20], [79] provided conclusive evidence that the main contribution to the corrosion process is the direct reduction of aqueous H<sub>2</sub>S on the steel surface (Reaction (9)).

This reaction can be either under charge transfer control or limited by mass transfer. The overall current density for direct reduction of aqueous H<sub>2</sub>S on the steel surface can be calculated in a similar way as was done for H<sup>+</sup> reduction, shown in Table 7 [20].

Table 8: Calculation of H<sub>2</sub>S reduction current density

$$\frac{1}{i_{c(H_2S)}} = \frac{1}{i_{\alpha(H_2S)}} + \frac{1}{i_{d(H_2S)}} \quad (21)$$

$$i_{\alpha(H_2S)} = i_{o(H_2S)} 10^{(-E_{corr} - E_{rev(H_2S)})/b_{c(H_2S)}} \quad [20] \quad (22)$$

$$i_{o(H_2S)} = i_{o_{ref}} \left( \frac{c_{(H_2S)}}{c_{ref(H_2S)}} \right)^{0.5} \left( \frac{c_{(H^+)}}{c_{ref(H^+)}} \right)^{-0.5} e^{\frac{-\Delta H}{R} \left( \frac{1}{T} - \frac{1}{T_{ref}} \right)} \quad (23)$$

$$i_{o_{ref}} = 0.00015 \text{Am}^{-2} \quad c_{(H_2S)_{ref}} = 1.10^{-4} \text{molL}^{-1} \quad c_{(H^+)_{ref}} = 1.10^{-4} \text{molL}^{-1} \quad \Delta H = 60 \text{kJmol}^{-1}$$

$$i_{d(H_2S)} = k_{m(H_2S)} F c_{(H_2S)} \quad (24)$$

$$D_{H_2S} = D_{refH_2S} \frac{T_K}{T_{ref}} \frac{\mu_{ref}}{\mu} \quad (25)$$

$$c_{(H_2S)} = K_{sol(H_2S)} P_{H_2S} \quad (26)$$

$$K_{sol(H_2S)} = 10^{-6.34 - 2709/T_K - 0.11132 \cdot 10^{-3} T_K + 2 \frac{16719}{T_K} - 261.9 \log T_K}$$

[96] (27)

### H<sub>2</sub>O Reduction

In acidic aqueous solutions containing H<sub>2</sub>S, direct water reduction is rarely significant, however, it was included in the model in order to enable a better comparison with the potentiodynamic sweeps, as shown below.



There is no mass transfer limitation for the water reduction reaction, thus it was assumed that it is always under charge transfer control (Table 9).

Table 9: Calculation of H<sub>2</sub>O reduction current density

$$i_{c(H_2O)} = i_{\alpha(H_2O)} = i_{o(H_2O)} 10^{(-E_{corr} - E_{rev}(H_2O)) / b_c(H_2O)} \quad (29)$$

$$i_{o(H_2O)} = i_{o(ref)} \left( \frac{c_{(H_2S)}}{c_{ref(H_2S)}} \right)^{-0.1} \left( \frac{c_{(H^+)}}{c_{ref(H^+)}} \right)^{-0.5} e^{\frac{-\Delta H}{R} \left( \frac{1}{T} - \frac{1}{T_{ref}} \right)} \quad [20] \quad (30)$$

$$i_{o(ref)} = 0.00002 \text{Am}^{-2} \quad c_{(H_2S)ref} = 1.10^{-4} \text{molL}^{-1} \quad c_{(H^+)ref} = 1.10^{-4} \text{molL}^{-1} \quad \Delta H = 30 \text{kJmol}^{-1} \quad [97]$$

### *Anodic Dissolution of Iron*

In the presence of HS<sup>-</sup> in H<sub>2</sub>S aqueous solutions, the iron dissolution process follows a similar mechanism as originally proposed by Bockris, *et al.*, [95] for strong acids, and introduced by Ma, *et al.* [48]:



It is noteworthy that the current model does not take into account the H adsorption/absorption on the steel surface. It was assumed that iron dissolution was always under charge transfer control, with the anodic current density calculated using a Tafel equation as shown in Table 10.

Table 10: Calculation of current density for iron dissolution

$$i_{\alpha\text{Fe}} = i_{\text{oFe}} 10^{(-E_{\text{corr}} - E_{\text{rev}}(\text{Fe})) / b_a}$$

$$bc = 40\text{mVdecades}^{-1}$$

[95](34)

$$i_{\text{o(Fe)}} = i_{\text{oref}} \theta_{\text{HS}^-} e^{\frac{-\Delta H}{R} \left( \frac{1}{T} - \frac{1}{T_{\text{ref}}} \right)}$$

$$i_{\text{oref}} = 0.33\text{Am}^{-2} \quad \Delta H = 37.5\text{kJmol}^{-1}$$

[20](35)

$$\theta_{\text{HS}^-} = \frac{K_2 c_{\text{(HS}^-)}}{1 + K_2 c_{\text{(HS}^-)}}$$

$$K_2 = 3.5 \cdot 10^6$$

[20](36)

$$c_{\text{(HS}^-)} = \frac{K_{\text{H}_2\text{S}} c_{\text{(HS}^-)}}{c_{\text{(H}^+)}}$$

(37)

$$K_{\text{(H}_2\text{S)}} = 10^{(782.43945 + 0.361261 T_{\text{K}} - 1.6722 \cdot 10^{-4} T_{\text{K}}^2 \frac{20565}{T_{\text{K}}} - 142.741722 \ln T_{\text{K}})}$$

[98](38)

### Calculation Procedure

The model requires the temperature, pH, p<sub>H<sub>2</sub>S</sub>, RCE diameter and rotational velocity as the inputs, then it calculates the corrosion (open circuit) potential by solving the charge balance equation:

$$i_{\text{Fe}} = i_{\text{H}^+} + i_{\text{H}_2\text{S}} + i_{\text{H}_2\text{O}} \quad (39)$$

To calculate the corrosion current density the calculated corrosion potential is substituted into the expression for the anodic current density, shown in Table 10. The conversion from corrosion current density in  $A/m^2$  into the corrosion rate in mm/yr was done using Faraday's law:

$$CR = \frac{i_{\text{corr}} M_{\text{Fe}}}{2F\rho} (3600 \cdot 24 \cdot 365) \quad (40)$$

In order for the model to generate potentiodynamic sweeps needed for a comparison with the experimental data, the potential was varied across the whole measured range and the absolute value of the net current (total cathodic minus total anodic) is calculated as:

$$i = \left| i_{\text{H}^+} + i_{\text{H}_2\text{S}} + i_{\text{H}_2\text{O}} - i_{\text{Fe}} \right| \quad (41)$$

### Results and Discussion

To establish a baseline, the model calculations were first compared to potentiodynamic sweep data obtained in  $N_2$  saturated aqueous solutions at pH 2.0 and pH 3.0; the data were collected at room temperature in the absence of  $H_2S$ . The experimental repeatability and accuracy of the electrochemical measurements were quantified by repeating the experiments multiple times as shown in Figure 4. There, the points represent the average value of the current obtained in different repeats and the error bars denote the maximum and minimum values, all taken at exactly the same potential.

Figure 4 (a) shows that for pH 2.0, the experimentally measured current densities deviated from the model predictions by approximately 50% in the charge transfer region and about 25% in the limiting current region. The deviation seen in the limiting currents is statistically significant and possibly stems from excessive evolution of hydrogen gas

bubbles, which altered the otherwise well controlled mass transfer conditions in the vicinity of the electrode surface [12] at high current densities. The apparently large discrepancy seen in the charge transfer region of the potentiodynamic sweeps is not as significant, since the difference between calculated values and the averages of the measured values is of the same order of magnitude as the variation within the measured values themselves. In addition, it should be pointed out that the model was not developed to accurately predict in such low pH conditions and there may be some physico-chemical processes that are not captured well for the case of steel corrosion in strong acids. However, this is not a big concern since pH 2.0 lays outside the typical pH range seen in most H<sub>2</sub>S dominated conditions.

The situation is markedly better at pH 3.0 as shown in Figure 4 (b), where a very good agreement between the model and the measured data is seen, particularly for the cathodic reaction. These two sets of results obtained in the absence of H<sub>2</sub>S confirm that, both the model performance and the experimental procedures/techniques were at an acceptable level, providing a good foundation for the next step – comparison of the model with the data obtained in H<sub>2</sub>S saturated conditions.

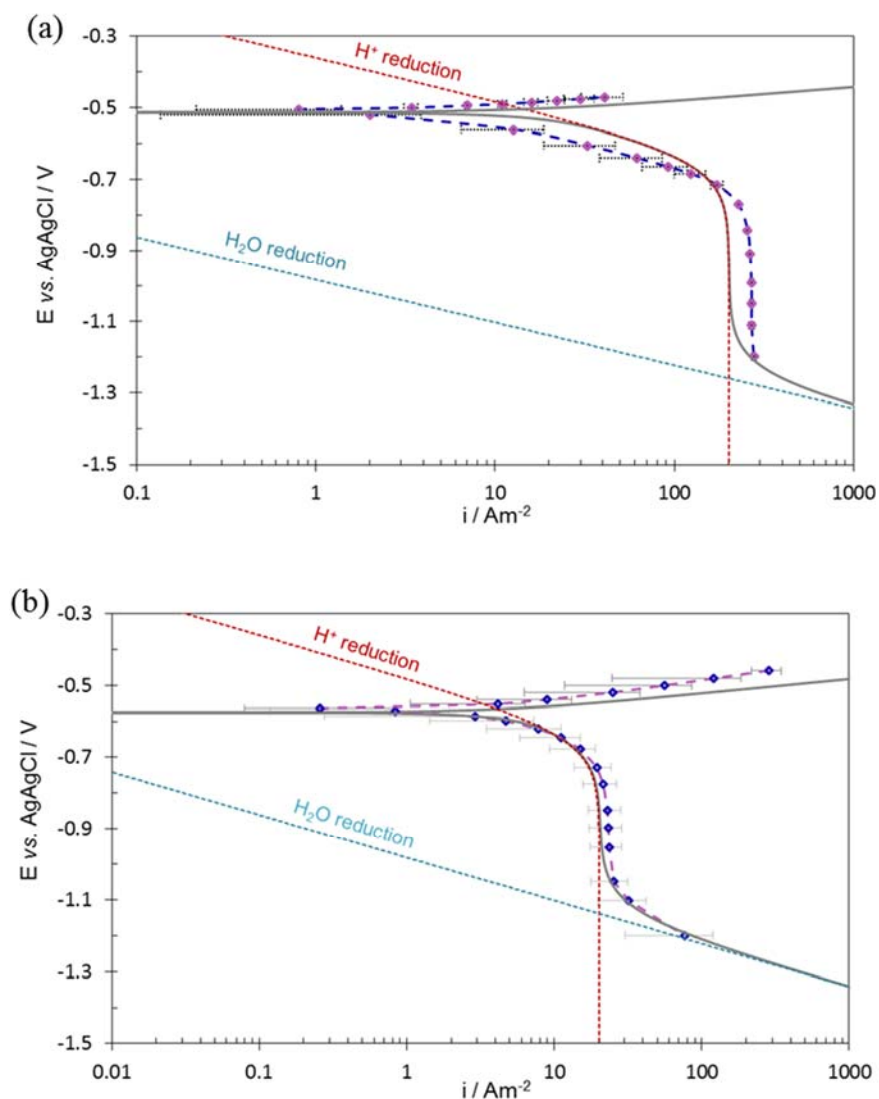


Figure 4: Potentiodynamic sweeps on mild steel in N<sub>2</sub> purged solutions, 1 wt. % NaCl, 30°C, and 1000 rpm RCE, scan rate 5 mV/S, (a) pH 2.0 (2 repeats); (b) pH 3.0 (6 repeats).

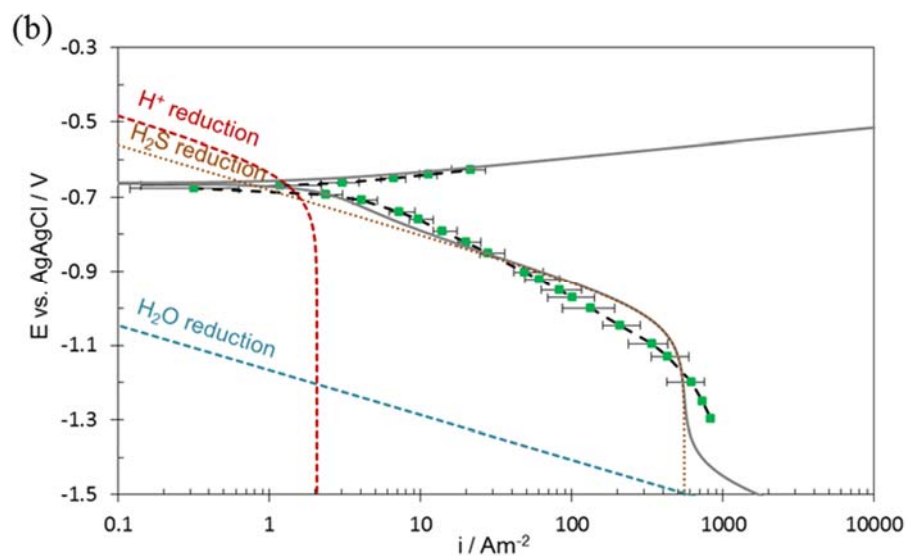
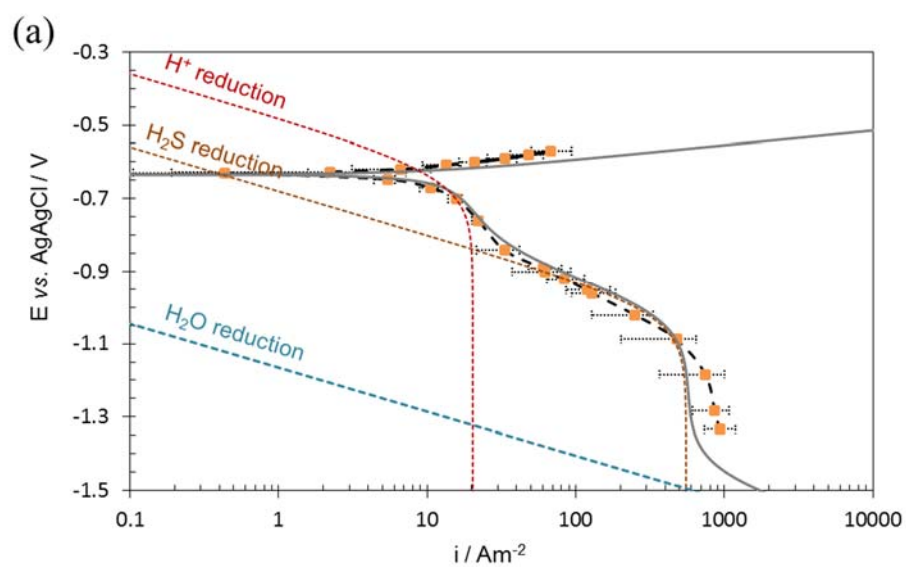
If we now turn our focus to H<sub>2</sub>S saturated solution, the effect of pH is shown in Figure 5. In Figure 5 (a) the measured data points show an average obtained from five repeats, conducted at pH 3.0. There is a very good agreement between the measured data and the calculated values, particularly at the lower current densities (<10 A/m<sup>2</sup>). The deviation in the limiting current at very high current densities (>500 A/m<sup>2</sup>) was probably

due to excessive formation of hydrogen gas bubbles at the electrode surface. The existence of the so called “double wave” comes from the two independent cathodic reactions and their limiting currents [20], [99].

Similar results were obtained at pH 4.0, see Figure 5 (b), which shows the averages of the data collected from four repeated experiments. Data from the experiments conducted at pH 5.0 are presented in Figure 5 (c), which shows the averages from experiments repeated six times. It is clear that at the higher pH values, the reduction of H<sub>2</sub>S dominates the rate of the cathodic reaction, as a result of a lower rate of H<sup>+</sup> reduction due to a lower concentration of H<sup>+</sup> ions. There seems to be a slight deviation between the measured and calculated Tafel slope for H<sub>2</sub>S reduction, which is difficult to explain. It may be due to a measurement error obtained at the higher current densities (>10 A/m<sup>2</sup>) or a result of the inaccuracy of the model at these conditions. Either way, this is not expected to affect the corrosion rate calculation in a significant way, since the corrosion current densities are typically below 10 A/m<sup>2</sup>.

For data collected at pH 5.0, presented in Figure 5 (c), there is an approximately 50 mV deviation between the calculated and the measured OCP. This problem is most likely associated with the modeling of the anodic (iron dissolution) current. To confirm this and eliminate any possible experimental error associated with iron sulfide layer formation during the cathodic sweeps (which were conducted first), a new experiment was organized where the anodic sweep was conducted on a freshly polished specimen. The results were consistent and provided conclusive evidence that the OCP deviation was not a result of erroneous measurements. It is difficult to postulate what the exact problem is, without a

more extensive investigation of the anodic reaction in H<sub>2</sub>S environments, which exceeds the scope of the present work. It is worth noting that the effect of adsorbed OH<sup>-</sup> on the rate of anodic iron dissolution was not considered in the model [20]. However, whether this is the main cause of the discrepancy seen at pH 5.0 requires further research.



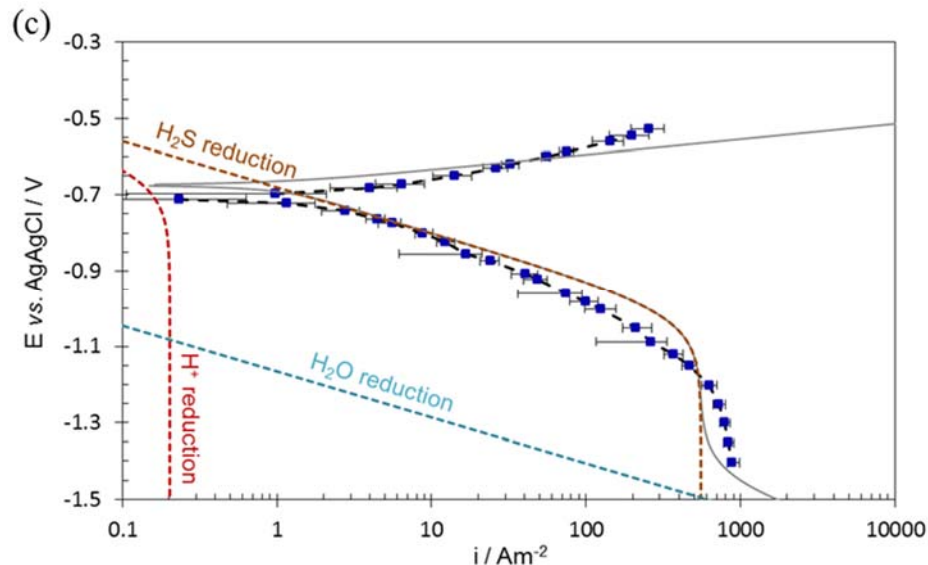


Figure 5: Potentiodynamic sweeps on mild steel in  $\text{H}_2\text{S}$  saturated solution with 0.096 MPa  $\text{H}_2\text{S}$  (960,000 ppm) in the gas phase, 3 wt. % NaCl, 30°C, and 1000 rpm RCE, scan rate 5 mV/s, (a) pH 3.0 (5 repeats); (b) pH 4.0 (4 repeats); (c) pH 5.0 (6 repeats).

The performance of the model at lower velocity is shown in Figure 6. This 100 rpm experiment was repeated twice. In this condition the measured data are in good agreement with the calculated values, particularly at the lower current densities. At the higher current densities the discrepancy seen in the cathodic limiting current is due to the abovementioned hydrogen gas bubble evolution. For the anodic reaction, the deviation is most likely due to accumulation of ferrous ions at the steel surface at lower rotation speed and formation of an iron sulfide layer, leading to some type of “pre-passivation” behavior.

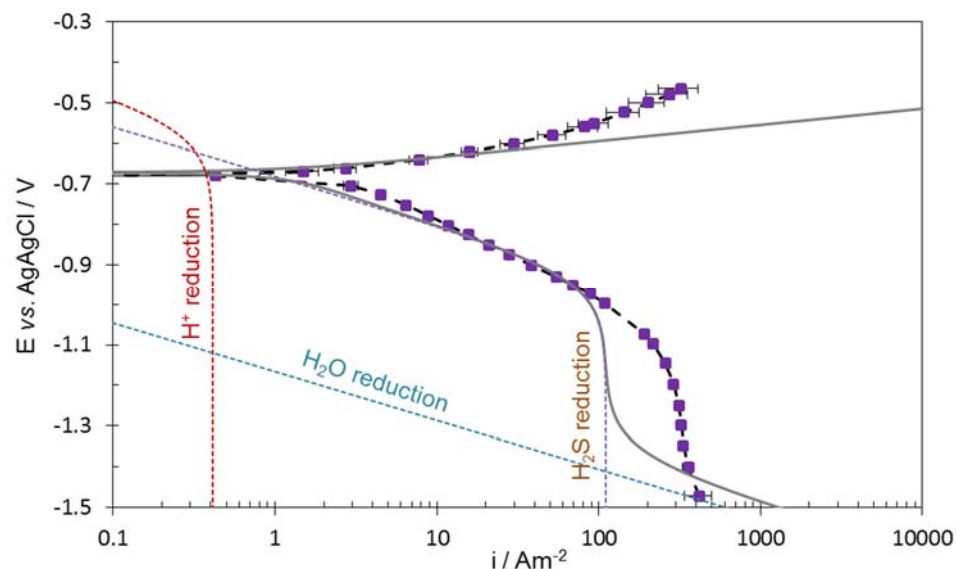


Figure 6: Potentiodynamic sweeps on mild steel in  $\text{H}_2\text{S}$  saturated solution with 0.096 MPa  $\text{H}_2\text{S}$  (960,000 ppm) in the gas phase, pH 4.0, 3 wt. % NaCl, 30°C, and 100 rpm RCE, scan rate 5 mV/s, 2 repeats.

Data from a higher temperature are presented in Figure 7, where the average of data from two potentiodynamic sweeps conducted at 80°C is shown. It is important to mention that the  $\text{pH}_{\text{H}_2\text{S}}$  in these experiments was 0.053 MPa due to an increase of the water vapor in the glass cell that was at atmospheric conditions. Similar to previous conditions, at lower current densities there is a very good agreement between measured and calculated data, while the discrepancies at higher current densities are present for the same reasons as described above.

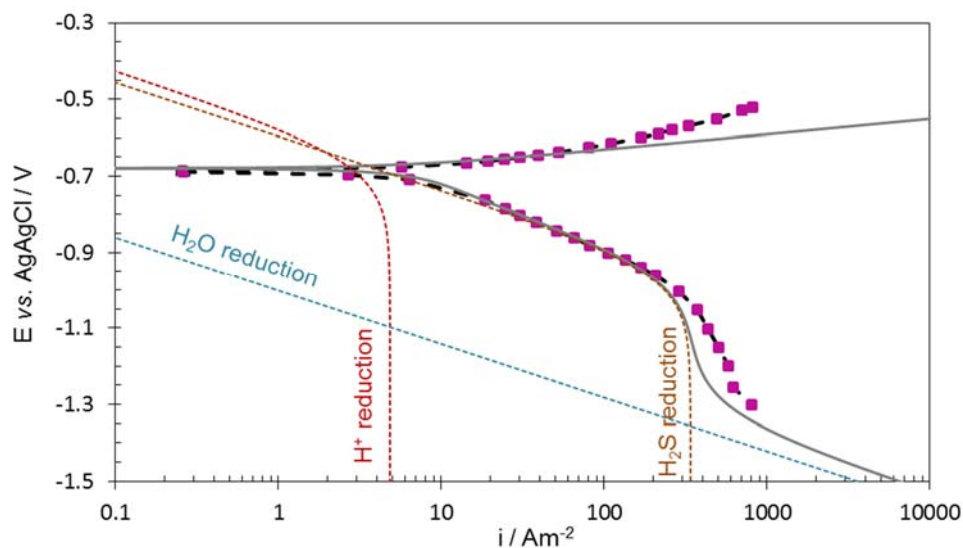


Figure 7: Potentiodynamic sweeps on carbon steel in H<sub>2</sub>S saturated solution with 0.053 MPa H<sub>2</sub>S (530,000 ppm) in the gas phase, pH 4.0, 3 wt. % NaCl, 80°C, and 1000 rpm RCE, scan rate 5 mV/S, 2 repeats.

LPR measurements were conducted in each experiment to measure the uniform corrosion rate, and the results are summarized in Figure 8. The bars are the average of the measured corrosion rate values from repeated experiments, and the error bars show the maximum and minimum deviation from the average. As would be expected, the bare steel corrosion rate decreased with pH but increased with velocity and temperature. The comparison of calculated and measured uniform corrosion rates is shown in Figure 9 as a parity plot. The open symbols are the original experimental data reported by Zheng, *et al.*, [20] for lower pH<sub>2</sub>S, which are almost in perfect agreement with the predicted corrosion rate. This is to be expected as the model [20] was developed and calibrated using the same low pressure data (ranging from 10<sup>-7</sup> – 10<sup>-2</sup> MPa pH<sub>2</sub>S). The bold squares in Figure 9 are the results from the current study, conducted at approximately 0.1 MPa pH<sub>2</sub>S, and are also

in good agreement with the model calculations. This is of importance as the current data were obtained in an independent study conducted at a much higher pH<sub>2</sub>S.

The current study confirmed that the physico chemical processes underlying H<sub>2</sub>S corrosion in the absence of protective iron sulfides are very similar across a wide range of pH<sub>2</sub>S. It also demonstrated that the abovementioned mechanistic corrosion model is valid across a broad range of pH<sub>2</sub>S conditions.

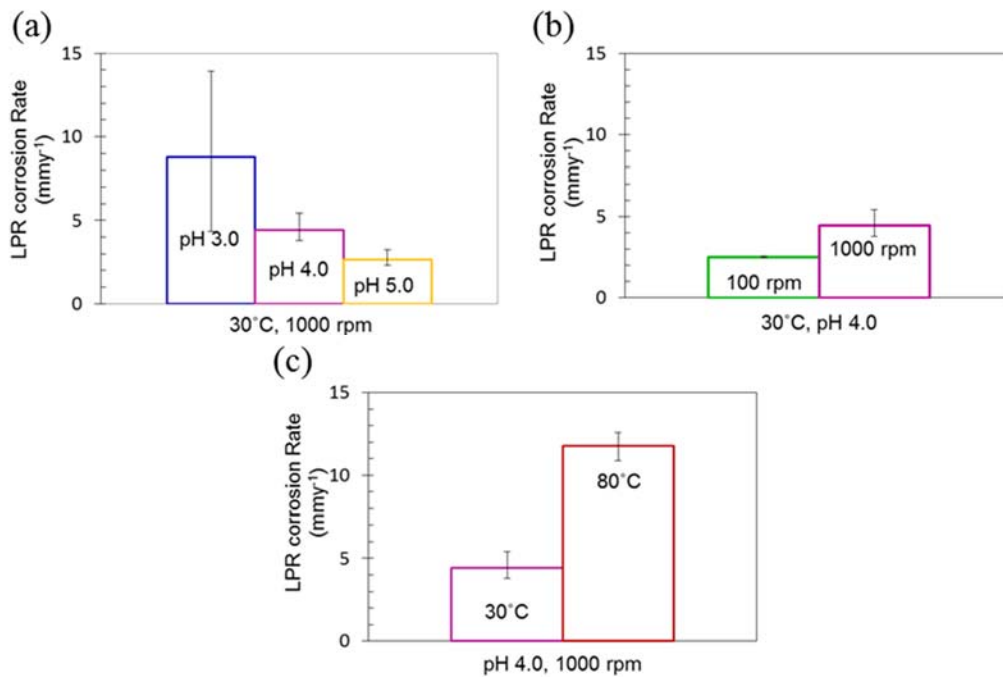


Figure 8: LPR uniform corrosion rate of X65 in a bulk solution (a) 0.096 MPa H<sub>2</sub>S (960,000 ppm), 30°C, 1000 rpm, (b) 0.96 bar H<sub>2</sub>S, 30°C, pH 4.0, (C) 0.096 and 0.053 MPa H<sub>2</sub>S, pH 4.0, 3 wt% NaCl, B= 23 mV/decade less than 2 hours exposure.

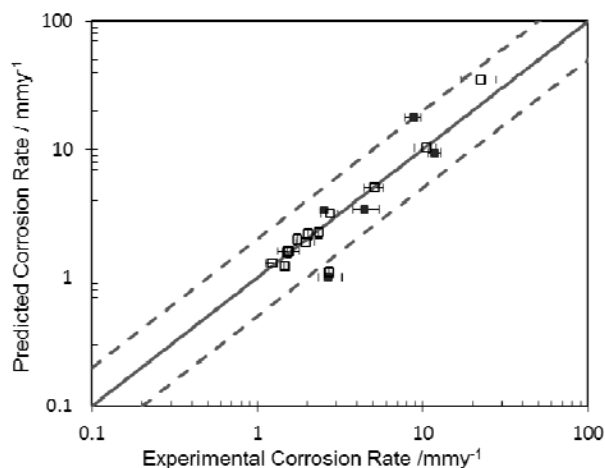


Figure 9: Parity plot of the predicted uniform corrosion rate using a mechanistic sour corrosion model [20] for short term exposure of mild steel to H<sub>2</sub>S environments at different conditions in the absence of an iron sulfide layer on the surface vs. measured LPR corrosion rate.

### Summary

- There is a lack of reliable, systematically collected, coherent corrosion data from experiments conducted at high pH<sub>2</sub>S, based on sound electrochemical measurements. The presented work was conducted to close this gap.
- It was found that the physico-chemical processes underlying H<sub>2</sub>S corrosion in the absence of protective iron sulfides are very similar across a wide range of pH<sub>2</sub>S.
- The existence of the so-called “double wave” in the cathodic sweeps arises from the two independent cathodic reactions: H<sup>+</sup> reduction and direct H<sub>2</sub>S reduction.
- It was demonstrated that the calculated corrosion rates based on the mechanistic corrosion model of Zheng, et al., [20], [79] are in reasonable

agreement with the experimental data for a broad range of H<sub>2</sub>S concentrations (up to 0.1 MPa partial pressure of H<sub>2</sub>S).

## CHAPTER 5: LOCALIZED CORROSION OF MILD STEEL IN H<sub>2</sub>S CONTAINING ENVIRONMENTS<sup>6</sup>

### Rate of Reduction Reactions on Iron Sulfides in Aqueous Acidic Solutions

The electrochemistry of iron sulfides investigated to date has been mostly focused on anodic reactions, such as phase transformation and dissolution [89], [100]–[103] which are predominantly important in weathering of iron sulfides in nature, oxidation during mining [104], [105] and transportation and metal extraction [100], [101], [106]. Other researchers in the same field focused almost exclusively on O<sub>2</sub> reduction on the surface of iron sulfides, which is the most important cathodic process in such systems [107]–[109]. Limited work has been reported on cathodic reactions in acidic media. In a study that was mostly focused on iron sulfide dissolution by both anodic and cathodic currents, Peters [102] stated that pyrite facilitates H<sup>+</sup> reduction due to its low overpotential. Some additional information on rates of hydrogen evolution on iron sulfide surfaces was reported in fuel cell related research, where it was found that pyrite is more active than greigite and pyrrhotite [43], [110].

The formation of iron sulfide corrosion product layers on mild steel corroding in aqueous H<sub>2</sub>S environments is common across a broad range of conditions. These porous layers offer some degree of protection by presenting a diffusion barrier and by covering

---

<sup>6</sup> This chapter has been published as three journal publications: The Electrochemical Society Journal, 164, No. 12, p. C664 (2017), Corrosion J., 73, No.9, p. 1099 (2017), and Corrosion J., 74 (2017) and also as two conference proceedings and one abstract at NACE Internationals 2018 Phoenix AZ, and ECS National Harbor MD (2017) respectively.

the steel surface, leading to retardation in anodic dissolution of iron. However, the semi-conductive nature of the iron sulfide of the corrosion product layers could also result in an acceleration of corrosion by significantly increasing the surface area for the cathodic reactions, leading to a galvanic coupling [111]. The significance of this effect remains unclear since the electrocatalytic properties of different iron sulfides are unknown. Furthermore, the presence of different iron sulfide layers has been associated with onset of localized corrosion [24], [46], [76], [112]. The exact mechanism behind this phenomenon is not yet clear. One possible explanation is related to different electroactivity of the various iron sulfides. Therefore, understanding of the rate of cathodic reduction of corrosive species in acidic media on different iron sulfide surfaces, as compared to steel, is of crucial importance. The work presented below covers an investigation of the cathodic reaction rates on the surfaces of pyrite, pyrrhotite, troilite, and mild steel in strong acid, CO<sub>2</sub> and H<sub>2</sub>S aqueous solutions at different pH values.

#### *Experimental Method and Set-Up*

Experiments were carried out in a glass cell containing 1 wt% NaCl solution as described in the experimental procedure in the previous chapter and the key experimental conditions as summarized in Table 11. Prior to each experiment, the solution was deoxygenated with N<sub>2</sub> or CO<sub>2</sub> gas for at least 3 hours. For the H<sub>2</sub>S experiments, following the N<sub>2</sub> purge, H<sub>2</sub>S was added to the gas stream introduced into the glass cell. The gas flow was maintained continuously throughout the duration of the experiments. Upon exiting the glass cell, the gas containing H<sub>2</sub>S was scrubbed using a 5 molL<sup>-1</sup> NaOH solution and

multiple dry carbon scrubbers. The solution pH was monitored<sup>7</sup> by a pH probe, deoxygenated HCl or NaOH solution was used to adjust the pH.

Four different types of working electrode were used in the current study, made from API 5L X65 steel, geological specimens of pyrite and pyrrhotite, and synthesized troilite. Scientific grade pyrite was purchased from Alfa Aesar<sup>8</sup>, pyrrhotite specimens were provided by Ward's Science<sup>9</sup> and synthesized troilite was purchased from Merck Group<sup>10</sup>. XRD analyses were conducted on the powdered samples of the iron sulfides to assure that there were no substantial impurities present. The results of XRD analyses are shown in Figure 10 confirming that the specimens did not contain any appreciable amount of impurities.

The X65 steel electrode was machined into a disc with a diameter of 5 mm and mounted onto a rotating disc holder made with Teflon<sup>TM</sup>. To make the iron sulfide electrodes, iron sulfide particles 3 to 7 mm in size were selected; they were sputter palladium (Pd) coated on one side and connected to a wire using a silver paste<sup>11</sup>, then embedded in a clear epoxy and mounted onto the rotating disc Teflon holder. The Pd coating was implemented to enhance the wiring connection with the iron sulfide surface, and minimize ohmic drop, which could interfere with the electrochemical measurements. The specimens were then sequentially abraded and polished down to a finish obtained with a 0.25  $\mu\text{m}$  diamond suspension, rinsed with DI water and cleaned with alcohol in an

---

<sup>7</sup> OMEGA 5992-02

<sup>8</sup> M03D03

<sup>9</sup> 470025

<sup>10</sup> CAC-No:1317-37-9

<sup>11</sup> SPI Supply 05063-AM

ultrasonic bath. Then they were dried using N<sub>2</sub> and photographed. Soon after, they were inserted into the experimental cell so that the exposure to air was minimized in order to avoid any oxide formation. The photographs were processed using ImageJ<sup>12</sup> open source software, in order to determine the irregularly shaped surface area of the iron sulfide working electrodes. Due to the deviation from a perfect circle, some discrepancy between measured and calculated limiting current densities was to be expected.

Electrochemical measurements were conducted using a Gamry Reference 600<sup>13</sup> potentiostat on rotating disc electrodes (RDEs) in a conventional three electrode setup, where a platinum mesh was used as a counter electrode and a saturated Ag/AgCl reference electrode, connected via a 1 molL<sup>-1</sup> KCl salt bridge and a Luggin capillary. OCP measurements were conducted prior to each potentiodynamic sweep, in order to make sure that it was stable, which took typically less than 5 minutes. X65 steel exposed to aqueous H<sub>2</sub>S environments is subject to formation of iron sulfide in H<sub>2</sub>S environments, given the relatively fast kinetics of reactions in such environments. However, due to the short term exposure before each potentiodynamic sweep, the possible interference of the iron sulfide layer on the measurements was minimized as previously demonstrated [20], [113]. EIS (DC potential 0 mV vs. OCP, AC potential 10 mV, frequency range 10KHz to 1 Hz at 10 points/dec), was performed in order to determine the ohmic drop in the solution at high frequencies (ca. 10 kHz), which was used to correct the raw potentiodynamic sweep data. Potentiodynamic sweeps were performed by polarizing the working electrode from the

---

<sup>12</sup> Trade name

<sup>13</sup> Trade name

OCP in the cathodic direction at a scan rate of  $1\text{mVs}^{-1}$ . The potentiodynamic sweeps were repeated at least three times for each condition, in some cases without removing the electrode from the solution and in other cases by using freshly polished electrodes in a newly prepared solution. The data reported below are the averages obtained in multiple repeats.

Table 11: Experimental matrix

Parameters	Conditions
Total pressure	0.1 MPa
Temperature	30 °C
Solution	1 wt% NaCl
Test condition	250, 1000 rpm
Material	API 5L X65, pyrite, pyrrhotite, troilite
Methods	EIS, and Potentiodynamic Sweep
Purged gas	Strong acid : 0.096 MPa N <sub>2</sub>
	aqueous CO <sub>2</sub> : 0.096 MPa CO <sub>2</sub>
	aqueous H <sub>2</sub> S : 0.01 MPa H <sub>2</sub> S, 0.086 MPa N <sub>2</sub>
pH value	2.0, 3.0, 4.0 and 5.0 ( $\pm 0.1$ )

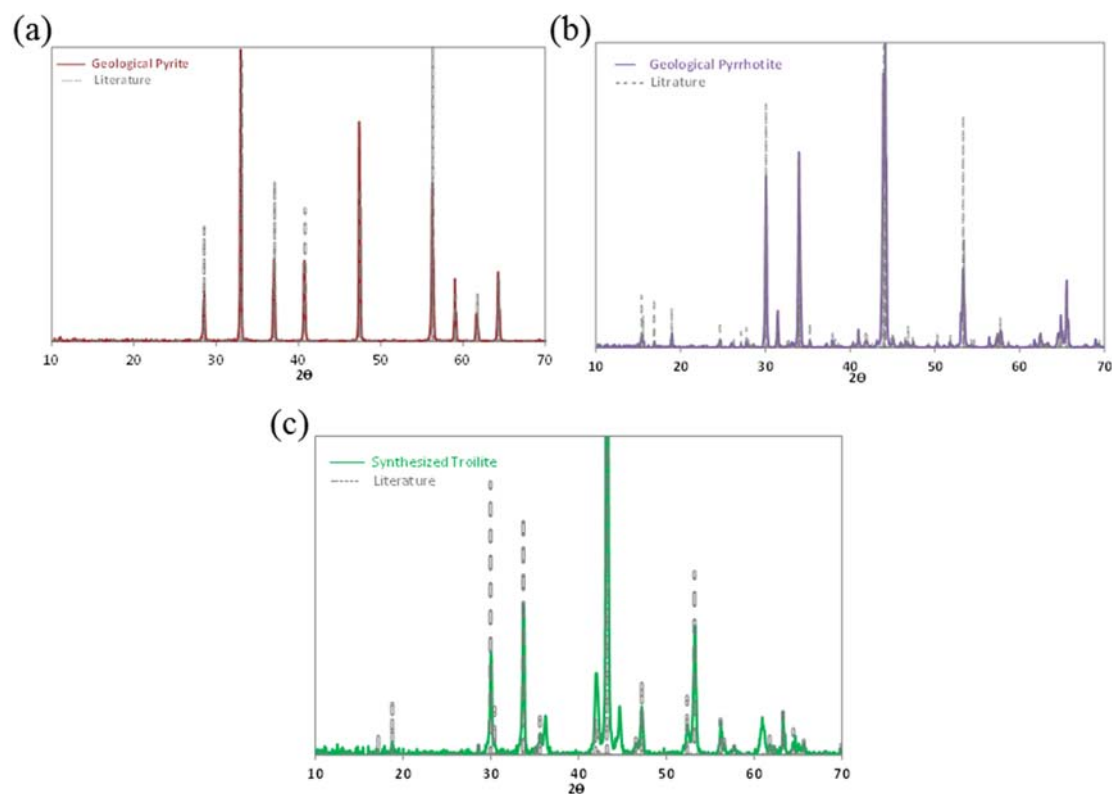


Figure 10: XRD data (a) geological pyrite (b) geological pyrrhotite (c) synthesized troilite.

## Results and Discussion

### Strong Acid Aqueous Solutions

In the first series of experiments shown in Figure 11, negative potential sweeps were obtained on pyrite, pyrrhotite, and X65 steel in NaCl + HCl aqueous solutions purged by N<sub>2</sub> at pH 2.0, pH 3.0, pH 4.0, and pH 5.0; the data were collected at room temperature. The points shown represent the average value of the current density obtained in different repeats at the same potential, while the error bars denote the maximum and minimum values. The lines represent the calculated current density for H<sup>+</sup> reduction on a mild steel surface obtained by using an electrochemical model previously proposed by Zheng *et al.* [79] and Esmaeely *et al.* [113]

In the current series of experiments,  $H^+$  reduction was considered as the main cathodic reaction (Reaction (11)) and water reduction was neglected.

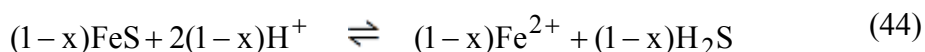
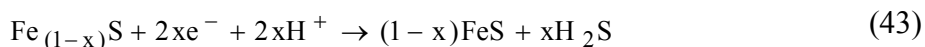
In the strong acid solution at pH 2.0 and pH 3.0, the pyrite surface showed similar electroactivity as the X65 steel surface (Figure 11 (a) and (b)). A full overlap of the  $H^+$  reduction curves can be seen in both the charge transfer and the mass transfer controlled regions, agreeing well with the model. However, the charge transfer rate for  $H^+$  reduction on pyrrhotite was approximately an order of magnitude slower, while the limiting current density was the same as on pyrite and X65 steel. Since the limiting current density is mass transfer controlled, one would expect that it is independent of the nature of the substrate. At pH 4.0 this behavior was not as obvious, while at pH 5.0 no clear limiting current density could be observed and the electroactivity of the different surfaces does not appear to follow the trend seen at lower pH (Figure 11 (c) and (d)). This will be discussed in more detail further below.

At pH 2.0, pH 3.0, and pH 4.0 the potentiodynamic sweeps on pyrrhotite showed an extra “wave”, with a limiting current density in the range much smaller than what was observed for  $H^+$  mass transfer. In order to understand the nature of the reduction reaction behind this extra wave, the potentiodynamic sweeps were conducted on pyrrhotite at different pH values (pH 2.0 to pH 5.0) as shown in Figure 12. It can be observed that the position of this wave changes with pH, with a limiting current density decreasing at higher pH values. This was further investigated by conducting potentiodynamic sweeps at different rotational speeds, as shown in Figure 13. There it can be seen that the limiting current densities for both  $H^+$  reduction and the extra wave approximately halved when the

rotational speed decreased by a factor of 4. This is consistent with the RDE mass transfer limiting current density expression defined by Levich.

$$i_d = (0.62)nFD^3\omega^{2/3}\nu^{-1/6}C \quad (42)^{14}$$

These experiments provided evidence that the extra wave obtained on the pyrrhotite surface was related, at least in part, to bulk conditions. Considering that in a deoxygenated strong acid solution the only reducible species are  $H^+$  and  $H_2O$ , the reaction behind the extra wave must have involved  $H^+$  as one of the reactants. Given that the extra wave was seen only on pyrrhotite it was presumed that the reaction involved both pyrrhotite and the  $H^+$  ions. Nicol *et al.*[114], and Mikhlin *et al.*[115] proposed that the following reactions take place upon pyrrhotite exposure to an acidic solution. pyrrhotite first reduces to troilite, followed by the chemical dissolution of troilite with release of  $H_2S$ .



The first reduction Reaction (43) is pH dependent, with an  $H^+$  dependency order of  $2x$  (where  $x = 0 - 0.2$  is the extent of  $Fe^{2+}$  deficiency in the pyrrhotite crystal lattice) [116]. This reaction proceeds faster at higher  $H^+$  concentrations. Therefore, it is hypothesized that the extra wave was due to reduction of pyrrhotite to troilite according to Reaction (43). The pH and velocity dependency shown in Figure 12 and Figure 13, as well as the order of the reaction are all consistent with this hypothesis.

---

<sup>14</sup> The nomenclature is defined in a separate section at the end of the document.

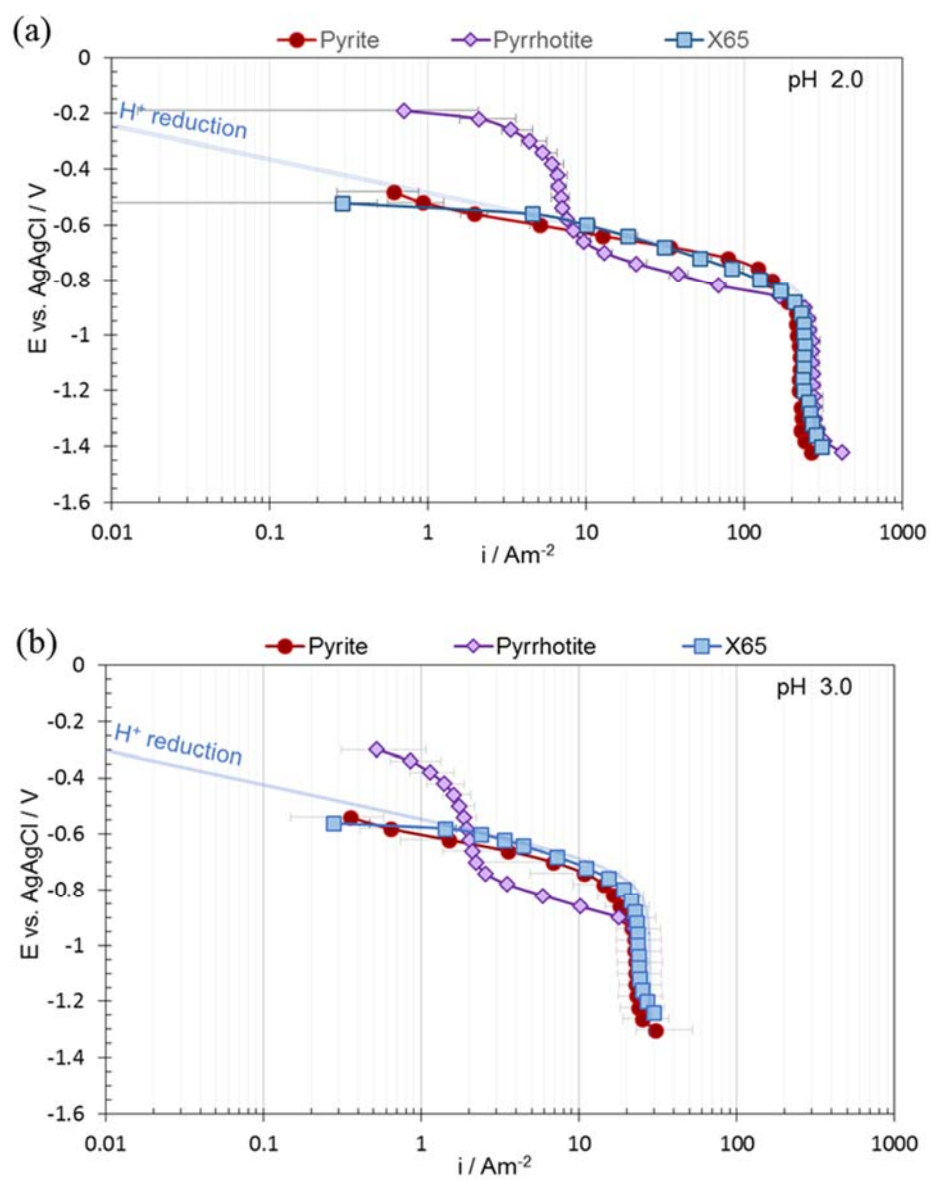
To confirm that the extra wave is reduction of pyrrhotite to troilite, potentiodynamic sweeps were repeated on troilite electrodes. Results obtained at two different pH values are compared with the ones from a pyrrhotite electrode shown in Figure 14. The absence of the extra wave on troilite and the overlap of the sweeps at both pH values provided convincing evidence for the abovementioned assumption. Therefore, we can conclude that upon cathodic polarization the surface of pyrrhotite converts to troilite, and the  $H^+$  reduction on pyrrhotite and troilite surfaces proceeds at practically the same rates.

One might wonder why XRD analyses were not conducted to investigate the transformation process. It is noteworthy that the transformation of pyrrhotite to troilite is a surface phenomenon, which takes place on the surface of pyrrhotite in an order of nano layers. Thus, conventional XRD would not be able to detect the thin layer of troilite on the transformed pyrrhotite electrode. More sensitive techniques such as XPS would be required for such analyses, although conducting such analyses *ex situ* would always be difficult.

In all experiments conducted on iron sulfide electrodes, another minor “wave” was obtained in the potentiodynamic sweeps at very low current densities in the OCP range for the iron sulfides, not shown in the graphs; this was presumed to be related to the impurities present at the surface of the electrodes, thus it was ignored. Peters and Majima also observed similar behavior during polarization of iron sulfides and attributed it to minor impurities in the parent material [101], [102].

The electroactivity of pyrite at higher pH values (pH 4.0 and pH 5.0) slightly decreased when compared to X65 steel (Figure 11 (c) and (d)) and the reason behind this behavior is unclear. Pyrrhotite at pH 4.0 showed similar behavior to that seen at lower pH

values, however, at pH 5.0, the potentiodynamic sweeps on pyrrhotite were very different, as it appeared that there is an acceleration of the  $H^+$  reduction. It is believed that this is an experimental artifact and is the result of  $H_2S$  production due to pyrrhotite conversion to troilite and troilite dissolution according to Reaction (43) and Reaction (44). The produced  $H_2S$ , in the vicinity of the electrode surface alters the surface pH through a buffering effect. Moreover, produced  $H_2S$  at the surface can be reduced, which leads to even larger overall cathodic current densities. At pH 2.0, pH 3.0, and even pH 4.0, due to a considerably higher  $H^+$  concentration, the generation of a small amount of  $H_2S$  did not produced a significant interference. In summary, the potentiodynamic sweeps obtained at pH 4.0 and particularly at pH 5.0 should be interpreted with this in mind.



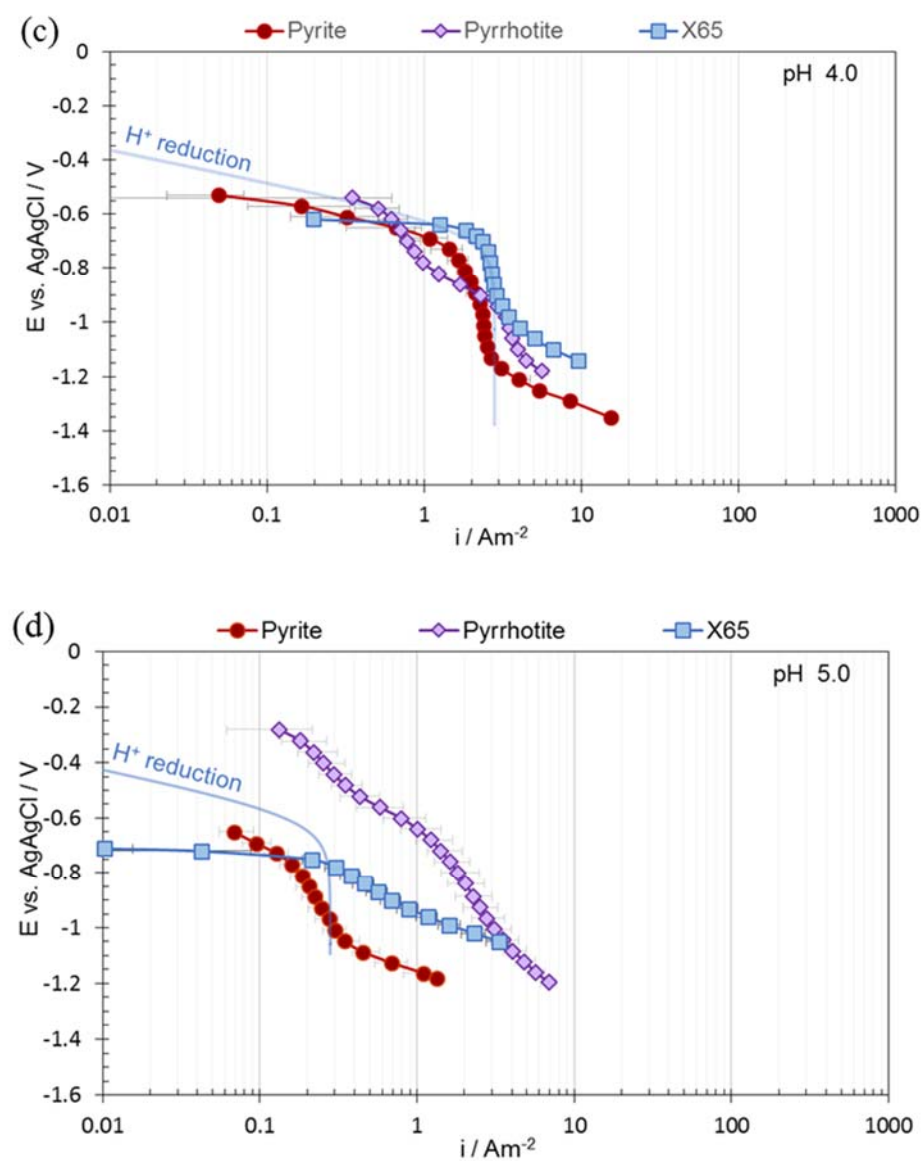


Figure 11: Potentiodynamic sweeps on X65 mild steel, pyrite, and pyrrhotite in N<sub>2</sub> purged solutions, 1 wt% NaCl, 30°C, and 1000 rpm RDE, scan rate 1 mVs<sup>-1</sup>, (a) pH 2.0, (b) pH 3.0, (c) pH 4.0 (d) pH 5.0.

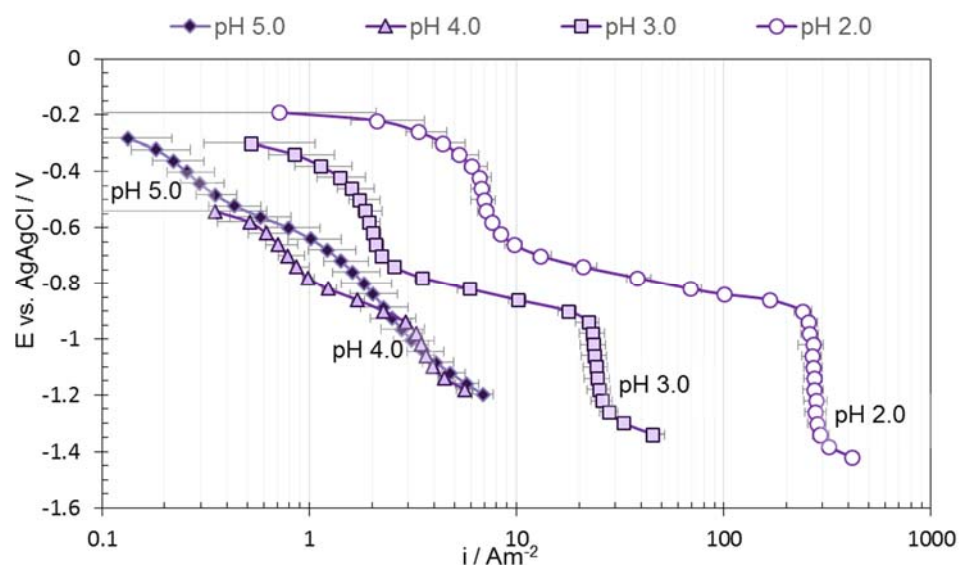


Figure 12: Potentiodynamic sweeps on pyrrhotite in  $N_2$  purged solutions, 1 wt% NaCl,  $30^\circ\text{C}$ , scan rate  $1 \text{ mVs}^{-1}$ , 1000 rpm at different pH.

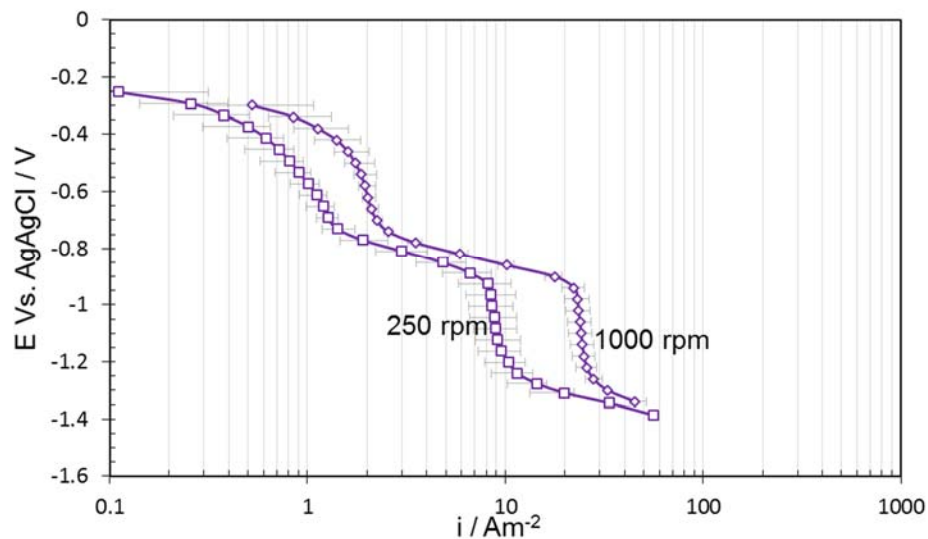


Figure 13: Potentiodynamic sweeps on pyrrhotite in  $N_2$  purged solutions, 1 wt% NaCl,  $30^\circ\text{C}$ , scan rate  $1 \text{ mVs}^{-1}$ , pH 3.0, at different rotational velocity.

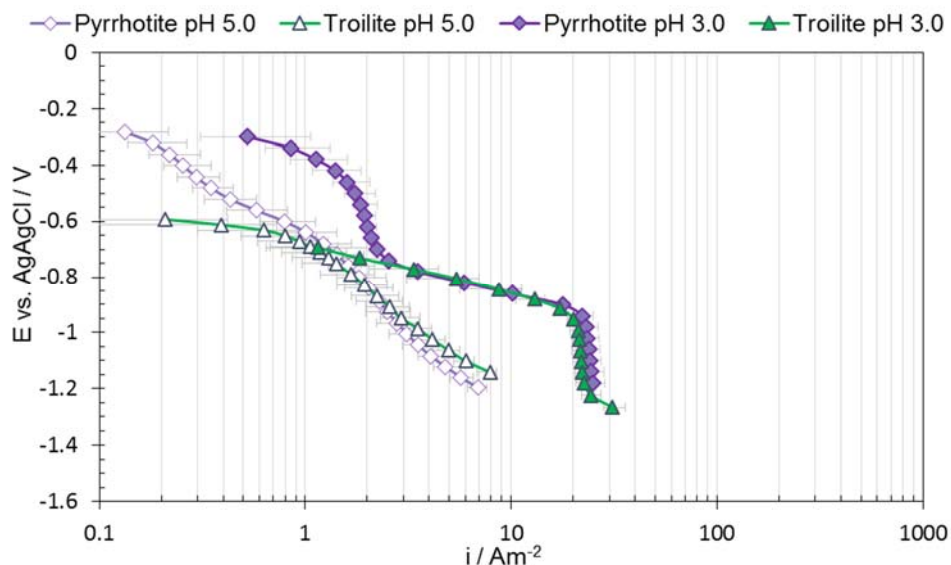
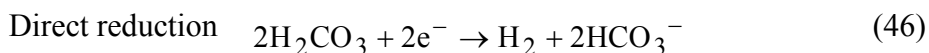


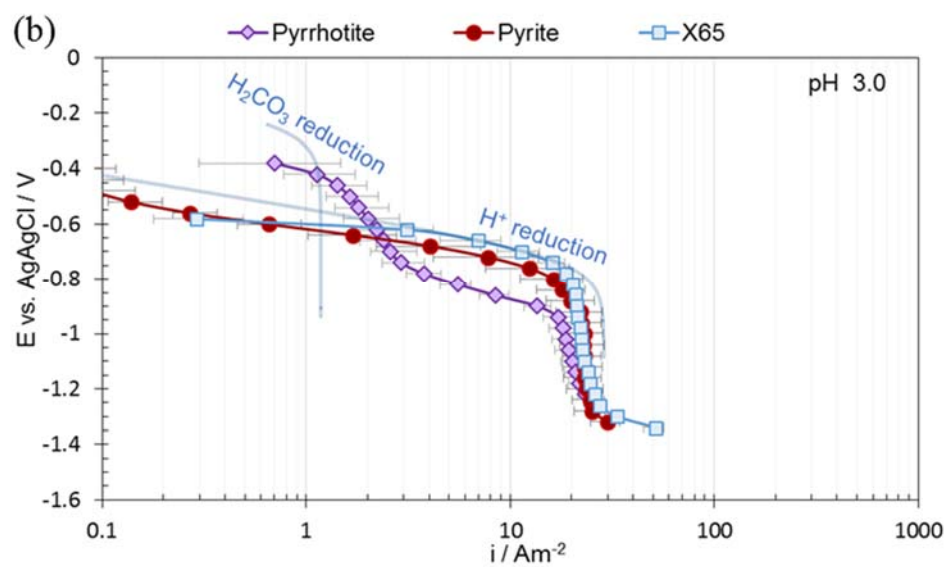
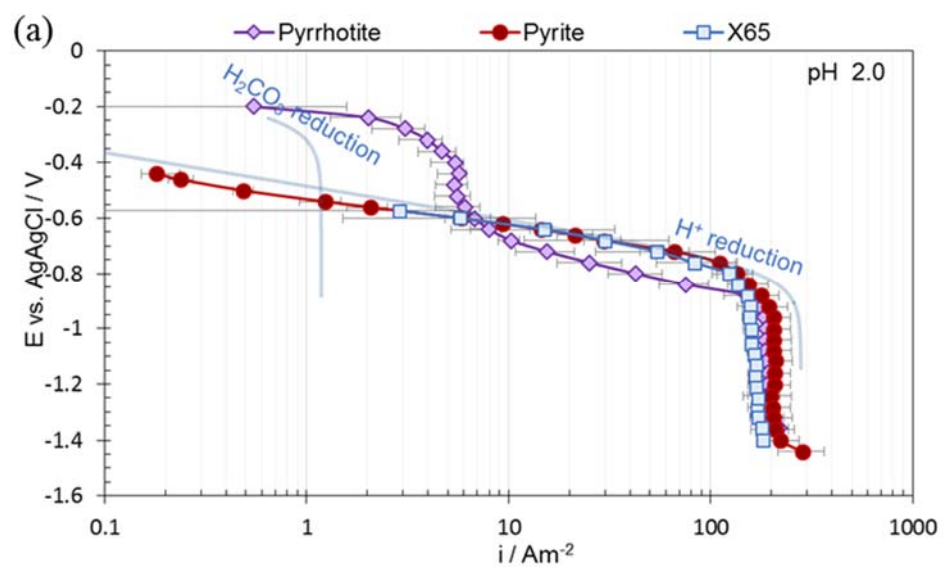
Figure 14: Potentiodynamic sweeps on pyrrhotite and troilite in  $N_2$  purged solutions, 1 wt% NaCl, 30°C, scan rate  $1 \text{ mVs}^{-1}$ , different pH at 1000 rpm.

#### *Aqueous $CO_2$ Solution*

In aqueous  $CO_2$  solutions,  $CO_2$  hydration results in carbonic acid ( $H_2CO_3$ ) formation (Reaction (45)).  $H_2CO_3$  is a weak acid that contributes to the corrosion process through the buffering effect (Reaction (47)), where additional  $H^+$  ions are produced, and possibly via direct reduction at the electrode surface (Reaction (46)). The direct reduction of  $H_2CO_3$  mechanism was broadly accepted over the past forty years [117] however, it was challenged in recent years [118]–[120]. The exact mechanism of  $H_2CO_3$  reduction remains open to discussion, however, in the current study, it was assumed that in addition to  $H^+$  reduction there was a direct reduction of  $H_2CO_3$ . The  $H_2O$  reduction was not considered here.



Similar behavior to what was observed in strong acid experiments was observed in aqueous CO<sub>2</sub> solutions (Figure 15). At lower pH values pyrite showed similar electroactivity to what was obtained on X65 steel when exposed to the same condition. The measured current densities on pyrrhotite surfaces were approximately one order of magnitude smaller. The extra wave attributed to reduction of pyrrhotite to troilite was also present across all the experimental conditions in aqueous CO<sub>2</sub> solutions. At pH 2.0 and pH 3.0, the cathodic reaction was dominated by H<sup>+</sup> reduction, just like what was seen in strong acid solutions at the same pH, as indicated by the lines generated using the model. At pH 4.0 and pH 5.0, the potentiodynamic sweeps are more complicated to interpret in the same way as they were in NaCl + HCl solutions without CO<sub>2</sub>. At pH 4.0, the rate of reactions on pyrite appears to be somewhat slower than on X65 steel, for reasons that are not well understood. The same is true at pH 5.0, however, it also seems that the reactions on pyrrhotite are greatly accelerated at this pH. Just like in NaCl + HCl solutions, this is an artifact of the experimental conditions, where small amounts of H<sub>2</sub>S produced by conversion of pyrrhotite to troilite and troilite dissolution (Reaction (43) and Reaction (44), respectively) were immediately reduced leading to higher current densities.



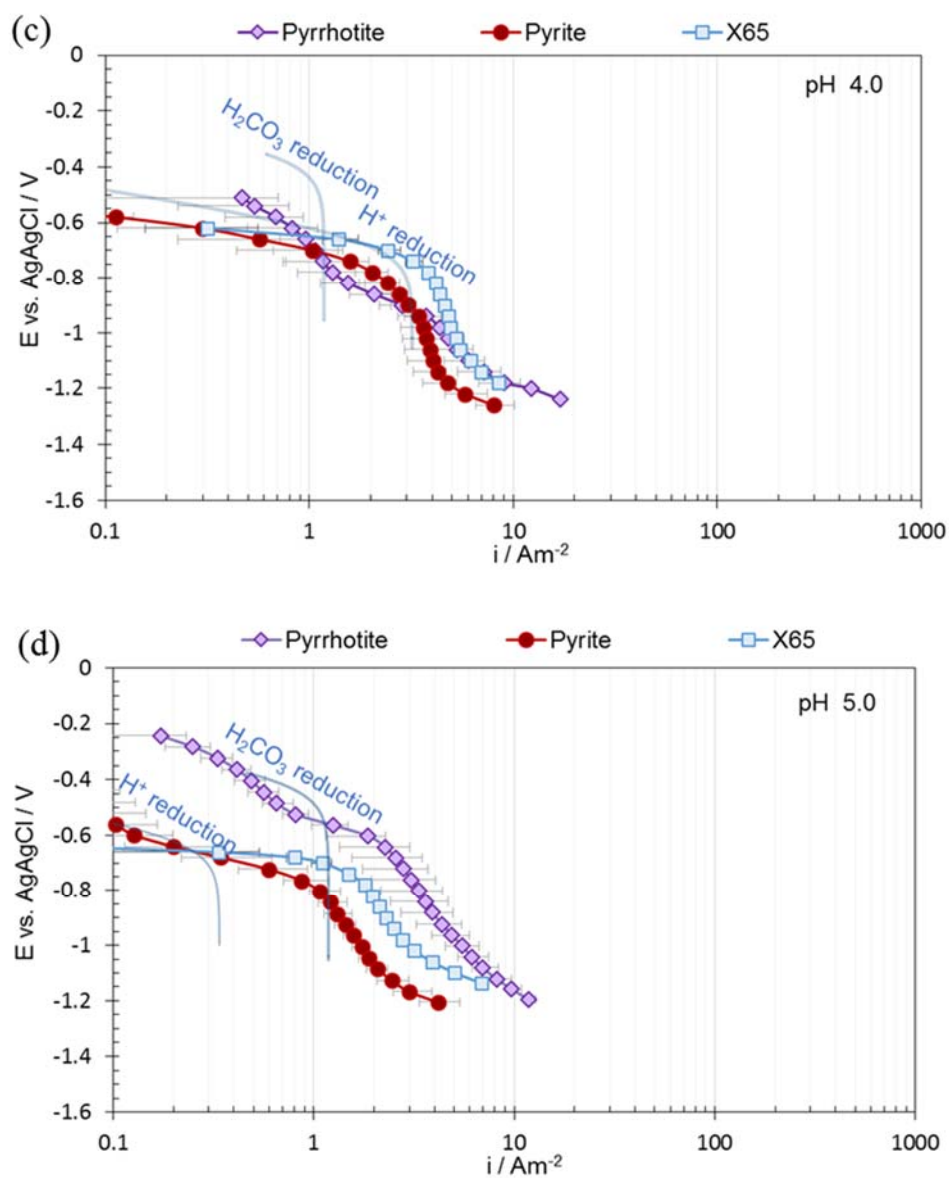


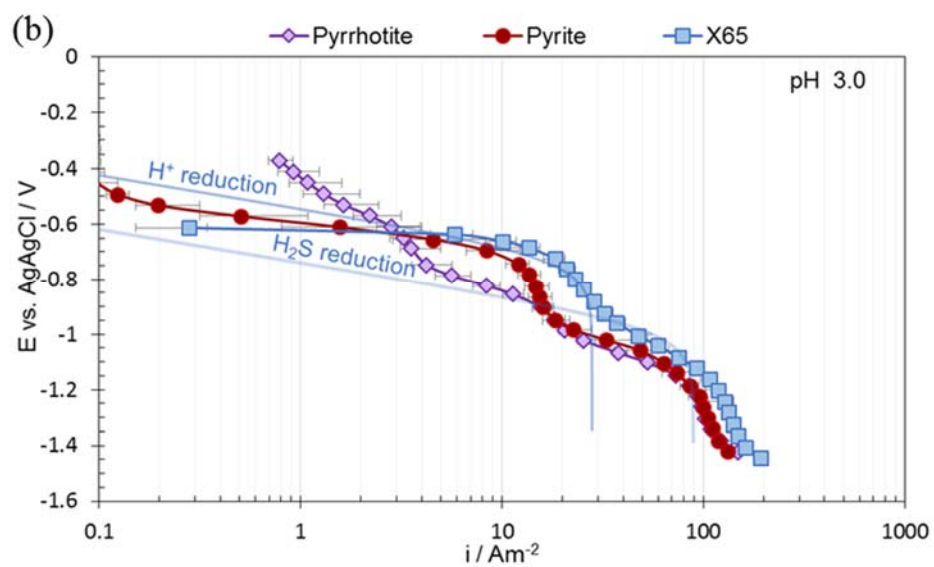
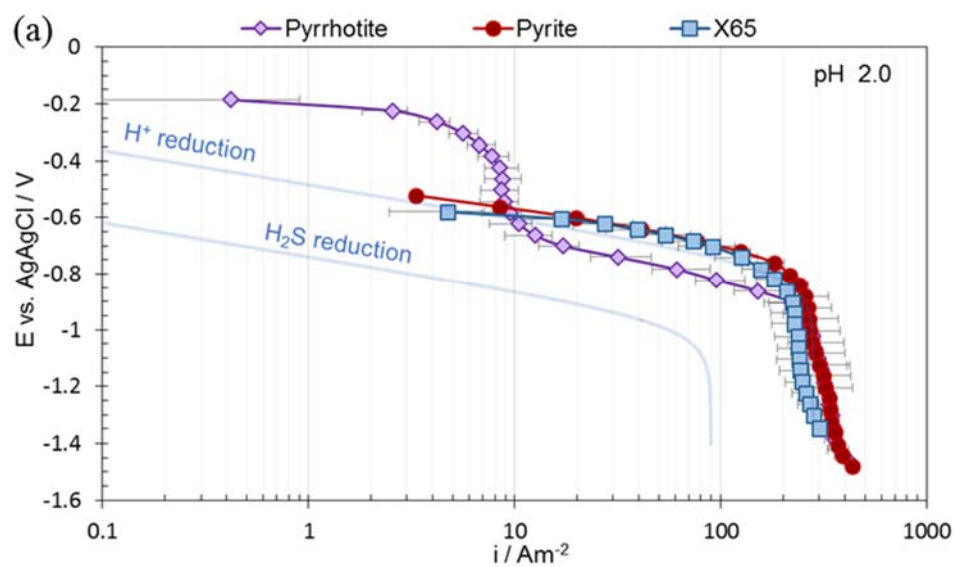
Figure 15: Potentiodynamic sweeps on X65 mild steel, pyrite and pyrrhotite in  $\text{CO}_2$  purged solutions, 1 wt. % NaCl,  $30^\circ\text{C}$ , 1000 rpm, scan rate  $1 \text{ mVs}^{-1}$ , (a) pH 2.0, (b) pH 3.0, (c) pH 4.0, (d) pH 5.0.

### *Aqueous $\text{H}_2\text{S}$ Solution*

In aqueous  $\text{H}_2\text{S}$  solutions, in addition to  $\text{H}^+$  reduction, the dissolved  $\text{H}_2\text{S}$  is also directly reduced on the surface of the electrode (Reaction (9)), which manifests itself in the

form of an extra wave on the potentiodynamic sweeps. This was discussed in detail in recent publications by Zheng *et al.* [20], [79], Kittel *et al.* [13], and Esmaeely *et al.* [113]

Potentiodynamic sweeps conducted at pH 2.0 in an aqueous H<sub>2</sub>S solution are shown in Figure 16 (a), where the dominant cathodic reaction was H<sup>+</sup> reduction. The relatively large error in the measured limiting current could be attributed to the irregular surface geometry of the electrodes as was noted above. There, similar behavior was seen to what was observed in strong acid solution shown in Figure 14 (a); reduction rates of H<sup>+</sup> on pyrite and mild steel overlapped, while on pyrrhotite approximately one order of magnitude smaller current density was observed. The extra wave related to reduction of pyrrhotite to troilite was also present. However, at higher pH values, the H<sub>2</sub>S reduction is dominant (Figure 16 (c)-(d)). There, it is observed that the H<sub>2</sub>S reduction rate is slightly lower (2 to 3 times) on both pyrite and pyrrhotite as compared to the rate on the X65 steel surface. Thus, the H<sup>+</sup> reduction wave, which was overpowered by the H<sub>2</sub>S reduction on X65 steel, was observable on both pyrite and pyrrhotite (Figure 14 (b)-(d)). The H<sub>2</sub>S reduction rates on pyrrhotite and pyrite were approximately the same. The pyrrhotite to troilite reduction wave was consistently present across all the experimental conditions. However, in aqueous H<sub>2</sub>S solutions the artifact related to H<sub>2</sub>S production as a result of the reduction of pyrrhotite to troilite and troilite dissolution, which were observed in the strong acid and aqueous CO<sub>2</sub> solution, was not observed here; the small amounts of produced H<sub>2</sub>S were negligible in H<sub>2</sub>S saturated solutions.



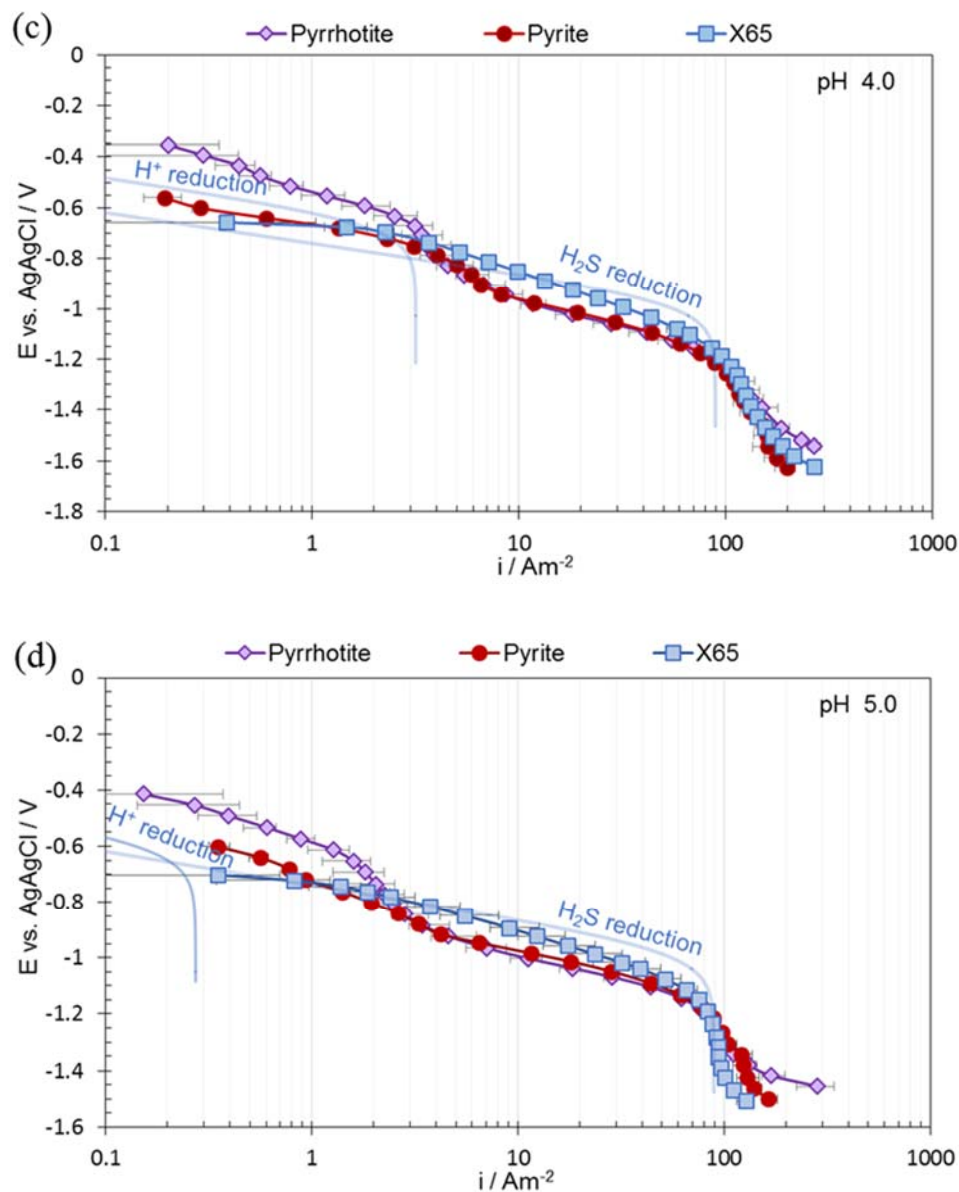


Figure 16: Potentiodynamic sweeps on X65 mild steel, pyrite, and pyrrhotite in aqueous solutions with 0.01 MPa H<sub>2</sub>S, 1 wt. % NaCl, 30°C, 1000 rpm, scan rate 1 mVs<sup>-1</sup>, (a) pH 2.0, (b) pH 3.0, (c) pH 4.0, (d) pH 5.0.

### Summary

Cathodic potentiodynamic sweeps were conducted on the surfaces of different iron sulfides including pyrite, pyrrhotite and troilite in deoxygenated acidic aqueous solutions.

- A comparison of the data obtained on iron sulfides with what was observed on X65 steel showed that in conditions dominated by  $H^+$  reduction, pyrite had similar electroactivity as the steel. There was some minor deviation at pH 4.0 and pH 5.0, for reasons that remain unclear.
- In the same conditions, the cathodic current densities obtained on pyrrhotite were almost the same and approximately one order of magnitude smaller than what was observed on pyrite and X65 steel.
- Cathodic sweep data on pyrrhotite showed an extra wave at the lower current densities obtained at more positive range of potentials, which was identified to be due to pyrrhotite reduction to troilite.
- In aqueous  $CO_2$  solutions, similar results were obtained as in strong acid solutions.
- In  $H_2S$  containing aqueous environments, both pyrite and pyrrhotite showed similar electroactivity with corrosion current densities that were slightly smaller than what was measured on X65 steel.

#### Galvanic Current between X65-Pyrite and X65-Pyrrhotite

Over the past decade, the role of conductive iron sulfides on localized corrosion in  $H_2S$  saturated aqueous solutions has become a focus area for corrosion scientists [24], [46], [56], [76], [121], [122]. However, the research, has not yielded decisive insights into the mechanisms and the possible role of different conductive iron sulfides [24], [46], [76]. Several studies on corrosion of mild steel in  $H_2S/CO_2$  gas mixtures have been conducted where experiments involved investigation of multiple parameters including the effect of

pH and glycol [24], [56]–[58], [69], [123]–[125]. In a recent study, Kvarekvål, *et al.*, [24] reported intensified uniform and localized corrosion rates under a pyrrhotite/troilite layer in the presence of a conductive electrolyte. However, due to the complexity of their experimental conditions, the corrosion mechanisms related to the observed localized corrosion remained unclear.

As for the role of conductive corrosion product layers on localized corrosion, Ning, *et al.*, [46] demonstrated that a mild steel surface could undergo localized corrosion when in direct contact with pyrite, in the presence of a corrosive electrolyte. They proposed that localized corrosion takes place as a result of galvanic coupling between pyrite and the steel. This was attributed to pyrite being conductive, hence forming a galvanic cell with the exposed part of the steel surface. However, the authors did not report localized corrosion in the presence of pyrrhotite/troilite. Considering that pyrrhotite/troilite are in a similar conductivity range as pyrite, one can expect that they could also act as a driving force for localized corrosion [81]–[83] (Table 4). Furthermore, they all have a similar open circuit potential (OCP), much more positive than mild steel [87]–[89] (Table 4). Hypothetically, when in contact with a mild steel surface, all of them could act as a cathode and lead to an increase in the corrosion rate through a galvanic effect [126].

There are earlier studies that addressed this problem. Adam, *et al.*, [127] investigated the galvanic coupling of pyrrhotite with various steels and reported a larger potential difference and a higher current between the pyrrhotite and mild steel as compared to other types of galvanic couples. The authors reported a higher galvanic current at lower pH where the mild steel is not passivated. Considering the observed electroactivity on

pyrrhotite [43], [128] and pyrite [102], [128] for the hydrogen evolution reaction, if the steel is coupled with one or both of these iron sulfides in a conductive acidic media, higher corrosion rates would be observed; either locally or uniformly due to an increase in cathodic surface area [129]. The abovementioned properties have recently made iron sulfide corrosion product layers the center of attention in research focused on H<sub>2</sub>S corrosion of mild steel. When conditions for establishing a galvanic cell are present, a corrosion product layer containing iron sulfide phases could enhance the rate of cathodic reactions by providing a larger cathodic surface area. Also, the mixed potential established for these layers coupled with mild steel is more positive than the OCP for the uncoupled steel. This will result in an increased iron dissolution rate, which would lead to localized corrosion at locations where the steel is exposed to the corrosive media.

The reported evidence for a galvanic effect related to iron sulfides coupling to mild steel to date has been mostly circumstantial. The galvanic corrosion that was attributed to such conditions was a conclusion that was obtained through deductive reasoning, without direct evidence. In the current study, zero resistance ammeter (ZRA) measurements were utilized to directly measure the magnitude of the galvanic current between coupled X65-pyrite and X65-pyrrhotite electrodes. The coupled currents were then validated by conducting potentiostatic measurements on the uncoupled electrode at their coupled potentials.

#### *Experimental Method and Set-Up*

Experiments were conducted in a conventional glass cell filled with 2 L of DI water and 20.2 g NaCl to obtain a 1.0 wt% solution. For the CO<sub>2</sub> experiments, the solution was

deoxygenated and saturated with CO<sub>2</sub> gas at least 2 hours prior to specimen immersion into the cell. For the other experiments, the solution was deoxygenated by purging with N<sub>2</sub> gas for 3 hours prior to each experiment and then sparged with 0.1 bar H<sub>2</sub>S gas; the gas flow was maintained throughout the experiment. The gas outlet was scrubbed using a 5 molL<sup>-1</sup> NaOH and a series of dry carbon scrubbers. The solution pH was adjusted to the desired value by addition of a deoxygenated HCl or NaOH solution. A 0.5" stir bar was used to create a well-mixed solution. It was deemed that equilibrium in the solution was reached approximately 1 hour after the introduction of H<sub>2</sub>S gas into the glass cell.

Mineralogical pyrite and pyrrhotite specimens were used to make electrodes for the current study; a scientific grade of pyrite was purchased from Alfa Asar<sup>15</sup> and student grade of pyrrhotite was purchased from Ward's Science<sup>16</sup>. Prior to the electrodes' preparation, XRD analysis on powdered pyrite and pyrrhotite detected no substantial impurities in either material [128]. Iron sulfide particles were handpicked within the same size range of 8 to 10 mm and arranged to form a ring shape in order to embed them in a clear epoxy. Upon curing, the back of the epoxied electrode was polished and the iron sulfides were sputter palladium (Pd) coated and connected to a wire using silver paste<sup>17</sup>. The Pd sputter coating was used to enhance the electrical connection for wires added to the back of each iron sulfide specimen. An API 5L X65 mild steel disc with a surface area of 0.19 cm<sup>2</sup> was placed in a hole, drilled through the center of the epoxied iron sulfides, with a wire soldered to its surface. Finally, the entire electrode was embedded in epoxy again to assure that all

---

<sup>15</sup> Fisher Scientific

<sup>16</sup> Ward's Science

<sup>17</sup> SPI

the wiring would be shielded from the solution (Figure 17). This special arrangement provided a good current distribution between the iron sulfide and the mild steel specimen with a cathode to anode surface area ratio in the range 7 to 20 and minimized the solution resistance between the two.

Electrochemical measurements were conducted using an Ag/AgCl reference electrode and a Pt counter electrode (when required). OCP of the two electrodes was measured first to ensure that a reasonably stable state was reached, where the OCP drift was less than  $\pm 1$  mV per min. The OCP measurements were immediately followed by electrochemical EIS, in order to determine the IR drop between the cathode and the anode, and these measurements were followed by LPR in order to measure the uncoupled corrosion current on X65 steel and compare the galvanic corrosion current with it. In galvanic measurements the X65 electrode was externally coupled with either pyrite or pyrrhotite via a ZRA, to monitor the galvanic current between the coupled electrodes for 500 seconds. In order to validate and better understand the galvanic current measurements by ZRA, the electrodes were then uncoupled and potentiostatic measurements were done at their coupled potential to measure the uncoupled currents of the anode and the cathode. Where the LPR measurements were not conducted, FREECORP™<sup>18</sup> 2.0 was used in order to compare the predicted uniform corrosion rates with the galvanic corrosion rates.

---

<sup>18</sup> Trade name

Table 12: Experimental matrix

Parameters	Conditions
Total pressure	0.1 MPa
Temperature	30°C
Solution	1 wt% NaCl
Flow condition	300 rpm, 0.5" stir bar
Materials	pyrrhotite, pyrite, and API 5L X65
Methods	EIS, LPR, ZRA, and potentiostatic current measurements
Spurge gas	N <sub>2</sub> 0.096 MPa CO <sub>2</sub> 0.01 MPa H <sub>2</sub> S
Solution pH	3.0, 4.0, 5.0 ( $\pm 0.1$ )

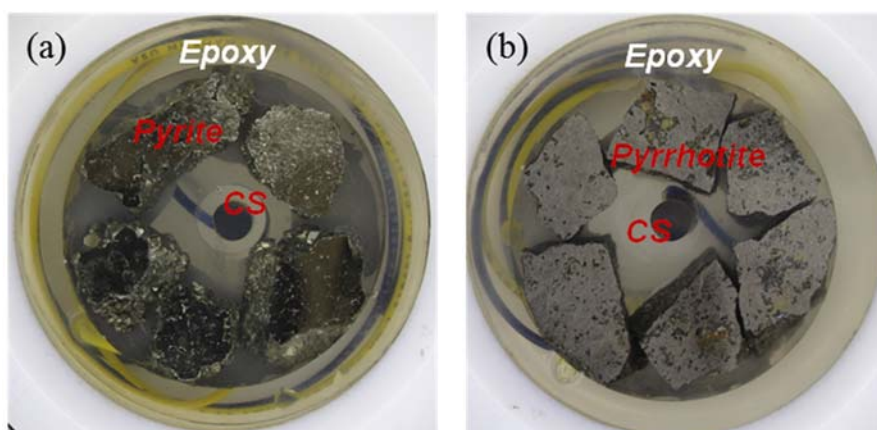


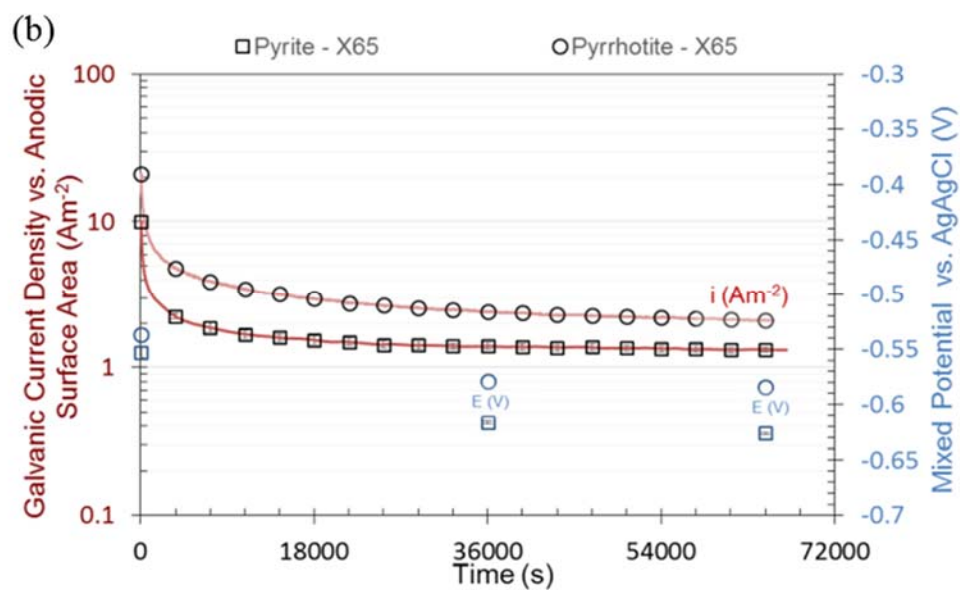
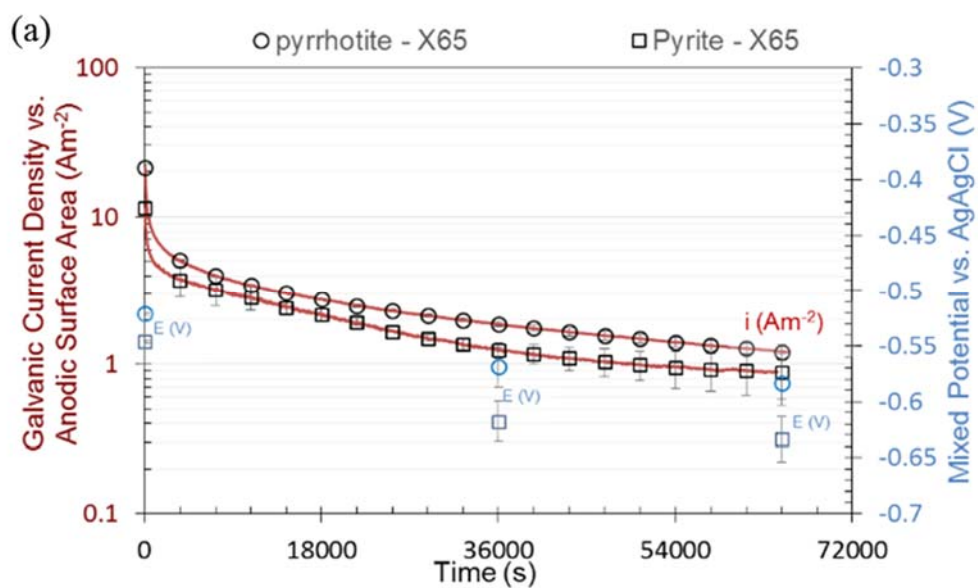
Figure 17: Galvanic current measurement specimens of mild steel X65 (CS) with (a) pyrite or (b) pyrrhotite geological materials.

### *Results and Discussion*

The galvanic currents for coupled X65-pyrite and X65-pyrrhotite are reported in terms of current density based on the X65 (anodic) surface area in order to make it comparable with the uniform corrosion current density of uncoupled mild steel. Figure 17 (a - c) shows the galvanic current density and the mixed potentials of coupled X65-pyrite

and X65-pyrrhotite exposed to different aqueous environments. It was observed that at pH 4.0 with the same cathode to anode surface area ratio, the galvanic current densities for X65-pyrite and X65-pyrrhotite were similar, with the latter being slightly higher. Note the OCP's provided are for coupled materials where the uncoupled X65 was approximately  $-680 \pm 5$  mV and the uncoupled pyrite and pyrrhotite were  $-100 \pm 50$  mV and  $-200 \pm 50$  mV vs. a saturated Ag/AgCl reference electrode, respectively. A decrease of approximately one order of magnitude in current density from the initial measured values was observed shortly after the electrodes were coupled. This was not an unexpected phenomena, given that a potential difference of approximately 40 mV exists between the uncoupled OCPs for either of the iron sulfides and the X65 specimen. When connecting two materials much higher currents are initially observed until the mass transfer and other accompanying chemical and electrochemical processes reach a stable value. Once the equilibrium potential is reached, a much smaller current is observed.

The experimental results show that the galvanic currents of coupled X65-pyrite and X65-pyrrhotite predominantly depended on the pH value rather than the nature of the aqueous environment, given that the results were approximately the same across different environmental conditions with strong acid solution in Figure 18 (a), aqueous CO<sub>2</sub> solution in Figure 18 (b), and aqueous H<sub>2</sub>S solution in Figure 18 (c).



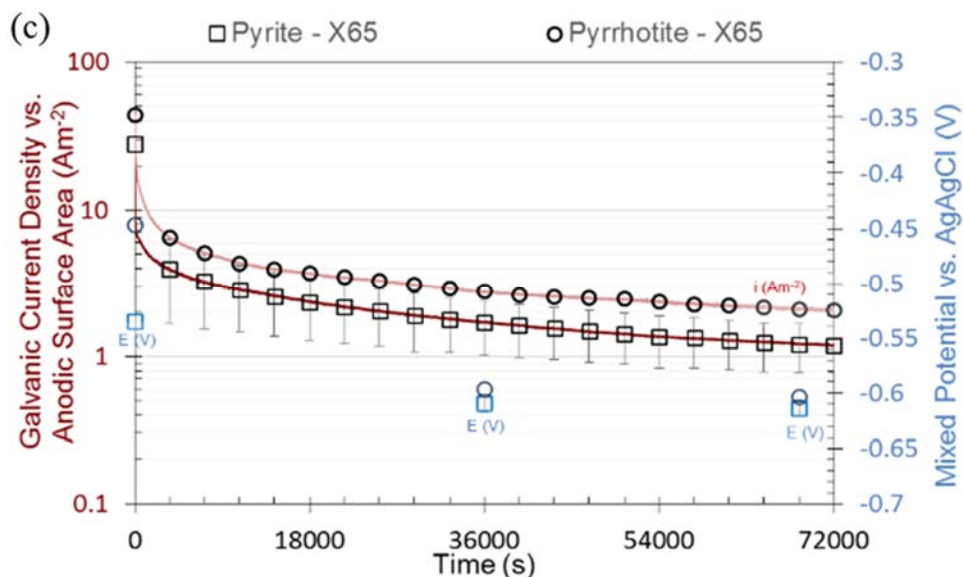


Figure 18: X65 galvanic current density with respect to anodic surface area coupled with pyrite or pyrrhotite, in aqueous (a) strong acid purged with N<sub>2</sub>, (b) CO<sub>2</sub> sparged with 0.96 bar CO<sub>2</sub>, and (c) H<sub>2</sub>S sparged with 0.1 bar H<sub>2</sub>S, pH 4.0, at 30°C, 1wt% NaCl, 400 rpm 0.5" stir bar, cathode to anode surface area ratio was approximately 20 for each case.

In order to compare the galvanic corrosion rates with the uniform corrosion rates of an uncoupled freely corroding X65 steel, the galvanic corrosion rates were calculated using the stabilized values of the galvanic current; defined where the change in current was less than 1 mA/min, taken after 20 hours (Figure 19). In aqueous CO<sub>2</sub> and strong acid solutions, the uniform corrosion rate measured by LPR was smaller than the galvanic corrosion rate of a coupled X65-pyrite or X65-pyrrhotite, however, the difference was not substantial. In an aqueous H<sub>2</sub>S solution, the galvanic corrosion rate was much larger than the uniform corrosion rate ratio, nonetheless, this was not due to a significantly higher galvanic effect. Rather, the difference arises from the much smaller uniform corrosion rate in aqueous H<sub>2</sub>S solutions as compared to other conditions. This makes the galvanic coupling of X65-pyrite and X65-pyrrhotite a serious problem in H<sub>2</sub>S containing

environments, where the existence of a conductive / semi-conductive corrosion product layer may be expected. In conditions where X65 steel is coupled with such layers, corrosion rate of the exposed steel could be accelerated through a galvanic effect, which could result in extensive localized corrosion.

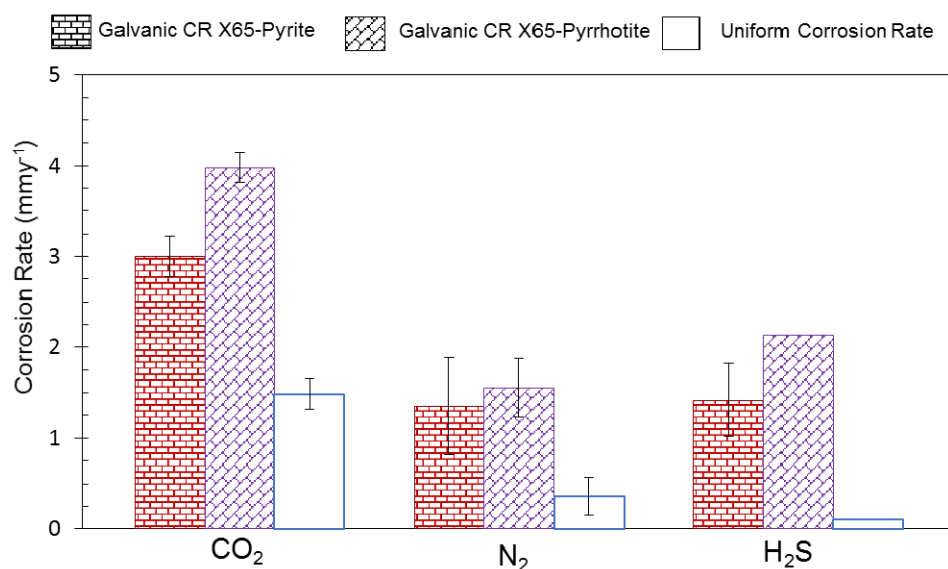


Figure 19: Galvanic corrosion rate and uniform corrosion rate of X65 exposed to different aqueous solutions at pH 4.0, 30°C, 1wt% NaCl, 400 rpm 0.5" stir bar, cathode to anode surface area ratio approximately 20, 20 hours of exposure.

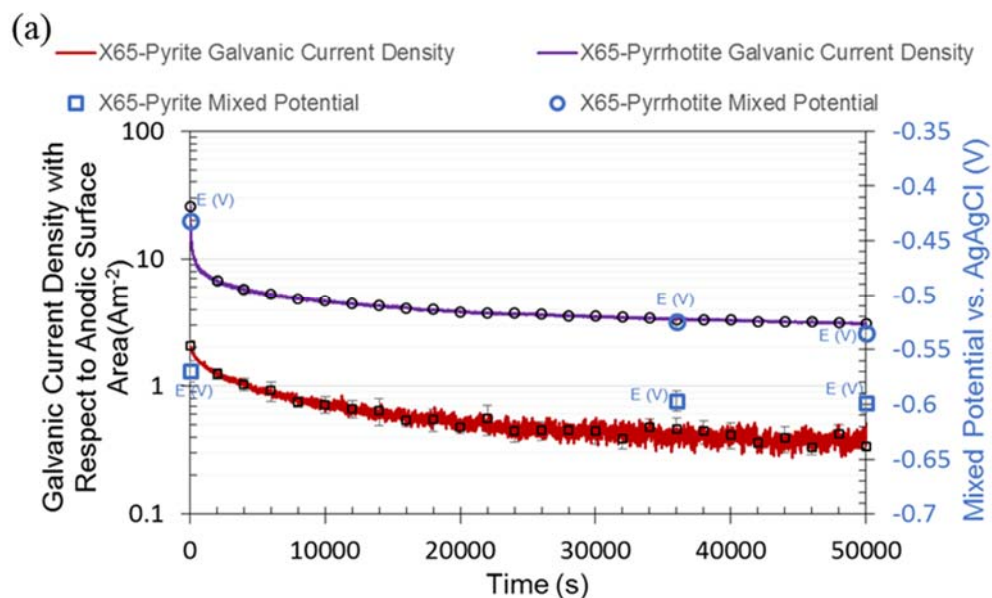
The reduction of corrosive species on pyrite and pyrrhotite surfaces could be a determining factor in their role as an additional cathode in the corrosion process. In aqueous solutions at pH 2.0 and pH 3.0, pyrite and pyrrhotite demonstrated similar electroactivity to that observed on X65 when it comes to H<sup>+</sup>, H<sub>2</sub>CO<sub>3</sub> or H<sub>2</sub>S reduction rates, with the measured current density on the pyrrhotite surface somewhat smaller than what was measured on the X65 and pyrite surfaces. However, it was observed that there was an additional reduction reaction occurring on the pyrrhotite surface once it was exposed to an

aqueous solution containing  $H^+$  that contributed to the measured current, which was identified as transformation of pyrrhotite into troilite [128]. At pH 4.0 and pH 5.0, the obtained results were different. At pH 4.0, the experimental findings showed a slight retardation for the current measured on pyrite and pyrrhotite surfaces; the reason of which remains unclear. At pH 5.0 the potentiodynamic sweeps on the pyrrhotite surface presented substantially higher currents than one would expect. It was originally hypothesized that this could be due to  $H_2S$  formation as a result of pyrrhotite reduction to troilite and troilite dissolution; however, this remains unclear since the observed currents require substantial amounts of  $H_2S$  at the experimental condition in order to produce such high current densities [128]. On the other hand, pyrite showed similar behavior to what was observed at pH 4.0.

Considering that both the measured currents on pyrite and pyrrhotite electrodes presented unexpectedly low values, it was deemed important to investigate the galvanic current of coupled X65-pyrite and X65-pyrrhotite in solutions purged with  $N_2$  at different pH values (Figure 20(a–c)), where the galvanic currents were validated using potentiostatic measurements. The experiments (with the exception of X65-pyrrhotite at pH 5.0) were repeated and the reported data are the average of two measurements with the error bars denoting the deviation (max and min) of the measured values. A substantially higher galvanic current was observed with coupled X65-pyrrhotite at pH 3.0 and pH 5.0 as compared to the galvanic current with coupled X65-pyrite with a similar cathode to anode ratio. At pH 4.0, as was reported earlier, the measured galvanic current on both iron sulfide coupled with X65 was approximately the same. At pH 5.0, the substantially higher galvanic

current at the X65-pyrrhotite surface resulted in a prompt consumption of any available  $H^+$ , which imposed a rapid change in the solution pH to the extent that any attempt to keep the pH stable was ineffective; thus, repeating this experiment with consistent environmental conditions was a challenge. The higher galvanic current at this condition could be explained by the pyrrhotite reduction to troilite and troilite dissolution where  $H_2S$  gas was produced as a byproduct, however, this could not explain the extent of the measured currents. Thus, in order to fully understand the underlying mechanism in such conditions, further study is required [114], [128].

The experiment with a coupled X65-pyrite presented much smaller currents, where the pH stayed relatively stable and the change was less than 0.1 unit of pH.



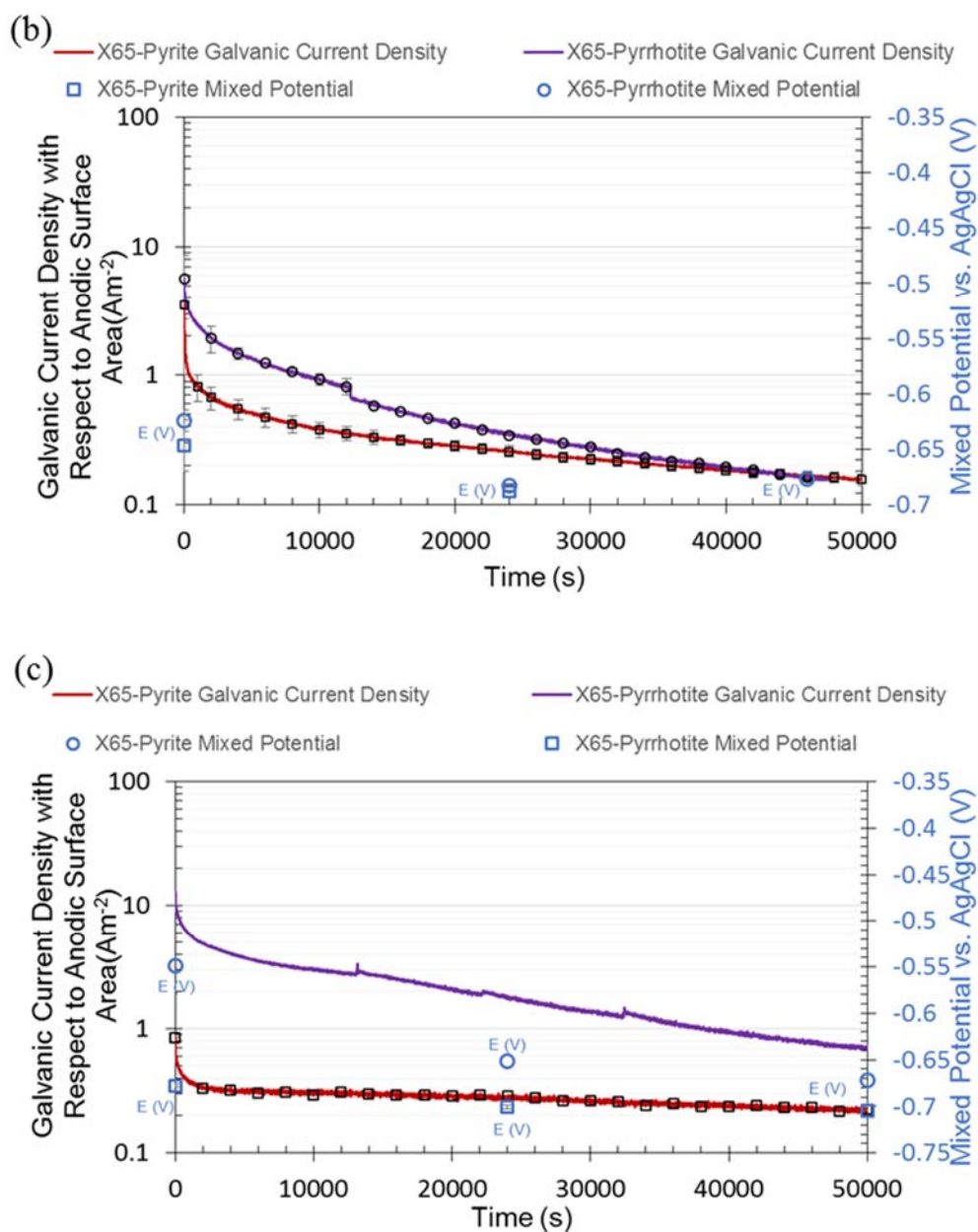
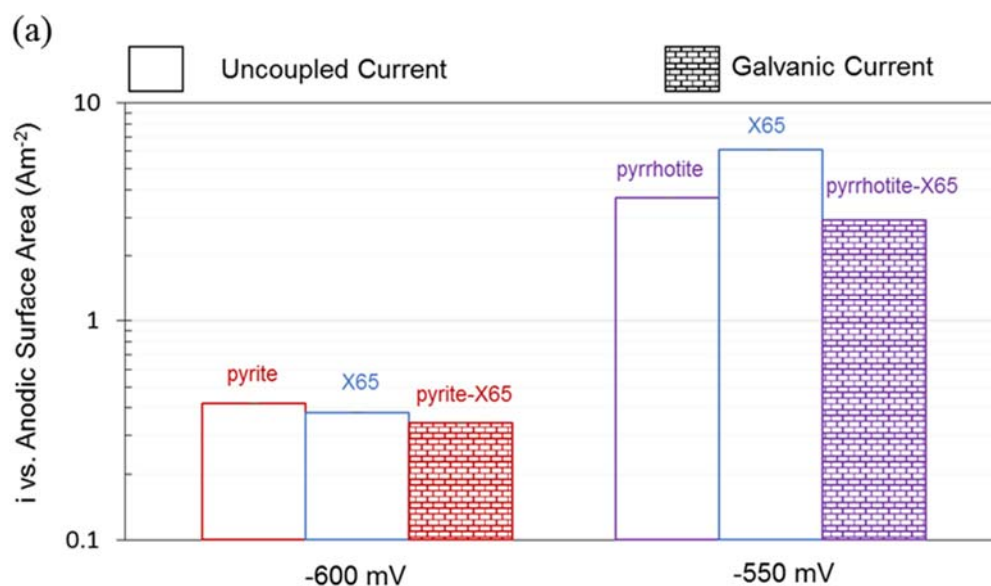


Figure 20: Galvanic current for pyrite or, pyrrhotite and X65 at their mixed potential in aqueous strong acid sparged with  $N_2$ , at (a) pH 3.0, (b) pH 4.0, (c) pH 5.0,  $30^\circ C$ , 1wt% NaCl, and 300 rpm 0.5" stir bar.

In order to validate the galvanic current measurements, it was of key importance to measure the uncoupled currents of each electrode at their mixed potential using the

potentiostatic mode. The results of the potentiostatic measurements are shown Figure 21 in terms of current density versus the anodic surface area. The similar values of the coupled and the uncoupled currents confirmed the accuracy of the galvanic current measurements. It is noteworthy that one has to consider the difference in the mixed potentials of coupled X65-pyrrhotite and X65-pyrite before drawing any comparison between the galvanic currents of the coupled materials. It should be noted that the X65-pyrrhotite mixed potential was more positive than the X65-pyrite mixed potential at pH 3.0 and pH 5.0, while they were the same at pH 4.0. Both mixed potentials were always more positive than the OCP of uncoupled X65. In Figure 21 (a) and (c), the 30 to 50 mV higher mixed potential of the coupled X65-pyrrhotite resulted in substantially higher galvanic current between X65-pyrrhotite as compared to X65-pyrite. In Figure 21 (b), the similar mixed potentials resulted in similar galvanic currents.



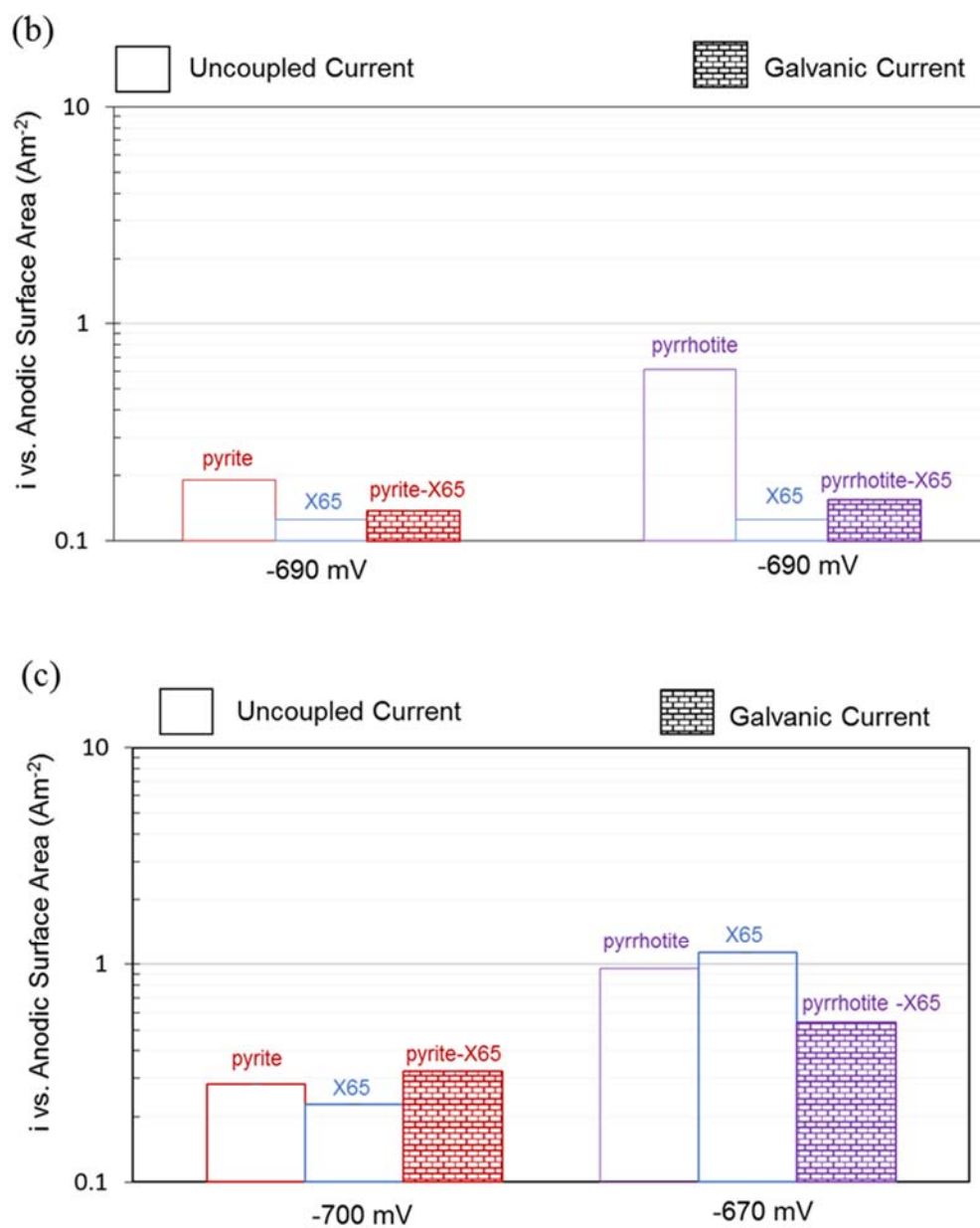


Figure 21: Potentiostatic current on uncoupled pyrite, pyrrhotite and X65 at the stable mixed potential of coupled pyrite-X65 and pyrrhotite-X65 in N<sub>2</sub> purged solution at (a) pH 3.0, (b) pH 4.0, (c) pH 5.0, 30°C, 1wt% NaCl, and 300 rpm 0.5" stir bar.

Given that pyrrhotite is not as stable as pyrite, it was suspected that the pyrrhotite surface transformation could play a role in the unexpected decline in the galvanic current.

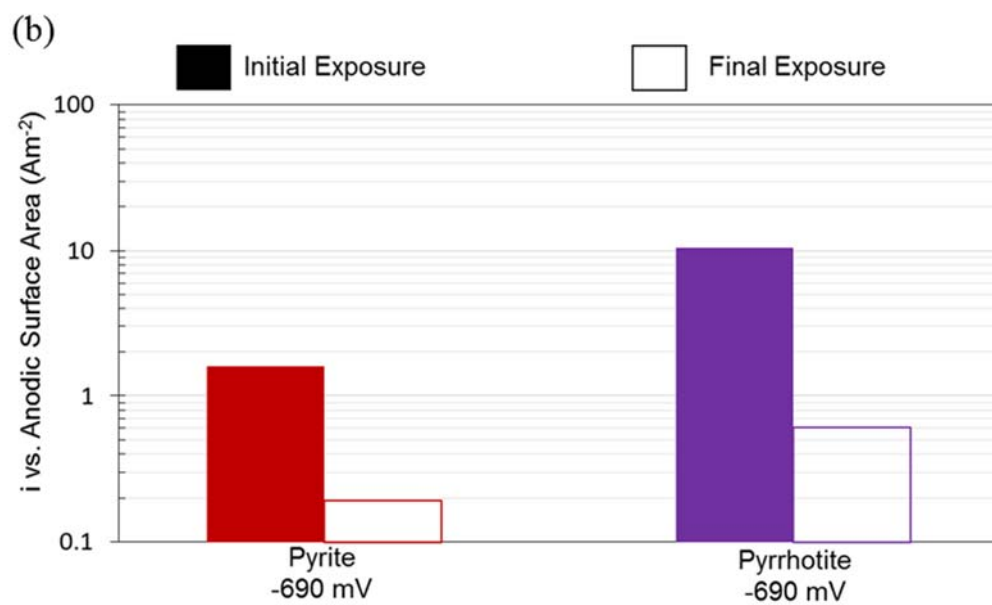
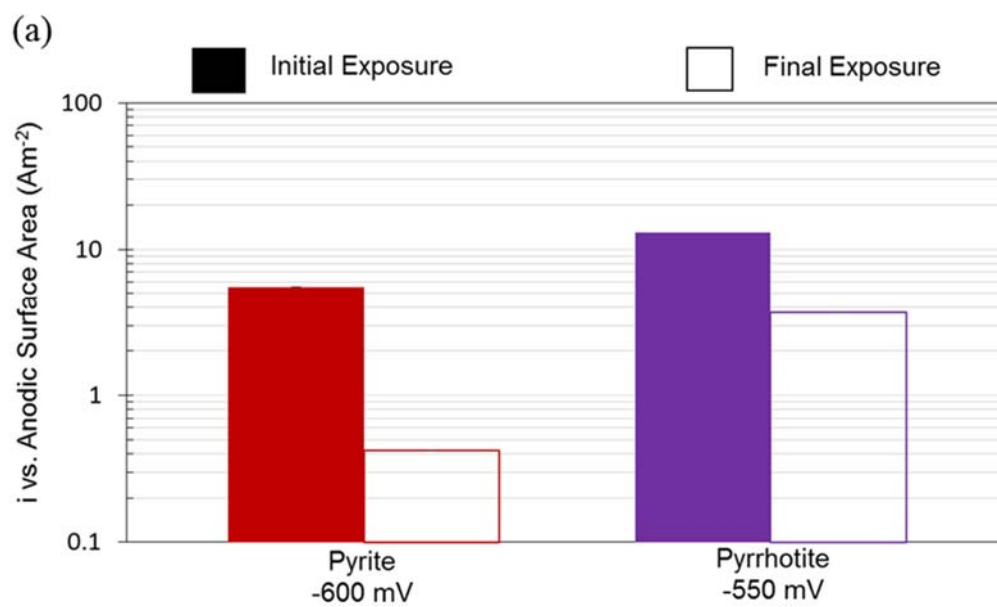
Thus, in order to examine this possibility, the uncoupled current at the surface of pyrrhotite and pyrite were measured at their mixed potentials (when they were coupled with X65) in the beginning and at the end of their exposure to the experimental conditions.

The results were compared (Figure 22) in order to investigate any changes that could have happened. It was observed that on both pyrite and pyrrhotite there was an approximately one order of magnitude decay of the measured current. Given that pyrrhotite is not a stable phase of iron sulfide in aqueous environments containing  $H^+$ , it was not unexpected to see a change in the measured current after the pyrrhotite electrode being exposed to such an environment for 20 hours.

On the other hand, pyrite is the most stable phase of iron sulfides with a very slow kinetics of dissolution [35], [90]; thus, a change on the measured current was most likely not the result of pyrite dissolution or surface transformation, as was true for pyrrhotite. A literature review showed that pyrite is susceptible to hydrogen permeation, where its rate has been reported to be of the same order as hydrogen permeation rate into the mild steel [130], [131]. Thus, it is suggested that the decay in pyrite electroactivity was most likely a result of hydrogen permeation into its structure, which affected the rate of  $H^+$  reduction on the pyrite surface. This phenomena was not directly investigated in the current study and its direct impact on the decay of the measured current remains a plausible speculation.

When it comes to pyrrhotite, the change in the measured current was expected given that there is an active reduction of pyrrhotite to troilite taking place on the pyrrhotite surface; given that the electrodes are stationary, the altered layer at the surface did not dissolve quickly. Thus, the measured uncoupled current at the end of each experiment was

most likely the measured current on the troilite surface rather than on the pyrrhotite underneath. However, the results presented a more complicated pattern depending on the mixed potential of the X65-pyrrhotite electrode; the potentiostatic current measured before and after the exposure could vary. In case the mixed potential was in the potential range of pyrrhotite reduction, for example, -550 mV *versus* Ag/AgCl at pH 3.0 in Figure 22 (a), the current change was not as substantial as when the mixed potential was in the H<sup>+</sup> reduction range where it is expected to have a thin layer of troilite on the surface. The substantial difference in the current in such potentials (-670 mV and -690 mV *versus* Ag/AgCl) in Figure 22 (b-c) arises from the fact that potentiostatic measurements were conducted immediately after the electrodes were uncoupled without allowing the OCP to reach the stable value. Thus, the current was most likely measured on the very thin layer of troilite found on the pyrrhotite surface because in stagnant conditions troilite dissolution is slow; if the potentiostatic measurements were conducted shortly upon uncoupling the electrodes, the measurements most likely took place on the troilite surface where the current is substantially lower. It should be pointed out that no surface analyses were conducted in order to examine the proposed scenario.



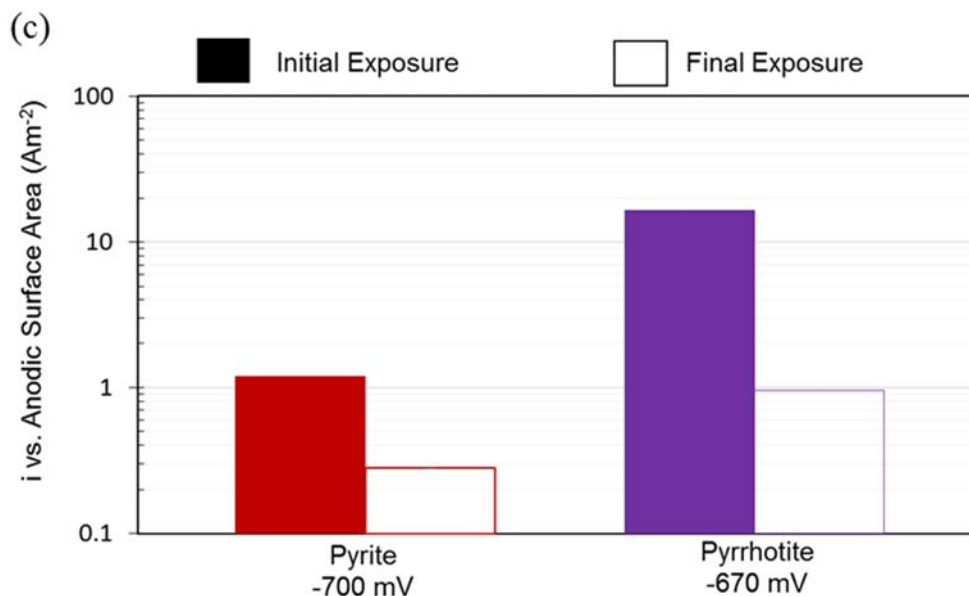


Figure 22: Initial and final potentiostatic current on uncoupled pyrite and pyrrhotite at the stable mixed potential of coupled pyrite-X65 and pyrrhotite-X65 in N<sub>2</sub> sparged solution at (a) pH 3.0 (b) pH 4.0, (c) pH 5.0, 30°C, 1wt% NaCl, 300 rpm 0.5" stir bar.

The galvanic corrosion rates of the coupled X65-pyrite and X65-pyrrhotite were compared with the uniform corrosion rates of an X65 steel utilizing FREECORP™ 2.0 software, since no LPR measurements were available at these conditions. The result shows that the galvanic corrosion rate of coupled X65-pyrrhotite or X65-pyrite (having a 7 times higher cathodic surface area) is approximately 4 to 6 times higher than the uniform corrosion rate at pH 5.0. At pH 3.0 the galvanic current of the coupled X65-pyrrhotite was close to 10 times higher than the galvanic current of the coupled X65-pyrite. At pH 4.0, the measured galvanic currents were similar between the coupled X65-pyrrhotite and coupled X65-pyrite, but smaller than what was observed at pH 5.0 or at pH 3.0. These results do not yield an explanation of the exact effect of pH on iron sulfides and X65 galvanic current and more detailed studies are required in the future. The unifying

conclusion from the results reported in Figure 19 and Figure 21 is that the galvanic corrosion rate became particularly significant when a protective corrosion product layer formed that lowered the uniform corrosion rates.

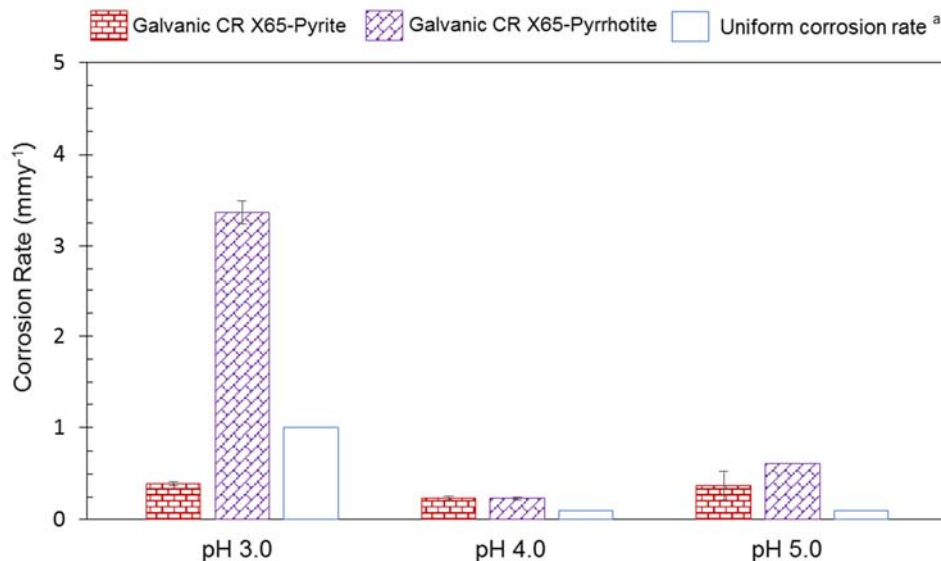


Figure 23: Galvanic corrosion rate and uniform corrosion rate of X65 exposed to N<sub>2</sub> sparged aqueous solutions at pH 3.0, pH 4.0, and pH 5.0, at 30°C, 1wt% NaCl, 300 rpm 0.5" stir bar, cathode to anode surface area ratio approximately 7, 20 hours of exposure.

### *Modeling*

The electrochemical model proposed in the current study is based on mathematical expressions of the underlying electrochemical, chemical and mass transfer processes describing the aqueous reduction of H<sup>+</sup> on the pyrite and pyrrhotite surfaces in aqueous strong acid solutions. It should be noted that the H<sub>2</sub>O reduction was not considered in the current model, as this reaction is not significant in the range of potentials being of interest.

The first step was to estimate the pH dependency of the current density on pyrite and pyrrhotite utilizing the experimental results reported earlier. The trendline slope of the

$\log(i)$  versus pH at fixed potentials shows the reaction order of hydrogen evolution reaction (HER) on pyrite (Figure 24) and HER relating to pyrrhotite to troilite reduction (Figure 25). It was observed that HER on the pyrite surface presented reaction orders in the range of 0.5 to 0.8, however, a comparison with the experimental results showed that reaction order of 0.5 provides a better match.

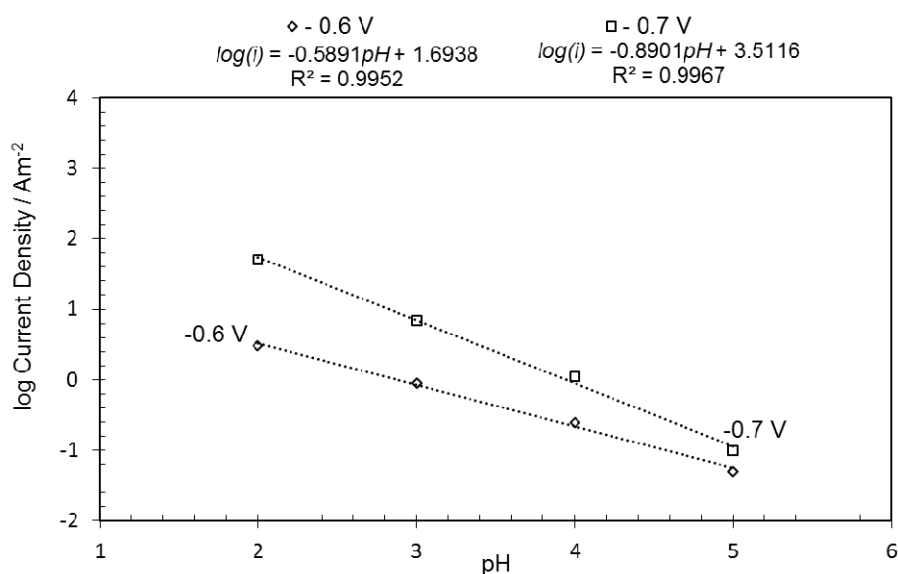


Figure 24: pH dependence of current density for pyrite electrode at -0.6V and -0.7 V (vs. saturated Ag/AgCl), at 1000 rpm, 30°C and 1 wt% NaCl.

The pH dependency of current density on the pyrrhotite electrode provides a reaction order for both pyrrhotite reduction to troilite and HER depending on the potential range. The reaction order for pyrrhotite reduction to troilite in the potential range of -0.25 and 0.3 V vs. saturated Ag/AgCl was found to be 0.9 and the reaction order for HER was estimated to be 0.8 in the potential range of -0.75 and 0.8 V vs. saturated Ag/AgCl. A comparison with the experimental results showed that a reaction order of 1 resulted in a

better fit. It is noteworthy that given the complexity of iron sulfide behavior at higher pH values the pH range where the reaction orders are investigated remains limited.

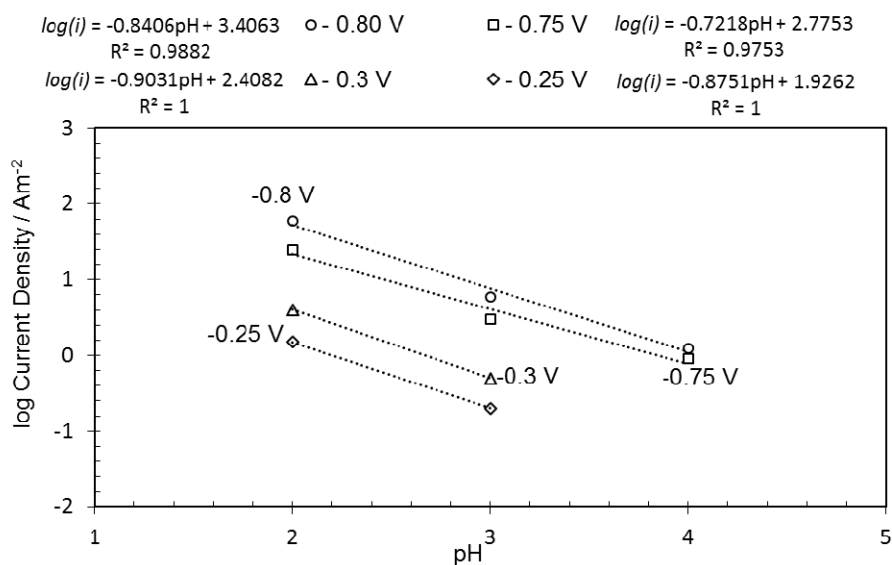


Figure 25: pH dependence of current density for pyrrhotite electrode at -0.25V, -0.3 V, -0.75 V, and -0.8 V (vs. saturated Ag/AgCl), at 1000 rpm, 30°C and 1 wt% NaCl.

### *H<sup>+</sup> Reduction*

The current density for H<sup>+</sup> reduction, including both charge transfer and the mass transfer limiting currents are calculated using the equations in Table 13; the reaction orders are reported separately for pyrite and pyrrhotite.

Table 13: Calculation of the H<sup>+</sup> reduction current density on pyrite and pyrrhotite<sup>19</sup>

$$\frac{1}{i_{c(H^+)}} = \frac{1}{i_{\alpha(H^+)}} + \frac{1}{i_{d(H^+)}} \quad (48)$$

$$i_{\alpha(H^+)} = i_{o(H^+)} 10^{(-E_{\text{corr}} - E_{\text{rev}(H^+)})/b_{c(H^+)}} \quad (49)$$

$$i_{o(H^+)} = i_{o_{\text{ref}}} \left( \frac{c_{(H^+)}}{c_{\text{ref}(H^+)}} \right)^{\beta} e^{\frac{-\Delta H}{R} \left( \frac{1}{T} - \frac{1}{T_{\text{ref}}} \right)} \quad (50)$$

$$\beta = 0.5 \quad i_{o_{\text{ref}}} = 0.01 \text{ Am}^{-2} \text{ for pyrite}$$

$$\beta = 1 \quad i_{o_{\text{ref}}} = 0.00012 \text{ Am}^{-2} \text{ for pyrrhotite}$$

$$c_{\text{ref}(H^+)} = 1 \cdot 10^{-4} \text{ molL}^{-1} \quad \Delta H = 30 \text{ kJmol}^{-1}$$

[94]

$$E_{\text{rev}(H^+)} = -\frac{2.303 RT}{F} \text{pH} - \frac{2.303 RT}{2F} \log P_{H_2} \quad (51)$$

$$b_c = 0.11 \text{ Vdecade}^{-1} \text{ for pyrite, } b_c = 0.11 \text{ Vdecade}^{-1} \text{ for pyrrhotite}$$

$$i_d = (0.62)nFD^3\omega^2\nu^{\frac{-1}{6}}C \quad (52)$$

$$D_{H^+} = D_{\text{ref}H^+} \frac{T_K}{T_{\text{ref}}} \frac{\mu_{\text{ref}}}{\mu} \quad (53)$$

$$\mu = \mu_{\text{ref}} 10^{\frac{1.3272(20-T_C) - 0.001053(20-T_C)^2}{T_C + 105}} \quad (54)$$

<sup>19</sup> The nomenclature is defined in a separate section at the end of the document.

*Pyrrhotite Reduction to Troilite*

The current density related to pyrrhotite reduction to troilite when exposed to an aqueous environment containing  $H^+$ , [114], [128] (Reaction (43) and (44)) is calculated using equations provided in Table 14. Here, the limiting current is presumed to be the current where the surface coverage of troilite (FeS) is close to 100% with a dependency of square root of  $H^+$  concentration based on the experimental observations.

Table 14: Calculation of pyrrhotite reduction current density

$$\frac{1}{i_{c\text{pyrr}}} = \frac{1}{i_{\alpha\text{pyrr}}} + \frac{1}{i_{d\text{pyrr}}} \quad (55)$$

$$i_{\alpha(\text{pyrr})} = i_{o(\text{pyrr})} 10^{(-E_{\text{corr}} - E_{\text{rev}(\text{pyrr})})/b_c(\text{pyrr})} \quad (56)$$

$$i_{o(\text{pyrr})} = i_{o\text{ref}} \left( \frac{c_{(\text{H}^+)}}{c_{\text{ref}(\text{H}^+)}} \right) e^{\frac{-\Delta H}{R} \left( \frac{1}{T} - \frac{1}{T_{\text{ref}}} \right)} \quad (57)$$

$$i_{o\text{ref}} = 0.35 \text{ Am}^{-2} \quad c_{\text{ref}(\text{H}^+)} = 1 \cdot 10^{-4} \text{ molL}^{-1} \quad \Delta H = 30 \text{ kJmol}^{-1}$$

$$b_c = 0.11 \text{ Vdecade}^{-1} \quad [114]$$

$$i_d = 0.065 * (0.62) n F D^3 \omega^2 \nu^{-1} \frac{1}{6 C^2} \quad (58)$$

$$D_{\text{H}^+} = D_{\text{refH}^+} \frac{T_K \mu_{\text{ref}}}{T_{\text{ref}} \mu} \quad (59)$$

Figure 26 and Figure 27 shows the experimental potentiodynamic sweeps on pyrite and pyrrhotite, respectively, compared with the calculated sweeps using the model presented above. It is noteworthy that the observed deviation of the limiting currents could be an artifact of the experiments given the irregular shape of the electrodes.

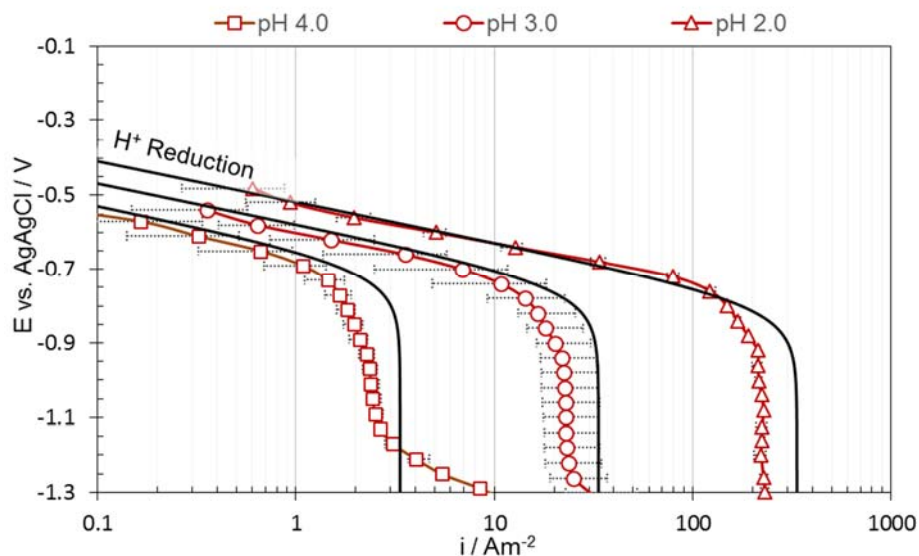


Figure 26: Potentiodynamic sweeps on pyrite in deoxygenated solutions, 1 wt% NaCl, 30°C, and 1000 rpm RDE, scan rate 1 mVs<sup>-1</sup>, at different pH values.

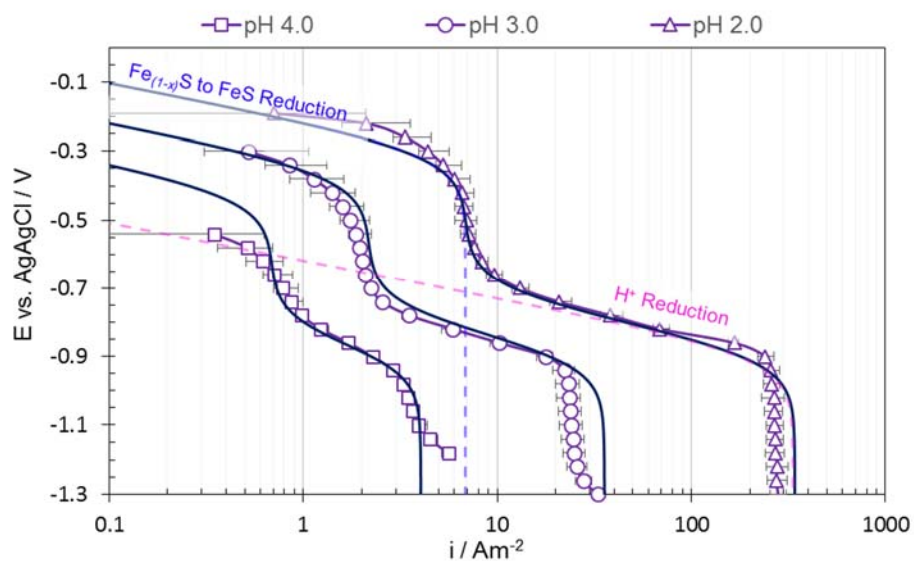


Figure 27: Potentiodynamic sweeps on pyrrhotite in deoxygenated solutions, 1 wt% NaCl, 30°C, and 1000 rpm RDE, scan rate 1 mVs<sup>-1</sup>, at different pH values.

The model proposed above describes the rate of reduction reactions that take place on a freshly polished pyrite or pyrrhotite, given the experimental results it is based on.

However, it is reasonable to assume that iron sulfide surface exposed to aqueous conditions undergoes transformations during exposure which could result in an altered rate of  $H^+$  reduction on their surfaces. In the current study the changes on the surface of pyrrhotite was the primary concern, where the reduction of pyrrhotite to troilite could have a substantial effect.

The ultimate goal of the current study was to propose a model that is applicable for galvanic current predictions in longer exposures. In a pyrrhotite-steel galvanic couple pyrrhotite is under constant cathodic polarization where it is reduced to troilite (Reaction (43)). In order to investigate any changes in rate of  $H^+$  reduction that could arise from such cathodic polarization, long term potentiostatic measurements (12 to 24 hours) were conducted, where the iron sulfide's potential was maintained at a potential that is the mixed potential for a coupled X65-pyrrhotite. The effect of any surface changes were then investigated by comparing the cathodic potentiodynamic sweeps conducted after the potentiostatic experiments with the sweeps before the potentiostatic measurements.

Results unveiled unexpected behavior of pyrrhotite concerning the  $H^+$  reduction rate; the results provided a clue to explain the higher galvanic currents with the couple X65-pyrrhotite than one could expect given the reported electroactivity of pyrrhotite. At pH 3.0 potentiodynamic sweeps conducted after the potentiostatic experiments presented an unexpected increase on  $H^+$  reduction rate. Potentiodynamic sweeps were conducted in two steps, first immediately after the potentiostatic experiment without allowing the OCP reaching a stable value. The second sweep was conducted after the OCP reached the stable value for the pyrrhotite electrode. Considering that the changes appeared in the part of the

sweeps at lower potentials, which overlap with  $H^+$  reduction on troilite, [128] the same measurements were done on a troilite electrode and the results were compared. It was observed that both pyrrhotite and troilite followed approximately the same pattern of  $H^+$  reduction, with the rate increasing to a value similar to what was measured on a pyrite surface (Figure 28 (a)).

In Figure 28 (b) the label (1) relates to the initial sweep on the pyrrhotite electrode surface, label (2) is the sweep immediately after the potentiodynamic experiment and (3) is the one after a stable OCP was achieved. The abovementioned changed behavior of pyrrhotite was taken into account in the galvanic model where the reaction order and the exchange current density for  $H^+$  reduction were changed to  $\beta = 0.5$ ,  $i_{\text{oref}} = 0.003 \text{ Am}^{-2}$  (similar to what was found for pyrite). The solid blue lines represent the calculated sweeps before and after surface changes. It is noteworthy that in order to find the accurate reaction order and exchange current density, these experiments would need to be conducted across a broader range of pH. Also, it remains speculative as to what the changes on the surface that results in this behavior exactly were, something that requires further investigation.

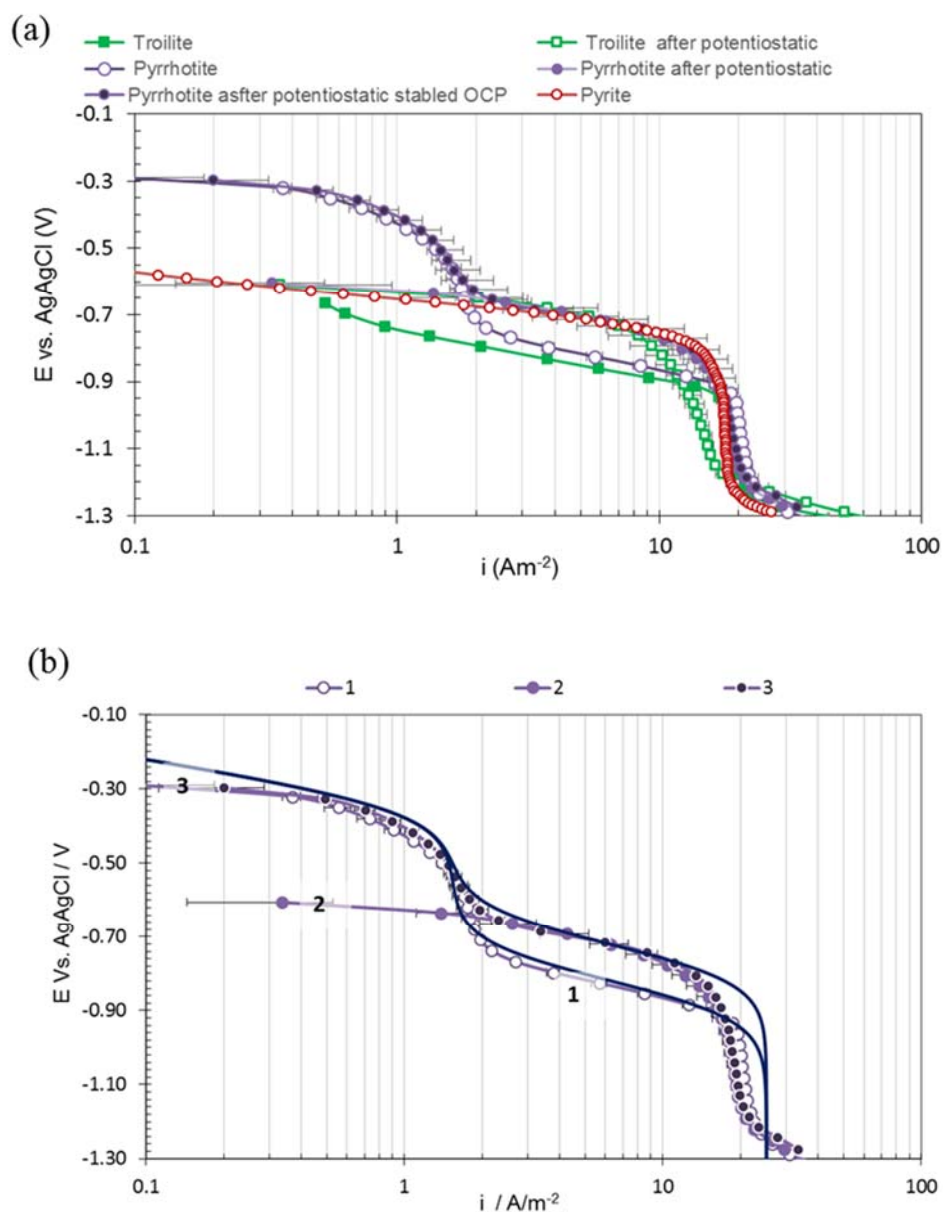


Figure 28: Cathodic potentiodynamic sweeps prior and after potentiostatic experiments (a) pyrrhotite and troilite (b) measured and modeled pyrrhotite.

Although pyrite is the most stable phase of iron sulfide with the lowest kinetics of dissolution [35], [90] and a surface transformation in a similar way to what was observed on pyrrhotite and troilite was not anticipated, potentiostatic experiments before and after

ZRA measurements (reported earlier) unveil the possibility of hydrogen permeation into pyrite, what is postulated here to affect the pyrite reactivity. Similar potentiostatic measurements were conducted on pyrite, which yielded a different outcome compared to what was obtained on pyrrhotite and troilite electrodes. The potentiodynamic sweeps conducted immediately after the potentiostatic measurements showed a retardation of the  $H^+$  reduction rate on the pyrite surface (Figure 29). This retardation was not as pronounced for the sweeps done after the OCP was allowed to reach a stable value. This is hypothesized to be the result of hydrogen permeation into the pyrite structure, which decreases the net rate of hydrogen evolution at the pyrite surface as mentioned earlier. It is believed that the absorbed hydrogen gradually reemerged from the pyrite while the OCP was allowed to stabilize, resulting in sweeps that show that pyrite electroactivity was restored to the original state.

This effect should be taken into account in the galvanic coupling scenario, given that in such conditions pyrite will be cathodically polarized by the steel. Thus, the observed changes in pyrite electroactivity were implemented in the abovementioned model via its effect on the exchange current density of  $H^+$  reduction on the pyrite surface;  $i_{\text{oref}} = 0.0006 \text{ Am}^{-2}$  was found to best fit the model with the experimental data.

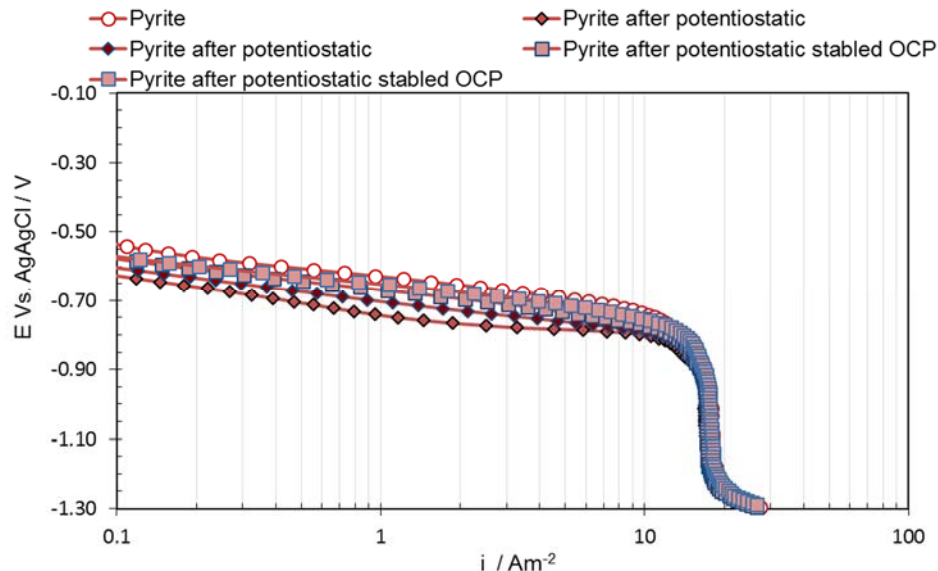
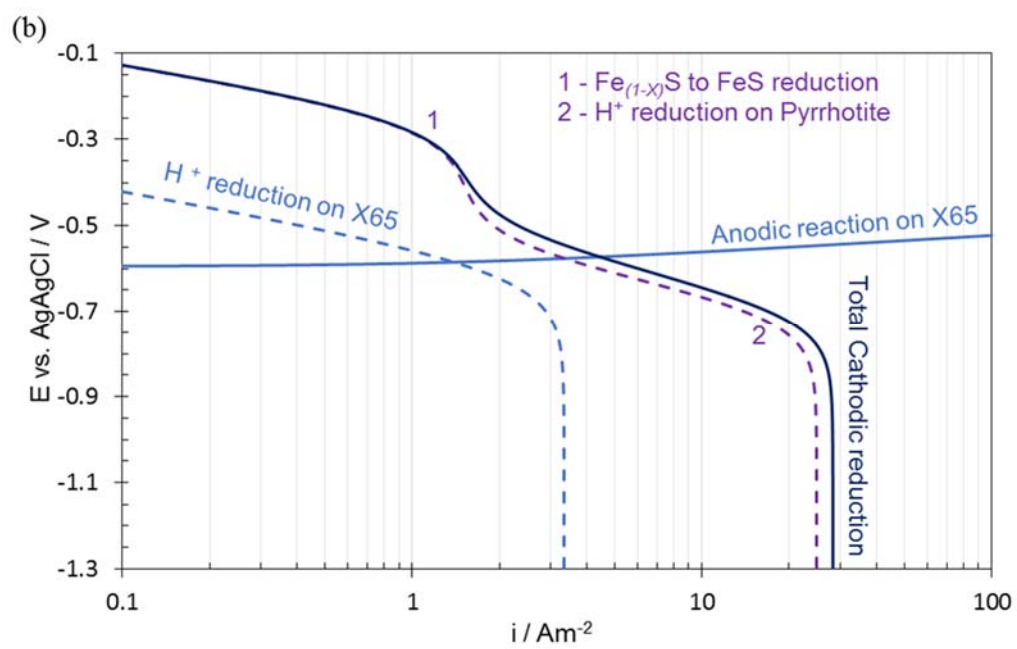
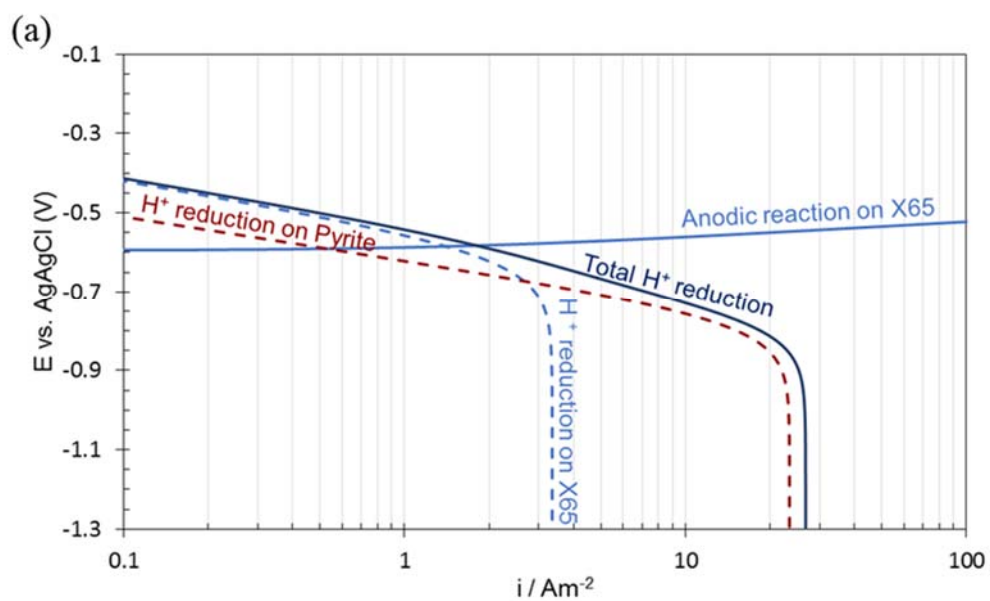
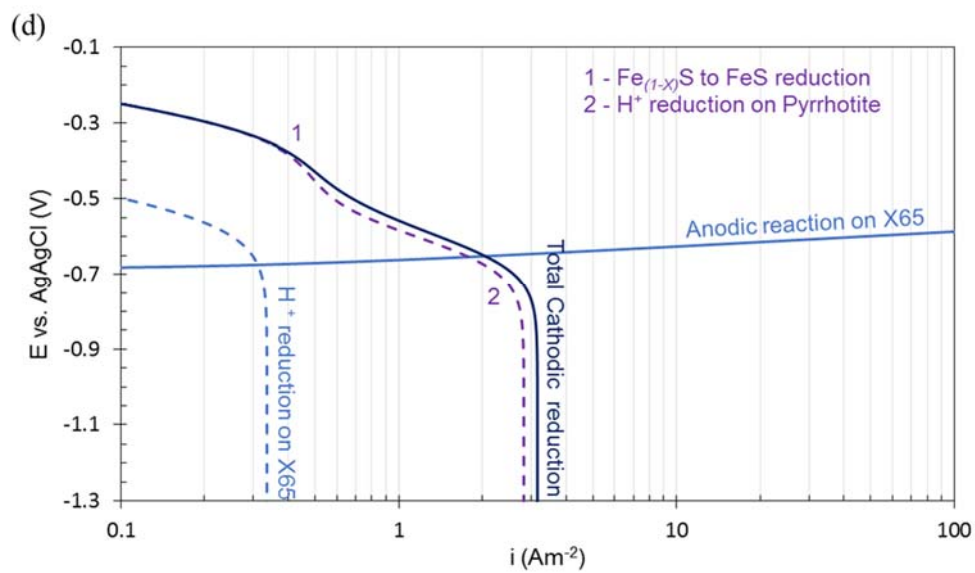
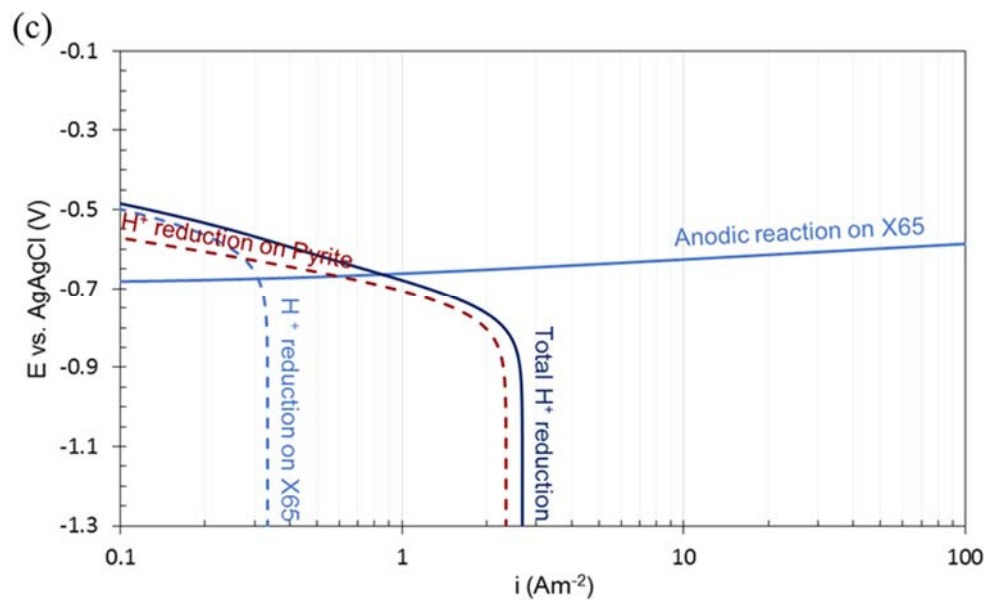


Figure 29: Cathodic potentiodynamic sweeps prior and after potentiostatic experiments on pyrite.

Given that the proposed model was postulated based on the potentiodynamic measurements conducted on pyrite and pyrrhotite, the galvanic current and potentiostatic measurements were used to calibrate and further validate the model. It is noteworthy that the current model is in its early stages of development. Given that the experimental conditions required to validate the model are limited, extra care should be taken into account while utilizing this model outside the range of tested conditions.

Figure 30 shows the modeled X65-pyrite and X65-pyrrhotite galvanic cell with 7 times higher cathodic surface area. The results were compared with the experimental measurements and presented in Figure 31. It can be observed that there is approximately a factor of 2 difference between the experimental results and the calculated currents.





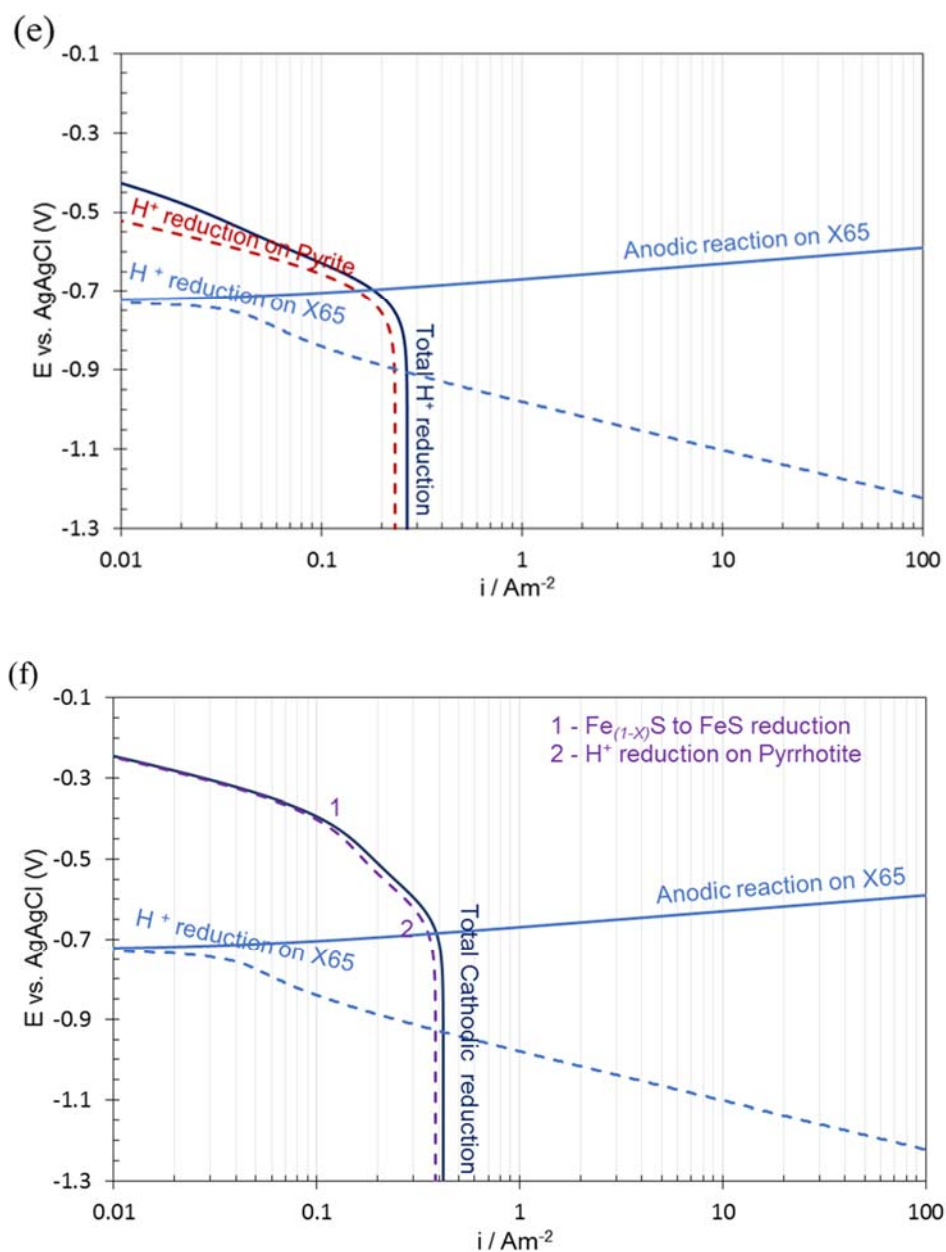


Figure 30: Modeled galvanic currents with a 7 times higher cathodic surface area in deoxygenated solutions, 1 wt% NaCl, 10 rpm RDE, (a) X65-pyrite at pH 3.0 (b) X65-pyrrhotite at pH 3.0, (c) X65-pyrite at pH 4.0, (d) X65-pyrrhotite at pH 4.0, (e) X65-pyrite at pH 5.0, (f) X65-pyrrhotite at pH 5.0.

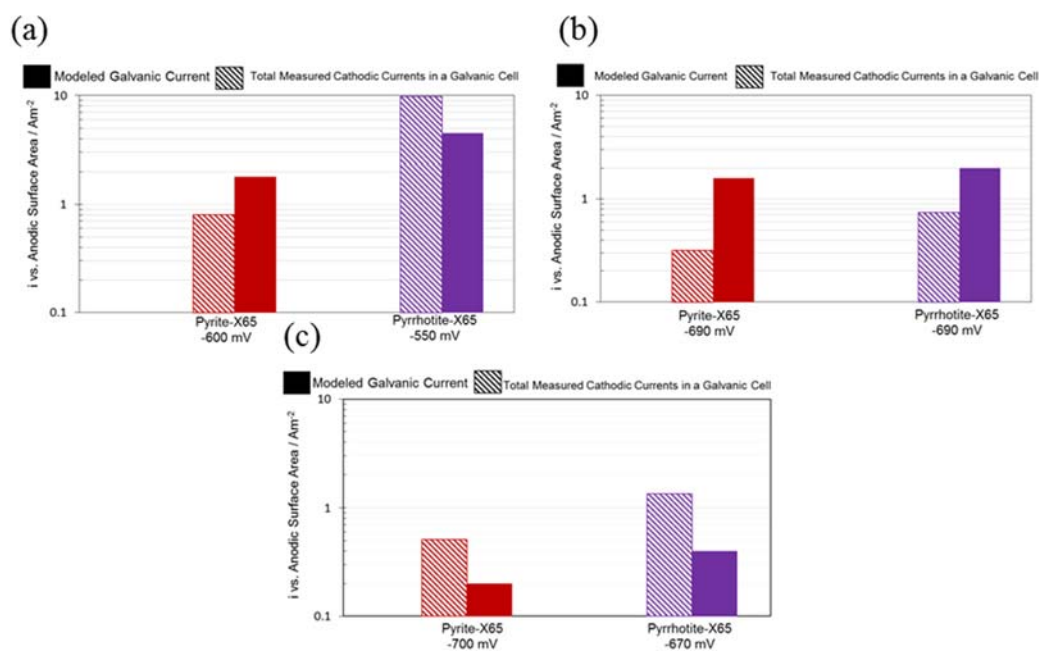


Figure 31: Measured galvanic corrosion versus calculated galvanic corrosion in deoxygenated solution, 1 wt% NaCl, 30°C, (a) pH 3.0, (b) pH 4.0, (c) pH 5.0.

In order to estimate the surface area for a porous iron sulfide layer, the geological samples were crushed and sieved to less than 100  $\mu\text{m}$  diameter particle size. BET<sup>20</sup> measurement was implemented on the iron sulfide powder.<sup>21</sup> The BET theory for specific surface area determination is based on the amount of gas adsorbed at its liquid temperature on the surface of the solid at a given pressure. BET has been widely used in order to measure iron sulfides' specific surface area. [132]–[135] Considering that the powder size

<sup>20</sup> BET, named after Stephen Brunauer, P. H. Emmet and Edward Teller in 1938, is a method to measure the specific surface area of a powder. BET

<sup>21</sup> BET measurements were conducted by Dr. Santosh Vijapur at Center for Electrochemical Engineering and Research at Ohio University.

changes the specific surface area of a given iron sulfide, a direct comparison of the obtained values in the current study with what was reported in the literature is challenging.

The BET results in  $\text{gcm}^{-3}$  were converted to the surface area of a layer with a known thickness using the density of the geological mineral used with an estimated porosity of 5.0%. Table 15 shows the results of the estimated surface area for a pyrite/pyrrhotite layer with a thickness of 100  $\mu\text{m}$  and 1 mm of a 1  $\text{cm}^2$  surface area of the steel underneath the iron sulfide layer.

The results show that for every unit surface area of steel there is an average of 50 times higher cathodic surface area for a 100  $\mu\text{m}$  layer of pyrite/pyrrhotite. In case the iron sulfide layer grows further to a 1 mm thick layer, the cathodic surface area increases to 500 times more for every 1  $\text{cm}^2$  unit surface area of the mild steel.

Table 15: Pyrite and pyrrhotite surface area

Particle < 104 $\mu\text{m}$	Thickness $\mu\text{m}$	Porosity %	Density $\text{gcm}^{-3}$	BET measurements $\text{cm}^2\text{g}^{-1}$	Surface Area $\text{cm}^2$
Pyrite	100	5	5.01	1594	40
	1000	5	5.01	1594	400
Pyrrhotite	100	5	4.61	2559	60
	1000	5	4.61	2559	600

The effect of the increased cathodic surface area on the corrosion current was implemented on the charge transfer current in the galvanic corrosion model, considering that the iron sulfide layers are porous and will not affect the limiting current. The calculated current density of mild steel without an iron sulfide layer and mild steel with iron sulfide layers with various thicknesses are listed in Table 16. The results show an increase of the

corrosion current with an iron sulfide corrosion product layer. However, the currents do not show a change between a 100  $\mu\text{m}$  and a 1 mm thick layer; this was a result of current being under a mass transfer control.

Table 16: Galvanic current densities vs. uncoupled X65 current densities

at pH 3.0, 10 rpm RDE flow, 30°C			
Iron sulfide layer	Thickness / $\mu\text{m}$	Surface Area / $\text{cm}^2$	$i / \text{Am}^{-2}$
Pyrite	100	40	4.5
	1000	400	4.5
Pyrrhotite	100	60	4
	1000	600	4.8
No layer	-	-	1.5

### *Summary*

- ZRA measurements were conducted and a galvanic corrosion current was directly measured between a mild steel and pyrite or pyrrhotite.
- The results showed that galvanic corrosion of an X65 steel coupled with the iron sulfide becomes a serious concern where a protective corrosion product layer leads to low uniform corrosion rates.
- Potentiostatic measurements were in agreement with the ZRA measurements, confirming their validity.
- A model is proposed in order to predict the galvanic corrosion currents between mild steel and with pyrite or pyrrhotite. Currently, the model has many open questions and requires further research in order to make it more general.

### Partially Dissolved Pyrrhotite Layer

It was shown that a galvanic current between a mild steel X65 coupled with pyrrhotite was substantially higher than a galvanic current between X65 and pyrite. While there seems to be evidence of the role of pyrite in localized corrosion,[46] contradictory reports are found with respect to the role of pyrrhotite/troilite[24], [46] which motivated this part of the current study. Here, the focus is on underlying corrosion behavior of a mild steel under a pyrrhotite/troilite layer. Initial experiments were conducted in an aqueous electrolyte saturated with CO<sub>2</sub> followed by experiments in an H<sub>2</sub>S saturated electrolyte and finally a mixed CO<sub>2</sub>/H<sub>2</sub>S electrolyte was used. The experiments in an aqueous CO<sub>2</sub> solution were conducted first, for several reasons: (i) they are much simpler and provide a good training opportunity where most of the experimental problems and analyses could be worked out before moving the experimentation into an H<sub>2</sub>S environment which is much more challenging; (ii) the galvanic coupling between the pyrrhotite layer and the steel surface was present in both environments; and (iii) in order to study the behavior in a mixed CO<sub>2</sub>/H<sub>2</sub>S environment which is most realistic for field applications, it was beneficial to work with “pure” environments first. Ultimately, this approach provided valuable insights into the behavior of pyrrhotite on the steel surface and enabled deciphering of the complicated interactions between the steel, the pyrrhotite layer and the corrosive environment.

## *Experimental Method*

### *Experimental Setup (Electrochemical Measurements)*

Electrochemical experiments were conducted in a conventional three-electrode glass cell (2L DI water with 20.2 g of NaCl), following the experimental matrix described in Table 17. Electrochemical measurements were conducted with a three-electrode setup, where a pretreated disc electrode made of X65 pipeline steel with a pyrrhotite layer, served as the WE. A 20 mm × 30 mm platinum mesh was used as CE. A saturated Ag/AgCl reference electrode was connected *via* a salt bridge with a Luggin capillary. In addition to the steel WE, four small square steel specimens with a surface area of 3.4 cm<sup>2</sup> were included in the cell for the purpose of surface analysis. The H<sub>2</sub>S gas concentration was maintained using gas rotameters and the accuracy of the concentration was confirmed by employing a gas sample pump with colorimetric H<sub>2</sub>S detector tubes. The gas outlet was scrubbed using a 5 M NaOH and several dry carbon scrubbers to capture the H<sub>2</sub>S.

Prior to each experiment, the electrolyte was deoxygenated by sparging with either N<sub>2</sub> or CO<sub>2</sub> gas for at least 3 hours prior to the addition of H<sub>2</sub>S gas. The H<sub>2</sub>S was introduced into the experimental cell at the desired concentration for at least one hour prior to immersing of the specimens, in order to ensure that the electrolyte was in equilibrium with respect to aqueous H<sub>2</sub>S. The electrolyte was stirred at 200 rpm with a 12.7 mm stir bar to ensure proper mixing. The solution pH was adjusted to the desired value by adding a deoxygenated 1 M HCl or NaOH solution. Then, the X65 specimens were inserted into the glass cell.

The corrosion processes were monitored *via* OCP, LPR, and EIS measurements. The measured  $R_p$  obtained from LPR was corrected for ohmic drop using the  $R_s$  measured by EIS. The Tafel slopes used to calculate the corrosion rate from the  $R_p$  values were:  $-0.12$  V per decade for the cathodic reaction and  $0.04$  V per decade for the anodic reaction. Similar Tafel slopes were reported by Zheng *et al.* [20], [79], [80] and were confirmed in the first part of the current study in the presence of  $H_2S$  across different experimental conditions at different pH values. The abovementioned authors have explicitly identified that the Tafel slope for direct reduction of  $H_2S$  was also approximately  $-0.12$  V per decade.

#### *Specimen Pretreatment (Pyrrhotite Layer Generation)*

In order to study the effect of the pyrrhotite layer on localized corrosion, the X65 steel specimens were “pretreated” in a different experimental setup, used to develop a reproducible pyrrhotite layer prior to their immersion into the electrochemical glass cell described above [136], [137].

In high temperature sulfidation of steel in crude oil fractions seen in refinery conditions pyrrhotite is most often found as a corrosion product. Such pyrrhotite is the same compound as seen in aqueous corrosion of steel in the presence of  $H_2S$ . This was used, following the procedure described below, to reproducibly form a pyrrhotite layer on steel that could be used in subsequent experimentation. The thickness of the pyrrhotite layer was controlled by the duration of the high temperature sulfidation experiment. Its purity was established utilizing XRD analysis. The structure and properties of the high-temperature pyrrhotite layer was assumed to be the same as what is formed in aqueous  $H_2S$  environments.

Specimen pretreatment, which was used to form a pyrrhotite layer on the steel surface, was performed in a 1 L Inconel autoclave. A mineral oil with a sulfur content of 0.25 wt% was used to form the pyrrhotite layer on the steel surfaces. The autoclave has a magnetic stirrer that drives an internal impeller that homogenizes the pretreatment fluid and ensures good heat transfer. Two types of specimens made of X65 steel were pretreated in the 1 L autoclave. The first type were small square specimens with a surface area of 3.4 cm<sup>2</sup> and the second type were large cylindrical specimens with the active surface being 7.9 cm<sup>2</sup>. The small square specimens were suspended using Inconel wires and completely submerged in the experimental fluid during the pretreatment. The large cylindrical specimens were placed on the bottom of the autoclave with the flat corroding surface facing upwards.

At the beginning of the pretreatment procedure, nitrogen gas was used to purge and pressurize the autoclave headspace to 1.5 MPa, when the heating was turned on. The autoclave reached the preset temperature of 343°C after approximately 1.5 h and then maintained at this value for 24 hours under continuous stirring. At the end of the pretreatment procedure, the heating and stirring were turned off and the autoclave was allowed to gradually cool down to room temperature. Before opening the autoclave, the headspace was purged with N<sub>2</sub> to remove any gases generated during the pretreatment procedures. The specimens were extracted from the oil and stored in a chemically inert mineral oil until further use in corrosion experiments. Prior to each corrosion experiment, the pretreated specimens were thoroughly rinsed with toluene and acetone to remove all oil residues from their surfaces and washed with isopropanol.

### *Pyrrhotite Layer Surface Analysis*

The morphology of the corrosion product layer was analyzed utilizing scanning electron microscopy (SEM - GEOL6390LV). Compositional analyses were carried out using a Rigaku Ultima IV X-Ray diffractometer with Cu-K $\alpha$  radiation from 10 to 70 2 $\theta$ . An Alicona Infinite Focus G4 profilometer was used to measure pit depth.

Table 17: Experimental matrix

Parameters	Conditions
Total pressure	0.1 MPa
Temperature	30, 60°C
Solution	0 and 1 wt% NaCl
Flow condition	Agitated, 200 rpm, 12.7 mm stir bar
Material	X65 with Pyrrhotite Layer
Corrosion measurement methods	LPR, EIS, and weight loss
pH <sub>2</sub> S in the gas phase	0, 0.01 MPa in N <sub>2</sub> or CO <sub>2</sub>
H <sub>2</sub> S concentration in the liquid phase	9.3 $\times 10^{-3}$ molL <sup>-1</sup> at 30°C 5.5 $\times 10^{-3}$ molL <sup>-1</sup> at 60°C
pH	4.0, 6.2 ( $\pm 0.1$ )

### *Results and Discussion*

A detailed discussion of the experimental results will follow the review of characterization data for the pretreated specimens.

#### *Pretreated Specimens*

Figure 32 shows the SEM image of the corroded (top) surface and cross-section image of the pretreated specimens. In Figure 32 (a) one can see that there are two layers, a loose layer on top of a more compact layer underneath, each has a similar gross morphology; the visual difference between the upper and lower layer is associated with delamination phenomena routinely observed for iron sulfides grown on steel. The cross-

section image in Figure 32 (b) demonstrates that the layer on the pretreated specimen is continuous and is well attached to the surface.

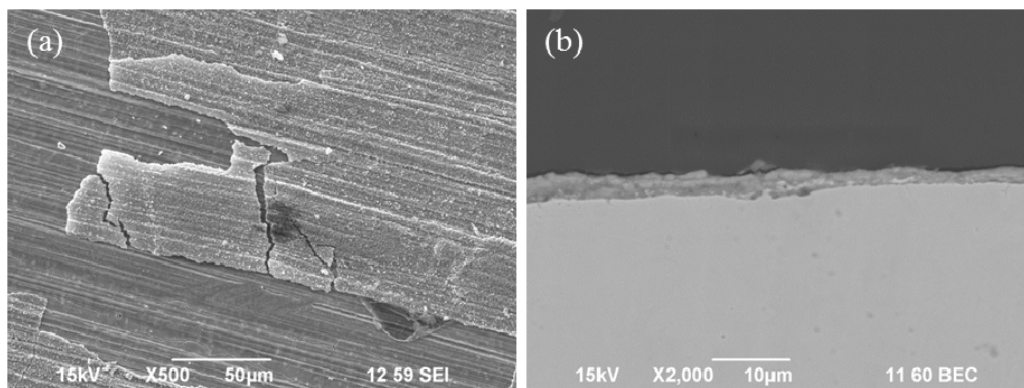


Figure 32: SEM images of representative pretreated steel specimen: (a) Top surface; (b) Cross-section.

Figure 33 shows the XRD pattern of the pretreated specimen. Based on initial peak analysis [61] troilite seemed to be the main component of the layer, however, a more thorough analysis revealed otherwise as described below.

Implementing a procedure as suggested by Arnold, *et al.*[138] who reported a relationship between the d-spacing corresponding to the (102) plane for pyrrhotite and the atomic percentage of metallic components, the  $\text{Fe}^{2+}$  content in the pretreated layer was determined. The authors [138] generated a graph for (102) d-spacing values *versus* iron content in atomic % for pyrrhotite. Utilizing this graph, the  $\text{Fe}^{2+}$  content of generated pyrrhotite layers was obtained. The obtained  $\text{Fe}^{2+}$  and the thermodynamic plot of temperature *vs.* phase formation of iron sulfides reported by Desborough, *et al.*, [139] was used to characterize the composition of the layer. It was concluded that the layer was mostly

composed of pyrrhotite with some troilite. This was later confirmed by using XRD quantitative analysis (using the PDXL software).

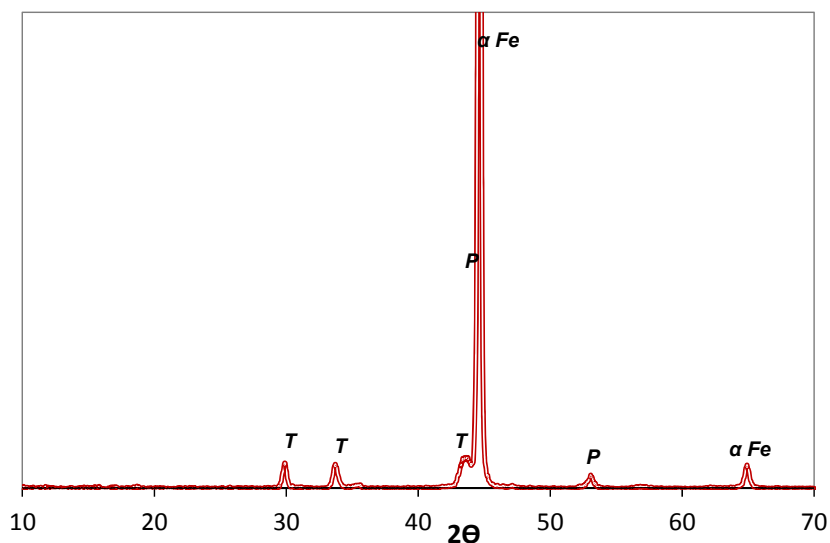


Figure 33: XRD pattern of the pretreated X65 specimens. (P: pyrrhotite, T: troilite).

*Corrosion of Steel with a Preformed Pyrrhotite Layer Exposed to an Aqueous CO<sub>2</sub> Solution*

In aqueous CO<sub>2</sub> corrosion, the pretreated specimen with a pyrrhotite layer was studied under two conditions: in a conductive 1 wt% NaCl electrolyte and a poorly conductive DI water in order to investigate the role of galvanic coupling. However, LPR measurements were not conducted in the experiments without NaCl due to the low solution conductivity. The solution pH which was monitored for the duration of the experiments, was relatively stable (changing from pH 4.0 to pH 4.5).

Figure 34 shows the average corrosion rate of the pretreated specimen exposed to a CO<sub>2</sub> saturated solution with 1 wt% NaCl. This experiment was repeated four times. The

average of the measured data is reported with the error bars denoting the maximum and minimum values. The initial corrosion rate was approximately  $0.7 \text{ mmy}^{-1}$ , compared to the expected bare steel corrosion rate of about  $2.0 \text{ mmy}^{-1}$  (as calculated using the mechanistic corrosion model described by Zheng, *et al.* [79]). The comparison indicates that the preformed pyrrhotite layer did offer some protection to the steel surface underneath. However, the initial corrosion rate was not as low as one would expect as a result of a compact and protective layer. When the corrosion rate is controlled by the rate of cathodic reduction then the conductive nature of the pyrrhotite layer should increase the uniform corrosion rate; this can be offset by the same porous layer acting as a diffusion barrier, what should have decreased the corrosion rate. Either way, over a period of three days the corrosion rate decreased to less than  $0.1 \text{ mmy}^{-1}$ . The specimen OCP increased approximately 20 mV during the experiment.

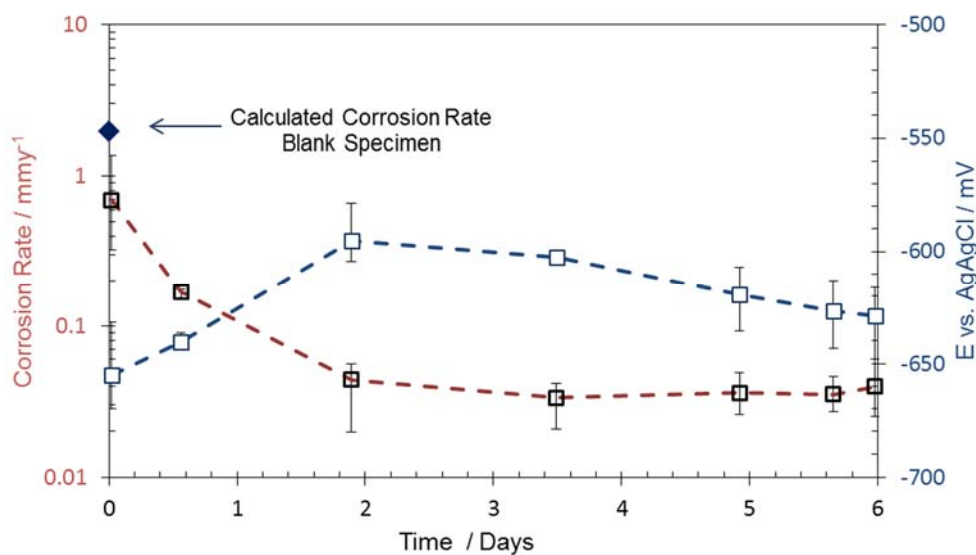


Figure 34: Corrosion rate and OCP of X65 specimen with pyrrhotite type layer vs. time of a sparged solution with 0.097 MPa  $\text{CO}_2$  at  $30^\circ\text{C}$  and pH 4.0.

Figure 35 shows the SEM image of the pretreated specimens after exposure to the aqueous CO<sub>2</sub> solutions. Irrespective of the presence of NaCl, the top layers on both images (Figure 35 (a) and Figure 35 (b)) appeared to be similar – with locations where the layer locally collapsed, which were later identified to be points of localized corrosion. Overall, the top layer morphology changed as a result of exposure to the aqueous CO<sub>2</sub> solution as compared to the original surface shown in Figure 32 (a).

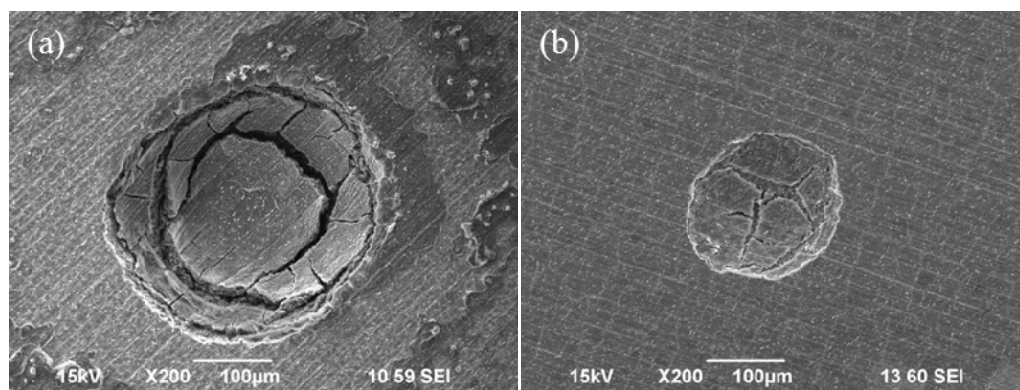


Figure 35: SEM image of pretreated specimens after exposure to an aqueous solution sparged with 0.097 MPa CO<sub>2</sub> at 30°C and pH 4.0 (a) 1 wt% NaCl, (b) no NaCl.

Figure 36 shows cross-sections of pits formed on the pretreated specimens exposed to the aqueous CO<sub>2</sub> solution with and without NaCl. A small amount of corrosion product was found in the pits, which suggests they were still actively corroding at the time when specimens were retrieved. The area in the vicinity of the pits on both images show that the corrosion product layer was thin, and therefore undetectable with XRD.

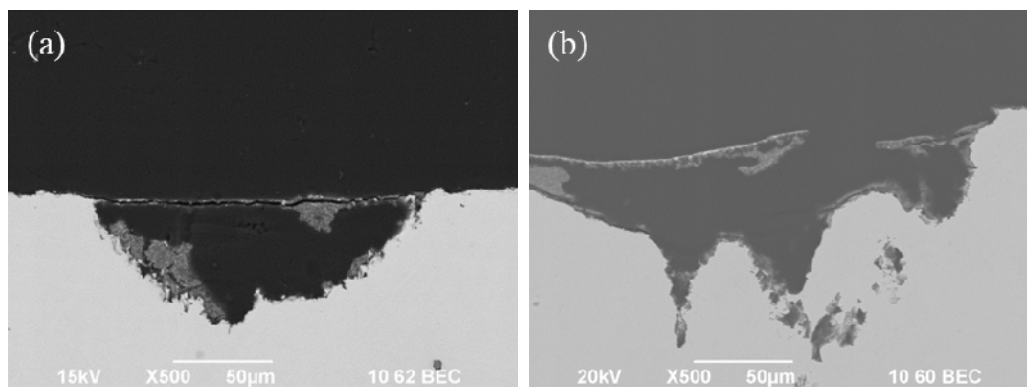


Figure 36: Cross-section image of pretreated specimens after exposure to an aqueous solution sparged with 0.097 MPa CO<sub>2</sub> at 30°C and pH 4.0 (a) 1 wt% NaCl, (b) no NaCl.

Experimental observation of the pretreated specimens revealed that the preformed pyrrhotite layer underwent dissolution upon its exposure to the aqueous CO<sub>2</sub> solution. Since the preformed layer was not in a thermodynamically stable condition, dissolution of the layer was expected under these test conditions. There have been multiple mechanisms proposed for pyrrhotite dissolution in acidic media. [114], [134], [140], [141] One of the reductive mechanisms suggests that H<sup>+</sup> adsorbs onto “anionic sites” on the surface of the pyrrhotite crystals, and this results in a transformation from a nonstoichiometric pyrrhotite to stoichiometric troilite (Reaction (43)) with production of H<sub>2</sub>S. This is followed by dissolution of troilite to form HS<sup>-</sup> and Fe<sup>2+</sup> shown by Reaction (44). [4], [36], [114], [116], [140]–[142]

In the current study, it seems that the preformed pyrrhotite layer underwent a dissolution process, which initially started locally and then proceeded to dissolve completely over time. Localized corrosion initiated on these local sites, where the preformed layer dissolved first, leaving a galvanic cell between the exposed steel surface

and the remaining pyrrhotite layer. The iron dissolution at the anode is accelerated by an additional cathodic reaction on the surrounding semiconductive pyrrhotite layer.

Pyrrhotite is a semiconductive iron sulfide, which in a conductive solution, forms a galvanic cell when in direct contact with a steel surface. Table 4 shows that pyrrhotite's potential is more positive compared to the steel surface. [87]–[89] Therefore, the steel surface becomes the anode and corrodes at a higher rate. This galvanic attack is accelerated due to a high cathode/anode surface area ratio, caused by the porous nature of the pyrrhotite layer, which is expected to enhance the rate of  $H^+$  reduction[126].

Figure 37 shows the XRD patterns of the pretreated specimen surface before and after it was exposed for 6 days to the aqueous  $CO_2$  solution. The diffraction patterns indicate that the layer post-exposure was too thin to be detectable by conventional XRD, confirming that the pyrrhotite layer dissolved by the end of the experiment.

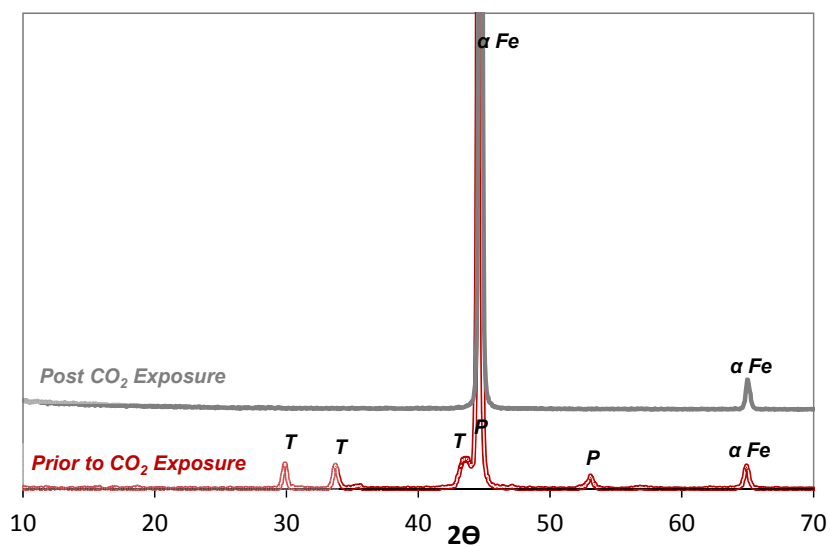


Figure 37: XRD of the pretreated specimen after exposure to an aqueous solution sparged with 0.097 MPa  $CO_2$  at 30°C and pH 4.0. (P: pyrrhotite, T: troilite).

There seems to be an additional process that took place at the same time. Dissolution of the pyrrhotite layer, produced small amounts of H<sub>2</sub>S as described above (Reaction 1), which then reacted with the adjacent steel surface, forming most likely a very thin mackinawite layer. Utilizing XPS analysis, it was shown by Lee [21] that a thin mackinawite layer forms on the surface of a mild steel upon exposure to low concentrations of H<sub>2</sub>S, even if it is undetectable by SEM/EDS/XRD. This mackinawite layer probably led to a reduction of the uniform corrosion rate, as shown in Figure 34, but did not affect the localized corrosion.

To confirm the galvanic nature of the observed localized attack, the conductivity of the aqueous solution was varied, which was expected to have a pronounced effect on the magnitude of the galvanic current. To that effect, experiments were conducted in the presence and absence of NaCl. Before the results are presented, it should be noted that in the literature, the role of chloride in localized corrosion is contradictory. [24], [71], [143]–[146] While some researchers have attributed localized corrosion initiation of mild steel to the presence of chlorides, work by Fang *et al.*, [71] revealed that the dominant effect is via solution conductivity. Thus, the role of NaCl on localized corrosion in the present study is attributed primarily to its impact on solution conductivity.

Figure 38 shows the SEM images of the pretreated specimens after exposure to solutions with and without NaCl and after the corrosion product layer was chemically removed using a Clarke Solution following the procedure described in the ASTM G1 standard[147]. Localized corrosion was observed on both specimens. Profilometry was utilized to measure the depth of the pits and to calculate the time averaged pit penetration

rate:  $PPR = h/t$ , where  $h$  is the deepest pit depth in mm, and  $t$  is the time in years. Figure 39 shows the profilometry images, indicating that the specimen exposed to a more conductive solution was attacked at a much higher rate ( $13.7 \text{ mmy}^{-1}$ ) than the specimen exposed to the less conductive solution ( $4.2 \text{ mmy}^{-1}$ ). Uniform bare steel corrosion rate under these conditions is of the order of 2 to 3  $\text{mmy}^{-1}$  making the localized attack in the conductive solution particularly severe, confirming its galvanic nature (see Figure 40).

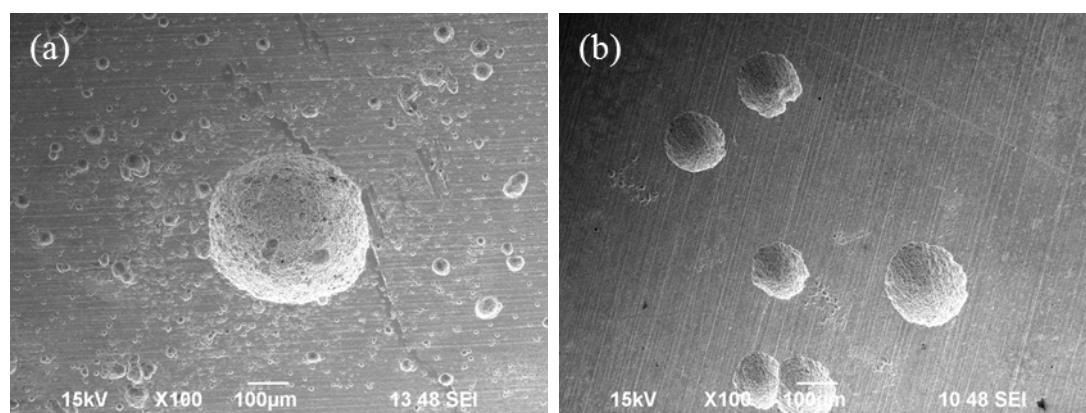


Figure 38: SEM image of pretreated specimens after exposure to an aqueous solution sparged with 0.097 MPa  $\text{CO}_2$  at 30°C and pH 4.0 without corrosion product layer (a) 1 wt.% NaCl, (b) no NaCl.

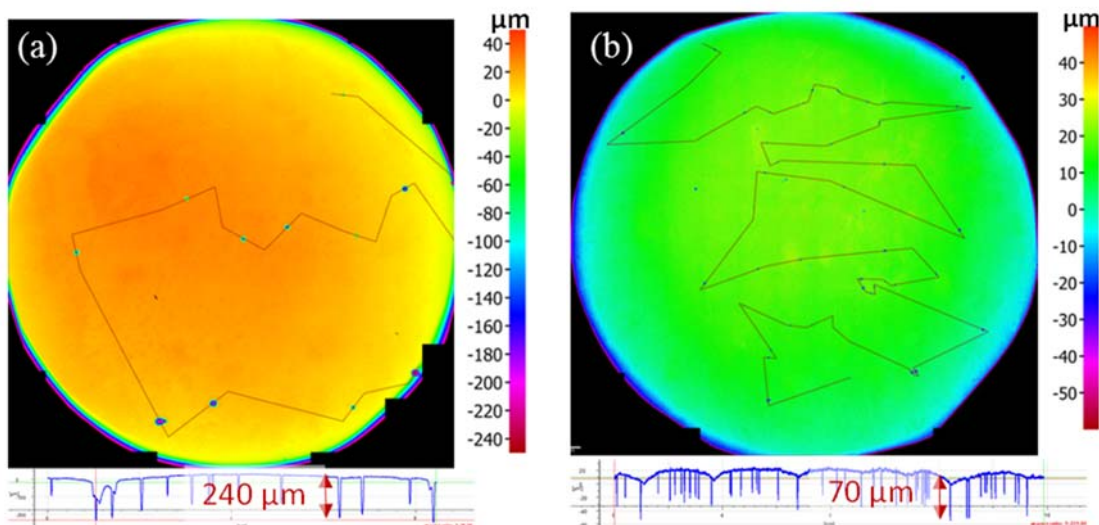


Figure 39: Profilometry image of pretreated specimens after exposure to an aqueous solution sparged with 0.097 MPa CO<sub>2</sub> at 30°C and pH 4.0 without layer (a) 1 wt% NaCl, (b) no NaCl.

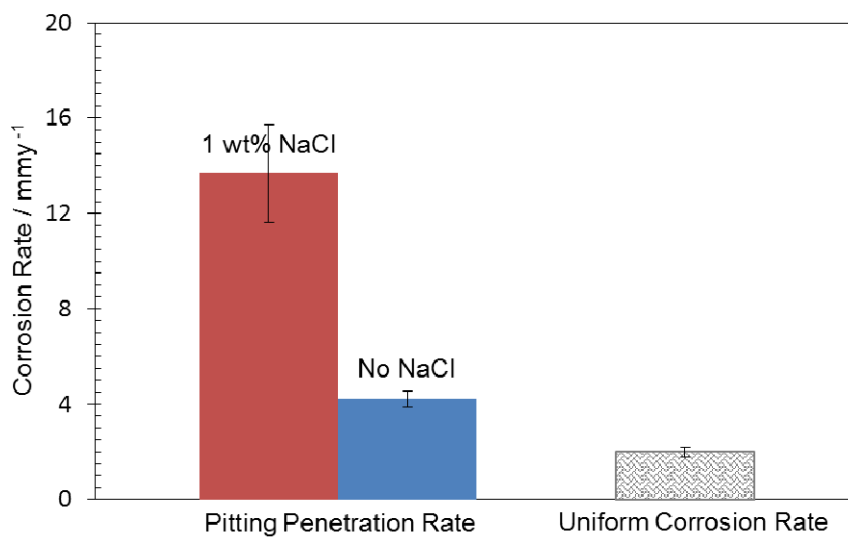


Figure 40: Pit penetration rate of the specimens in an aqueous solution sparged with 0.97 bar CO<sub>2</sub> at 30°C and pH 4.0.

*Corrosion of Steel with a Preformed Pyrrhotite Layer Exposed to Aqueous H<sub>2</sub>S**Solution*

Figure 41 shows the average LPR corrosion rate and the OCP data (from 2 repeated experiments) conducted with the pretreated specimen exposed to an aqueous solution sparged with 0.01 MPa H<sub>2</sub>S at two different conditions. The conditions were selected based on the thermodynamic stability of the pyrrhotite layer. In the first condition, the pyrrhotite layer should have been thermodynamically stable (the solution was slightly supersaturated) and was not expected to dissolve (60°C and pH 6.2 ± 0.1). The second condition (30°C and pH 4.0 ± 0.1) was selected so that pyrrhotite was not thermodynamically stable (the solution was under-saturated), and it was expected to dissolve. Experiments for each of these two conditions were repeated.

The initial corrosion rate was rather high and similar to that obtained with a bare steel (blank) under the same conditions (as calculated by the mechanistic model described by Zheng *et al.* [2-4]), suggesting that the preformed pyrrhotite layer did not initially offer any appreciable corrosion protection to the steel surface in these conditions. However, the corrosion rate decreased significantly within the first day of exposure to a value close or less than 0.1 mmy<sup>-1</sup> depending on the experimental conditions (Figure 41 (a)). The OCP change over time (Figure 41 (b)) shows a stable OCP throughout the experiment for the pH 4.0 and 30 °C condition, while for the experiment at pH 6.2, 60°C, OCP increased approximately by 100 mV.

The bulk pH did not change significantly for the case where the pyrrhotite layer was thermodynamically stable and did not dissolve (at pH 6.2). However, when the

pyrrhotite layer dissolved, the bulk pH increased from initial pH 4.0 to pH 5.0, bringing it close to saturation for pyrrhotite.

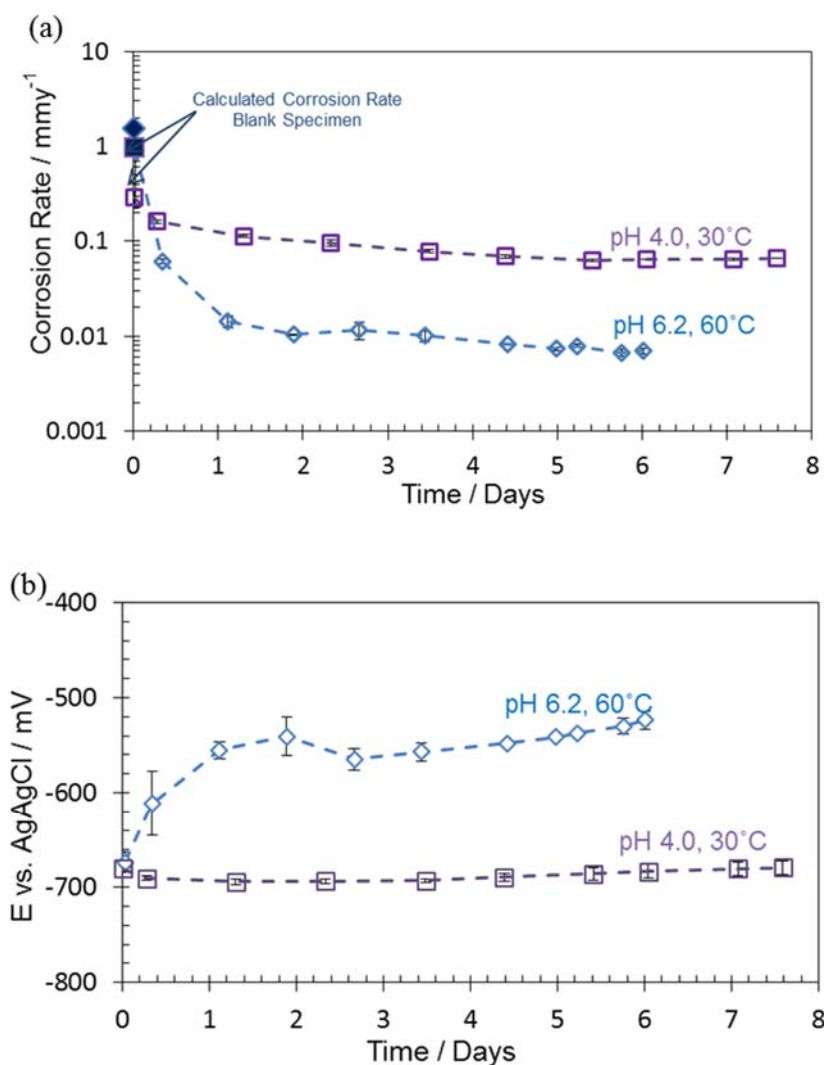


Figure 41: (a) Corrosion rate of pretreated specimen (b) the OCP vs. time in an aqueous solution sparged with 0.01 MPa H<sub>2</sub>S in N<sub>2</sub>, 1 wt% NaCl.

Figure 42 shows the SEM images of the specimen at the end of the experiment. It can be observed that the pretreated specimen exposed to the thermodynamically stable

condition, was uniformly covered by a corrosion product layer, Figure 42 (a). However, the specimen initially exposed to the under-saturated solution, Figure 42 (b), shows evidence of damage to the initial corrosion product layer as well as a layer below and some precipitation on top. Cross-section analyses were performed to identify the thickness and the morphology of these layers. Figure 43 shows that in both experimental conditions there was a bilayer on the surface. For the specimen exposed to the thermodynamically stable condition, Figure 43 (a), the original pyrrhotite layer seems to be intact (having a similar thickness as that shown in Figure 32 (b)), with an additional layer on top. For the specimen exposed to the under-saturated solution, the final corrosion product layer is much thinner due to pyrrhotite dissolution, Figure 43 (b).

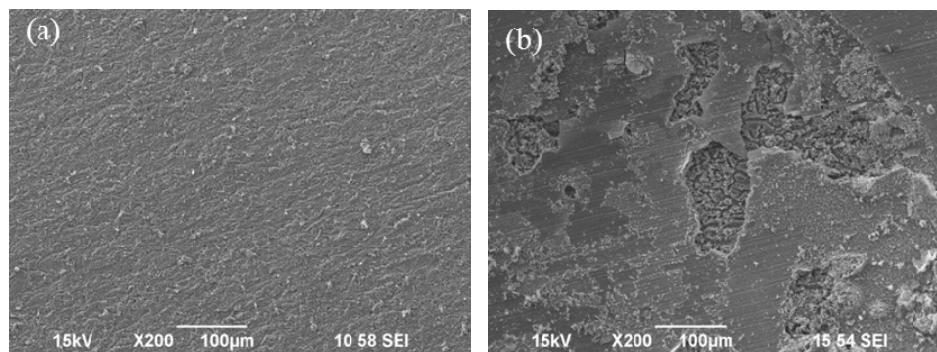


Figure 42: SEM image of pretreated specimens after exposure to an aqueous solution sparged with 0.01 MPa H<sub>2</sub>S, 1 wt% NaCl at (a) 60°C and pH 6.2 (b) 30°C and pH 4.1.

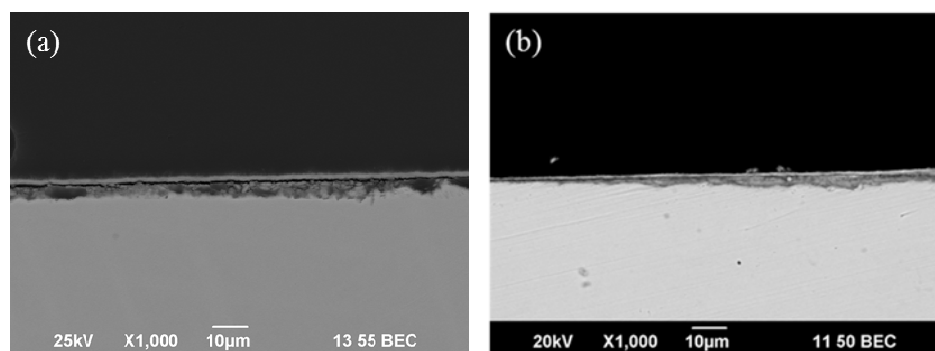


Figure 43: Cross-section image of pretreated specimens after exposure to an aqueous solution sparged with 0.01 MPa H<sub>2</sub>S, 1 wt% NaCl at (a) 60°C and pH 6.2 (b) 30°C and pH 4.1.

XRD analysis was conducted on specimens after their exposure to the aqueous H<sub>2</sub>S solution, in order to characterize the layers and any possible compositional change. Figure 44 shows the XRD patterns of the pretreated specimens before and after exposure to the two experimental conditions. The extra peaks seen on the two exposed specimens were identified to be mackinawite, marked as “M”, and troilite, marked as “T”. The appearance of troilite was expected since the product of a non-stoichiometric pyrrhotite transformation is a stoichiometric troilite (Reaction (44)).[4], [114], [142] Mackinawite has a similar solubility as pyrrhotite and appears to have precipitated. One could wonder why pyrite was not observed on the XRD analysis post H<sub>2</sub>S exposure. Less stable iron sulfides usually transform to the more stable iron sulfide polymorphs after longer exposures depending on thermodynamic conditions. In order to form pyrite, much higher pH, higher potentials or higher temperatures are required. The experiments described here were conducted at conditions where pyrite was not thermodynamically stable. Thus, it was not expected to observe any pyrite on the specimens. It is noteworthy that pyrite has a slow kinetics of formation which makes it even more difficult to obtain in laboratory experimentation.

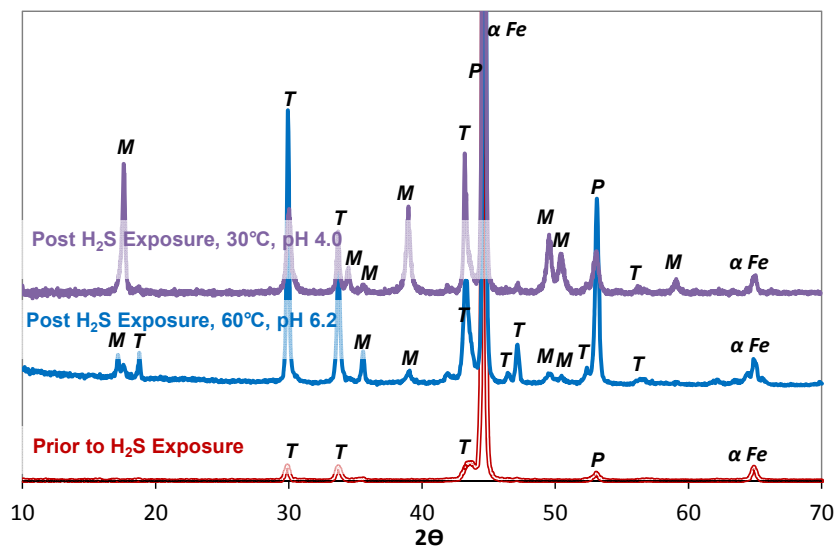


Figure 44: XRD of the pretreated specimens after exposure to an aqueous solution sparged with with 0.01 MPa H<sub>2</sub>S at 60°C and pH 6.2, 30°C and pH 4.0, 1 wt% NaCl. (P: pyrrhotite, T: troilite, M: mackinawite).

Figure 45 shows the SEM image of the specimens after the corrosion product layer was removed using a Clarke solution [147]. Figure 45 (a) shows a uniformly corroded surface of the specimen exposed to a thermodynamically stable condition, while Figure 45 (b) shows a non-uniform attack of the steel surface of the specimen exposed to the under-saturated solution. However, this non-uniform attack could not be detected in the profilometry image of the same surface shown in Figure 46, which indicates that these areas were rather shallow. In summary, no galvanic localized attack was detected in these experiments, at least not in the same way as was seen in CO<sub>2</sub> experiments reported above.

The cross-section images in Figure 43 show that upon exposure to the aqueous H<sub>2</sub>S solution, the preformed pyrrhotite layer was covered with a dense top layer where the pores were most likely filled with the secondary corrosion product layer. Based on XRD analyses, it is most likely that this layer was composed of precipitated mackinawite and

possibly troilite/pyrrhotite. It is here hypothesized that this layer, once it formed, has “blocked” the preformed pyrrhotite layer and the steel surface underneath, thereby limiting the mass transfer of species. Thus, any galvanic cell between the steel surface and the pyrrhotite layer was disrupted and, as a result, localized corrosion was retarded. In the experiment conducted in a supersaturated solution the dense top layer precipitated fast and therefore no localized attack is seen on Figure 45 (a). For the initially under-saturated solution, the dense top layer formed after approximately two days when the bulk solution reached saturation; in the interim the pyrrhotite layer partially dissolved and localized attack was initiated, which was then arrested due to the formation of the dense top layer. This is evidenced by the shallow pits seen in Figure 45 (b).

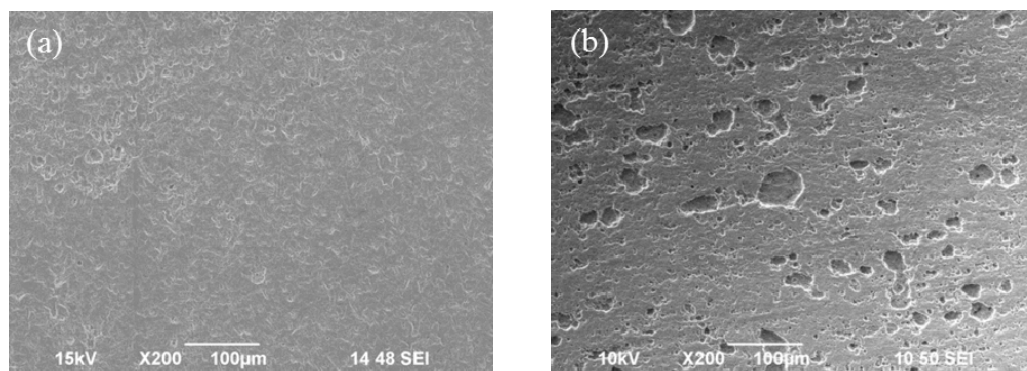


Figure 45: SEM image of the pretreated specimens after exposure to an aqueous solution sparged with 0.01 MPa H<sub>2</sub>S, 1 wt% NaCl at (a) 60°C and pH 6.2, (b) 30°C and pH 4.0, after removal of the corrosion product layer.

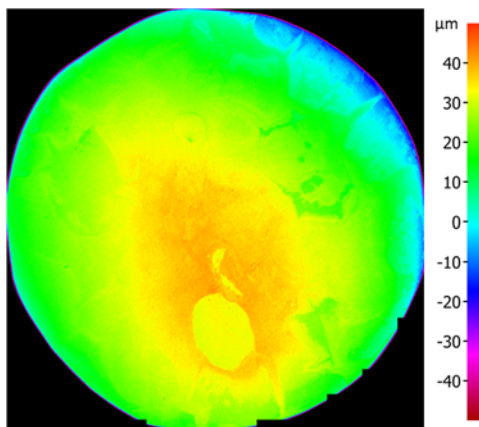


Figure 46: Profilometry image of the pretreated specimen after exposure to an aqueous solution sparged with 0.01 MPa H<sub>2</sub>S, 1 wt% NaCl at 30°C and pH 4.0 without layer.

*Corrosion of Steel with a Preformed Pyrrhotite Layer Exposed to a Mixed CO<sub>2</sub>/H<sub>2</sub>S*

*Solutions*

In Part 1 of the present study, it was shown that localized corrosion was observed on pretreated specimens exposed to an aqueous CO<sub>2</sub> solution, due to the uneven dissolution of the pyrrhotite layer which led to galvanic corrosion. In Part 2, it was shown that in an aqueous H<sub>2</sub>S solution, localized corrosion did not take place as a result of a dense layer formation on top of the pyrrhotite layer. It is therefore of interest to investigate the possibility of localized corrosion in mixed CO<sub>2</sub>/H<sub>2</sub>S environments, which corresponds to more realistic conditions as would be encountered in the field.

As shown in Figure 47 (a), the uniform corrosion rate was higher with CO<sub>2</sub> present than without it, for the same partial pressure of H<sub>2</sub>S. The calculated [20], [79], [80] bare steel corrosion rate is also shown in Figure 47 (a). The pH in the bulk solution was reasonably stable ( $\pm 0.1$  pH unit) throughout the experiments with and without CO<sub>2</sub>. The OCP change of the pretreated specimens exposed to the experimental conditions in Figure

47 (b) shows approximately 100 to 200 mV potential change for the specimen upon their exposure to the experimental solution.

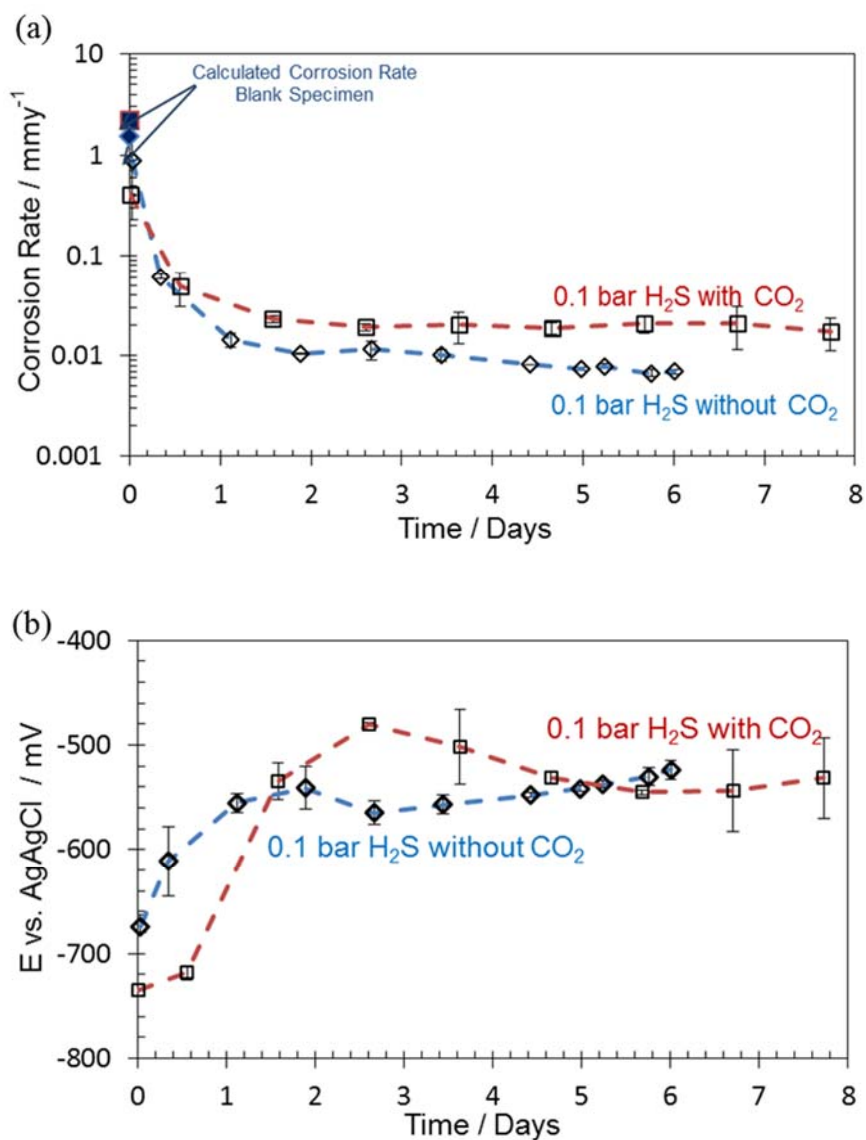


Figure 47: (a) Corrosion rate (b) OCP of pretreated specimen vs. time sparged with 0.01 MPa H<sub>2</sub>S with and without 0.07 MPa CO<sub>2</sub>, at pH 6.1 and 60°C, 1 wt% NaCl.

Figure 48 (a) shows the SEM images of the top surface the specimen after the exposure to an H<sub>2</sub>S only solution (in the absence of CO<sub>2</sub>) where a uniform corrosion product can be seen. A nonuniform appearance of the corrosion product layer is found in the presence of CO<sub>2</sub>, Figure 48 (b). If we compare the image in Figure 32 (a) of the pyrrhotite layer before exposure and the image in Figure 48 (b) after exposure to the mixed CO<sub>2</sub>/H<sub>2</sub>S environment, we can observe the partial transformation of the original pyrrhotite layer.

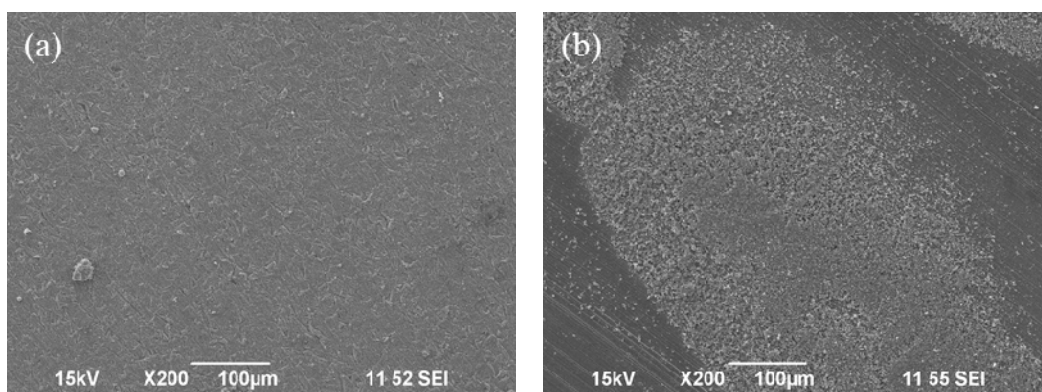


Figure 48: SEM image of pretreated specimens after exposure to an aqueous solution sparged with 0.01 MPa H<sub>2</sub>S, 1 wt% NaCl at 60°C and pH 6.2 (a) no CO<sub>2</sub>, (b) 0.07 MPa CO<sub>2</sub>.

This is confirmed in Figure 49 (b) where the thinning of the original pyrrhotite layer is obvious. According to the cross section image of the pretreated specimen in Figure 32 (b), the preformed pyrrhotite layer was approximately 3 to 4 µm. After exposure to 0.1 bar H<sub>2</sub>S in the absence of CO<sub>2</sub> as shown in Figure 49 (a), the layer grew to approximately 5 to 6 µm, while it thinned to around 2 µm when exposed to 0.1 bar H<sub>2</sub>S and 0.7 bar CO<sub>2</sub> Figure 49 (b). In the absence of CO<sub>2</sub> there is a dense top layer that formed as shown in Figure 49

(a) and also in Figure 43 (a) for a different location. However, this type of layer has not formed in the presence of CO<sub>2</sub> and an appearance of a different “fluffy” phase can be seen. Also, the pyrrhotite layer seems to have been locally detached from the steel surface in the presence of CO<sub>2</sub> which was not the case in the H<sub>2</sub>S only environment.

XRD analyses were carried out to determine the composition of the layer on the specimens as the preformed pyrrhotite underwent some transformation in the presence of CO<sub>2</sub>. The intensity of the peaks associated with troilite/mackinawite is stronger for the specimen exposed to the H<sub>2</sub>S only solution (see Figure 50). It is believed that the “fluffy” phase seen in Figure 48 (b) and Figure 49 (b) is mackinawite.

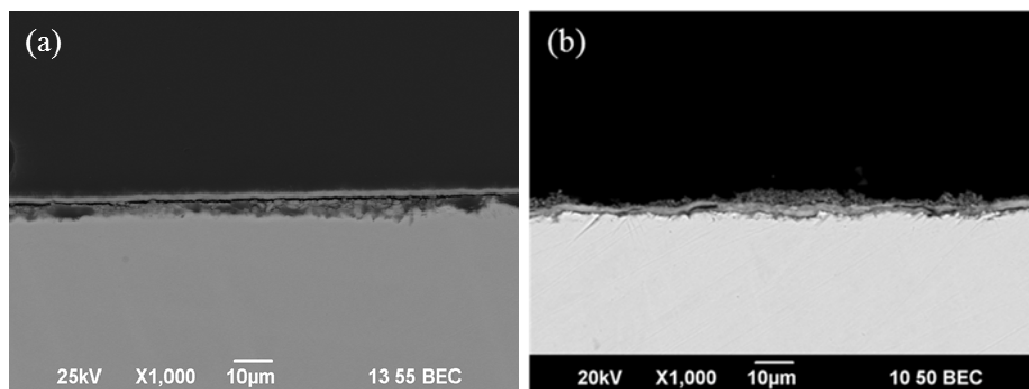


Figure 49: Cross section image of pretreated specimens after exposure to an aqueous solution sparged with 0.01 MPa H<sub>2</sub>S, 1 wt% NaCl at 60°C and pH 6.2 (a) no CO<sub>2</sub>, (b) 0.07 MPa CO<sub>2</sub>.

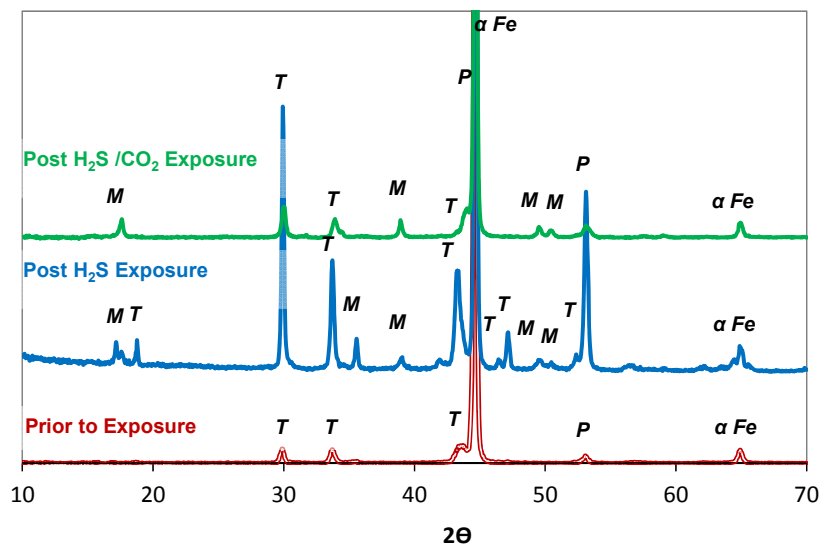


Figure 50: XRD of the pretreated specimens after exposure to an aqueous solution sparged with 0.01 MPa H<sub>2</sub>S at 60°C and pH 6.2 with and without 0.07 MPa CO<sub>2</sub>, 1 wt% NaCl. (P: pyrrhotite, T: troilite, M: mackinawite).

Following removal of the layer, Figure 51 (b) shows that the steel surface exposed to the mixed CO<sub>2</sub>/H<sub>2</sub>S solution underwent localized corrosion, which was not the case in the absence of CO<sub>2</sub> see Figure 51 (a). This could be explained by the fact that a different layer formed on the specimens upon exposure to different experimental conditions: a dense more protective layer formed in the H<sub>2</sub>S only solution and a “fluffy” mackinawite layer formed in the mixed CO<sub>2</sub>/H<sub>2</sub>S solution.

Profilometry was utilized to measure the depth of the observed pits. Figure 52 shows that the localized attack was found only in one section on the steel surface with the maximum pit depth of 133 μm corresponding to 5.5 (±0.5) mmy<sup>-1</sup> pit penetration rate. It should be noted that these experiments were repeated. In both experiments there were only a few pits concentrated in a limited area.

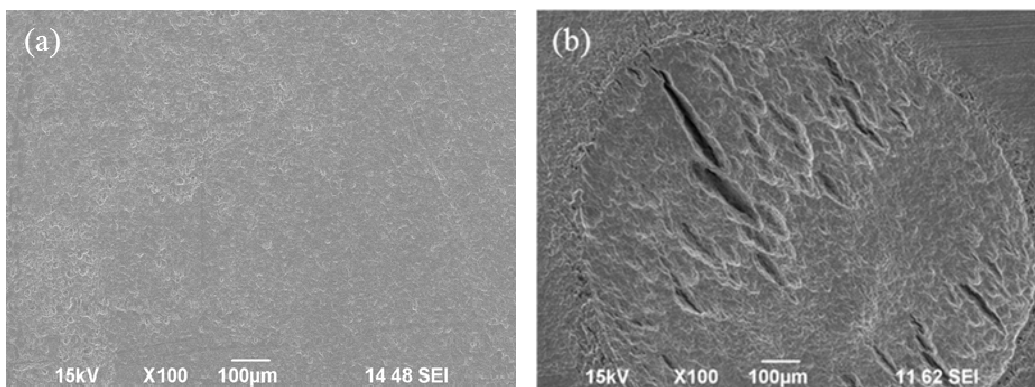


Figure 51: SEM image of the pretreated specimens after exposure to an aqueous solution sparged with 0.01 MPa H<sub>2</sub>S, 1 wt% NaCl at 60°C and pH 6.2, (a) without CO<sub>2</sub>, and (b) 0.07 MPa CO<sub>2</sub>, after removal of the corrosion product layer.

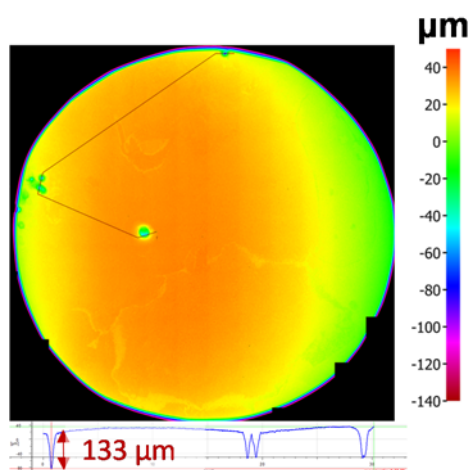


Figure 52: Profilometry image of pretreated specimen after exposure to an aqueous solution sparged with 0.01 MPa H<sub>2</sub>S, 0.07 MPa CO<sub>2</sub>, 1 wt% NaCl at 60°C and pH 6.2 without layer.

### *Summary*

- Localized corrosion occurred in an aqueous CO<sub>2</sub> solution with and without NaCl, where the conductive pyrrhotite layer underwent non-uniform dissolution, resulting in partial exposure of the steel surface, forming a galvanic couple.

- In an aqueous CO<sub>2</sub> solution the presence of 1 wt% NaCl led to a higher solution conductivity, where the localized corrosion rates were found to be approximately three times higher than the localized corrosion rate in the absence of NaCl, which confirmed the galvanic nature of the attack.
- Localized corrosion was found to a lesser extent in a mixed CO<sub>2</sub>/H<sub>2</sub>S aqueous solution containing 1 wt% NaCl, where the local dissolution of the pyrrhotite layer was slower and a partially protective mackinawite layer formed.
- A dense protective layer formed on top of the pyrrhotite layer on the specimen exposed to an aqueous H<sub>2</sub>S solution with 1 wt% NaCl. Thus, the preformed pyrrhotite layer dissolution was slowed down significantly, and no localized attack was observed.
- Overall it is concluded that when a non-uniform semi-conductive pyrrhotite layer is in contact with the steel surface in a corrosive electrolyte, this could lead to galvanically driven localized corrosion.

#### Localized Corrosion under Pyrrhotite Containing Deposit Layers

Localized corrosion associated with a pyrrhotite or pyrrhotite/pyrite mixed corrosion product layer has been observed across a wide range of experimental conditions. At high temperature (120°C) and partial pressures of H<sub>2</sub>S, Gao *et al.* [148] reported localized corrosion under a mixed layer of pyrrhotite and pyrite formed at different H<sub>2</sub>S partial pressures (0.5 to 2 bar p<sub>H<sub>2</sub>S</sub>). In their study, H<sub>2</sub>S partial pressure was varied across different experiments, where a different corrosion product layer was reported in each

condition. Under two conditions where a mixed pyrrhotite / pyrite layer formed, localized corrosion was observed; the different underlying corrosion behavior was most likely the aftermath of different corrosion product layers formed on the surface. It is of key importance to note that a more intense localized corrosion was observed, as the pyrite phase grew further in the corrosion product layer. In another study, Gao *et al.* [47] conducted experiments at constant aqueous H<sub>2</sub>S concentration (0.00385 mol.L<sup>-1</sup>, p<sub>H<sub>2</sub>S</sub> was close 0.1 to 0.18 bar) at different temperatures (80°C to 200°C), where they reported localized corrosion under pyrrhotite/pyrite layers, formed at 120°C and 200°C. What seems to be a common parameter in their experimental results is the formation of a mixed pyrrhotite and pyrite layer, which resulted in localized corrosion.

In atmospheric conditions (25 °C, 1 bar), it was reported that a mild steel under a preformed pyrrhotite layer endured localized corrosion where there was a partial dissolution of the preformed pyrrhotite layer. Overall, it is concluded that when a non-uniform semiconductive pyrrhotite layer is in contact with the steel surface in a corrosive electrolyte, this could lead to galvanically-driven localized corrosion.[149] The present study proposes that the observed localized corrosion in above mentioned cases ensued as there was some form of disruption resulting in discontinuity to the corrosion product (pyrrhotite) layer; such discontinuity was the aftermath of the partial dissolution of the preformed pyrrhotite layer [149], or the pyrite nucleation/growth in Gao *et al.*'s [148] study.

The disruption of a pyrrhotite layer via pyrite nucleation does not seem as intuitive as the partial dissolution of a layer does. Nonetheless, based on our current understanding

of semiconductive iron sulfide corrosion product layers, the hypothesis based disruption seems the best explanation that the present study could offer. Disruptive nucleation of pyrite within the pyrrhotite layer has been investigated in depth [38], [150], [151], where it has been proposed that as the pyrite phase nucleates in the “parent” pyrrhotite “micro-cracks” forms; this results in a disruption in the pyrrhotite layer depending on the conduit that this process follows. Pyrrhotite transformation to pyrite has been postulated to take place via three possible pathways; it could ensue through an intermediary phase, marcasite [151]; where, marcasite crystals follow a preferred orientation in the “parent pyrrhotite”. The transformation of marcasite to pyrite develops “micro cracks” around the pyrite crystal. The second pathway is the direct pyrrhotite transformation to marcasite/pyrite, where contrary to the pyrite crystals which form via transitional marcasite phase, this pathway results in a mostly random orientation for the pyrite crystals, with the final outcome being a porous layer [38]. It has also been reported that pyrite could directly form and replace pyrrhotite (the third pathway)[150]. The latter mechanism results in a less porous layer.

Although, the detailed study of iron sulfides transformation to a more stable phase has not been the focus of corrosion research, related studies [38], [150], [151] could offer some explanation into the corrosion product layer crystallography, which is not commonly discussed in research concerning corrosion. The transitional phases of a corrosion product layer could play a significant role in localized corrosion initiation. The abovementioned possibilities for pyrite formation within a pyrrhotite layer could ultimately lead to some clues for localized corrosion under disrupted corrosion product layers. The work presented

below investigates the corrosion behavior of a mild steel under three different deposit layers containing pyrrhotite, the results of which were compared with the result from a mild steel corrosion under silica sand deposit.

#### *Experimental Method and Set-Up*

Experiments were conducted in a conventional glass cell (2L 1wt% NaCl solution). The solutions were deoxygenated and saturated with CO<sub>2</sub> gas at least 2 hours prior to specimen's immersion into the cell. The solution pH was adjusted to the desired value by addition of a deoxygenated HCl or NaOH solution. A 0.5" stir bar was used to create a well-mixed solution.

Mineralogical pyrite and pyrrhotite specimens, and research grade silica<sup>22</sup> sand were used as a deposit layer which were placed on the specimen in order to investigate mild steel corrosion under four different deposit layers;

- silica sand,
- pyrrhotite,
- a mixture of pyrrhotite and pyrite, and
- a mixture of pyrrhotite and silica sand.

Iron sulfide specimens were sieved in order to obtain a particle size range of 100 – 400 µm and 400 – 1000 µm. An API 5L X65 mild steel disc with a surface area of 7.9 cm<sup>2</sup> polished with 150, 400 and 600 grit sand paper, rinsed with DI water and isopropyl

---

<sup>22</sup> Ottawa Sand provided by Fisher chemical

alcohol in an ultrasonic bath, N<sub>2</sub> dried mounted into the under deposit sample holder (Figure 53) and was used as the working electrode.

The deposit materials were rinsed with isopropyl alcohol and DI water, then sparged with CO<sub>2</sub> in a 1 wt% NaCl solution in a separate flask prior to their placement on the X65 surface. A pipet was used to transfer the particles to the experimental cell.

The specimen was pre-corroded for 30 min prior to the deposit placement; the desired deposit layer (as listed above) was deposited on the steel surface. The experiments lasted 5 to 6 days. Uniform corrosion rate was monitored conducting LPR measurements on the steel specimen. After the experiment, SEM and profilometry analysis were utilized in order to investigate the surface before and after removing any corrosion product layer.

Table 18: Experimental matrix

Parameters	Conditions
Total pressure	0.1 MPa
Temperature	30°C
Solution	1 wt% NaCl
Flow condition	300 rpm, 0.5" stir bar
Deposit materials	pyrrhotite, pyrite, and silica sand
Methods	EIS, LPR, SEM, profilometry
Spurge gas partial pressures	0.096 MPa CO <sub>2</sub>
Solution pH	4.0 (± 0.1)

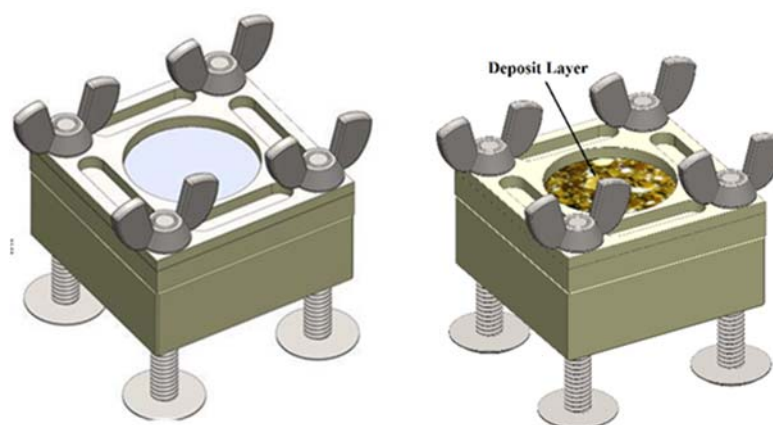


Figure 53: Under deposit specimen holder with and without the deposit layer<sup>23</sup>.

### *Results and Discussion*

Uniform corrosion rate of X65 under different deposit layers was monitored utilizing LPR measurements. It was observed that the uniform corrosion rates under pyrrhotite containing deposit layers was as low as  $0.1 \text{ mmy}^{-1}$ , where in the absence of pyrrhotite and under silica sand deposit, uniform corrosion rate was approximately five times higher. The experiments were repeated and the reported values are the average of the two performed measurements with the error bars denoting the maximum and minimum deviation from the average values. In order to monitor the changes on the X65 surface, the OCP was monitored (Figure 54); it was observed that the OCP increased to a more positive value shortly after the pyrrhotite containing deposit layers was placed on the steel specimen. However, it declined over the first hours of experiments, where the stable value was still 50 mV higher than the expected OCP for bare X65 in such conditions. Under silica

---

<sup>23</sup> Image is courtesy of Cody Shafer

sand deposit, the X65, the OCP did not show an initial increase; The OCP stabilized to around -650 mV, approximately the same as the stabled OCP under pyrrhotite containing deposits. It is essential to note that the OCP changes indicate different mechanisms; the first mechanism that is the most detrimental, is the acceleration of cathodic reactions. This could happen under galvanic coupling conditions, which results in an increase in the observed OCP. The second mechanism, which could result in a rise in the OCP, is the retardation of the anodic reaction that is commonly observed under protective layers. [66], [126]

In the current study, the OCP increase under the deposited layers was due to above mentioned mechanisms. Under pyrrhotite containing deposits, the OCP increased as a result of galvanic coupling of the X65 steel with the semi-conductive deposit layers. On the other hand, under sand deposit the rise in the OCP was the result of the anodic reaction being retarded via the presence of the sand deposit.

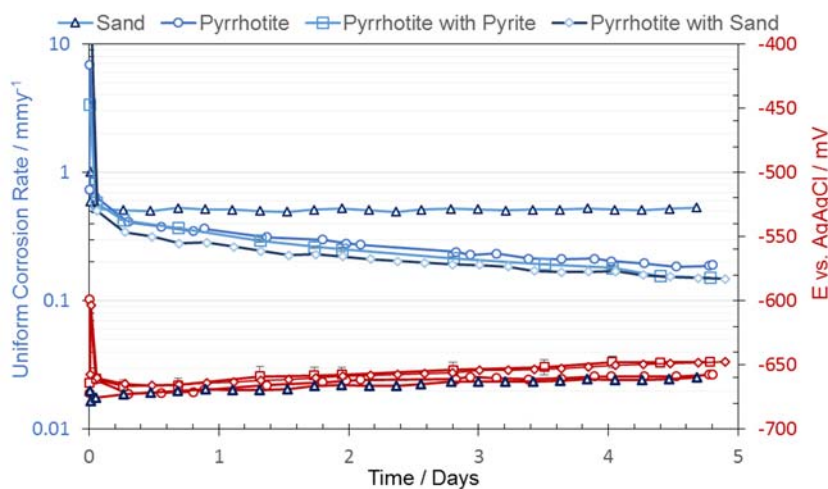


Figure 54: X65 under deposit corrosion in sparged with 0.96 bar CO<sub>2</sub>, at pH 4.0, 30°C, 1wt% NaCl, and 300 rpm 0.5" stir bar, 2 gr of deposit.

In order to investigate the X65 specimen surface changes and the corrosion product morphology under the deposit layers, SEM imaging was utilized. It seems that there was a thin layer of corrosion product layer on the surface of the specimens under pyrrhotite containing deposit (Figure 57 (b-d)). It is noteworthy that it is difficult to estimate the corrosion product layer thickness without cross sectional analysis, which was not conducted here. The surface morphology of the specimen under sand deposit seems rougher as compared to the other surfaces (Figure 57 (a)). Note that due to the mass transfer barrier provided by sand, which resulted in a relatively lower corrosion rate ( $0.5 \text{ mmy}^{-1}$  vs.  $1 \text{ mmy}^{-1}$ ), the specimen surface under sand deposit was not as damaged as one would expect in the absence of such barriers.

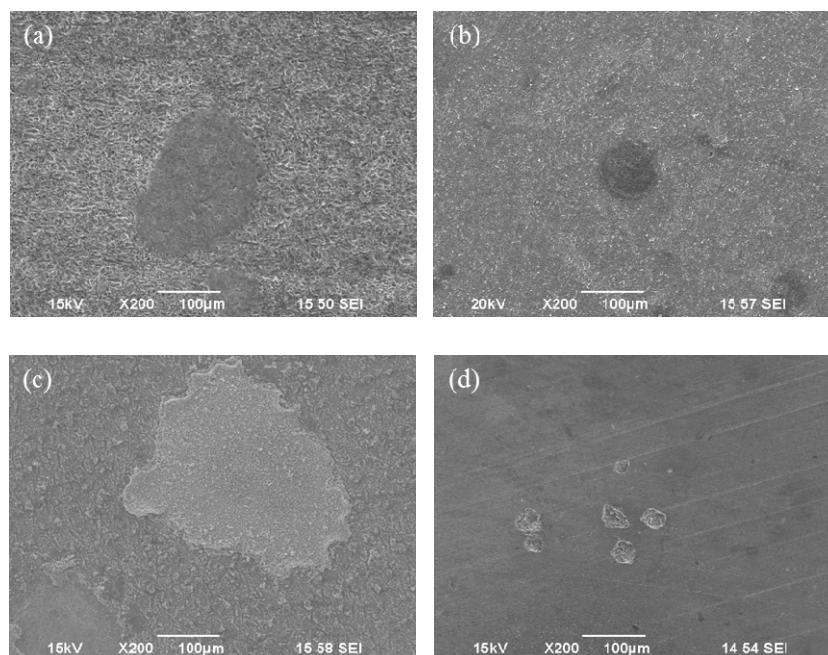


Figure 55: SEM top views of specimens under (a)  $0.25 \text{ gcm}^{-2}$  sand (b)  $0.25 \text{ gcm}^{-2}$  pyrrhotite (c)  $0.125 \text{ gcm}^{-2}$  pyrrhotite +  $0.125 \text{ gcm}^{-2}$  pyrite, and (d)  $0.125 \text{ gcm}^{-2}$  pyrrhotite +  $0.125 \text{ gcm}^{-2}$  sand deposit exposed to aqueous  $\text{CO}_2$  solution at pH 4.0,  $30^\circ\text{C}$ , 1wt% NaCl, 300 rpm 0.5" stir bar, 2 grams of deposit.

In order to investigate the underlying corrosion behavior, the corrosion product layer was chemically removed using Clarke solution [147]. A profilometer was utilized to investigate the existence or lack of any localized attack on the specimens' surface. The deepest measured pit was averaged over the duration of exposure in order to calculate the pitting penetration in  $\text{mm}\cdot\text{y}^{-1}$ . The specimen under a sand deposit did not undergo any localized attack while the specimens under the deposit layers containing pyrrhotite suffered from localized corrosion, the intensity of which increased with mixed layers (pyrrhotite + pyrite and pyrrhotite + sand) with the sand pyrrhotite mixture yielding the highest pitting penetration depth (Figure 57). Here, it is hypothesized that the pyrrhotite layer was interrupted when mixed with either pyrite or sand, which allowed the iron dissolution to proceed more freely. It is of key importance to note that a conductive / semi-conductive corrosion product layer facilitates corrosive reduction rate via transferring electrons from the steel surface to the corrosive species, which could get reduced at the interface of the layer with the bulk solution. Thus, such layers do not offer a mass transfer barrier to the corrosive species considering that they do not need to travel through the intra layer pores in order to be reduced at the steel surface.

However, there is an essential step in the corrosion process of mild steel, which is the  $\text{Fe}^{2+}$  being allowed to leave the iron lattice, otherwise corrosion does not proceed. A corrosion product layer, which is providing a full coverage to the steel surface via blocking the iron dissolution, would not result in substantial corrosion regardless of its ability to facilitate  $\text{H}^+$  reduction by transferring the electrons. In the current study, pyrite and sand

provided the opening to the pyrrhotite layer which facilitated the  $\text{Fe}^{2+}$  leaving the lattice more freely and ultimately resulting in an intensified localized corrosion.

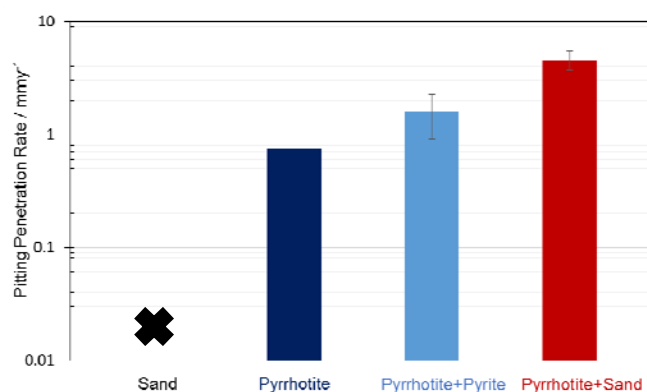


Figure 56: Pitting penetration of X65 under deposit exposed to aqueous  $\text{CO}_2$  solution, at pH 4.0,  $30^\circ\text{C}$ , 1wt% NaCl, 400 rpm 0.5" stir bar,  $0.25 \text{ gcm}^{-2}$  of deposit.

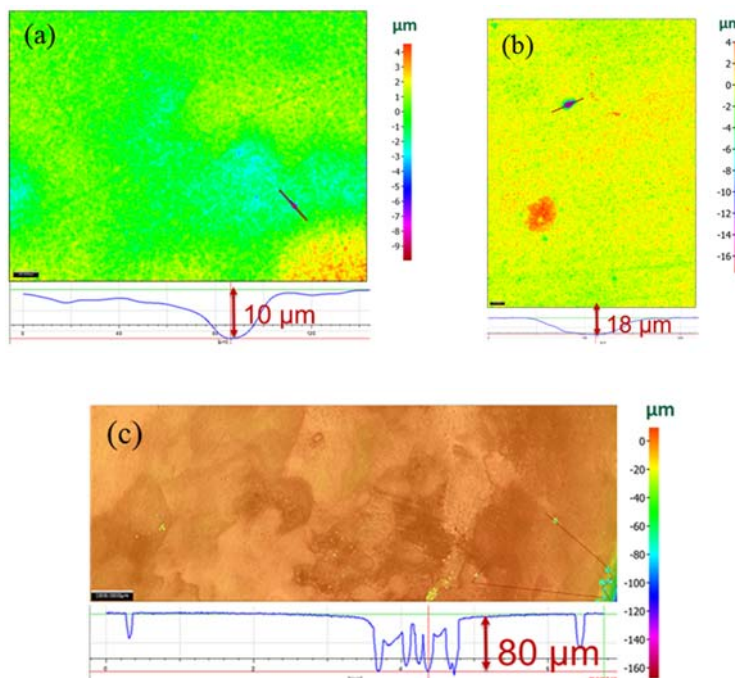


Figure 57: Profilometry image of the specimen under (a) pyrrhotite (b) pyrrhotite and pyrite (c) pyrrhotite and sand deposit, exposed to aqueous  $\text{CO}_2$  solution at pH 4.0,  $30^\circ\text{C}$ , 300 rpm 0.5" stir bar, 1 wt% NaCl after the corrosion product was removed.

The main hypothesis that can be derived from these results is that a disruption in the pyrrhotite layer facilitated the iron dissolution by providing a path for  $\text{Fe}^{2+}$  to leave the steel's lattice. Thus, one might expect a pyrrhotite deposit layer containing finer particles would result in less porosity / opening and ultimately not allowing the  $\text{Fe}^{2+}$  to leave the lattice that easily. Thus, X65 corrosion behavior under finer pyrrhotite particles was investigated. The uniform and localized corrosion rates for both conditions are reported in Figure 58, where it can be observed that although the uniform corrosion rates were approximately the same under both conditions, the X65 steel did not undergo localized corrosion under finer deposit layer. This provided more evidence to support the argument presented in the current study.

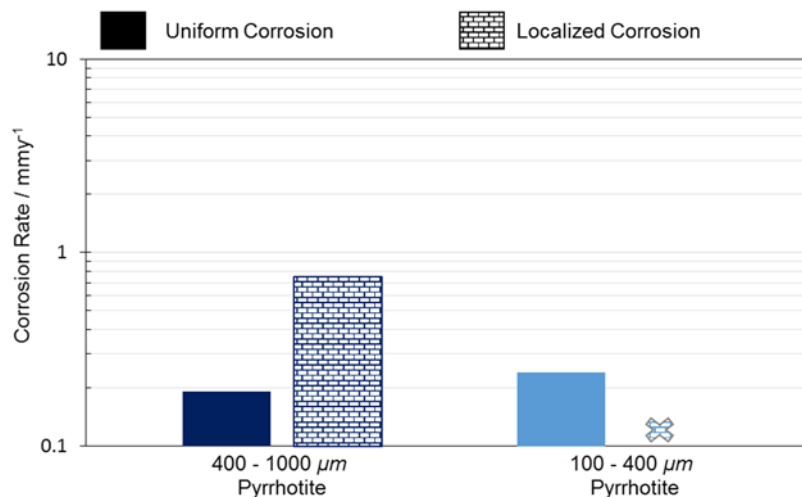


Figure 58: Comparison of general and localized corrosion rates of X65 under different size pyrrhotite particle deposits exposed to aqueous  $\text{CO}_2$  solution, at pH 4.0,  $30^\circ\text{C}$ , 1 wt% NaCl, 400 rpm 0.5" stir bar, 2 grams of deposit.

### *Summary*

- It was shown that under pyrrhotite containing deposit layers localized corrosion could be a concern if there is some degree of discontinuity on the layer.
- In the present study, the discontinuity was a result of either porous pyrrhotite deposit or the presence of other phases mixed with the pyrrhotite deposit.

#### Role of Poorly Formed Mackinawite Layer on Mild Steel Corrosion

In the oil and gas industry, one could encounter conditions with only trace amounts of H<sub>2</sub>S (in the ppm range), which are also referred to as “marginally sour” conditions. One example are sweet wells which become marginally sour over the lifetime of production, due to microbiological (SRB) activity in the reservoir.[152] Under these marginally sour conditions, CO<sub>2</sub> is the main cause of corrosion and it has been suggested that trace amounts of H<sub>2</sub>S lead to formation of a thin iron sulfide corrosion product layer, which has protective properties.[21], [153] Therefore, uniform corrosion rates of mild steel in marginally sour conditions were found to be lower than those seen under the same conditions without H<sub>2</sub>S. An early example was given by Lee,[21] where with only 3 ppm H<sub>2</sub>S/CO<sub>2</sub> (at atmospheric pressure) the sweet corrosion rate was halved, while at 15 ppm and higher the corrosion rate was almost an order of magnitude lower compared to conditions where there was no H<sub>2</sub>S .

Despite this apparently beneficial effect of a trace amount of H<sub>2</sub>S on uniform corrosion of mild steel, there are some indications that such conditions might lead to a

serious risk of localized attack. In a recent study, focused on top of the line corrosion (TLC) in sour environments, Yaakob *et al.*[74], [75] reported localized corrosion at 15 ppm and 30 ppm H<sub>2</sub>S, at room temperature and 1 MPa CO<sub>2</sub> partial pressure. In the same study localized corrosion was not observed at 80 ppm and 150 ppm H<sub>2</sub>S. This seems to suggest that there might be a threshold concentration of H<sub>2</sub>S below which localized corrosion occurs in marginally sour environments.

Despite the frequent encounter of marginally sour environments, most of the effort reported in literature has been on aqueous solutions that contain moderate to high amounts of H<sub>2</sub>S (pH<sub>2</sub>S = 0.01 MPa to 0.5 MPa) with temperatures ranging from 50°C to 150°C.[46], [71], [123], [153], [154] In an effort to investigate the corrosion behavior under marginally sour conditions, the experiments described below were conducted with trace amounts of H<sub>2</sub>S at low temperature (30°C) at atmospheric pressure.

#### *Experimental Method and Set-Up*

Experiments were conducted in a glass cell with the experimental conditions summarized in Table 19. In this setup, the cylindrical cell contained 2 L of 1 wt% NaCl electrolyte similar to what was described in earlier sections. The temperature was set to room temperature / 30°C. Electrochemical measurements were conducted using a three-electrode setup with a 5.4 cm<sup>2</sup> API 5L X65 (tempered martensitic microstructure) with elemental analysis given in Table 20, serving as the WE. A platinum mesh plate was used as the CE. A saturated Ag/AgCl reference electrode was connected *via* a Luggin capillary. The H<sub>2</sub>S gas concentration at the inlet was adjusted using gas rotameters and the accuracy was confirmed by taking a gas sample using a pump with colorimetric H<sub>2</sub>S detector tubes.

The gas outlet was scrubbed through a 1 M NaOH and a dry carbon scrubber to capture H<sub>2</sub>S.

In order to ensure that the solution was deoxygenated, it was purged with CO<sub>2</sub> gas for at least 2 hours prior to adding of H<sub>2</sub>S gas at the desired concentration. The solution pH was set to pH 5.0 by adding a deoxygenated 1 M NaOH solution. The electrolyte was stirred at 300 rpm with a 0.5" stir bar to ensure mixing.

In addition to the cylindrical WE, flat square specimens, with a surface area of 3.4 cm<sup>2</sup>, made from the same material, were suspended in the solution for the purpose of measuring weight loss and performing surface analysis. Prior to immersion all specimens were sequentially polished with silicon carbide sand paper from 150 to 600 grit, rinsed with DI water, cleaned with isopropanol in an ultrasonic bath and air dried and weighed.

The corrosion process was monitored by recording the OCP, and by performing LPR, and EIS measurements using a Gamry<sup>24</sup> Reference 600 potentiostat. The R<sub>p</sub> was obtained by polarizing the WE, sweeping the potential from 5 mV below the OCP to 5 mV above the OCP at a scan rate of 0.125 mVs<sup>-1</sup>. The B value of 23 mV was used in all cases to calculate the LPR corrosion rate. The R<sub>p</sub> was corrected for IR drop using the solution resistance (R<sub>s</sub>) measured by EIS at high frequencies (*ca.* 5 kHz).

Surface and compositional analyses were performed using scanning electron microscopy (SEM) and XRD respectively. XRD analyses were executed through a CuK $\alpha$  source ( $\lambda=1.5405$  Å, 40 kV and 44 mA), scanning from 10 to 70 2 $\Theta$  at a scan rate of 1

---

<sup>24</sup> Trade Name.

degree per minute. An Alicona InfiniteFocus<sup>25</sup> profilometer microscope was utilized to measure the pit depth after the corrosion product layer was chemically removed. The Fe<sup>2+</sup> concentrations were measured by UV-vis spectrophotometry.

Table 19: Experimental matrix - glass cell

Parameters	Conditions
Total pressure	0.1 MPa
Temperature	30°C
Solution	1 wt% NaCl
Flow condition	Agitated, 300 rpm 0.5 inch
Material	API 5L X65 steel
Corrosion measurement methods	LPR, EIS, and weight loss
pCO <sub>2</sub>	0.096 MPa
pH <sub>2</sub> S in the gas phase	0
	4×10 <sup>-6</sup> MPa (40 ppm)
	9×10 <sup>-6</sup> MPa (90 ppm)
pH	5.0 (± 0.1)

Table 20: API 5L X65 elemental analysis (wt%)

C	Mn	Si	P	S	Cr	V	Ni	Mo	Al	Fe
0.13	1.16	0.26	0.009	0.009	0.14	0.047	0.36	0.16	0.032	Balance

### Results

For each of the H<sub>2</sub>S concentrations, the experiments were repeated at least three times. The uniform corrosion rates and the measured OCP are shown in Figure 59 as a function of time. The points are averages across the different repeats. The error bars denote the maximum and the minimum deviation from the average value.

<sup>25</sup> Trade Name

The measured OCP (Figure 59 (a)) of each specimen shows a potential increase between 30 mV to 50 mV. This could be as a result of two possible mechanisms, an increased in the cathodic reaction rate, or a decrease in the anodic reaction rate.

In the absence of H<sub>2</sub>S, the CO<sub>2</sub> LPR corrosion rate increased over time ((Figure 59 (b)). This was due to the iron carbide, the part of the steel structure that is left on the steel surface as it does not corrode. It is well known that iron carbide is conductive and therefore this porous layer increases the cathodic surface area and as a result of a galvanic effect it leads to an increase in the corrosion current/rate [155]–[158]. This was reflected in the measured R<sub>p</sub>, however the magnitude of the corrosion rate increase is overestimated there, as the LPR method cannot properly account for different cathodic and anodic surface areas. The increase in the cathodic reaction rate also explains the positive shift in the specimen OCP shown in Figure 59 (a).

For the two conditions at 40 and 90 ppm H<sub>2</sub>S, the LPR corrosion rate (Figure 59 (b)) started out lower than in the absence of H<sub>2</sub>S, due to formation of a protective iron sulfide – mackinawite layer. The corrosion rate decreased further during the first day of exposure and then increased until the end of the experiment. One would be tempted to ascribe this increase to iron carbide layer formation, however, most of the surface was covered by a significantly thin layer, possibly made of a mixture of mackinawite and iron carbide, which could not produce any significant galvanic current. Another possibility is non-uniform attack that initiated and developed over time. Since LPR records the total current that is averaged across the surface area of the specimen, any failure of the protective

mackinawite layer and localized attack would present itself as an apparent increase in the LPR corrosion rate. Without proper surface analysis this assumption cannot be confirmed.

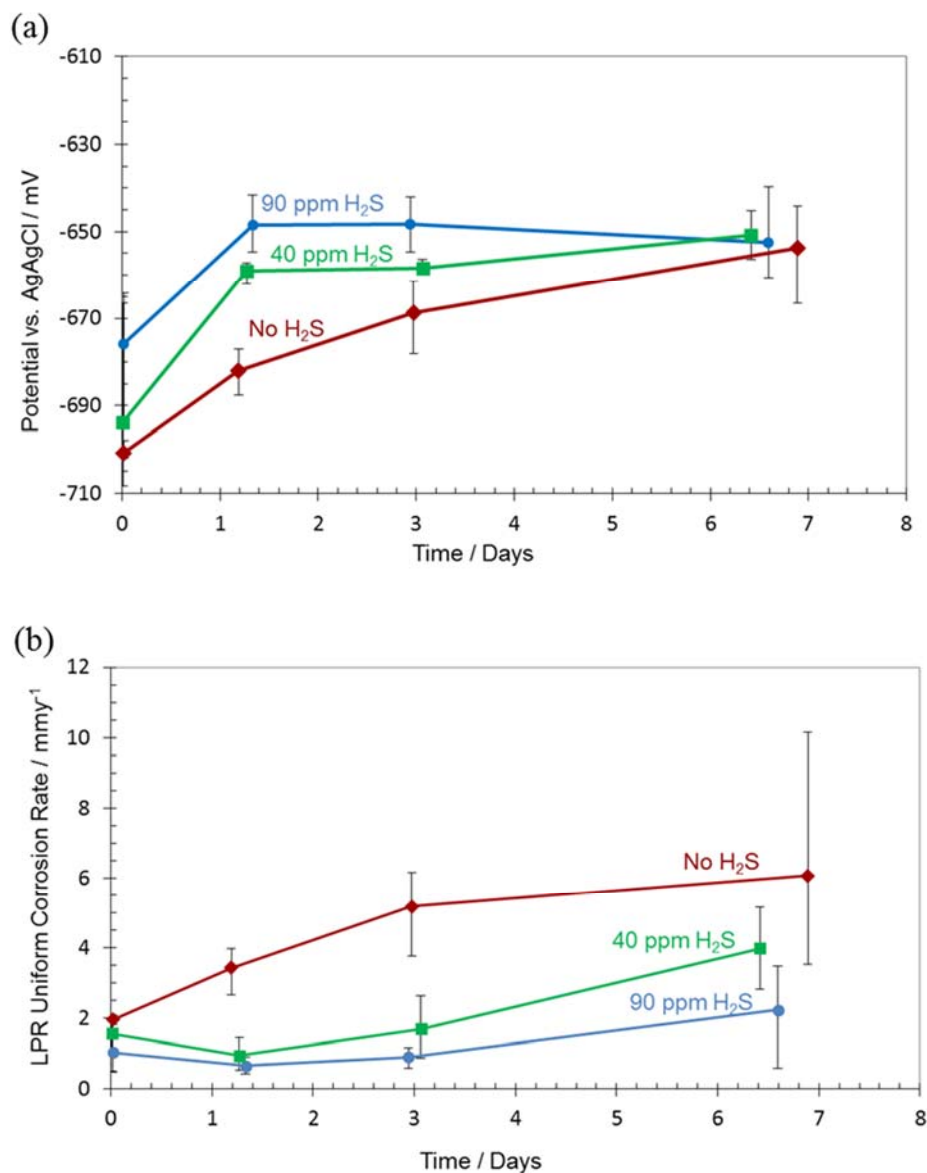


Figure 59: (a) OCP (b) LPR Corrosion rate from X65 specimen in a 1 wt% NaCl, CO<sub>2</sub> saturated solution at 30°C, pH5 at 0.1 MPa total pressure, with and without H<sub>2</sub>S.

Figure 60 shows the changes in bulk solution properties over the course of the experiments. Figure 60 (a) shows the pH variation; in order to keep the bulk pH value relatively stable, diluted deoxygenated HCl was occasionally injected into the experimental cell. Figure 60 (b) and (c) show calculated saturation values with respect to iron carbonate[159] (Equation (60)) and mackinawite[160] (Equation (62)) respectively.<sup>26</sup>

$$S_{\text{FeCO}_3} = \frac{c_{\text{Fe}^{2+}} c_{\text{CO}_3^{2-}}}{c_{\text{H}^+} + K_{\text{sp,FeCO}_3}} \quad (60)$$

$$K_{\text{sp,FeCO}_3} = -59.3498 - 0.041377 T - \frac{2.1963}{T} + 24.5724 \log(T) + 2.518 I^{0.5} - 0.657 I \quad (61)$$

$$S_{\text{FeS(Mackinawite)}} = \frac{c_{\text{Fe}^{2+}} c_{\text{HS}^-}}{c_{\text{H}^+} + K_{\text{sp,FeS(Mackinawite)}}} \quad (62)$$

$$K_{\text{sp,FeS(Mackinawite)}} = 10^{\frac{2848.779}{T} - 6.347 + \log(K_1)} \quad (63)$$

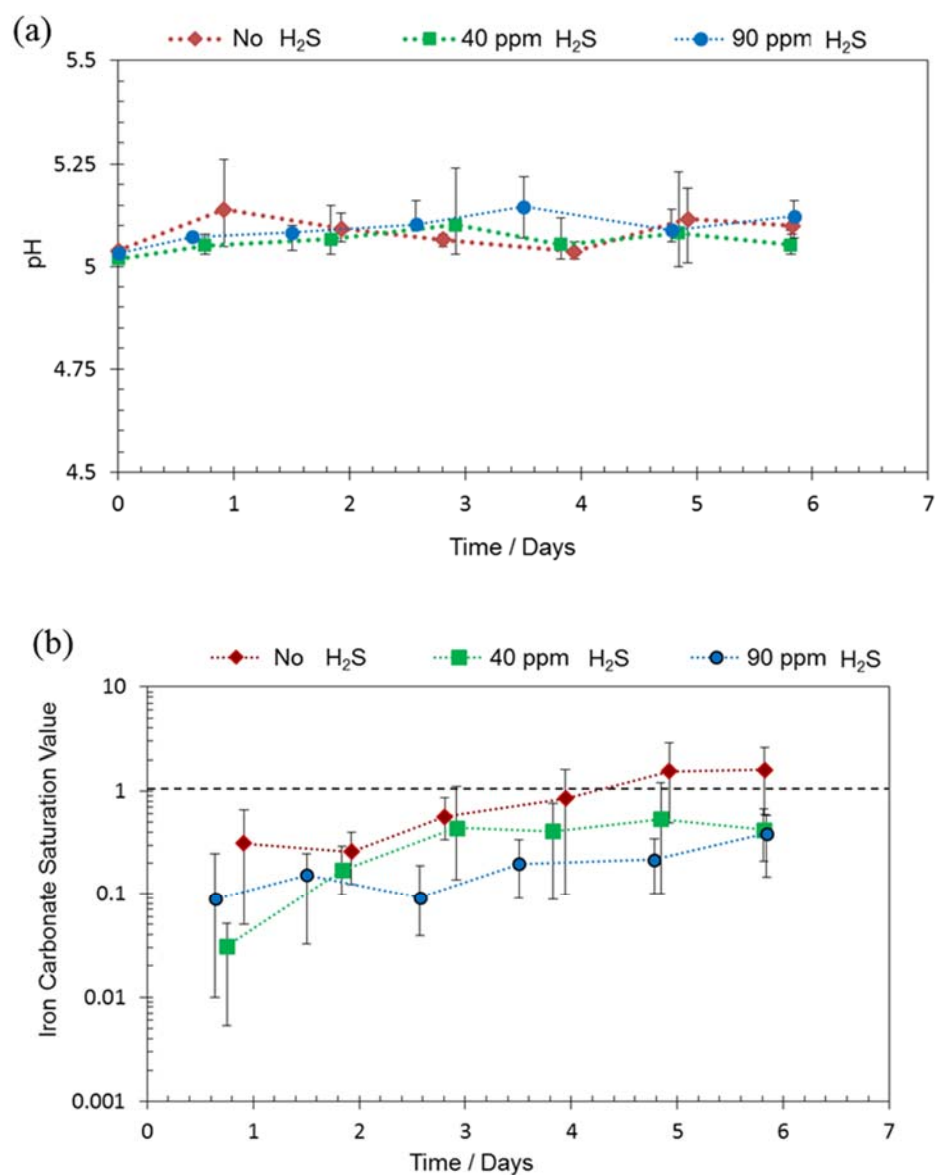
$$K_{(\text{H}_2\text{S})} = 10^{(782.43945 + 0.361261 T_K - 1.6722 * 10^{-4} T_K^2 \frac{20565}{T_K} - 142.741722 \ln T_K)} \quad (64)$$

In all the experiments, the bulk solution was under-saturated with respect to both iron carbonate and mackinawite. It should be emphasized that the surface pH is expected to be higher than the bulk pH which would result in higher saturation values in the vicinity of the corroding surface. It has been previously shown that the surface pH could vary from the bulk pH by 1 to 2 units depending on the level of mixing [161]. This suggests that both

---

<sup>26</sup> The nomenclature is defined in a separate section at the end of the document.

iron carbonate and mackinawite were likely supersaturated at the steel surface, which is a necessary precondition for formation of solid corrosion products layers.



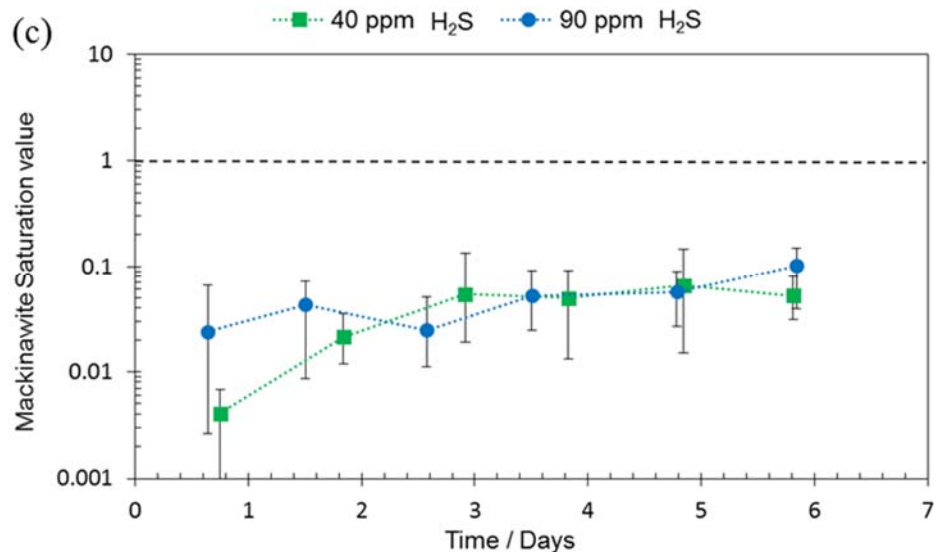


Figure 60: (a) pH variation (b) iron carbonate saturation degree (c) mackinawite saturation degree of the bulk solution during the experiments; 1 wt% NaCl CO<sub>2</sub> saturated solution at 30°C with at 0.1 MPa total pressure, with and without H<sub>2</sub>S.

Figure 61 shows the SEM images of the surface of exposed specimens. In the absence of H<sub>2</sub>S, a fractured layer on the surface is observed (Figure 61 (a)). With H<sub>2</sub>S present, the specimen surface was covered with a thin compact layer that seems to be following the original shape of the steel surface including the polishing marks. For the case of 40 ppm and 90 ppm H<sub>2</sub>S there are some local failures of the layer, which can be seen in Figure 61 (b) and Figure 61 (c).

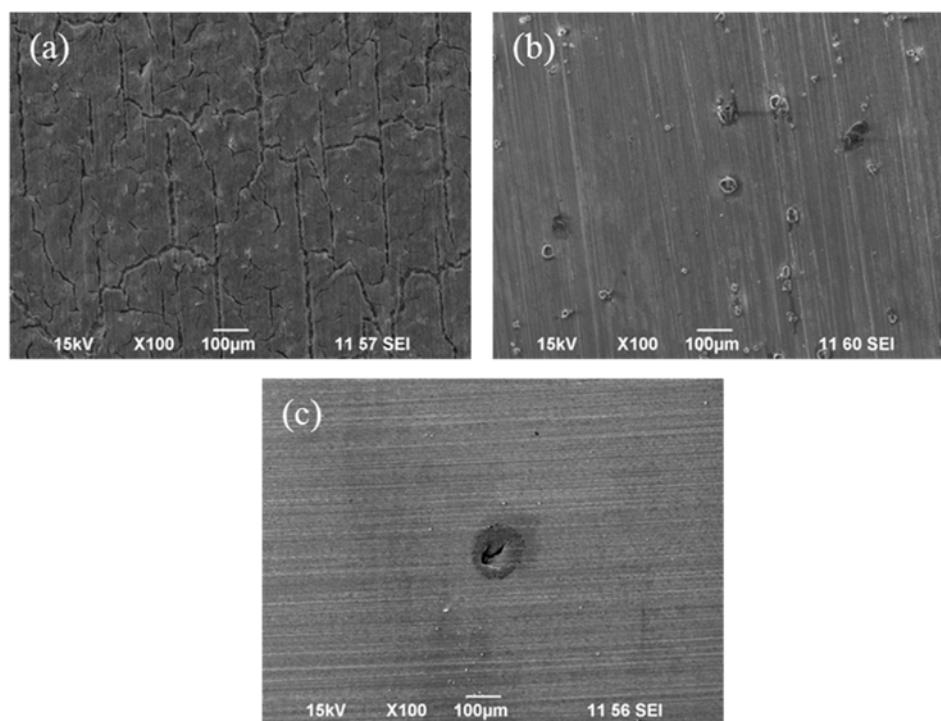


Figure 61: SEM image of recovered X65 specimens after 6 days of exposure to an aqueous solution sparged with (a) no H<sub>2</sub>S, (b) 40 ppm H<sub>2</sub>S, (c) 90 ppm H<sub>2</sub>S in CO<sub>2</sub> at 30°C and pH 5.0, 1 wt% NaCl, 6 days exposure.

XRD was utilized in order to identify the makeup of the corrosion product layer. Iron carbide was identified on the specimen exposed to a solution without H<sub>2</sub>S (Figure 62 (a)). However, the XRD patterns of the specimens exposed to 40 and 90 ppm H<sub>2</sub>S do not show any peaks that could correspond to mackinawite, iron carbonate nor iron carbide (Figure 62 (b) and Figure 62 (c)). The peaks on these two patterns at 44 2 $\theta$  and 65 2 $\theta$  are the alpha Fe peaks.[61] This shows that the layers formed on these surfaces was so thin (order of  $\mu\text{m}$ ) that the conventional XRD was not able to detect the layer. The elemental analysis using EDS, showed sulfur on the surface of the specimens exposed to 40 ppm and 90 ppm H<sub>2</sub>S after 6 to 7 days of exposure.

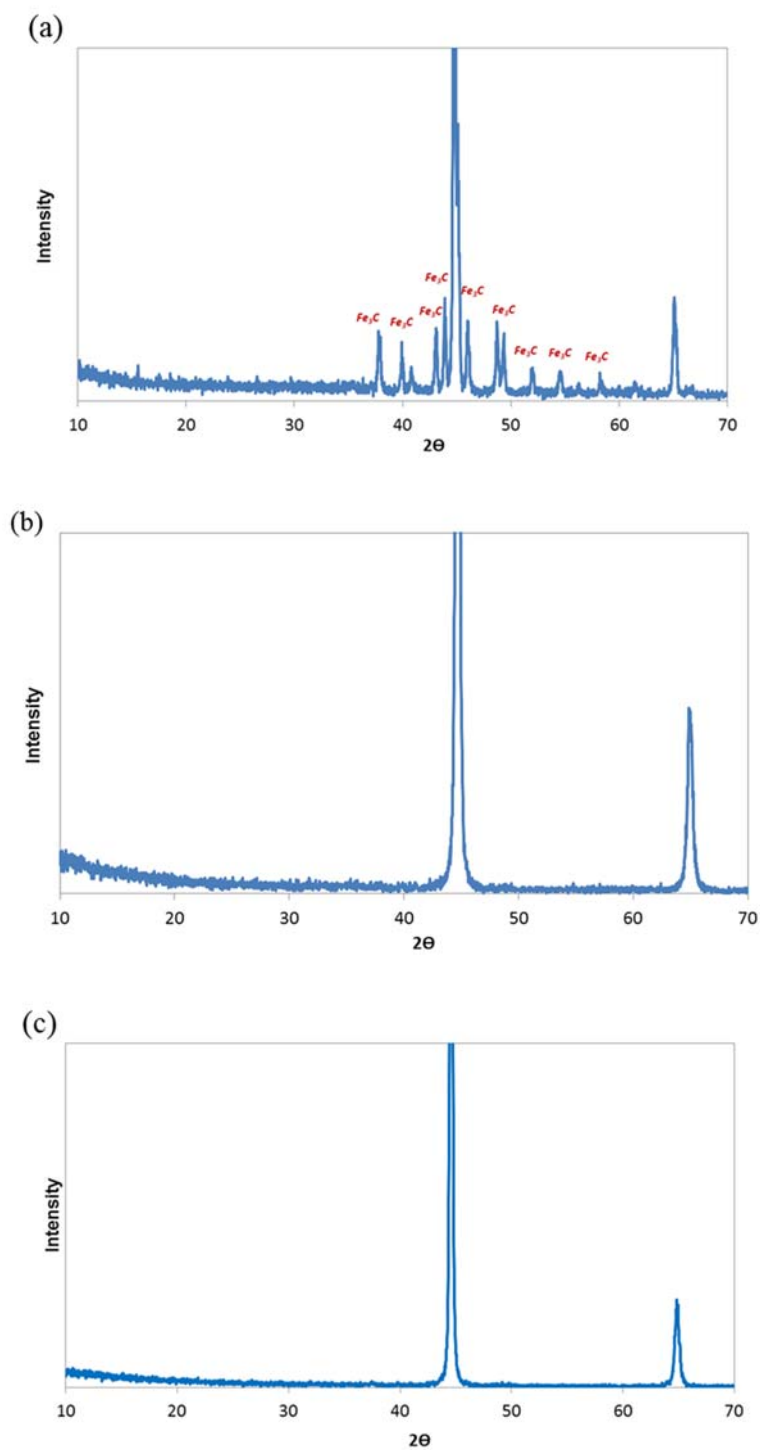


Figure 62: XRD of the recovered X65 after 6 days exposure to a saturated  $\text{CO}_2$  solution at  $30^\circ\text{C}$  and pH 5.0 (a) no  $\text{H}_2\text{S}$ , (b) 40 ppm  $\text{H}_2\text{S}$ , (c) 90 ppm  $\text{H}_2\text{S}$ , 1 wt% NaCl.

Cross section images of the specimens were analyzed in order to investigate the corrosion product layer thickness and the appearance of the pits. The specimen exposed to the aqueous CO<sub>2</sub> solution (in the absence of H<sub>2</sub>S) shown in Figure 63 (a) has a very porous and detached fragmented layer on the surface, which is made of iron carbide and lacks any protective properties. The specimens exposed to 40 ppm and 90 ppm H<sub>2</sub>S are shown in Figure 63 (b) and Figure 63 (c), respectively, showing pitting. These pits are partially filled with some corrosion product, which is not dense, neither is it well attached, therefore it is likely that these pits had remained active throughout the experiment. A very thin layer is seen on the steel surface in the vicinity of the pits, which explains the inability of the XRD to detect this layer.

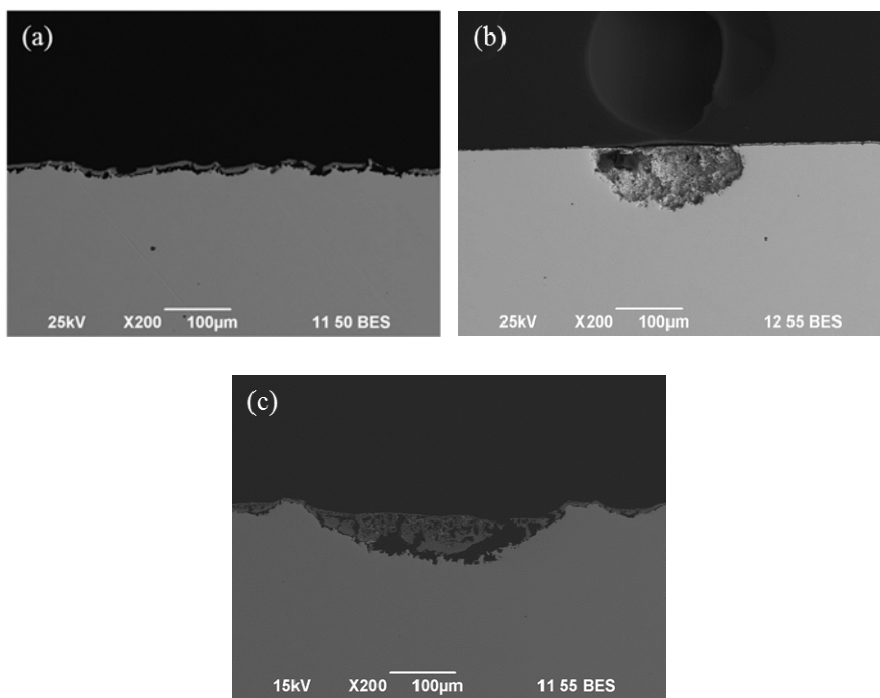


Figure 63: Cross section image of X65 specimen after 6 days of exposure to an aqueous CO<sub>2</sub> solution at 30°C and pH 5.0 (a) no H<sub>2</sub>S, (b) 40 ppm H<sub>2</sub>S, (c) 90 ppm H<sub>2</sub>S H<sub>2</sub>S, 1 wt% NaCl.

In order to investigate the morphology of the corrosion attack, the corrosion product layer was chemically removed following the procedure given in the ASTM G1[147] standard using Clarke solution. Figure 64 shows the SEM images of the specimen surface after the corrosion product layer was removed. Figure 64 (a) shows the specimen exposed to aqueous CO<sub>2</sub> in the absence of H<sub>2</sub>S and exhibits a relatively rough surface, which shows that the specimen underwent severe uniform corrosion. The specimens exposed to 40 ppm and 90 ppm H<sub>2</sub>S still have the original polishing marks on the majority of the surface, along with locally corroded areas (Figure 64 (b) and Figure 64 (c)).

Profilometry was utilized to measure the depth of the pits on the surface and the deepest pit depth was used to calculate the maximum pit penetration rate (PPR) (Figure 65). The specimen exposed to aqueous CO<sub>2</sub> solution (in the absence of H<sub>2</sub>S) does not show any features on the surface that could be considered as localized attack, just general roughening. The profilometry of the specimens exposed to 40 ppm and 90 ppm H<sub>2</sub>S shows evidence of pitting, more widespread at 40 ppm. A pit depth of more than 200 μm can be seen on both specimens in Figure 65 (b) and Figure 65 (c).

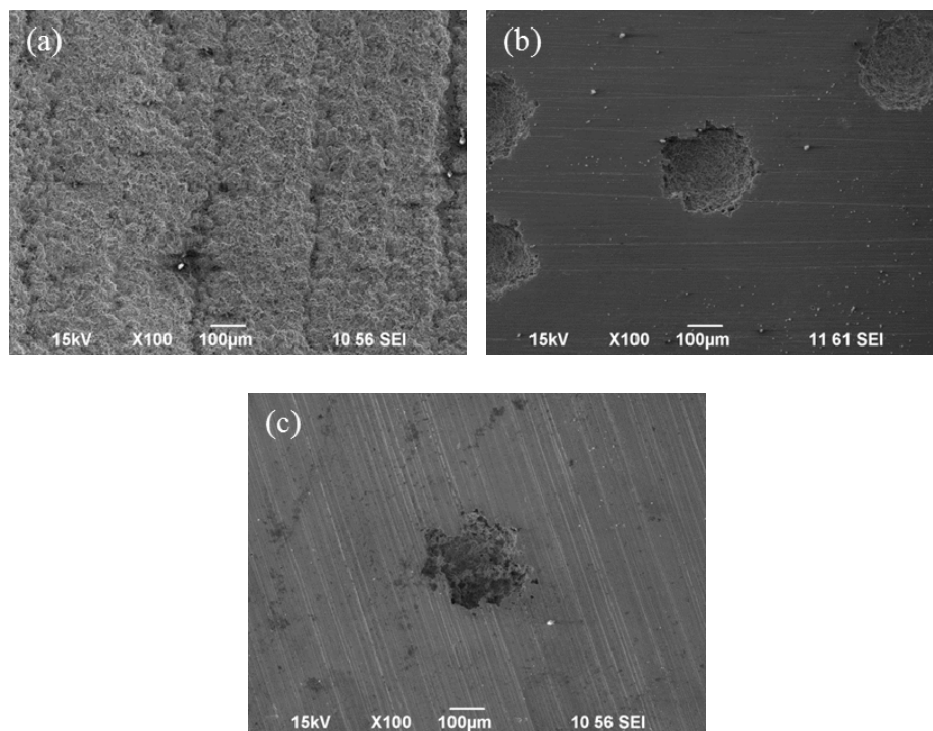


Figure 64: SEM image of X65 specimen after exposure to a saturated CO<sub>2</sub> solution at 30°C and pH 5.0 without corrosion product layer (a) no H<sub>2</sub>S, (b) 40 ppm H<sub>2</sub>S, (c) 90 ppm H<sub>2</sub>S, 1 wt% NaCl, 6 days exposure.

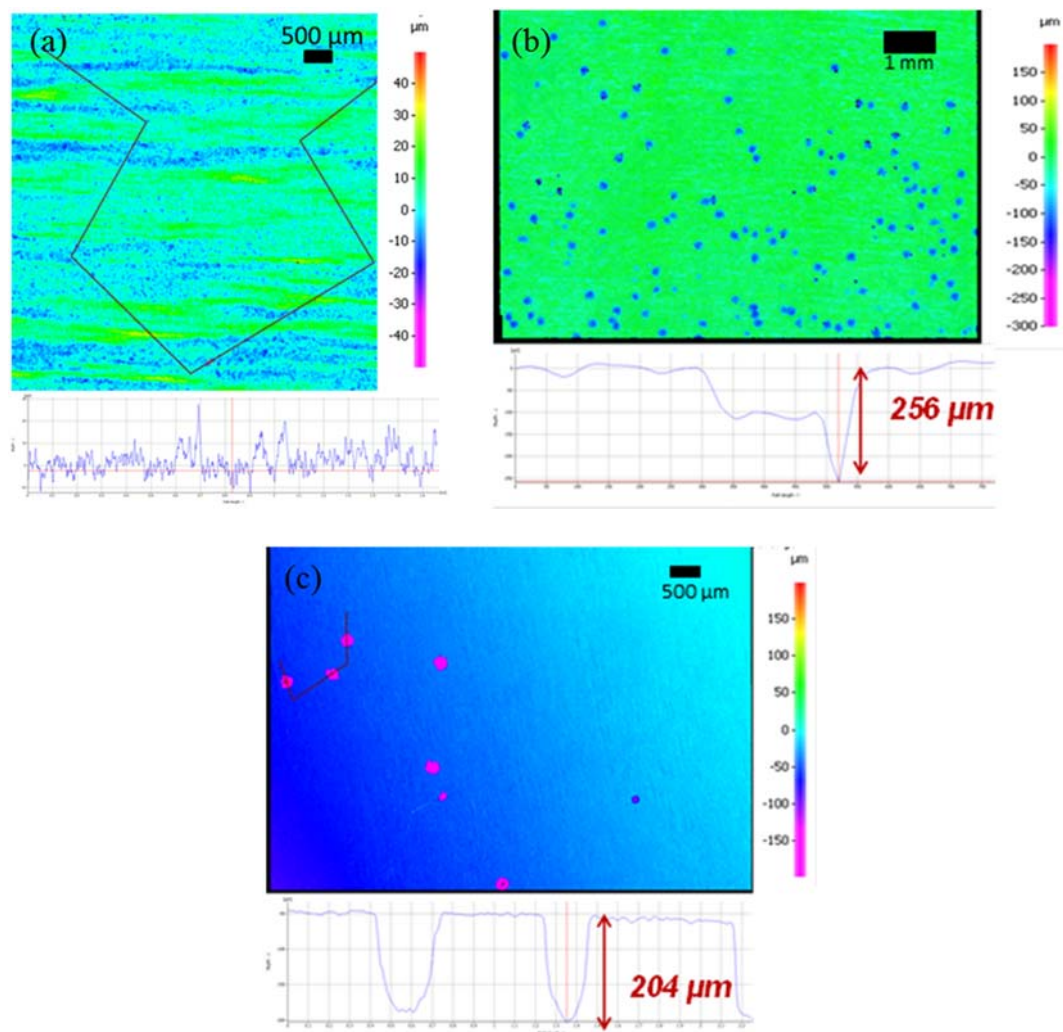


Figure 65: Profilometry image of recovered X65 specimens after 6 days of exposure to an aqueous CO<sub>2</sub> solution at 30°C and pH 5.0 without corrosion product layer (a) no H<sub>2</sub>S (b), 40 ppm H<sub>2</sub>S, (c) 90 ppm H<sub>2</sub>S, 1 wt% NaCl.

The specimens were weighed after the corrosion product layer was removed; the time averaged weight loss corrosion rate ( $\Delta m/t$  in  $\text{mm}^{-1}$ ) and the pit penetration rate of the specimens versus the H<sub>2</sub>S concentration are compared in Figure 66. The data shows that the overall mass loss decreased with an increase in H<sub>2</sub>S concentrations; however, 40 ppm and 90 ppm H<sub>2</sub>S triggered localized corrosion. For these two experiments, the pit

penetration rate was at least five times higher than the uniform corrosion rate of the specimen exposed to similar aqueous environment without H<sub>2</sub>S confirming localized corrosion [162].

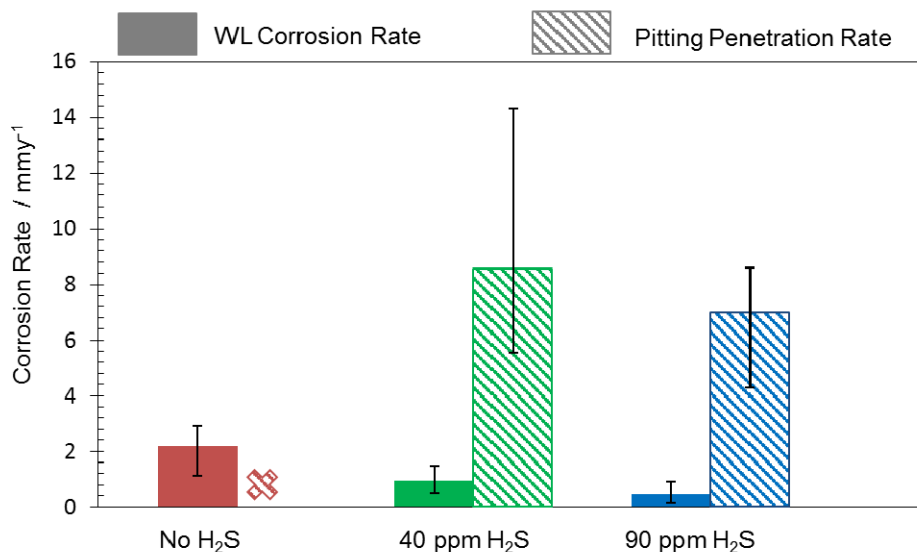


Figure 66: Weight loss corrosion rate and pitting penetration rate of X65 specimen in aqueous CO<sub>2</sub> solution with and without H<sub>2</sub>S at 30°C and pH 5.0, 1 wt% NaCl.

### Discussion

It was shown above that localized corrosion occurred on mild steel specimens exposed to aqueous CO<sub>2</sub> solutions with trace amounts of H<sub>2</sub>S. The bulk solution in all experiments was under-saturated with respect to corrosion products: iron carbonate and mackinawite. However, a corrosion product layer was observed on the corroded specimen SEM images. Based on XPS analysis reported by Lee *et al.* [21] and Choi *et al.*, [70] it is likely that the layer was mackinawite. This was not unexpected, since a corrosion process results in different water chemistry at the surface as compared to the bulk, with both the

pH and  $\text{Fe}^{2+}$  concentrations being higher at the corroding steel surface [161]. This is particularly pronounced in quiescent conditions, while the surface and the bulk water chemistry values converge in turbulent flow conditions.

In marginally sour environments, such as the one used in the current study, the higher pH and  $\text{Fe}^{2+}$  concentration at the surface allowed mackinawite layer formation, even if the bulk solution was under-saturated. As the mackinawite layer formed and grew in thickness it presented a diffusion barrier, which led to a reduction in the corrosion rate. Due to ongoing corrosion that was undermining the layer, it did not form uniformly [163]. It is well known that protectiveness of a corrosion product layer depends on the so called scaling tendency, which is a ratio of the precipitation rate and the corrosion rate [164]. When the scaling tendency is high, the precipitation overwhelms corrosion and protective layers form. Conversely, when rapid corrosion overpowers the precipitation and undermines the layer, non-protective layers form. In the current study, when there was more  $\text{H}_2\text{S}$ , the precipitation proceeded at a faster rate thus a more protective layer formed and vice versa. At lower  $\text{H}_2\text{S}$  concentrations, faults in the layer allowed the corrosive species to reach the steel surface. This resulted in localized corrosion at those locations. In addition, the outer surface of the growing mackinawite underwent dissolution. Therefore, the stability of this layer depended on the balance of: undermining by corrosion, precipitation at the steel/mackinawite interface and dissolution at the mackinawite/solution interface.

The observed localized corrosion rates in the present study were higher than the bare steel corrosion rate exposed to similar conditions without the presence of  $\text{H}_2\text{S}$ . It

should be noted that while H<sub>2</sub>S provided partial protection in these marginally sour environments, it would not have significantly contributed to the uniform corrosion rate due to the very low concentrations. It was the much higher content of CO<sub>2</sub> that led to the high corrosion rate (the corrosiveness of carbonic acid has been well documented) [66]. However, iron carbonate, which is the product of CO<sub>2</sub> corrosion, was not found at the surface of the steel under these conditions due to a much slower kinetics of formation when compared to that of mackinawite [21]. Therefore, it is believed that the observed localized corrosion was due to a galvanic effect. The galvanic effect was driven by a positive shift in the surface potential [126] at the mackinawite covered steel surface (Figure 59 (a)). It is not entirely clear at this time whether the increase in potential was due to an increase of the cathodic surface area, or due to the retardation of the anodic reaction as a result of coverage by the mackinawite layer. Either way, the potential difference between the large surrounding steel surface covered by mackinawite (that was more positive) and the uncovered steel in the pits (that was more negative) was the driving force for a galvanic couple, which led to localized corrosion.

Based on the finding in the current study, there seems to be a threshold value of pH<sub>2</sub>S which led to localized attack that was observed at concentrations up to 90 ppm H<sub>2</sub>S in CO<sub>2</sub>, but not at 150 ppm or more as it was reported by Esmaeely *et al.* [165]. For the sake of the present argument, one can assume that this threshold was of the order of 100 ppm H<sub>2</sub>S in CO<sub>2</sub> in the present study. It is expected that the threshold will vary with temperature and water chemistry (mostly affected by pH). At significantly higher temperatures and higher pH a lower threshold value is expected. It is of key importance to emphasize that

this threshold actually refers to the ratio of H<sub>2</sub>S to CO<sub>2</sub> gas partial pressures ( $p_{\text{H}_2\text{S}}/p_{\text{CO}_2} = 10^{-4}$ ) and not the actual H<sub>2</sub>S gas concentration as reported from the field, which is different due to the presence of hydrocarbon gases.

### *Summary*

In aqueous CO<sub>2</sub> environments with a trace amount of H<sub>2</sub>S at low temperatures where the solution was under-saturated with respect to both iron carbonate and mackinawite:

- mild steel underwent localized corrosion when there was not enough  $[\text{H}_2\text{S}]_{\text{aq}}$  to form a stable mackinawite layer;
- below 100 ppm H<sub>2</sub>S (when the ratio of H<sub>2</sub>S to CO<sub>2</sub> gas partial pressures was below  $10^{-4}$ ) localized attack was observed, while above this threshold the mackinawite layer provided a uniform protection to the steel surface;
- it is hypothesized that at lower H<sub>2</sub>S concentrations, faults in the corrosion product layer allowed the corrosive species to reach the steel surface. This resulted in localized corrosion.

## CHAPTER 6: OVERALL SUMMARY AND CONCLUSIONS

Given the baseline work conducted on electroactivity of different sulfides and the galvanic effects, all the different localized corrosion scenarios presented above seem to have certain common features that can be summarize as follows:

- any condition leading to poor formation or disruption, leading to a discontinuity in the iron sulfide corrosion product layer results in initiation of localized corrosion, and
- localized corrosion then propagates at that discontinuity via galvanic coupling between the underlying steel and the conductive iron sulfide corrosion product layer.

To support this, five rather different cases are used below, some from the present work, some from the previous work presented in open literature:

- Case 1: a partially dissolved pyrrhotite layer,
- Case 2: a disrupted pyrrhotite layer due to pyrite formation,
- Case 3: a disrupted pyrrhotite layer due to interference by sand,
- Case 4: a disrupted mackinawite layer due to pyrite interference, and finally
- Case 5: a poorly formed mackinawite layer.

### Case 1 - A Partially Dissolved Pyrrhotite Layer

As described above, pyrrhotite is electroactive [101], [102], [114] with a similar electroactivity as mild steel, when it comes to  $H^+$  or  $H_2S$  reduction [128]. When conditions are such that pyrrhotite forms a dense uniform corrosion product layer that is well attached to the steel surface, it offers good protection to the steel underneath, via retardation of the

anodic reaction due to surface blockage [72]. This is because a semiconductive pyrrhotite layer enables the corrosive species such as  $H^+$  and/or  $H_2S$  to be reduced at the outer surface of the layer, without needing to diffuse all the way to the steel surface. Under such conditions, the rate determining step is the rate of iron oxidation/dissolution rather than the rate of  $H^+$  and/or  $H_2S$  reduction. However, a pyrrhotite layer can also have a detrimental role when it is not dense or uniform.

It was shown in Chapter 5 that a mild steel specimens, with a preformed non-protective pyrrhotite layer, experienced localized attack when exposed to aqueous  $CO_2$  or aqueous  $CO_2/H_2S$  solutions [149]. In those experiments, the steel was pretreated at high temperature in a sulfur containing oil in order to form a layer of pyrrhotite via direct sulfidation. The pretreated specimens were then exposed to a range of aqueous  $CO_2$  and  $H_2S$  corrosion environments. In an aqueous  $CO_2$  solution the pyrrhotite layer underwent partial dissolution while in a mixed  $CO_2/H_2S$  solution the preformed pyrrhotite layer, partially transformed to troilite, with some mackinawite formation at the steel surface. Under both conditions, initiation of localized corrosion was observed: where  $Fe^{2+}$  dissolution from the steel lattice occurred more readily at the sites where the pyrrhotite layer dissolved or transformed into troilite.

It was reported in Figure 40 that the pitting penetration rate increased significantly when a more conductive electrolyte was used, approximately  $4 \text{ mmy}^{-1}$  in a solution without salt, and  $14 \text{ mmy}^{-1}$  in a 1 wt% NaCl solution. The semiconductive pyrrhotite layer surrounding the pit led to galvanically driven localized corrosion more so in a more conductive electrolyte [149].

According to the main hypothesis proposed here, the localized attack was initiated as a result of partial dissolution/transformation of the preformed pyrrhotite layer [149]. Subsequently the localized corrosion attack propagated at a high rate due to the galvanic coupling between the exposed mild steel surface and the surrounding conductive pyrrhotite layer.

#### Case 2 –A Disrupted Pyrrhotite Layer due to Pyrite Formation

Iron sulfide corrosion products form in a transient process; the initial product is mackinawite, having the fastest kinetics of formation. Given that the thermodynamics of the environment allow it – the final corrosion products are pyrrhotite or pyrite, which are the most thermodynamically stable iron sulfides [3], [26], [51], [90], [171]–[173].

Localized corrosion associated with a pyrrhotite or pyrrhotite/pyrite mixed corrosion product layer has been observed across a wide range of experimental conditions. Gao *et al.* [47] conducted autoclave experiments at constant aqueous H<sub>2</sub>S concentration (0.00385 mol.L<sup>-1</sup>, where p<sub>H<sub>2</sub>S</sub> was in the range of 0.1 to 0.18 bar) at different temperatures (80°C to 200°C). They reported localized corrosion under pyrrhotite/pyrite layers. In another study [148] conducted at high temperature (120°C) and partial pressures of H<sub>2</sub>S, similar results were observed by the same authors. Under these two rather distinct sets of conditions, one at a lower temperature (120°C) [148] with a higher p<sub>H<sub>2</sub>S</sub> (1 bar) and the other at a higher temperature (200°C) at a lower p<sub>H<sub>2</sub>S</sub> (0.18 bar), localized corrosion happened only when a mixed pyrrhotite/pyrite layer was observed. What seemed to be common between these two cases was formation of pyrite in a matrix of pyrrhotite. This is

consistent with the hypothesis where disruption of pyrrhotite corrosion product layer by pyrite led to initiation of localized corrosion.

The disruption of a pyrrhotite layer by pyrite nucleation has been investigated in mineralogy in great depth [38], [150], [151], [174]–[176], where disruptive nucleation of different phases in a “parent” phase (here pyrite within the pyrrhotite layer), has been well established. As the pyrite phase nucleates in the parent pyrrhotite phase, micro-cracks form; this results in a disruption in the pyrrhotite layer depending on the pathway that this process follows. Pyrrhotite transformation to pyrite has been postulated to take place via one of three possible pathways:

a) It could happen through formation of an intermediary phase, marcasite by solid state reaction, where, marcasite crystals follow the preferred orientation – hexagonal symmetry of the parent pyrrhotite; this transformation results in a volume reduction of iron sulfide by approximately 30% and large micron-size cracks; this is followed by solid state transformation of marcasite to pyrite with further formation of smaller cracks, due to additional volume reduction of approximately 3%. [151]

b) The second pathway is similar, except that the transformation of pyrrhotite to marcasite is by dissolution/precipitation with a random orientation for the crystals; this also results in the formation of micron-size cracks.

c) Pyrrhotite is directly transformed into pyrite by oxidative dissolution of pyrrhotite, followed by direct precipitation of pyrite, with the final outcome being a porous layer with very fine cracks and lower porosity. [38], [150]

These iron sulfide phase transformations occurring in a corrosion product layer play a significant role in localized corrosion initiation. It explains why in Gao *et al.*'s [148] experiments pyrite formation within a pyrrhotite layer led to disruption followed by galvanic attack stemming from the conductive nature of the pyrrhotite/pyrite layer in a conductive electrolyte. This resulted in propagation of localized corrosion.

### Case 3 – A Disrupted Pyrrhotite Layer due to Interference by Sand

Solid deposits containing various iron sulfide particles mixed with sand and organic particles are encountered in the field leading to localized corrosion. [177]–[179] Kvarekval and Svenningsen [24] reported localized corrosion under pyrrhotite/troilite deposit layers exposed to aqueous solutions at room temperature under high pressure conditions (10 bar H<sub>2</sub>S and 10 bar CO<sub>2</sub>). In their study, the cross section images of tested specimens showed that the corrosion product layers under the pyrrhotite/troilite particles had noticeable defects with the deposited particles penetrating into corrosion product layer, thereby disrupting it. The authors also reported localized attack under a mixed pyrrhotite/troilite layer including sand when exposed to similar conditions. In the current research, corrosion of mild steel under deposit layers containing pyrrhotite, pyrite and sand particles was investigated and reported in Chapter 5. In different experiments the pyrrhotite particles were mixed with pyrite particles or sand. In aqueous CO<sub>2</sub> conditions at atmospheric pressure, localized corrosion was not observed under deposits of very fine pyrrhotite particles. However, localized corrosion was observed under layers containing larger pyrrhotite particles and under a mixed pyrrhotite/pyrite or pyrrhotite/sand layer. Compared

to a pure pyrrhotite layer the intensity of localized attack was higher when pyrrhotite was mixed with pyrite and highest when it was mixed with sand.

In the experiments reported above, the mixed layer was an attempt to simulate the effect of a disrupted pyrrhotite layer. The experimental results showed that localized corrosion initiated as a result of that discontinuity/disruption and propagated due to the galvanic coupling of the steel surface and the semi-conductive pyrrhotite containing deposit layer, what is consistent with the hypothesis proposed above.

#### Case 4 – A Disrupted Mackinawite Layer due to Pyrite Interference

In a study conducted by Ning [32] localized corrosion was reported under a pyrite deposit layer, placed on a mild steel specimen surface exposed to an aqueous H<sub>2</sub>S solution. In the absence of pyrite particles these conditions lead to formation of a protective mackinawite layer. It was suggested by Ning [32] that pyrite formation improved the mackinawite layer's conductivity in the direction perpendicular to the steel surface what led to a more effective galvanic coupling. Ultimately, this resulted in localized corrosion according to Ning [32].

However, the proposed improvement in conductivity of the mackinawite layer does not seem to fully explain the occurrence of localized corrosion as reported by Ning [32]. A uniform mackinawite layer (with an improved conductivity) would lead to uniform corrosion, possibly at a higher rate due to a galvanic coupling. For localized corrosion to happen there needs to be a local disruption of the mackinawite layer, where corrosion happens unimpeded at a higher rate. This amounts to an initiation of localized attack.

Subsequently, the attack propagates much faster as a result of galvanic coupling of the exposed steel and the mixed iron sulfide corrosion product layer.

#### Case 5 - A Poorly Formed Mackinawite Layer

It has been reported [3], [18], [48], [68], [180], [181] that a thin iron sulfide corrosion product layer – mackinawite is formed on mild steel exposed to aqueous H<sub>2</sub>S/CO<sub>2</sub> environments, which typically decreases the uniform corrosion rate. However, as described in Chapter 5, when trace amounts of H<sub>2</sub>S are present in CO<sub>2</sub>, this leads to formation of a partially protective mackinawite layer, which results in localized corrosion [75], [165]. For example, mild steel underwent localized corrosion when exposed to an aqueous solution saturated with  $\leq 100$  ppm H<sub>2</sub>S in CO<sub>2</sub> gas phase, at atmospheric conditions, where the bulk solution was under-saturated with respect to both mackinawite and iron carbonate[165]. However, no localized corrosion occurred when H<sub>2</sub>S/CO<sub>2</sub> ratio was either larger than 100 ppm or in the absence of H<sub>2</sub>S.

It has been reported that mackinawite usually forms as thin layers parallel to the steel surface, what stems from its two dimensional/planar molecular structure [28], [183]. This leads to anisotropic electronic conductivity of mackinawite with much higher conductivity in the planar direction [86], [184]. When a protective mackinawite layer forms on the surface of the steel it leads to retardation of the mass transfer of the species involved in the corrosion process (Fe<sup>2+</sup> away from the surface and H<sup>+</sup> towards the surface), as well as blocking of the steel surface and making it unavailable for iron dissolution.

Under a poorly formed mackinawite layer, localized corrosion initiates as a result of discontinuities in the layer. This allows the corrosive species such as H<sup>+</sup>, to reach the

mild steel surface and be reduced there, while  $\text{Fe}^{2+}$  leaves the steel lattice more readily and diffuses away, allowing the corrosion process to proceed unimpeded at these locations. Given that the pitting penetration rates reported in abovementioned study, were significantly higher than the bare steel uniform corrosion rate at the same conditions, one can conclude that this is due to a galvanic coupling between the poorly protected mild steel and the conductive mackinawite layer.

Table 21 summarizes the five cases used to confirm the main hypothesis postulated in the current study.

Table 21: Summary

Case #	Condition	Initiation	Propagation
1	A partially dissolved pyrrhotite layer	Initiation of localized corrosion of mild steel occurred when the preformed pyrrhotite layer underwent partial dissolution	Propagation of localized corrosion occurred due to galvanic coupling between the steel surface and the remaining pyrrhotite layer
2	A disrupted pyrrhotite layer due to pyrite formation	Initiation of localized corrosion of mild steel occurred when the pyrrhotite layer was disrupted by formation of pyrite	Propagation of localized corrosion occurred due to galvanic coupling between the steel surface and the pyrrhotite/pyrite layer
3	A disrupted pyrrhotite layer due to the interference by sand	Initiation of localized corrosion of mild steel occurred when the pyrrhotite deposit was disrupted by pyrite and sand deposits.	Propagation of localized corrosion occurred due to galvanic coupling between the steel surface and the pyrrhotite layer.
4	A disrupted mackinawite layer due to the pyrite interference, and finally	Initiation of localized corrosion of mild steel occurred when the mackinawite layer was disrupted by the deposited pyrite layer	Propagation of localized corrosion occurred due to galvanic coupling between the steel surface and the pyrite layer
5	A poorly formed mackinawite layer	Initiation of localized corrosion of mild steel occurred when there was not enough $[H_2S]_{aq}$ to form a stable mackinawite layer (marginally sour environments).	Propagation of localized corrosion occurred due to galvanic coupling between the steel surface and the mackinawite/cementite corrosion product layer.

## CHAPTER 7: FUTURE WORK

The current study proposed a model for the galvanic corrosion of a mild steel coupled with pyrite or pyrrhotite that was based on a limited number of experiments conducted in a restricted set of environmental conditions. To improve the reliability and accuracy of the model, future work needs to cover experimental results across a wider range of conditions. Furthermore, some aspects of the current work could be substantially improved such as:

- A better analysis of H atom permeation into the pyrite structure and its long term effect on the galvanic current between pyrite and X65.
- More in-depth in-situ analysis of the pyrrhotite and troilite surface transition into a more active surface for  $H^+$  reduction.
- The current study speculated on the reason behind the higher currents measured at the pyrrhotite surface at pH 5.0 as compared to what one would expect, which was the formation and immediate reduction of aqueous  $H_2S$  at the pyrrhotite/troilite surface. However, the exact reason remains unclear and requires further clarification.
- Pyrrhotite and pyrite electroactivity at higher pH values which is closer to an operational conditions in the oil and gas industry. Also, effect of temperature was not taken into account in the current model.

## REFERENCES

- [1] W. R. Whitney, "The corrosion of iron," *J. Am. Chem. Soc.*, vol. 25, no. 4, pp. 394-406, 1903.
- [2] C. D. Bond and G. A. Marsh, "Corrosion of wet steel by hydrogen sulfide-air mixtures," *Corrosion*, vol. 6, p. 22, 1950.
- [3] F. H. Meyer, O. L. Riggs, R. L. McGlasson, and J. D. Sudbury, "Corrosion products of mild steel in hydrogen sulfide environments," *Corrosion*, vol. 14, pp. 69-75, 1958.
- [4] H. Tewari and B. Campbell, "Dissolution of iron during the initial corrosion of carbon steel in aqueous H<sub>2</sub>S solutions," *Can. J. Chem.*, vol. 57, pp. 188-196, 1979.
- [5] D. E. Milliams and C. J. Kroese, "Aqueous corrosion of steel by H<sub>2</sub>S and H<sub>2</sub>S/CO<sub>2</sub> mixture," *Internal and External Protection of Pipes*, pp. 205-214, 1979.
- [6] J. B. Sardisco and R. E. Pitts, "Corrosion of iron in an H<sub>2</sub>S-CO<sub>2</sub>-H<sub>2</sub>O system composition and protectiveness of the sulfide film as a function of pH," *Corrosion*, vol. 21, pp. 350-354, 1965.
- [7] J. B. Sardisco and R. E. Pitts, "Corrosion of iron in an H<sub>2</sub>S-CO<sub>2</sub>-H<sub>2</sub>O system, mechanism of sulfide film formation and kinetics of corrosion reaction," *Corrosion*, vol. 21, pp. 245-253, 1963.
- [8] Dravnieks and C. H. Samans, "Kinetics of reaction of steel with hydrogen sulfide-hydrogen mixtures," *J. Electrochem. Soc.*, vol. 105, no. 4, pp. 183-191, 1958.
- [9] E. C. Greco and W. B. Wright, "Corrosion of iron in an H<sub>2</sub>S-CO<sub>2</sub>-H<sub>2</sub>O system," *Corrosion*, vol. 18, pp. 119t-124t, 1962.
- [10] W. F. Rogers and J. A. Rowe, Jr, "Corrosion effect of hydrogen sulfide and carbon dioxide in oil production," in *Fourth World Petroleum Congress*, pp. 479-499, 1955.
- [11] S. N. Smith and M. W. Joosten, "Corrosion of carbon steel by H<sub>2</sub>S in CO<sub>2</sub> containing oilfield environments," in *CORROSION/2006*, Houston, TX: NACE International, 2006, paper no. 06115.
- [12] P. W. Bolmer, "Polarization of iron in H<sub>2</sub>S-NaHS buffers," *Corrosion*, vol. 21, no. 3, pp. 69-75, 1965.
- [13] B. Tribollet, J. Kittel, A. Meroufel, F. Ropital, F. Grosjean, and E. M. M. Sutter, "Corrosion mechanisms in aqueous solutions containing dissolved H<sub>2</sub>S. Part 2 : Model of the cathodic reactions on a 316L stainless steel rotating disc electrode," *Electrochem. Acta*, vol. 124, pp. 46-51, 2014.
- [14] S. P. Ewing, "Electrochemical studies of the hydrogen sulfide corrosion mechanism," *Corrosion*, vol. 11, pp. 51-55, 1955.
- [15] J. B. Sardisco, W. B. Wright, and E. C. Greco, "Corrosion of iron in an H<sub>2</sub>S-CO<sub>2</sub>-H<sub>2</sub>O system: corrosion film properties on pure iron," *Corrosion*, vol. 19, p. 354t-359t, 1963.

- [16] D. R. Morris, L. P. Sompaleanu, and D. N. Veysey, "The corrosion of steel by aqueous solutions of hydrogen sulfide," *J. Electrochem. Soc.*, vol. 127, no. 6, pp. 1228–1235, 1980.
- [17] Anderko, P. McKenzie, and R. D. Young, "Computation of rates of general corrosion using electrochemical and thermodynamic models," *Corrosion*, vol. 57, no. 3, pp. 202–213, 2001.
- [18] S. N. Smith, "A proposed mechanism for corrosion in slightly sour oil and gas production," in CORROSION/1993, Houston, TX: NACE International, 1993, paper no. 1304.
- [19] W. Sun and S. Nešić, "A mechanistic model of uniform hydrogen sulfide / carbon dioxide corrosion of mild steel," *Corrosion*, vol. 65, no. 5, pp. 291–307, 2009.
- [20] Y. Zheng, B. Brown, and S. Nešić, "Electrochemical study and modeling of H<sub>2</sub>S corrosion of mild steel," *Corrosion*, vol. 70, no. 4, pp. 351–365, 2014.
- [21] K. J. Lee, "A mechanistic modeling of CO<sub>2</sub> corrosion of mild steel in the presence of H<sub>2</sub>S," Ph.D. dissertation, Ohio University, Athens, OH, 2004.
- [22] W. Sun, "Kinetics of iron carbonate and iron sulfide scale formation in CO<sub>2</sub>/H<sub>2</sub>S Corrosion," Ph.D. dissertation, Ohio University, Athens, OH, 2006.
- [23] Y. Zheng, "Electrochemical mechanism and model of H<sub>2</sub>S corrosion of carbon steel," Ph.D. dissertation, Ohio University, Athens, OH, 2015.
- [24] J. Kvarekvål and G. Svenningsen, "Effect of iron sulfide deposits on sour corrosion of carbon steel," in CORROSION/2016, Houston, TX: NACE International, 2016, paper no. 7313.
- [25] B. N. Brown, "The influence of sulfides on localized corrosion of mild steel," Ph.D. dissertation, Ohio University, Athens, OH, 2013.
- [26] F. Shi, L. Zhang, J. Yang, M. Lu, J. Ding, and H. Li, "Polymorphous FeS corrosion products of pipeline steel under highly sour conditions," *Corros. Sci.*, vol. 102, pp. 103–113, 2016.
- [27] J. Ning, Y. Zheng, B. Brown, D. Young, and S. Nešić, "A thermodynamic model for the prediction of mild steel corrosion products in an aqueous hydrogen sulfide environment," *Corrosion*, vol. 71, no. 8, pp. 945–960, 2015.
- [28] D. W. Shoesmith, P. Taylor, M. G. Bailey, and D. G. Owen, "The Formation of ferrous monosulfide polymorphs during the corrosion of iron by aqueous hydrogen sulfide at 21°C," *J. Electrochem. Soc.*, 127, no. 5, pp. 1007–1015, 1980.
- [29] L. G. Benning, R. T. Wilkin, and H. Barnes, "Reaction pathways in the Fe–S system below 100°C," *Chem. Geol.*, vol. 167, pp. 25–51, 2000.
- [30] W. H. Thomason, "Formation Rates of Protective Iron Sulfide Films on Mild Steel in H<sub>2</sub>S-Saturated Brine as a Function of Temperature," CORROSION/1978, Houston, TX: NACE International, 1978, paper no. 41.
- [31] W. Zhao, Y. Zou, K. Matsuda, and Z. Zou, "Characterization of the effect of hydrogen sulfide on the corrosion of X80 pipeline steel in saline solution," *Materials*, vol. 102, pp. 455–468, 2016.

- [32] J. Ning, "The role of iron sulfide polymorphism in localized corrosion of mild steel," Ph.D. dissertation, Ohio University, Athens, OH, 2016.
- [33] G. Wikjord, T. E. Rummery, F. E. Doern, and D. G. Owen, "Corrosion and deposition during the exposure of carbon steel to hydrogen sulphide - water solutions," *Corros. Sci.*, vol. 20, pp. 651-671, 1980.
- [34] Z. A. Iofa, V. V. Batrakov, and C-N. Ba, "Influence of anion adsorption on the action of inhibitors on the acid corrosion of iron and cobalt," *Electrochem. Acta*, vol. 9, no. 12, pp. 1645-1653, 1964.
- [35] D.J. Vaughan and J.R. Craig, "Mineral chemistry of metal sulfides," first ed., Vail-Ballou, New York, 1978, pp. 17-117.
- [36] J.E. Thomas, W.M. Skinner, and R. ST.C. Smart, "A mechanism to explain sudden changes in rates and products for pyrrhotite dissolution in acid solution," *Geochim. Cosmochim. Acta*, vol. 65, pp. 1-12, 2001.
- [37] H. Wang and I. Salveson, "A review on the mineral chemistry of the non-stoichiometric iron sulphide,  $\text{Fe}_{(1-x)}\text{S}$  ( $0 \leq x \leq 0.125$ ): polymorphs, phase relations and transitions, electronic and magnetic structures," *Phase Transitions*, vol. 78, no. 7-8, pp. 547-567, 2005.
- [38] J. B. Murowchick, "Marcasite inversion and the petrographic determination of pyrite ancestry," *Econ. Geol.*, vol. 87, pp. 1141-1152, 1992.
- [39] P. Ramdohr, "The Ore Minerals and Their Intergrowths," 2nd ed. Pergamon, Oxford, 1980.
- [40] Y. Bi, Y. Yuan, C.L. Exstrom, S.A. Darveau, and J. Huang, "Air stable, photosensitive, phase pure iron pyrite nanocrystal thin," *Nano Lett.*, vol. 11, no. 11, pp. 4953-4957, 2011.
- [41] M. Cabán-Acevedo, M.S. Faber, Y. Tan, R.J. Hamers, and S. Jin, "Synthesis and properties of semiconducting iron pyrite ( $\text{FeS}_2$ ) nanowires," *Nano Lett.*, vol. 12, no. 4, pp. 1977-1982, 2012.
- [42] A. Ennaoui, S. Fiechter, Ch. Pettenkofer, N. Alonso-Vante, K. Buker, M. Bronold, Ch. Hopfner, and H. Tributsch, "Iron disulfide for solar-energy conversion," *Sol. Energy Mater. Sol. Cells*, vol. 29, no. 4, pp. 289-370, 1993.
- [43] C. Di Giovanni, W. Wang, S. Nowak, J. Greneche, H. Lecoq, L. Mouton, and M. Giraud, and C. Tard, "Bioinspired iron sulfide nanoparticles for cheap and long-lived electrocatalytic molecular hydrogen evolution in neutral water," *ACS Catal.*, vol. 4, pp. 681-687, 2014.
- [44] L. Qnuchukwu, "Hydrogen evolution on iron pyrite ( $\text{FeS}_y$ ) in sodium chloride solution," *Electrochim. Acta*, vol. 27, no. 4, pp. 529-533, 1982.
- [45] W. Sun, S. Nešić, and S. Papavinasam, "Kinetics of corrosion layer formation. Part 2-iron sulfide and mixed iron sulfide/carbonate layers in carbon dioxide / hydrogen sulfide Corrosion," *Corrosion*, vol. 64, no. 7, pp. 586-599, 2008.
- [46] J. Ning, Y. Zheng, B. Brown, D. Young, and S. Nešić, "The Role of Iron Sulfide Polymorphism in Localized  $\text{H}_2\text{S}$  Corrosion of Mild Steel," *Corrosion*, vol. 73, no. 2, pp. 155-168, 2017.

- [47] S. Gao, P. Jin, B. Brown, D. Young, S. Nešić, and M. Singer, "Corrosion behavior of mild steel in sour environments at elevated temperatures," *Corrosion*, vol. 73, no. 8, pp. 915-926, 2017.
- [48] H. Ma, X. Cheng, G. Li, S. Chen, Z. Quan, S. Zhao, and L. Niu, "The influence of hydrogen sulfide on corrosion of iron under different conditions," *Corros. Sci.*, vol. 42, pp. 1669-1683, 2000.
- [49] H. Vedage, T. A. Ramanarayanan, J. D. Mumford, and S. N. Smith, "Electrochemical growth of iron sulfide films in H<sub>2</sub>S-saturated chloride media," *Corrosion*, vol. 49, no.2, pp. 114–121, 1993.
- [50] D. Rickard and G. W. Luther, "Chemistry of iron sulfides," *Chemical Rev.*, vol. 107, no. 2, pp. 514-562, 2007.
- [51] J. Morse, F. Millero, J. Cornwell, and D. Rickard, "The chemistry of the hydrogen sulfide and iron sulfide systems in natural waters," *Earth-Science Rev.*, vol. 24, pp. 1–42, 1987.
- [52] R. Murphy and D.R. Strongin, "Surface reactivity of pyrite and related sulfides," *Surf. Sci. Rep.*, vol. 64, no. 1, pp. 1–45, 2009.
- [53] J.M. Guevremont, J. Bebie, A.R. Elsetinow, D.R. Strongin, and M.A. Schoonen, "Reactivity of the (100) plane of pyrite in oxidizing gaseous and aqueous environments: effects of surface imperfections," *Environ. Sci. Technol.*, vol. 32, no. 23, pp. 3743–3748, 1998.
- [54] H. Omar, Y. Gunaltun, J. Kvarekval, and A. Dugstad, "H<sub>2</sub>S corrosion of carbon steel under simulated kashagan field conditions," CORROSION/2005, Houston, TX: NACE International, 2005, paper no. 05300.
- [55] J. Kvarekval, "Morphology of localized corrosion attacks in sour environments," in CORROSION/2007, Houston, TX: NACE International, 2007, paper no. 7659.
- [56] J. Kvarekval "Corrosion layer breakdown and localized corrosion in CO<sub>2</sub>/H<sub>2</sub>S environments," CORROSION/2012, Houston, TX: NACE International, 2012, paper no. 01537.
- [57] J. Kvarekval and A. Dugstad, "Corrosion mitigation with pH stabilisation in slightly sour gas/condensate pipelines," CORROSION/2006, Houston, TX: NACE International, 2006, paper no. 06646.
- [58] J. Kvarekval and A. Dugstad, "Pitting corrosion in CO<sub>2</sub>/H<sub>2</sub>S containing glycol solutions under flowing conditions," CORROSION/2005, Houston, TX: NACE International, 2005, paper no. 05631.
- [59] R. De Médicis, "Cubic FeS, a metastable iron sulfide," American Association for the Advancement of Science, vol. 170, no. 3963, pp. 1191–1192, 2014.
- [60] N. Yaakob, M. Singer, and D. Young, "Top of the line corrosion behavior in highly sour environments: Effect of the Gas/Steel Temperature," CORROSION/2014, Houston, TX: NACE International, 2014, paper no. 3807.
- [61] Mineralogy Database, <http://webmineral.com/>, 2016 (accessed 07.02.15).
- [62] L. Smith and K. de Waard, "Corrosion prediction and materials selection for oil and gas production environments," CORROSION/2005, Houston, TX: NACE International, 2005, paper no. 5648.

- [63] S.N. Smith and J.L. Pacheco, "Prediction of corrosion in slightly sour environments," CORROSION/2002, Houston, TX: NACE International, 2002, paper no. 2241.
- [64] D. Rickard, "Experimental concentration-time curves for the iron (II) sulphide precipitation process in aqueous solutions and their interpretation," *Chem. Geol.*, vol. 78, pp. 315–324, 1989.
- [65] P.H. Tewari, M.G. Bailey, and A.B. Campbell, "The erosion-corrosion of carbon steel in aqueous H<sub>2</sub>S solutions up to 120°C and 1.6 MPa pressure," *Corros. Sci.*, vol. 19, pp. 573–585, 1979.
- [66] S. Nešić, "Carbon Dioxide Corrosion of Mild Steel" (2011), R. Winston Revie, Uhlig's Corrosion Handbook, 3rd ed., Hoboken, NJ, pp. 229-245.
- [67] W. Sun and S. Nešić, "Corrosion in acid gas solutions" (2010), J. A. Richardson, Shreir's Corrosion, 2nd ed., Elsevier, pp.1270–1298.
- [68] X.B. Huang, Z. F. Yin, H. L. Li, Z. Q. Bai, and W. Z. Zhao, "Corrosion of N80 tubing steel in brine at 1.2 MPa CO<sub>2</sub> containing trace amounts of H<sub>2</sub>S," *Corrosion Eng. Sci. and Tech*, vol. 47, pp. 78-83, 2012.
- [69] K. Videm and J. Kvarekvål, "Corrosion of carbon steel in carbon dioxide-saturated solutions containing small amounts of hydrogen sulfide," *Corros. Sci.*, vol. 51, pp. 260–269, 1995.
- [70] Y.-S. Choi, S. Nešić, and S. Ling, "Effect of H<sub>2</sub>S on the CO<sub>2</sub> corrosion of carbon steel in acidic solutions," *Electrochim. Acta*, vol. 56, no. 4, pp. 1752 - 1760, 2011.
- [71] H. Fang, "Investigation of localized corrosion of carbon steel in H<sub>2</sub>S environments," Ph.D. dissertation, Ohio University, Athens, OH, 2012.
- [72] D.D. MacDonald, B. Roberts, and J.B. Hyne, "The corrosion of carbon steel by wet elemental sulphur," *Corros. Sci.*, vol. 18, pp. 411–425, 1978.
- [73] G. Schmitt, "Effect of elemental sulfur on corrosion in sour gas systems," *Corrosion*, vol. 47, no. 4, pp. 285–308, 1999.
- [74] N. Yaakob, "Top of the Line Corrosion in CO<sub>2</sub>/H<sub>2</sub>S Environments," Ph.D. Dissertation, Ohio University, 2015.
- [75] N. Yaakob, F. Farelas, M. Singer, S. Nešić, and D. Young, "Localized top of the line corrosion in marginally sour environments," CORROSION/2016, Houston, TX: NACE International, 2016, paper no. 7695.
- [76] O. Yepez, N. Obeyesekere, and J. Wylde, "Study of sour corrosion mechanism under controlled pH," CORROSION/2016, Houston, TX: NACE International, 2016, paper no. 7795.
- [77] B.F.M. Pots, R.C. John, I.J. Rippon, M.S. Thomas, S. D. Kapusta, M.M. Girgis, and T. Whitham, "Improvements on De Waard-Milliams corrosion prediction and applications to corrosion management" CORROSION/2002, Houston, TX: NACE International, 2002, paper no. 02235.
- [78] H. Fang, B. Brown, and S. Nešić, "Effects of sodium chloride concentration on mild steel corrosion in slightly sour environments," *Corrosion*, vol. 67, no. 1, pp. 015001-1 - 015001-12, 2011.

- [79] Y. Zheng, J. Ning, B. Brown, and S. Nešić, “Electrochemical model of mild steel corrosion in a mixed H<sub>2</sub>S/CO<sub>2</sub> aqueous environment in the absence of protective corrosion product layers,” *Corrosion*, vol. 71, no. 3, pp. 316–325, 2015.
- [80] Y. Zheng, J. Ning, B. Brown, and S. Nešić, “Advancement in predictive modeling of mild steel corrosion in CO<sub>2</sub> and H<sub>2</sub>S containing environments,” *Corrosion*, vol. 72, no. 5, pp. 679–691, 2016.
- [81] D.F. Pridmore and R.T. Shuey, “The electrical resistivity of galena, pyrite, and chalcopyrite,” *Am. Mineral.*, vol. 61, pp. 248–259, 1976.
- [82] C.I. Pearce, A.D. Patrick, and D.J. Vaughan, “Electrical and magnetic properties of sulfides,” *Rev. Mineral. Geochem.*, vol. 61, pp. 127–180, 2006.
- [83] R. Schieck, A. Hartmann, S. Fiechter, R. Konenkamp, and H. Wetzel, “Electrical properties of natural and synthetic pyrite (FeS<sub>2</sub>) crystals,” *J. Mater. Res. Soc.*, vol. 5, pp. 1567–1572, 1990.
- [84] P.K. Abraitis, R.A.D. Patrick, and D.J. Vaughan, “Variations in the compositional, textural and electrical properties of natural pyrite: a review,” *Int. J. Mine. Process*, vol. 74, pp. 41–59, 2004.
- [85] A.R. Lennie, K.E.R. England, and D. Vaughan, “Transformation of synthetic mackinawite to hexagonal pyrrhotite: a kinetic study,” *Am. Mineral.*, vol. 80, pp. 960–967, 1995.
- [86] K. D. Kwon, K. Refson, S. Bone, R. Qiao, W. Yang, Z. Liu, and G. Sposito, “Magnetic ordering in tetragonal FeS: evidence for strong itinerant spin fluctuations,” *Phys. Rev.*, vol. B83, pp. 064402-1 - 064402-7, 2011.
- [87] C. Almeida, and B.F. Giannetti, “The electrochemical behavior of pyrite–pyrrhotite mixtures,” *J. Electroanal. Chem.* vol. 553, pp. 27–34, 2003.
- [88] K.K. Mishra and K. Osseo-Asare, “Aspects of the interfacial electrochemistry of semiconductor,” *J. Electrochem. Soc.* vol. 135, no. 10, pp. 2502–2509, 1988.
- [89] L.C. Hamilton and R. Woods, “An investigation of surface oxidation of pyrite and pyrrhotite by linear potential sweep voltammetry,” *J. Electroanal. Chem.* vol. 118, pp. 327–343, 1981.
- [90] W. Davison, “The solubility of iron sulfides in synthetic and natural-waters at ambient-temperature,” *Aquat. Sci.*, vol. 53, no. 4, pp. 309–329, 1991.
- [91] D. Abayarathna, “The Effect of surface films on corrosion of carbon steel in a CO<sub>2</sub>-H<sub>2</sub>S-H<sub>2</sub>O system,” CORROSION/2005, Houston, TX: NACE International, 2005, paper no. 05624.
- [92] M. Liu, J. Wang, W. Ke, and E.-H. Han, “Corrosion behavior of X52 anti-H<sub>2</sub>S pipeline steel exposed to high H<sub>2</sub>S concentration solutions at 90°C,” *J. Mater. Sci. Technol.* vol. 30, pp. 504–510, 2014.
- [93] M. Eisenberg, C.W. Tobias, C.R. Wilke, “Ionic mass transfer and concentration polarization at rotating electrodes,” *J. Electrochem. Soc.*, vol. 101, no. 6, pp. 306-320, 1954.
- [94] M. Nordsveen, S. Nešić, R. Nyborg, and A Stangeland, “A mechanistic model for carbon dioxide corrosion of mild steel in the presence of protective iron

- carbonate films-part 1: theory and verification,” *Corrosion*, vol.59, no. 5, pp. 443-456, 2003.
- [95] J.O. Bockris, D. Drazic, A.R. Despic, “The electrode kinetics of the deposition and dissolution of iron,” *Electrochim. Acta*, vol.4, no. 2-4, pp. 325-361, 1961.
- [96] O.M. Suleimenov, and R.E. Krupp, “Solubility of hydrogen sulfide in pure water and in NaCl solutions, from 20 to 320°C and at saturation pressures,” *Geochim. Cosmochim. Acta*, vol. 58, pp. 2433–2444, 1994.
- [97] S. Nešić, J. Postlethwaite, and S. Olsen, “An electrochemical model for prediction of corrosion of mild steel in aqueous carbon dioxide solutions,” *Corrosion*, vol. 52, no. 4, pp. 280-294, 1996.
- [98] O. M. Suleimenov and T. M. Seward, “A Spectrophotometric Study of Hydrogen Sulphide Ionisation in Aqueous Solutions to 350°C,” *Geochim. Cosmochim. Acta*, vol. 61, pp. 5187–5198, 1997.
- [99] A. Kahyarian, B. Bruce, and S. Nešić, “Mechanism of cathodic reactions in acetic acid corrosion of iron and mild steel,” *Corrosion*, vol. 72, no. 12, pp. 1539-1546, 2016.
- [100] R.E. Meyer, “Electrochemistry of FeS<sub>2</sub>,” *J. Electroanal. Chem.*, vol. 101, pp. 59-71, 1979.
- [101] E. Peters and H. Majima, “Electrochemical reactions of pyrite in acid perchlorate solutions,” *Can. Metall.*, vol. 7, no. 3, pp. 111-117, 1968.
- [102] E. Peters, “The electrochemistry of sulfide minerals,” in: J.O’M. Bockris, D.A.J. Rand and B.J. Welch (Eds.), *Trends in electrochemistry*, Plenum Press, New York, pp. 267–290, 1977.
- [103] T. Biegler and D.A. Swift, “Anodic behaviour of pyrite in acid solutions,” *Electrochim. Acta*, vol. 24, no. 4, pp. 415-420, 1979.
- [104] D.K. Nordstrom, “Aqueous pyrite oxidation and the consequent formation of secondary iron minerals,” *Soil Science Society of America*, pp. 37–56, 1982.
- [105] P.C. Singer and W. Stumm, “Acidic mine drainage: the rate-determining step,” *American Association for the Advancement of Science*, vol. 167, no. 3921, pp. 1121–1123, 1970.
- [106] N.J. Welham and G.H. Kelsall, “Recovery of gold from pyrite FeS<sub>2</sub> by aqueous chlorination II reduction of aqueous chlorine on pyrite (FeS<sub>2</sub>),” *J. Electrochem. Soc.*, vol. 147, no. 1, pp. 164–175, 2000.
- [107] T. Biegler, D.A.J. Rand, and R. Woods, ‘Oxygen reduction on sulphide minerals Part I. kinetics and mechanism at rotated pyrite electrodes,” *J. Electroanal. Chem.*, vol. 60, pp. 151-162, 1975.
- [108] T. Biegler, “Oxygen reduction on sulphide minerals part II. relation between activity and semiconducting properties of pyrite electrodes,” *J. Electroanal. Chem.*, vol. 70, pp. 265-275, 1976.
- [109] D.A.J. Rand, “Oxygen reduction on sulphide minerals part III. comparison of activities of various copper, iron, lead and nickel mineral electrodes,” *J. Electroanal. Chem.*, vol. 83, pp. 19-32, 1977.
- [110] C. Di Giovanni, A. Reyes-Carmona, A. Coursier, S. Nowak, J-M. Greneche, H. Lecoq, L. Mputon, J. Roziere, D. Jones, J. Peron, M. Giraud, and C. Tard,

- “Low-cost nanostructured iron sulfide electrocatalysts for PEM water electrolysis,” *ACS Catal.*, vol. 6, no. 4, pp. 2626-2631, 2016.
- [111] R.L. Pozzo and I. Iwasaki, “Electrochemical Study of Pyrrhotite-Grinding Media Interaction Under Abrasive Conditions” , *Corrosion*, vol. 43, no. 3, pp. 159-164, 1987.
- [112] M. Tjelta and J. Kvarekval, “Electrochemistry of iron sulfide and its galvanic coupling to carbon steel in sour aqueous solution”, CORROSION/2016, Houston, TX: NACE International, 2016, paper no. 7478.
- [113] S.N. Esmaeely, B. Brown, and S. Nešić, “Verification of an electrochemical model for aqueous corrosion of mild steel for H<sub>2</sub>S partial pressures up to 0.1 MPa,” *Corrosion*, vol. 73, no. 7 pp.144-154, 2017.
- [114] M.J. Nicol and S.D. Scott, “The kinetics and mechanism of the non-oxidative dissolution of some iron sulphides in aqueous acidic solutions,” *J. South African Inst. Min. Metall.*, pp. 298-305, 1979.
- [115] Y. Mikhlin, “Reactivity of pyrrhotite surfaces: an electrochemical study”, *J. Phys. Chem.*, vol. 2, no. 24, pp. 5672-5677, 2000.
- [116] A.V Kuklinskii, Y.L. Mikhlin, G.L. Pashkov, V.F. Kargin, and I.P. Asanov, “Conditions for the formation of a nonequilibrium nonstoichiometric layer on pyrrhotite in acid solutions,” *Rus. J. Electrochem.*, vol. 37, no. 12, pp. 1269-1276, 2001.
- [117] C. de Waard and D.E. Milliams, “Carbonic acid corrosion of steel,” *Corrosion*, vol. 31, no. 5, pp. 177–181, 1975.
- [118] A. Kahyarian, M. Singer, and S. Nešić, "Modeling of uniform CO<sub>2</sub> corrosion of mild steel in gas transportation systems: A review," *J. Nat. Gas Sci. and Eng.*, vol. 29, pp. 530–549, 2016.
- [119] E. Remita, B. Tribollet, E. Sutter, V. Vivier, F. Ropital, and J. Kittel, “Hydrogen evolution in aqueous solutions containing dissolved CO<sub>2</sub>: quantitative contribution of the buffering effect,” *Corros. Sci.*, vol. 50, pp. 1433–1440, 2008.
- [120] T. Tran, “Corrosion Mechanisms of Mild Steel in Weak Acids,” Ph.D. dissertation, Ohio University, Athens, OH, 2014.
- [121] B. Valery, “Effect of pre-exposure of sulfur and iron sulfide on H<sub>2</sub>S corrosion at different temperatures,” Master Thesis, University of Stavanger, Stavanger, Norway, 2011.
- [122] R.C. Woollam, A. Huggins, C. Mendez, J. R. Vera, and W. H. Durnie, “Localized corrosion due to galvanic coupling between FeS-covered and uncovered areas: another Oilfield Myth,” CORROSION/2013, Houston, TX: NACE International, 2013, paper no. 2715.
- [123] J. Kvarekval, R. Nyborg, and M. Seiersten, “Corrosion product films on carbon steel in semi-sour CO<sub>2</sub>/H<sub>2</sub>S environments,” CORROSION/2002, Houston, TX: NACE International, 2002, paper no. 2296.
- [124] J. Kvarekval, A. Dugstad, and M. Seiersten, “Localized corrosion on carbon steel in sour glycolic solutions,” CORROSION/2010, Houston, TX: NACE International, 2010, paper no. 10277.

- [125] J. Amri and J. Kvarekval, "Simulation of solid-state growth of iron sulfides in sour corrosion conditions," CORROSION/2011, Houston, TX: NACE International, 2011, paper no. 11078.
- [126] D.A. Jones, "Principles and Prevention of Corrosion," 2nd ed., Prentice-Hall, New Jersey, 1996, pp. 168-198.
- [127] K. Adam, K.A. Natarajan, S.C. Riemer, and I. Iwasaki, "Electrochemical aspects of grinding media-mineral interaction in sulfide ore grinding," *Corrosion*, vol. 43, no. 8, pp. 440-447, 1986.
- [128] S.N. Esmaeely and S. Nešić, "Reduction reactions on iron sulfides in aqueous acidic solutions," *J. Electrochem. Soc.* vol. 164, no. 12, pp. C664-C670, 2017.
- [129] P.R. Holmes and F.K. Crundwell, "Kinetic aspects of galvanic interactions between minerals during dissolution," *Hydrometallurgy*, vol. 39, pp. 353-375, 1995.
- [130] M. Bungs and H. Tributsch, "Electrochemical and photoelectrochemical insertion and transport of hydrogen in pyrite," *J. Phys. Chem.*, vol. 101, no. 12, pp. 1844-1850, 1997.
- [131] S.M. Wilhelm, J. Vera, and N. Hackerman, "Transport of hydrogen through pyrite," *J. Electrochem. Soc.*, vol. 130, no. 10, pp. 2129-2132, 1983.
- [132] V.U.S. Rao, "Evaluation of particle size measurement techniques for dispersed iron catalysts," *Energy&Fuel*, vol. 8, no. 1, pp. 44-47, 1994.
- [133] J.M. Lambert, P.L. Walker, A.J. Perrotta, J.P. McCullough, and H. Beuther, "Physical characterization and pressure temperature microscopy of the pyrite pyrrhotite transformation," *Fuel*, vol. 62, pp. 1474-1480, 1983.
- [134] M.P. Janzen, R.V. Nicholson, and J.M. Scharer, "Pyrrhotite reaction kinetics reaction rates for oxidation by oxygen ferric iron and for non-oxidative dissolution," *Geochim. Cosmochim. Acta*, vol. 64, no. 9, pp. 1511-1522, 2000.
- [135] F.V. Stohl, "The effects of iron sulphide surface area variations on coal liquefaction," *Fuel*, vol. 62, pp. 122-126, 1983.
- [136] P. Jin, W. Robbins, and G. Bota, "Mechanism of magnetite formation in high temperature corrosion by model naphthenic acids," *Corros. Sci.*, vol. 111, pp. 822-834, 2016.
- [137] P. Jin and S. Nešić, "Mechanism of magnetite formation in high temperature naphthenic acid corrosion by crude oil fractions," *Corros. Sci.*, vol. 115, pp. 93-105, 2017.
- [138] R. G. Arnold and L. E. Reichen, "Measurement of the metal content of naturally occurring metal-deficient, hexagonal pyrrhotite by an X-Ray spacing method," *Amer. Mineral.* vol. 47, pp. 105-111, 1962.
- [139] G.A. Desborough and R.H. Carpenter, "Phase Relations of Pyrrhotite," *Econ. Geol.*, vol. 60, pp. 1431-1450, 1965.
- [140] P. Chiriță and J.D. Rimstidt, "Pyrrhotite dissolution in acidic media," *Appl. Geochem.*, vol. 41, pp. 1-10, 2014.
- [141] P.H. Tewari and A. Campbell, "Dissolution of iron sulfide (troilite) in aqueous sulfuric acid," *J. Phys. Chem.*, vol. 80, no. 17, pp. 1844-1848, 1976.

- [142] P. H. Tewari, C. Wallace, and A.B. Campbell, "The solubility of iron sulfides and their role in mass transport," *Internal Report Atomic Energy of Canada*, 1978.
- [143] X. Jiang, Y.G. Zheng, D.R. Qu, and W. Ke, "Effect of calcium ions on pitting corrosion and inhibition performance in CO<sub>2</sub> corrosion of N80 steel," *Corros. Sci.* vol. 48, pp. 3091–3108, 2006.
- [144] C.Q. Ren, X. Wang, L. Liu, H.E. Yang, and N. Xian, "Lab and field investigations on localized corrosion of casing," *Mater. Corros.*, vol. 63, no. 2, pp. 168–172, 2012.
- [145] Z.F. Yin, W.Z. Zhao, Y.R. Feng, and S.D. Zhu, "Characterization of CO<sub>2</sub> corrosion scale in simulated solution with Cl<sup>-</sup> ion under turbulent flow conditions," *Corrosion*, vol. 44, no. 6, pp. 453–461, 2009.
- [146] S.N. Esmaeely, D. Young, B. Brown, and S. Nešić, "Effect of incorporation of calcium into iron carbonate protective layers in CO<sub>2</sub> corrosion of mild steel," *Corrosion*, vol. 73, no. 3, pp. 238-246, 2017.
- [147] ASTM Standard G1, Standard Practice for Preparing, Cleaning, and Evaluating Corrosion Test, Reapproved 2011.
- [148] S. Gao, "Effect of pH<sub>2</sub>S on the corrosion of carbon steel at high temperature," in publication, 2018.
- [149] S. N. Esmaeely, G. Bota, B. Brown, and S. Nešić, "Influence of pyrrhotite on the corrosion of mild steel," *Corrosion*, vol. 74, no. 1, 2018.
- [150] G. Qian, F. Xia, J. Brugger, W. M. Skinner, J. Bei, G. Chen, and A. Pring, "Replacement of pyrrhotite by pyrite and marcasite under hydrothermal conditions up to 220 °C: an experimental study of reaction textures and mechanisms," *Am. Mineral.*, vol. 96, pp. 1878–1893, 2011.
- [151] M.E. Fleet, "Structural aspects of the marcasite-pyrite transformation," *Can. Mineral.*, vol. 10, pp. 225-231, 1970.
- [152] N. Tsesmetzis, E.B. Alsop, A. Vigneron, F. Marcelis, I.M. Head, and B.P. Lomans, "Microbial community analysis of three hydrocarbon reservoir cores provides valuable insights for the assessment of reservoir souring potential," *Int. Biodeterior & Biodegrad*, pp. 1-12, 2016.
- [153] B.N. Brown, "H<sub>2</sub>S multiphase flow loop: CO<sub>2</sub> corrosion in the presence of trace amounts of hydrogen sulfide," Master thesis, Ohio University, Athens, OH, 2004.
- [154] J. Tang, Y. Shao, J. Guo, T. Zhang, G. Meng, and F. Wang, "The effect of H<sub>2</sub>S concentration on the corrosion behavior of carbon steel at 90 °C," *Corros. Sci.*, vol. 52, pp. 2050–2058, 2010.
- [155] S. Al-Hassan, B. Mishra, D.L. Olson, and M.M. Salama, "Effect of microstructure on corrosion of steels in aqueous solutions containing carbon dioxide," *Corrosion*, vol. 54, no. 6, pp. 480-491, 1998.
- [156] F. Farelas, M. Galicia, B. Brown, S. Nešić, and H. Castaneda, "Evolution of dissolution processes at the interface of carbon steel corroding in a CO<sub>2</sub> environment studied by EIS," *Corros. Sci.*, vol. 52, pp. 509–517, 2010.

- [157] A. Fragiel, R. Schouwenaarf, R. Guardián, and R. Pérez, “Microstructural characteristics of different commercially available API 5L X65 steels,” *J. New Mater. Electrochem. Syst.*, vol. 8, pp. 115–119, 2005.
- [158] D.N. Staicopolus, “The role of cementite in the acidic corrosion of steel,” *J. Electrochem. Soc.*, vol. 110, no. 11, pp. 1121–1124, 1963.
- [159] W. Sun, S. Nešić, and R.C. Woollam, “The effect of temperature and ionic strength on iron carbonate ( $\text{FeCO}_3$ ) solubility limit,” *Corros. Sci.*, vol. 51, pp. 1273–1276, 2009.
- [160] W. Sun, S. Nešić, D. Young, and R.C. Woollam, “Equilibrium expressions related to the solubility of the sour corrosion product,” *J. Ind. Eng. Chem. Res.*, vol. 47, no. 5, pp. 1738–1742, 2008.
- [161] J. Han, B. Brown, D. Young, and S. Nešić, “Mesh-capped probe design for direct pH measurements at an actively corroding metal surface,” *J. Appl. Electrochem.*, vol. 40, no. 3, pp. 683–690, 2010.
- [162] B. Brown, “The likelihood of localized corrosion in an  $\text{H}_2\text{S}/\text{CO}_2$  environment,” CORROSION/2011, Houston, TX: NACE International, 2011, paper no. 5855.
- [163] P. Sarin, V.L. Snoeyink, D.A. Lytle, and W.M. Kriven, “Iron corrosion scales: model for scale growth, iron release and colored water formation,” *J. Environ. Eng.*, vol. 130, pp. 364–373, 2004.
- [164] W. Sun and S. Nešić, “Kinetics of corrosion layer formation: part 1—iron carbonate layers in carbon dioxide Corrosion,” *Corrosion*, vol. 64, no. 4, pp. 334–346, 2008.
- [165] S.N. Esmaeely, W. Zhang, B. Brown, M. Singer, and S. Nešić, “Localized corrosion of mild steel in marginally sour environments,” *Corrosion*, vol. 73, no. 9, pp. 1098–1106, 2017.
- [166] M.F. Cai, Z. Dang, Y.W. Chen, and N. Belzile, “The passivation of pyrrhotite by surface coating,” *Chemosphere*, vol. 61, pp. 659–667, 2005.
- [167] N. Belzile, Y.W. Chen, M.F. Cai, Y. Li, “A review on pyrrhotite oxidation,” *J. Geochem. Explor.* Vol. 84, pp. 65–76, 2004.
- [168] J.S. Smith and J.D. Miller, “Nature of sulphides and their corrosive effect on ferrous metals: A review,” *Br. Corros. J.* vol. 10, pp. 136–143, 1975.
- [169] Y. Mikhlin, A. Kuklinskii, G.L. Pashkov, I.P. Asanov, “Pyrrhotite electrooxidation in acid solutions,” *Russ. J. Electrochem.*, vol. 37, pp. 1277–1282, 2001.
- [170] Y. Mikhlin, V. Varnek, I. Asanov, Y. Tomashevich, A. Okotrub, A. Livshits, G. Selyutin, G. Pashkov, “Reactivity of pyrrhotite ( $\text{Fe}_9\text{S}_{10}$ ) surfaces: Spectroscopic studies,” *Phys. Chem. Chem. Phys.*, vol. 2, pp. 4393–4398, 2000.
- [171] P. Bai, S. Zheng, H. Zhao, Y. Ding, J. Wu, C. Chen, “Investigations of the diverse corrosion products on steel in a hydrogen sulfide environment,” *Corros. Sci.*, vol. 87, pp. 397–406, 2014.
- [172] R. Gee and Z.Y. Chen, “Hydrogen embrittlement during the corrosion of steel by wet elemental sulphur,” *Corros. Sci.*, vol. 37, pp. 2003–2011, 1995.

- [173] U.M. Graham and H. Ohmoto, “Experimental study of formation mechanisms of hydrothermal pyrite”, *Geochim. Cosmochim. Acta.*, vol. 58, pp. 2187–2202, 1994.
- [174] J.W. Matthews and A.E. Blakeslee, “Defects in epitaxial multilayers”, *J. Cryst. Growth.*, vol. 32, pp. 565–273, 1976.
- [175] R. Hull, J.C. Bean, D.J. Werder, and R.E. Leibenguth, “Activation barriers to strain relaxation in lattice-mismatched epitaxy”, *Phys. Rev.*, vol. B40, pp. 1681–1684, (1989).
- [176] H.H. Abass, H.A. Nasr-El-Din, M.H. BaTaweel, Sand control: sand characterization, failure mechanisms, and completion methods, *Soc. Pet. Eng.*, <https://doi.org/10.2118/77686-MS>, 2002.
- [177] K. Chokshi, W. Sun, and S. Nestic, Iron carbonate scale growth and the effect of inhibition in CO<sub>2</sub> corrosion of mild steel, CORROSION/2005, Houston, TX: NACE International, 2005, Paper No. 05285.
- [178] J.L. Crolet, N. Thevenot, and S. Nestic, “Role of conductive corrosion products in the protectiveness of corrosion layers”, *Corrosion*, vol. 54, pp. 194–203, 1998.
- [179] S. Grousset, M. Bayle, A. Dauzeres, D. Crusset, V. Deydier, Y. Linard, P. Dillmann, F. Mercier-Bion, and D. Neff, “Study of iron sulphides in long-term iron corrosion processes: Characterisations of archaeological artefacts”, *Corros. Sci.*, vol. 112, pp. 264–275, 2016.
- [180] M. Wolthers, L. Charlet, P.R. van Der Linde, D. Rickard, and C.H. van Der Weijden, “Surface chemistry of disordered mackinawite (FeS)”, *Geochim. Cosmochim. Acta.*, vol. 69, pp. 3469–3481, 2005.
- [181] G. Genchev, K. Cox, T.H. Tran, A. Sarfraz, C. Bosch, M. Spiegel, and A. Erbe, “Metallic, oxygen-containing reaction products after polarisation of iron in H<sub>2</sub>S saturated saline solutions”, *Corros. Sci.*, vol. 98, pp. 725–736, 2015.
- [182] A.J. Devey, R. Grau-Crespo, and N. De Leeuw, “Combined density functional theory and interatomic potential study of the bulk and surface structures and properties of the iron sulfide mackinawite (FeS)”, *J. Phys. Chem.*, vol. 112, pp. 10960–10967, 2008.

## APPENDIX A: PUBLICATIONS

## Journal Publications

1. Navabzadeh Esmaeely S., Nešić, S., "Reduction Reactions on Iron Sulfides in Aqueous Acidic Solutions, *Journal of The Electrochemical Society*, 164, No. 12, p. C664 (2017).
2. Navabzadeh Esmaeely S., Bota, G., Brown, B., Nešić, S., "Influence of Pyrrhotite on the Corrosion of Mild Steel", *Corrosion Journal*, 74 (2017).
3. Navabzadeh Esmaeely S., Zheng W., Brown, B., Singer M., Nešić, S., "Localized Corrosion of Mild Steel in Marginally Sour Environments", *Corrosion Journal*, 73, No.9, p. 1099 (2017).
4. Navabzadeh Esmaeely S., Brown, B., Nešić, S., "Verification of an Electrochemical Model for Aqueous Corrosion of Mild Steel for H<sub>2</sub>S Partial Pressures up to 0.1 MPa", *Corrosion Journal*, 73, No.2, p. 144 (2017).
5. Navabzadeh Esmaeely S., Brown, B., Nešić, S., "Electrochemical Model of Sour Corrosion of Mild Steel: Validation at High H<sub>2</sub>S Partial Pressures", *Corrosion Journal*, 72, No.10, p. 1220 (2016).

## Conference Publications

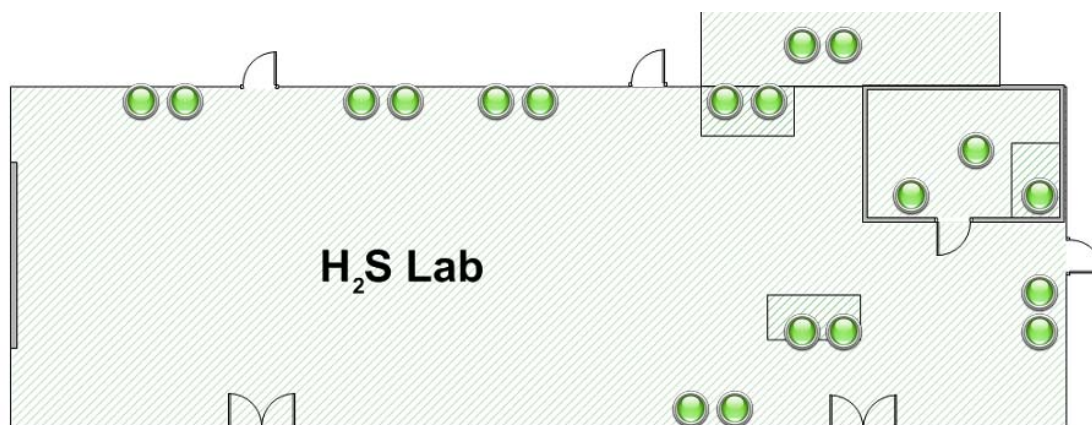
1. Navabzadeh Esmaeely S., Zheng W., Brown, B., Singer M., Nešić, S., "Mild steel Localized Corrosion in Marginal Sour Environments", NACE International Corrosion Conference, Phoenix, AZ, 2018.

2. Navabzadeh Esmaeely S., Bota, G., Brown, B., Nešić, S, “Mild Steel Corrosion under Pyrrhotite layer in CO<sub>2</sub>/H<sub>2</sub>S Environments”, NACE International Corrosion Conference, Phoenix, AZ, 2018.
3. Navabzadeh Esmaeely S., Nešić, S., “Iron Sulfides Electroactivity in Environments in the Presence of Strong Acid, Carbonic Acid and Aqueous Hydrogen Sulfide”, ECS meeting, National Harbor, MD, 2017.
4. Navabzadeh Esmaeely S., Brown, B., Nešić, S., “Electrochemical Model of Sour Corrosion of Mild Steel - Validation at High H<sub>2</sub>S Partial Pressures”, NACE International Corrosion Conference, New Orleans, LA, 2017.

## APPENDIX B: SAFETY

H<sub>2</sub>S is a life threatening gas, even at any concentration as low as 10 ppm. It affects oxygen utilization in the human body through binding with hemoglobin in the blood. Throughout this study the experiments containing H<sub>2</sub>S gas at concentrations above 100 ppm were conducted in a secure, specially equipped room at the institute. The H<sub>2</sub>S laboratory is equipped with multiple sensors in order to detect any H<sub>2</sub>S gas leakage at concentrations as low as 1 ppm. Figure 67 shows the layout of these sensors in the room. There are multiple scrubbers in the room that remove H<sub>2</sub>S gas before any is released to the atmosphere, including any scenario where the combustion system does not activate. If any two of the fixed wall sensors detects H<sub>2</sub>S gas at 10 ppm or more the combustion system is activated. This burns the H<sub>2</sub>S gas in order to prevent any release into the atmosphere. In emergency cases, the alarm system goes off and sends an emergency message to 911. The laboratory will be evacuated immediately until the H<sub>2</sub>S release is resolved.

Any person who will work with H<sub>2</sub>S gas shall attend and be certified in the annual H<sub>2</sub>S safety course. In operating conditions, the person entering the room shall be suited with a self-contained breathing apparatus (SCBA). A second person similarly equipped, or “buddy”, shall be present outside of the room at all times.


 Advanced

ID	Description	Status	PPM
Sensor 1	Manifold	OK	0
Sensor 2	Manifold	OK	0
Sensor 3	Storage	OK	0
Sensor 4	Storage	OK	0
Sensor 6	Vent Exhaust	OK	0
Sensor 7	Floor H2S	OK	0
Sensor 8	Cabinet H2S	OK	0
Sensor 9	South Wall West End	OK	0
Sensor 10	South Wall West End	OK	0
Sensor 11	South Wall Center	OK	0
Sensor 12	South Wall Center	OK	0
Sensor 13	South Wall Gas Storage Cabinet	OK	0
Sensor 14	South Wall Gas Storage Cabinet	OK	0
Sensor 15	Center of Room AutoClave	OK	0
Sensor 16	Center of Room AutoClave	OK	0
Sensor 19	North Wall East End	OK	0
Sensor 20	North Wall East End	OK	0
Sensor 21	East Wall	OK	0
Sensor 22	East Wall	OK	0
Sensor 23	Exit of Scrubber	OK	0
Sensor 24	Exit of Scrubber	OK	0

Figure 67: H<sub>2</sub>S detection sensor layout in the H<sub>2</sub>S laboratory.



**OHIO**  
UNIVERSITY

Thesis and Dissertation Services